Technische Universität München

Fakultät für Maschinenwesen

Lehrstuhl für Windenergie

Numerical simulation of wind farm control

Chengyu Wang

Vollständiger Abdruck der von der Fakultät für Maschinenwesen der Technischen Universität München zur Erlangung des akademischen Grades eines

Doktor-Ingenieurs (Dr.-Ing.)

genehmigten Dissertation.

Vorsitz:	Prof. Rafael Macián-Juan, Ph.D.
Prüfer der Dissertation:	1. Prof. Dr. Carlo Bottasso
	2. Prof. Rafael Palacios, Ph.D.

Die Dissertation wurde am 18.12.2020 bei der Technischen Universität München eingereicht und durch die Fakultät für Maschinenwesen am 23.02.2021 angenommen.

Technische Universität München
Fakultät für Maschinenwesen
Lehrstuhl für Windenergie
Boltzmannstraße 15
D-85748 Garching bei München
Germany
Tel.: +49 (0) 89 / 289 – 16681
Fax.: +49 (0) 89 / 289 – 16611
Email: info@wind.tum.de
Web: www.wind.mw.tum.de

ABSTRACT

This dissertation develops digital wind turbine models and uses computational fluid dynamics (CFD) tools to simulate and explore various wind farm control strategies. The two main research methods applied are computational fluid dynamics (CFD) simulation and wind tunnel experimentation. While experimental measurements serve to validate the numerical results obtained with CFD, the detailed insights enabled by CFD help explain physical mechanisms in the experiments. In previous works conducted by the Wind Energy Institute of TUM, a scaled wind turbine model named G1 was designed to conduct experiments on the turbines in the wind tunnel. The G1 is a three-bladed clockwise-rotating wind turbine designed to display a natural energy conversion process and wake behavior. The rotor size of the model resulted from a compromise between Reynolds number mismatch, miniaturization constraints, limited wind tunnel blockage, and the ability to simulate multiple wake interactions within the wind tunnel. The G1 is capable of active individual pitch, torque, and yaw control, meaning that modern control strategies at the turbine and farm levels are feasible. In this work, a digital duplicate of the G1 was developed and used for numerical simulations. One crucial step towards obtaining a high-quality digital copy is to estimate the airfoil polars. Given the small size of the airfoil, even modest manufacturing imperfections and regular blades wear can lead to deviations from the nominal shape. Thus, the airfoils were identified by a maximum likelihood method that explicitly considered all measurement uncertainties. The G1 digital model was used to conduct CFD simulations of various wind farms that were governed with different control strategies, including yaw misalignment control, dynamic induction control, and individual pitch control. The effects of each control strategy were validated with experimental data, while the physical mechanism of each strategy was explained. Thanks to the controlled and repeatable environment that prevails inside the wind tunnel, it was possible to evaluate the effects of all the control mentioned above strategies with high levels of accuracy and reliability. Since all these works were done with the scaled model G1, an important question remains to be answered: How accurate are the wakes compared to actual ones in the field? It is crucial to quantify the level of realism of wind tunnel simulated wakes and identify which aspects faithfully represent the full-scale truth and which aspects do not. For this purpose, a full-scale turbine model was designed simulated with the same CFD code. The full-scale model was designed with realistic airfoil and structural constraints, and it matches the non-dimensional circulation distribution of the G1 for the majority of the blade span in the meantime. The CFD simulation results of the full-scale turbine and G1 were compared for both wind-aligned and misaligned conditions. Various metrics were compared, including wake shape, path, speed profile, Reynolds shear stresses, and power available at downstream locations. The comparison demonstrates that the physical processes associated with a scaled wind turbine operated in a wind tunnel can be highly representative of the full-scale turbine operating in the field, showing that the research findings for scaled wind farms can be used as a proxy for full-scale wind farm wake behaviors.

ACKNOWLEDGMENTS

I would like to thank my supervisor, Professor Carlo L. Bottasso, who granted me the opportunity to research wind energy as a Ph.D. candidate. Your guidance and advice are extremely valuable for my academic life. Your generosity and kindness are worth learning during my whole life.

I want to appreciate my mentor, Dr. Filippo Campagnolo, who guided me during the four years of research by giving theoretical instructions and sharing valuable data. I want to express my appreciation to a friend and previous colleague, Jiangang Wang, who educated and supported me intensively during the initial phase of my work.

I also want to thank all the current and previous members of the Wind Energy Institute at TUM: Alberto, Arturo, Bastian, Bruno, Carlo S., Elli, Franz, Helena, Johannes, Manos, Pietro, Robert, Siva teja, Stefan, Stefano, and Robin. The collaboration among us has been a great pleasure.

I want to appreciate our project partners at Imperial College London, Professor Rafael Palacios, Dr. Sylvain Laizet, Dr. Georgios Deskos, and Arturo Muñóz-Simon. The collaboration with you was a valuable chance to learn and a nice experience.

My thanks should also be expressed to all the students whom I had chances to supervise: Arijit, Daniel B., Daniel C., Fabio, Fanglin, Jorge, Martin, Santiago, and Stefania. As I supervised you, I also learned from you.

Last but not least, I would like to thank my mother, Hong Li, my father, Ziyu Wang, and my uncle, Hang Li. You have supported me mentally to go through all difficulties since I went abroad six years ago till the destination.

Contents

CHAPTER 1

Introduction

The growth rate of primary energy consumption over the past ten years is, on average, 1.6% per year. Although the main sources of primary energy are still traditional ones such as oil and coal, renewables have grown by a record increment, making the largest contribution (41%) to growth in primary energy, with the level of renewable power generation exceeding nuclear power for the first time. The wind made the largest contribution to the growth of renewables, followed closely by solar [1]. According to the latest statistics of the World Wind Energy Association, the overall capacity of all wind turbines installed worldwide reached 650.8 GW by the end of 2019. After hydropower, wind energy has become the second-largest contributor to renewable energy. A clear advantage of wind energy compared to oil and coal is its cleanliness. The carbon footprint of coal is almost 90 times larger than that of wind energy. In addition, compared with other renewables, wind energy has a very low relative carbon footprint [2].

The key to facilitating the growth of wind energy is to decrease the levelized cost of energy (LCOE). The cost range of onshore turbines can be as low as 33 $/MWh, while the lowest value for offshore turbines can be 83 $/MWh [3]. Together with improving aerodynamic efficiency and decreasing maintenance costs, wind farm control is an important method to decrease LCOE. Wind farm control can be employed to improve power capture and reduced loading [4, 5], and it can also serve to fulfill the provision of grid [6], e.g., by tracking the power requirement of the grid [7, 8].

The goal of this dissertation is to build up high-fidelity numerical tools to understand and explore wind farm control. The numerical tools include a fast and relatively low-fidelity blade element momentum model (BEM) and a high-fidelity computational fluid dynamics (CFD) model. The primary data used for this work is measurements obtained with scaled wind turbines operated in a boundary layer wind tunnel. Serving the final goal, three primary steps are taken as follows.

1. Build up and validate the numerical tools with wind tunnel measurements of scaled wind turbines and farms operated with various operating conditions.

2. Evaluate the effectiveness and explain the physical mechanisms of various wind farm control strategies applied to scaled wind farms by using numerical tools.

3. Demonstrate how realistic is the behavior and wakes of scaled wind turbines compared with full-scale turbines with numerical tools.

The validation of numerical tools with experimental measurements is paramount, and this step is typically non-trivial. In the last decade, a blind test of various numerical codes showed that the code predictions were not good enough: the power predicted by different codes in blind tests ranged from 25% to 175% of the measured value for a no-yaw, steady-state, and no-stall operating condition [9]. A well-validated numerical tool should be able to match the measurements under a wide range of operating conditions, and only such a tool is capable of giving plausible insights into the physical phenomena in wind farms. A fully validated CFD tool can be easily applied to turbines with different sizes, from a rotor diameter of several centimeters [10] to above one hundred meters [11]. The

comparison between the wakes of turbines with different sizes can indicate the level of realism of the turbine wakes measured in wind tunnels.

The turbine wakes play a vital role in wind farm control research. Wind turbine wakes are formed behind rotors and typically characterized by lower speed and higher turbulence intensity compared to the ambient flow. Wake interference among wind turbines not only results in power losses on downstream turbines [12], but also increases their fatigue loading significantly [13]. While power losses directly lead to a reduction in annual energy production, fatigue loading decreases turbine lifetime expectations and increases maintenance cost. Ultimately, both factors have negative effects on the cost of energy [11]. Mitigating such negative effects is a problem of major relevance in the field, and it has strong implications on the design and operation of wind power plants [14]. The emerging discipline of wind farm control is based on the concept of mitigating the effects of wake interactions by the cooperation and coordinated action of the various turbines within a farm. The effectiveness of such measures is typically associated with trade-off among turbines, as well as between power and fatigue loading. For example, a turbine located upstream can be deliberately yawed out of the wind to deflect its wake away from the downstream ones in order to boost the power of downstream turbines. However, such an action decreases the power of the upstream machine and increases the fatigue loading of the downstream machine, so there are already two pairs of trade-off in this scenario. Therefore, it is important to quantify relevant positive and negative effects with precise models.

In general, any mitigating action, either adopted for a newly designed wind farm or an existing wind farm – is based on two fundamental prerequisites: understanding the problem and being able to accurately model and simulate it. Due to the high sensitivity of turbine power to the inflow wind speed that is often influenced by wakes, the requirement for the accuracy of numerical models is high. Once the numerical models are well-validated, they can be used to evaluate subtle changes caused by various actions with high accuracy, abundant details, very low costs, and the best repeatability.

1.1 Research topics and innovative content

A wind farm is a typical example of a multi-scale physical problem, ranging from the diffusion of the flow of the order of Kolmogorov microscales [15] of 0.1 millimeters to the whole scale of a wind farm, which can be several kilometers [16]. The physical phenomena are complex, while numerical modeling is challenging. To understand the complex phenomena at play in wind farms, it is necessary to employ both experimental and numerical methods. Wind tunnel experiments [17] form the basis of this investigation and are used to validate the numerical models. Fully validated numerical models provide an insight into the physical processes operating inside wind farms and play an essential role in the mechanism-explanation of wake development and recovery. Numerical models are also employed to enable rapid testing of various control methods at a much lower cost than experimentation. When a control method is confirmed to be effective by both the wind tunnel experiment and numerical simulation, field testing can serve as the final validation.

1.1.1 Wind tunnel experiments

State of the art

The non-dimensional physical quantities can be calculated on the basis of the Buckingham π theorem [18]. This theory states: an equation with n variables and k dimensions can be rewritten with a set of $n-k$ dimensionless parameters that are constructed from the original variables. Modern wind turbines typically have large sizes, which makes field experiments very expensive or even impractical, especially regarding the control of boundary conditions. Based on the Buckingham theory, the investigation of small-scale wind turbines that can be operated in wind tunnels [17] can be a good substitute for direct research using full-scale turbines. Except for the much lower experiment costs, the ability to

control boundary conditions and measure detailed physical quantities are also major advantages of wind tunnel experiments.

Various types of scaled wind turbine models were tested in different wind tunnels. A simple way of developing a scaled turbine is to use a porous disk to model the wind turbine rotor according to the actuator disk method [19]. Although the turbine wake of such simple models is not distinguishable after 3D [20], it is impossible to research wind turbine control with them. The first wind tunnel test of a scaled turbine was conducted in [21], which was limited to laminar inflow cases when studying the near wake. A scaled turbine [9] with a rotor diameter of 10 m was used to study dynamic stall, rotational augmentation effects as well as the influence of the tower on wake recovery, and the study focused solely on experiments. The MEXICO project [22] validated both BEM and RANS-CFD models with a scaled turbine with a rotor diameter of 4.5 m. While this study reveals details of pressure distribution around airfoils and tip vortices shed by the rotor, little attention has been paid to wind turbine and farm control. LES-CFD simulations were conducted for a miniature turbine with a 0.15 m-diameter-rotor in [10]. The match between experiments and simulations was excellent. The turbine model matches the tip speed ratio of field-scale turbines, but its small size limits its ability to mimic the wake behavior of field-size turbines, while pitch control of the blades is not yet feasible. Later, a scaled turbine model G2 with a rotor diameter of 2 m, good aerodynamic properties, and full pitch, speed, and yaw control was developed and introduced in [17]. The turbine model is equipped with both pitch and torque systems as well as various types of sensors, which allow it to be used for conducting non-aerodynamic and non-standard experiments. G2 was tested in a wind tunnel [23] in Politecnico di Milano with a cross-section area of 52.44 m^2. Similarly, another scaled turbine MoWiTO [24] with a diameter of 1.8 m was designed, and the model is capable of individual pitch control. MoWiTO was tested in the wind tunnel of the University of Oldenburg that has a cross-section of 9 m^2. A drawback of both G2 and MoWiTo is their relatively large sizes compared to the cross-section of the corresponding wind tunnels, which might result in a blockage effect that hinders its suitability for use in investigations of wind farm control, where a cluster of turbine models is typically desirable.

The G1 is a smaller turbine model with a rotor diameter of 1.1 m, which was designed to support wind farm control research [25]. The size of the G1 represents a design compromise between Reynolds mismatch, miniaturization constraints, limited wind tunnel blockage, and the ability to simulate multiple wake interactions in the wind tunnel. The G1 model is capable of the individual pitch, torque, and yaw control to enable its use in testing modern control strategies at both turbine and farm levels. The G1 model was also operated in the wind tunnel in Politecnico di Milano. Therefore, the G1 model is one of the main objects of investigation employed in this study.

Innovative contribution

The G1 model is used to test three different kinds of wind farm control strategies. Although the author of this dissertation did not participate in the experiments directly, the author performed numerical simulations and data post-processing for the tests.

The first application is the yaw misalignment control, one of the most promising methods to increase wind farm power. Yaw control can be used both to increase wind farm power [26, 27] and alleviate loads [28], and it is even considered during the design of wind farm layouts [29]. The focus of this work is about power increase.

While most studies in the literature present the effectiveness of yaw control based only on CFD studies, few results were obtained from experiments. In addition, detailed measurements of flow and turbine power have not been conducted for this control strategy. In this work, a measurement of the mean flow speed on a horizontal slice for a scaled wind farm was shown, together with detailed measurements of turbine power and thrust. In the experiment, three misaligned G1 wind turbines were put into operation in the wind tunnel. The power and thrust were measured by the on-board sensors. A novel aspect of the experiment was the measurement of flow using two scanning LiDARs [30]. The LiDARs scanned the flow field to obtain an average flow field by averaging the scanned data over

multiple passes. Measurements were conducted for both wind turbines with greedy control and those with optimal yaw misalignment control. The results reveal the path of the wake and the mechanism of power enhancement by the yaw misalignment control. The secondary deflection effects caused by a yawed wind turbine was observable from the measurement data.

The second verified control strategy is dynamic induction control (DIC), a novel method that exploits natural instabilities in the near-wake vortex structures so as to enhance wake recovery [31, 32]. This strategy was first obtained by numerical simulation using the actuator disk method (ADM), then first validated experimentally in the wind tunnel [33]. The technique works by sinusoidally varying the rotor thrust in an open-loop; when performed at the right frequency, this perturbation has the effect of speeding up the breakdown of the vortex and enabling the recovery of the wake.

In [31, 32], only simulation results were presented, and there were no corresponding experiments. In the wind tunnel in Politecnico di Milano, experiments with a cluster of three aligned G1 wind turbines were conducted in the wind tunnel to study the parametrization of the DIC control. The experiments specifically studied the relationship between wind farm power and the non-dimensional Strouhal number. An increase in wind farm power was observed for the proper values of the Strouhal number.

The third control method tested is individual pitch control (IPC) that reduces the periodic loads caused by shear and wind misalignment using pitch activity [34].

While the load-reduction function of IPC is already indisputable [35], the impact of IPC on turbine wake has not previously been studied in detail, especially for wake-steering turbines with yaw misalignment. Therefore, wind tunnel experiments were conducted with G1 models in different yaw misalignment conditions with and without IPC control. While a significant load reduction was observed, the influence of IPC on wake path, wake recovery, turbine power, and wind farm power was quantified in detail. The effects attributable solely to IPC can be isolated from the other factors by analyzing the experimental data.

1.1.2 Parameter identification

State of the art

Airfoil polars are used for modeling the aerodynamics of rotors using lifting lines, in conjunction with blade element momentum (BEM) and computational fluid dynamic (CFD) models. BEM methods are routinely used for the aeroservoelastic analysis of wind turbines and provide most of the industrial-level simulation capabilities for load analysis nowadays, design, and control development activities [36].

One crucial component of the simulation chain has been a method for estimating the polars directly from the operational data of the turbines [37]. In fact, the blades of scaled wind turbine models operate in low Reynolds regimes, where even relatively small changes in the operating conditions can cause significant changes in the aerodynamic characteristics of the blade sections. In addition, given the small size of these models, even modest manufacturing imperfections and normal wear of the blades can lead to deviations from their nominal shape. Using the method of [37], the nominal airfoil polars are augmented with parametric correction terms, which are identified using a maximum likelihood (ML) criterion based on operational power and thrust measurements.

These measurements were collected on the turbine at various operating conditions, selected in order to span the desired range of angles of attack and Reynolds numbers. Since a large number of free parameters are necessary to represent the correction terms, the resulting problem is ill-posed, and the parameters are collinear. To address this issue, the original parameters are transformed into a new orthogonal set by using the singular value decomposition (SVD). Because the new parameters are uncorrelated with each other, one can select an observability threshold, discard the unobservable set and solve only for the observable one. After having solved the identification problem, which is now well-posed, the solution is mapped back onto the space of the original physical parameters.

Innovative contribution
Although the traditional maximum likelihood method works well in practice, it still suffers from assumptions that limit its effectiveness. Indeed, the classical ML formulation is based on an input-output model and assumes errors in the outputs only [38, 39]. Following this approach, outputs differ from available measurements because of measurement errors and model deficiencies. However, errors are not explicitly accounted for in the inputs, which are assumed to be equal to their measured values. In the present context, inputs represent the operating conditions of the turbines, which are expressed by the ambient air density and wind speed, the rotor angular velocity, and the blade pitch setting. Errors in such quantities have a non-negligible effect on the outputs and should be taken into account in a rigorous statistical sense.

To address this issue, the present dissertation proposes a new general formulation of ML identification that includes errors both in the outputs and in the inputs. This generalized formulation leads to an optimization problem in the model parameters and the unknown model inputs, which can now differ from their measured values. The proposed method is again cast within the SVD-based reformulation of the unknowns to deal with the ill-posedness and redundancy of the parameters. A few measures to accelerate the identification, including a filtering technique, are proposed and applied. In addition, the new method considers the dependency of polars on the Reynolds number and the corresponding constraints. The new formulation was applied to the identification of the polars of small-scale controlled wind turbines developed to support wind farm control and wake research [33, 40, 41].

1.1.3 Computational Fluid Dynamics

State of the art
CFD simulation of wind turbines has been a major object of investigation for more than a decade. The practice began with Reynolds-averaged Navier–Stokes (RANS) simulations of turbines, for instance, the simulation of near wake behavior with RANS equations in [42]. [43] simulated wind turbine clusters and compared RANS to the higher-fidelity large-eddy simulation (LES) method, which showed that RANS was not sufficiently accurate, as it typically displayed excessive numerical diffusion. Thanks to improvements in computational power, LES has been increasingly adopted by the wind farm research community due to its ability to resolve more features in the flow and to deliver more accurate results. For example, the LES results shown in [10] match extremely well with the experimental measurements. Later, an open-source software SOWFA [44] based on the open-source repository OpenFOAM [45] has become one of the most important CFD tools for use with wind farms. Results in [44] demonstrate the ability of SOWFA to simulate turbines with yaw misalignment with high accuracy.

Besides the turbulence model, the way that the turbine is modeled is critical to the accuracy of the results. The actuator disk method (ADM) was the first to be widely used. It has non-rotating and rotating versions, as shown in [10]. However, the actuator disk model does not directly resolve the locations and motions of turbine blades, which can result in a loss of fidelity, especially in the near wake. The actuator line method (ALM) proposed in [46] models the blades directly and gives results that match well with measurements. It is gradually becoming one of the most widely used methods for wind turbine LES. The BEM code FAST [47] can be used in conjunction with ALM to model wind turbine blades. A similar method to ALM, known as actuator curve embedding (ACE), was put forward in [48]. One of the major differences between ACE and ALM is the way in which they compute body forces. While ALM loops over all actuator points and projects body forces in spherical regions using a Gaussian function with a kernel ϵ, ACE loops directly over cells and can project body forces in cylindrical domains. Nevertheless, ALM and ACE are both capable of capturing the major characteristics of the blade-flow interaction, while the former has been adopted and discussed more widely. The simulations in this study are conducted with ALM. One major topic of discussion with ALM is the choice of Gaussian kernel ϵ, as it directly influences the power prediction of the turbine

model. While some authors suggest that it should be chosen as a constant multiple of the grid size [49], some prefer choosing ϵ as distribution along the blade span [50]. Other approaches were discussed in great detail using LES with a relatively dense mesh [51] or coarse mesh [52]. There is no consensus on a unique method of body force projection since different rotors were investigated. Nevertheless, it is clear that realistic flow solutions typically have a relatively small kernel compared to the chord of the blade, while a kernel that is too small results in numerical instabilities. While blades are the most relevant components in aerodynamics, the nacelle and tower also influence the wake of a turbine. For full-scale turbines, the impact of the nacelle and tower is so small that it is neglected by many researchers. Nevertheless, [53] models the nacelle and tower with ALM and obtains reasonable results. One shortcoming of such a model is that it cannot prevent the flow from going through the body of the nacelle and tower. Models with higher fidelity are therefore desirable, especially for scaled wind turbines operated in wind tunnels since the relative sizes of nacelle and tower are typically larger when compared with full-scale turbines.

Innovative contribution

The CFD simulations in this study were conducted with SOWFA. Since it is open-source, it can be modified to enable the use of SOWFA in simulations of scaled wind turbines. This study uses ALM to model wind turbine blades. A tip loss model has implemented such that the blade tip loads are much smaller than they would be without the tip loss model. This slight modification avoids non-physical high loading being predicted at the tip. Rather than using ALM as described in [53], this work uses the immersed boundary method [54] to model the nacelle and tower, which solves the issue of flow passing through the bodies of the nacelle and tower and allows accurate modeling of the surfaces. In this work, the airfoil polars are identified from measurements such that the power and thrust predictions of BEM simulations match the experiments. Rather than attempting to find a universal approach to distributing the body force for different kinds of rotors, the ϵ distribution of G1 is tuned to match the blade load distribution predicted by BEM simulation. A direct result of matching the blade load distribution is the match of power. Therefore, a customized choice of ϵ results in the highest possible accuracy for CFD simulations.

The FAST and SOWFA codes were modified significantly to enable the implementation of various types of wind turbine and wind farm controllers, respectively. While most researchers simulate wind turbines rotating at constant rotor speed [10, 44], realistic turbines are able to accelerate in accordance with the unbalance between the generator torque and the aerodynamic torque. As reported in [55], if the generator torque controller is properly implemented in the CFD simulation, the rotor speed fluctuates in a similar manner to the measured value, while the spurious and non-physical oscillation of the rotor power with constant-rotor-speed can be eliminated. Turbine controllers for dynamic induction control and individual pitch control, as described above, were implemented and validated with experimental power, thrust, and wake data. The implementations included dynamic induction control, individual pitch control, yaw misalignment control on the wind turbine level, and gradient-based control on the wind farm level.

Another innovation of this study is the precursor simulations. Common methods of precursor simulation include atmospheric simulation by CFD [56] and engineering models such as TurbSim [57]. The approach taken in this work differs from those commonly adopted but is the most suitable for use in wind tunnel applications with a passive method of generating turbulence. A cluster of spires was placed close to the inlet of the wind tunnel to create turbulence. The process was replicated digitally by generating a high-quality structured spire mesh and using it for LES. The precursor simulation aims to match both the horizontal and vertical wind shear as well as the turbulence intensity distribution by adopting an iterative approach. In the first iteration, a uniform inflow condition was used for the precursor simulation, while for subsequent iterations, the inflow speed was rendered non-uniform by taking the mismatches between the simulation and experiment results in the previous iteration into account. After several iterations, it was possible to achieve an excellent match of the mean wind speed

distribution. The precursor simulation was conducted for two different cases, a medium turbulence intensity setup that corresponds to typical offshore conditions and a high turbulence intensity one that represents onshore situations.

1.1.4 Comparison between different scales

State of the art

Wind turbine wakes are a primary form of coupling within a wind plant. Therefore, understanding their behavior and being able to accurately simulate their effects are important problems in wind energy science nowadays, which have direct practical payoffs on design, operation, and maintenance. Wake effects have been researched in many recent works [17, 25, 58–61] in great detail.

Compared with full-scale field testing, wind tunnel experiments have many important advantages, including repeatable inflow conditions, detailed flow measurements, and limited costs. Controlled and repeatable wind tunnel tests contribute significantly to the current understanding of wind turbines and farms, generating valuable data for the validation and calibration of mathematical models, offering opportunities for the verification of control technologies.

These features are advantageous, but a critical question still remains to be answered: how realistic are the wakes obtained in the wind tunnel compared to actual ones in the field? Without this question being properly answered, it is still reasonable to doubt the actual usefulness of wind tunnel testing based on a perceived lack of realism of scaled tests. An analysis of the scaling effect was performed by [62], considering the effects caused by the mismatch of the rotor-based Reynolds number. Experimental results based on a miniature wind turbine showed that wake behavior is unaffected by this parameter when it is larger than $9.3 \cdot 10^4$. However, in reality, the behavior of the blades and the wake is much more strongly affected by the chord-based Reynolds number, as initially discussed in [17]. In addition, there are many other factors driving differences in wakes, including circulation distribution and different torque coefficient. Although there are plenty of CFD simulations for both full-scale turbines [11, 44] and scaled turbines operated in wind tunnels [10], a rigorous comparison between wakes of scaled and full-scale turbines has not been conducted. Therefore, it is important to quantify the level of realism of wind tunnel simulated wakes and to identify which aspects faithfully represent the full-scale truth and which aspects do not.

Innovative contribution

Following [58] and [63], dimensional analysis has been done to review the main factors driving wake behavior. The analysis also reveals which physical aspects of full-scale wakes cannot be matched at the reduced scale with the considered experimental setup. In fact, the much lower Reynolds regime of a small scale model compared to a full-scale machine implies very different aerodynamic characteristics of the blade airfoils, which in turn drive a number of specific design choices of the scaled model [58, 63]. Due to the relatively lower efficiency of the airfoils used by scaled turbine models, the models typically have a lower power coefficient compared to full-scale ones.

With the aim to conduct a rigorous comparison between different scales, full-scale turbines were designed that match some of the scaled-model parameters. Various versions of these models were considered, ranging from a more realistic full-scale turbine —with a larger number of mismatched effects with respect to the scaled model— to less realistic ones that match more quantities of the scaled model.

The investigation mainly depends on the validated LES-ALM simulation framework [40]. The simulation tool was used to simulate both full-scale and scaled wind turbines. The underlying assumption is that, since the code was found to be in very good agreement with measurements obtained in the scaled experiments, the same code based on the same numerical setup should deliver results of similar accuracy even at full scale. The numerically simulated scaled and full-scale wakes were compared. The comparison reveals the similarities and discrepancies between wakes of scaled and full-scale turbines.

Factors that drive discrepancies in the wakes were identified. It was found that the level of realism of the G1 wake is high enough to justify the usefulness of wind tunnel experiments.

1.2 Publications

Eight publications are included in this dissertation. Figure 1.1 presents an overview of these publications, grouped according to category.

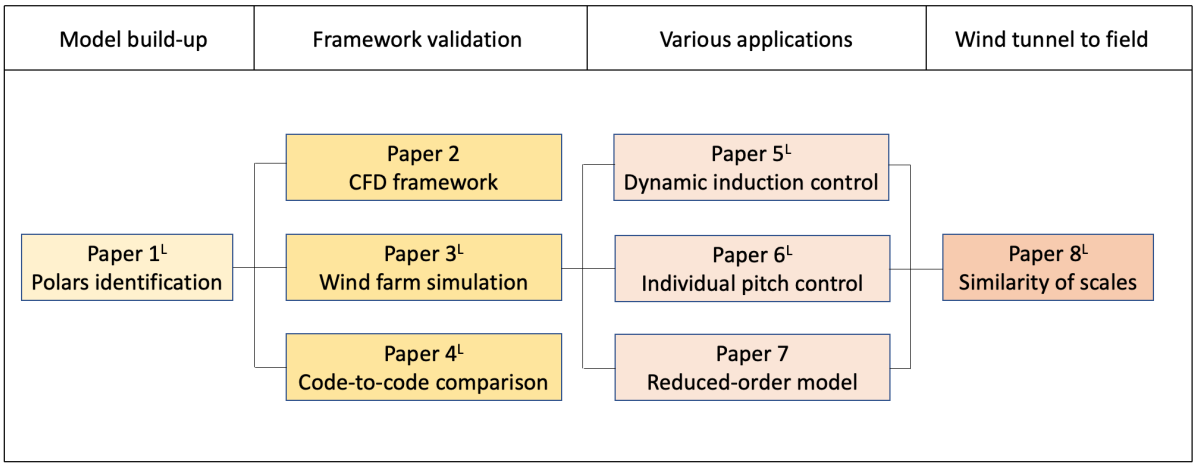

Figure 1.1: Research topic and publications.

Paper 1 proposes the system identification method used to identify the polars of the scaled G1 wind turbine model. In this section, the BEM G1 model is built and validated. Next, the CFD simulation framework is validated in accordance with various aspects. **Paper 2** serves as a basic validation work by comparing the inflow and turbine wake profiles between simulations and experiments. **Paper 3** goes one step further by including a generator torque controller in the CFD simulation. This paper also validates the yaw misalignment wind farm control strategy. **Paper 4** compares the second-order finite volume method that is used in this dissertation with a sixth-order compact finite difference scheme. The objective was to study whether a second-order solver is generally sufficient for resolving dominant physical phenomena in wind farms. Then, the simulation framework is applied to a variety of applications, including the dynamic induction control presented in **Paper 5**, the individual pitch control discussed in **Paper 6**, and the reduced-order model of the computation-intensive CFD proposed in **Paper 7**. All aforementioned papers are based on the scaled wind turbine model G1, the aim being to conduct a thorough validation of the CFD framework. The final topic in this dissertation responds to the question of how realistic the wind tunnel experiments conducted with scaled wind turbine models are. The answer to this question is discussed in detail in **Paper 8**, by comparing CFD simulations of scaled wind turbines with full-scale ones. The results indicate a strong resemblance between the dominant physical phenomena of the two different scales, with only minor limited mismatches displayed. Paper 8 has been submitted, while other papers have been published.

Publications lead by the author:

- **Paper 1**: C. Wang, F. Campagnolo, and C. L. Bottasso, "Identification of airfoil polars from uncertain experimental measurements," *Wind Energy Science*, vol. 5, pp. 1537–1550, 2020. doi: https://doi.org/10.5194/wes-5-1537-2020

- **Paper 3**: C. Wang, J. Wang, F. Campagnolo, D. Carraón, and C. Bottasso, "Validation of large-eddy simulation of scaled waked wind turbines in different yaw misalignment conditions," in *Journal of Physics: Conference Series*, vol. 1037, no. 6. IOP Publishing, 2018, p. 062007. doi: 10.1088/1742-6596/1037/6/062007

- **Paper 4**: C. Wang, A. Muñóz-Simon, G. Deskos, S. Laizet, R. Palacios, F. Campagnolo, and C. Bottasso, "Code-to-code-to-experiment validation of les-alm wind farm simulators," in *Journal of Physics: Conference Series*, vol. 1618, no. 6. IOP Publishing, 2020, p. 062041. doi: 10.1088/1742-6596/1618/6/062041

- **Paper 5**: C. Wang, F. Campagnolo, A. Sharma, and C. Bottasso, "Effects of dynamic induction control on power and loads, by les-alm simulations and wind tunnel experiments," in *Journal of Physics: Conference Series*, vol. 1618, no. 2. IOP Publishing, 2020, p. 022036. doi: 10.1088/1742-6596/1618/2/022036

- **Paper 6**: C. Wang, F. Campagnolo, and C. Bottasso, "Does the use of load-reducing IPC on a wake-steering turbine affect wake behavior?" in *Journal of Physics: Conference Series*, vol. 1618, no. 2. IOP Publishing, 2020, p. 022035. doi: 10.1088/1742-6596/1618/2/022035

- **Paper 8**: C. Wang, F. Campagnolo, H. Canet, D. J. Barreiro, and C. L. Bottasso, "How realistic are turbine wakes in wind tunnel tests?" *Wind Energy Science, in review*, 2020. doi: https://doi.org/10.5194/wes-2020-115

Publications with significant scientific contribution by the author:

- **Paper 2**: J. Wang, C. Wang, F. Campagnolo, and C. L. Bottasso, "Wake behavior and control: comparison of les simulations and wind tunnel measurements," *Wind Energy Science*, vol. 4, no. 1, pp. 71–88, 2019. doi: https://doi.org/10.5194/wes-4-71-2019

- **Paper 7**: A. Fortes-Plaza, F. Campagnolo, J. Wang, C. Wang, C. Bottasso *et al.*, "A POD reduced-order model for wake steering control," in *Journal of Physics: Conference Series*, vol. 1037, no. 3, 2018. doi: 10.1088/1742-6596/1037/3/032014

CHAPTER 2

Methods

This study began by taking experimental measurements of scaled wind turbines and their wakes in a boundary layer wind tunnel, with the aim of building and validating numerical simulation tools. The tools include a computational fluid dynamics (CFD) framework and digital models of scaled wind turbines. Wind turbines were measured and simulated under different operating conditions, so the simulation model is capable of matching experimentation not just under one set of operating conditions but generally.

The accuracy of the scaled wind turbine model is the most critical aspect of tool validation. While some properties of the model are directly measurable, e.g., chord distribution and rotor speeds, other quantities such as the lift and drag coefficients (polars) are not. In this study, the polars of blade airfoils were obtained using a polar identification method. Improvements in the identification method resulting from this study enable high-quality polar data to be obtained.

The simulation tool was applied to a set of applications to investigate wind farm control. This includes open-loop control schemes such as yaw misalignment control, individual pitch control (IPC), and dynamic induction control. A strategy of closed-loop wind farm control with gradient-based automatic yaw misalignment was also demonstrated. In all cases, a good match was obtained between simulation and experiment.

The validated simulation tool was then applied to full-scale turbines. The aim was to demonstrate the similarities and differences between scaled and full-scale turbines. The full-scale wind turbines were designed to match the characteristics of the scaled wind turbines. The airfoil properties of the full-scale turbines were simulated using high-resolution CFD with body-conforming mesh. Based on the simulation results of the scaled and full-scale wind turbines, it is possible to draw conclusions regarding the extent to which wind tunnel experiments can guide wind farm design and control.

Section 2.1 presents the experimental facilities, including the wind tunnel and the scaled wind turbines; Section 2.2 introduces the numerical model of the scaled wind turbine; Section 2.3 describes the polars identification method; Section 2.6 explains the large-eddy simulation scheme; Section 2.7 explains the method of numerically duplicating the turbulent inflow condition in the wind tunnel; and finally, Section 2.8 introduces the design and model of the full-scale turbine.

2.1 Wind tunnel experiments

A closed return wind tunnel [23] located in Politecnico di Milano in Italy was used for all the wind tunnel experiments presented in this work. Figure 2.1 shows the arrangement of the wind tunnel. The civil test section of the wind tunnel has a cross-section of 13.8 m × 3.8 m and a length of 36 m. It is big enough to contain an array of scaled wind turbines while at the same time avoiding significant blockage effects. A cluster of 14 fans in the lower layer of the wind tunnel can generate wind speeds of up to 14 m/s in the civil test section. A coordinate system for this test section is used consistently throughout this work and is shown in Fig. 2.1. The origin of the coordinate system is located at the center bottom of the inflow slice of the test chamber, as indicated in Fig. 2.1. The x-axis points downstream along the streamwise direction while the z-axis points vertically up.

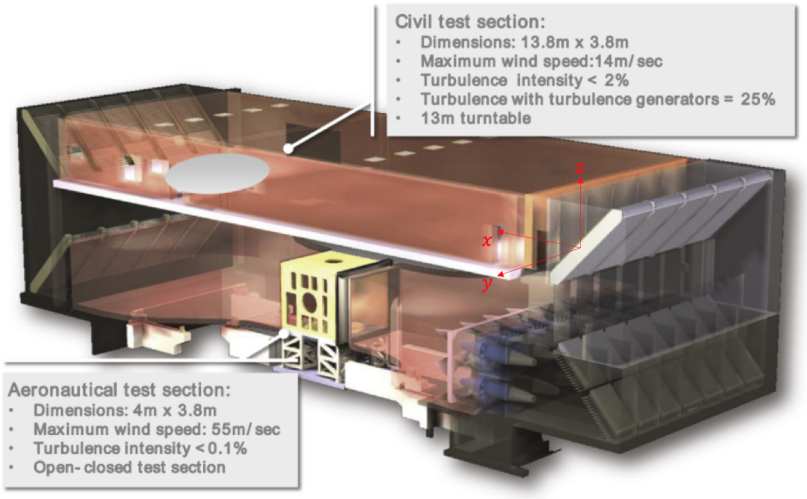

Figure 2.1: Structure of the wind tunnel. The upper low-speed test section is used in this work [23].

The turbulence intensity in the civil test section is about 1% if no spires are placed in the wind tunnel. However, a flow with a higher turbulence intensity is typically more useful for wind energy applications because it better mimics the atmospheric boundary layer. There are several ways of generating turbulence in the wind tunnel, such as passive and active grids [70, 71], pressurized tubes [72], active air-jet [73], and spires and roughness elements [74, 75]. For the wind tunnel used in this study, spires and roughness elements were used to generate the turbulence [74]. Different turbulence intensities can be triggered with spires of different numbers, positions, and shapes. Typical onshore and offshore turbulence was replicated experimentally in the wind tunnel.

Scaled wind turbine models of different sizes were designed by the Technical University of Munich and Politecnico di Milano for the purpose of investigating wind farm control in wind tunnels, resulting in a three-bladed scaled wind turbine model G1 [25]. Fig.2.2 shows the layout of the G1. It has a rotor diameter of 1.1 m and a rated rotor speed of 850 rpm. It is equipped with a closed-loop control system that permits active yaw control and individual pitch control. G1 mimics the aerodynamic properties of full-scale wind turbines and can be used to investigate wind farm control in the wind tunnel.

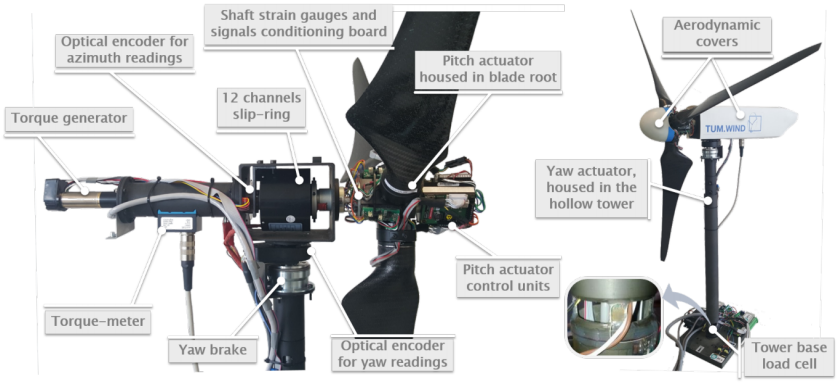

Figure 2.2: G1 model layout [25].

2.2 Turbine numerical model

Two different aerodynamic models are needed to support different simulation needs: a fast lower fidelity BEM for repetitive simulations during model identification and a high-fidelity CFD model for wake and wind farm research. The CFD model reuses the BEM model partially to include wind turbines in simulations.

2.2.1 BEM model

The numerical model of turbine blades used in this study is based on the blade element theory first proposed by William Froude (1878), David W. Taylor (1893), and Stefan Drzewiecki. It is assumed that the whole blade is subdivided into segments that operate relatively independently of each other. Each segment is modeled with a two-dimensional airfoil, whose properties can be either measured or estimated. Therefore, the theory links the behavior of a complex three-dimensional blade to the properties of two-dimensional airfoils, which simplifies the analysis. Loads of each blade element are computed according to the local flow condition. The total force and moment are obtained by integrating from the blade root to the tip. Despite its simplicity, the blade element theory has reasonable accuracy. The state-of-the-art approach to modeling blade-flow interaction is based on the blade element momentum (BEM) theory proposed by Glauert and Betz [76]. BEM methods are routinely used for the aeroservoelastic analysis of wind turbines and provide most of today's industrial-level simulation capabilities for load analysis and design and control development activities [77–79]. The blade-flow interaction to be solved by BEM works as follows: the flow applies lift and drag forces to the airfoil, while the airfoil results in the induction of the flow. Therefore, the solutions of forces and induction are coupled, so it is done iteratively. Despite the need for iteration, BEM simulation typically takes very little time to solve, and the accuracy is sufficient for many applications. The accuracy of polars is important for the quality of a BEM model. In this work, the polars were identified from experimental measurements using the BEM model instead of CFD. The polars identification requires evaluation of power and thrust under various operating conditions with different values of polars, typically for millions of times. Due to the constraints of time and resource consumption, the BEM model is a much more reasonable choice compared with a CFD model.

In this dissertation, an open-source code, FAST [47], based on BEM, is used to perform rapid simulation of turbines under laminar inflow conditions and different operating conditions. The BEM simulation of FAST takes into account the tip and hub losses of the blades as well as the axial and tangential inductions of the flow. The code is well-validated and widely used in industry and academic research. FAST models of all scaled and full-scale turbines used in this work were built and validated.

2.2.2 ALM-CFD model

The tool used to investigate turbine wakes and wind farm control is CFD simulation. The turbine models used in the CFD simulation are again the FAST ones. However, in the circumstance of CFD simulation, the flow induction is solved directly by CFD, rather than by using the BEM method. FAST and CFD are coupled through SOWFA [44]. SOWFA samples the velocity in the vicinity of the turbine blades and passes the results on to FAST, which computes the forces on each blade element before returning them to SOWFA. Following the approach proposed in [46], the forces $\mathbf{f}$ are projected as body forces $\mathbf{f}_\epsilon$ in the computational domain. For any point in the domain, the distance from that point to the blade point is noted as d, and the body force is then calculated as follows:

$$\mathbf{f}_\epsilon = \epsilon^{-2}\pi^{-3/2} exp[-(\frac{d}{\epsilon})^2]\mathbf{f}, \tag{2.1}$$

where ϵ is a parameter that affects the spread width of the body forces in the domain. As indicated by the formula, the body force decays exponentially with the distance d, and it is truncated when the distance is big enough. The choice of ϵ has an impact on the prediction of turbine power by indirectly influencing the velocity distribution in the blade vicinity. Decreasing ϵ results in more concentrated force distribution, which typically leads to lower power predicted by the model. Thus, the choice of ϵ has been investigated in many pieces of literature [49–52, 80, 81]. The use of very fine mesh, typically four cells across the chord of the blade, is an optimal way of choosing ϵ to obtain a highly realistic solution. However, such fine mesh is not usually feasible for wind farm simulations due to its excessive size. With a mesh of intermediate fineness, roughly equal to the chord of the blade, there is a trade-off between projecting body forces realistically and stabilizing the CFD solver. An excessively small ϵ causes the solver to crash due to a too concentrated body force, while an excessively big ϵ results in unrealistic force projection since the body force becomes high even far away from the blade. Inspired by the guideline [50], the value of ϵ is distributed along the blade span. However, the approach adopted in this study differs from the equivalent ellipse distribution proposed in [50]. The ϵ distribution is chosen, such that the blade load distribution along the blade span matches the prediction of BEM simulations. In this way, CFD results are not only realistic but also consistent with BEM simulations.

2.3 Polars identification

Both BEM and ALM-CFD models rely on polars. The polars, including lift and drag coefficients, represent the aerodynamic characteristics of the airfoils used on the blade. Clearly, the quality of model outputs is directly related to the accuracy of the polars. However, it is non-trivial to obtain precise values. Traditionally, polars are obtained with wind tunnel experiments or numerical simulations for isolated airfoils. Both approaches are able to give accurate nominal values of polars. Nevertheless, there are many factors that make the actual polars of a specific blade be different from the nominal ones. The difference is not always negligible in terms of predicting turbine power and thrust. This dissertation proposes a novel approach for estimating polars based on operational turbine data. The methodology is based on a maximum likelihood method described in [82].

The method directly estimates the polars from the operational data of the turbines [37]. For wind tunnel applications, the blades of scaled wind turbine models operate in low Reynolds regimes, making the aerodynamic properties sensitive to changes in operating conditions. In addition, the small size of these models also increases the sensitivity of polars to manufacturing imperfections. Thus, medium deviations from the nominal shape lead to non-negligible differences between the actual and nominal polars. The method proposed in [37] augment the nominal airfoil polars with parametric correction terms identified using the maximum likelihood (ML) criterion based on operational power and thrust measurements. These turbine operational conditions are chosen with the purpose to span the required range of angles of attack and Reynolds numbers. There are four parameters to describe each operational condition, including the wind speed, air density, rotor speed, and blade collective pitch angle. Polars at different Reynolds number and angle attack are to be identified, giving a large number of unknown parameters, so the resulting problem is ill-posed, and the parameters are collinear. A special coordinate transformation is conducted using the singular value decomposition (SVD) method, and the new parameters are decoupled from each other and are sorted according to a descending observability order. Thus, truncation can be performed to discard weakly observable parameters. The transformation and truncation not only improves the posedness of the identification problem but also decreases the complexity and computational burden of it. The solution in the new coordinate space is then transferred back into the original space.

The maximum likelihood method, coupled with the SVD method, still has some limitations since the classical ML formulation assumes errors in the outputs only [83, 84]. Under such an assumption, differences between model outputs and experimental measurements can only be attributed to mea-

surement errors of outputs, model deficiencies, and errors in parameters. However, errors of model inputs are neglected, which is another important error source. In the context of polars identification, model inputs include wind speed, air density, rotor speed, and blade collective pitch angle. Errors of these quantities should be considered explicitly in the identification process. Hence, this study proposes a new general formulation of ML identification that includes errors both in the outputs and in the inputs. This generalized formulation produces an optimization problem not only for the model parameters but also for the actual model inputs. Despite the increased complexity, the computational costs are not increased significantly for several reasons. First, the optimization of polars and model inputs are done separately. The optimization problem is broken into two steps whose coupling is done by iterating among them. Second, the outer iteration is accelerated by providing high-quality initial guesses with a filtering technique. Third, the optimization of the model inputs must be done for each operating condition, but it can be separated into a series of decoupled inexpensive optimization problems. Fourth, the SVD-based coordinate transformation of the unknowns can still be applied to accelerate the identification, but it is limited to the model parameters. The concrete realization of these measures is discussed in the following.

Consider a system described by the parametric model

$$\boldsymbol{y} = \boldsymbol{h}(\boldsymbol{p}, \boldsymbol{u}), \tag{2.2}$$

where $\boldsymbol{u} \in \mathbb{R}^l$ are the inputs, including the air density, wind speed, blade pitch angle and rotor speed, $\boldsymbol{p} \in \mathbb{R}^n$ the model parameters, including the lift and drag coefficients by different angle of attack and Reynolds number, and $\boldsymbol{y} \in \mathbb{R}^m$ the outputs, including the power and thrust coefficients. In correspondence to the N inputs $\mathscr{U} = \{\boldsymbol{u}_1^*, \boldsymbol{u}_2^*, \ldots, \boldsymbol{u}_N^*\}$, N experimental measurements of the outputs are available and noted $\mathscr{Y} = \{\boldsymbol{y}_1^*, \boldsymbol{y}_2^*, \ldots, \boldsymbol{y}_N^*\}$. Because of modeling and measurement errors, the experimental measurements are in general not identical to the outputs predicted by the model (2.2), and there are differences that can be quantified by the residual $\boldsymbol{r} = \boldsymbol{y}^* - \boldsymbol{y}$. The goal of the estimation problem is to find the model parameters $\boldsymbol{p}$ that minimize the residuals $\boldsymbol{r}$.

The formulation of ML that accounts for errors both in the outputs and inputs requires to expand the parametric model (2.2) as

$$\hat{\boldsymbol{y}} = \left\{ \begin{array}{c} \boldsymbol{y} \\ \boldsymbol{u} \end{array} \right\} = \left\{ \begin{array}{c} \boldsymbol{h}(\boldsymbol{p}, \boldsymbol{u}) \\ \boldsymbol{u} \end{array} \right\}. \tag{2.3}$$

Given the modeling and measurement errors, the experimental output measurements $\boldsymbol{y}^*$ are in general not identical to the model-predicted outputs $\boldsymbol{y}$, while the experimental inputs $\boldsymbol{u}^*$ are in general not identical to the nominal ones $\boldsymbol{u}$. These differences can be synthetically quantified by the residual $\hat{\boldsymbol{r}} = \hat{\boldsymbol{y}}^* - \hat{\boldsymbol{y}}$, where now $\hat{\boldsymbol{y}}^*$ is an expanded vector that contains measurements of both outputs and inputs:

$$\hat{\boldsymbol{y}}^* = \left\{ \begin{array}{c} \boldsymbol{y}^* \\ \boldsymbol{u}^* \end{array} \right\}. \tag{2.4}$$

The goal of the estimation problem is to find the model parameters $\boldsymbol{p}$ and system inputs $\boldsymbol{u}_i$ that maximize the probability of obtaining the measurements $\boldsymbol{y}^*$ and $\boldsymbol{u}^*$. According to the maximum likelihood criterion, the goal of the optimization is

$$\boldsymbol{p}, \boldsymbol{u}_1, \ldots, \boldsymbol{u}_N = \arg\min_{\boldsymbol{p}, \boldsymbol{u}_i} \frac{1}{2} \sum_{i=1}^{N} w_i^2 \hat{\boldsymbol{r}}_i^T(\boldsymbol{p}, \boldsymbol{u}_i) \hat{\boldsymbol{R}}^{-1} \hat{\boldsymbol{r}}_i(\boldsymbol{p}, \boldsymbol{u}_i), \tag{2.5}$$

where w_i is the weighting for each experimental measurement. The weighting is assigned since different conditions have different probabilities and significance in turbine operations. The error covariance matrix is calculated as

$$\hat{\boldsymbol{R}} = \frac{1}{N} \sum_{i=1}^{N} w_i^2 \hat{\boldsymbol{r}}_i(\boldsymbol{p}, \boldsymbol{u}_i) \hat{\boldsymbol{r}}_i^T(\boldsymbol{p}, \boldsymbol{u}_i). \tag{2.6}$$

The optimization problem is decoupled by the following iteration:

1. Initialize $\boldsymbol{p}$ and set $\boldsymbol{u}_i = \boldsymbol{u}_i^*$, $i = [1, N]$.

2. Calculate $\hat{\boldsymbol{R}}$ from Eq. (2.6).

3. Assuming temporarily frozen inputs $\boldsymbol{u}_i$, solve

$$\boldsymbol{p} = \arg\min_{\boldsymbol{p}} \frac{1}{2} \sum_{i=1}^{N} w_i^2 \hat{\boldsymbol{r}}_i^T(\boldsymbol{p}, \boldsymbol{u}_i) \hat{\boldsymbol{R}}^{-1} \hat{\boldsymbol{r}}_i(\boldsymbol{p}, \boldsymbol{u}_i). \tag{2.7}$$

   This is formally identical to the classical (error-in-the-outputs-only) ML formulation, which can be solved with the SVD-based re-formulation in terms of uncorrelated parameters [37].

4. Assuming temporarily frozen parameters $\boldsymbol{p}$, solve

$$\boldsymbol{u}_j = \arg\min_{\boldsymbol{u}_j} \frac{1}{2} \sum_{i=1}^{N} w_i^2 \hat{\boldsymbol{r}}_i^T(\boldsymbol{p}, \boldsymbol{u}_i) \hat{\boldsymbol{R}}^{-1} \hat{\boldsymbol{r}}_i(\boldsymbol{p}, \boldsymbol{u}_i), \qquad j = [1, N]. \tag{2.8}$$

   These are N decoupled small size problems that are inexpensive and give the values of the model inputs.

5. Return to step 2, and repeat until convergence.

To accelerate the iteration from step 2 to step 5, a filtering technique can be used to provide a better initial guess of $\mathbf{p}$ for step 1. The filtering uses a priori information on the expected uncertainties. The unknown true inputs $\boldsymbol{u}_i$ can be bounded as

$$\boldsymbol{u}_i^* - \Delta\boldsymbol{u} \le \boldsymbol{u}_i \le \boldsymbol{u}_i^* + \Delta\boldsymbol{u}, \tag{2.9}$$

where $\Delta\boldsymbol{u}$ are the expected uncertainty bounds. This a priori information can be used to retain in the cost function J only those measurements for which the corresponding residual cannot be simply explained by the uncertainties (2.9). The residual $\boldsymbol{r}_i$ is a function of $\boldsymbol{p}$ and $\boldsymbol{u}_i$, i.e.

$$\boldsymbol{r}_i(\boldsymbol{p}, \boldsymbol{u}_i) = \boldsymbol{y}_i^* - \boldsymbol{h}(\boldsymbol{p}, \boldsymbol{u}_i). \tag{2.10}$$

Indicating the j-th component of residual $\boldsymbol{r}_i$ as r_{i_j}, its maximum and minimum values for a given $\boldsymbol{p}$ are computed as

$$r_{i_j}^M = \max_{\boldsymbol{u}_i} r_{i_j}(\boldsymbol{p}, \boldsymbol{u}_i), \tag{2.11a}$$

$$r_{i_j}^m = \min_{\boldsymbol{u}_i} r_{i_j}(\boldsymbol{p}, \boldsymbol{u}_i), \tag{2.11b}$$

$$\text{subject to:} \quad \boldsymbol{u}_i^* - \Delta\boldsymbol{u} \le \boldsymbol{u}_i \le \boldsymbol{u}_i^* + \Delta\boldsymbol{u}. \tag{2.11c}$$

If the maximum $r_{i_j}^M$ and minimum $r_{i_j}^m$ have different signs, then $r_{i_j} = 0$ lies somewhere within this range, and hence this residual component can be fully explained by input uncertainties. Therefore, it cannot drive meaningful changes in the parameters and should be neglected. Otherwise, this residual carries valuable information and should be retained. To account for this, a filtered residual $\tilde{r}_{i_j}$ is defined as

$$\tilde{r}_{i_j} = \min(|r_{i_j}|). \tag{2.12}$$

The a priori estimates are used to initialize the parameters $\boldsymbol{p}$ at step 1 of the iterative algorithm. A standard ML method is used for the initialization, considering only errors in the outputs and replacing

the residual components r_{i_j} by the filtered ones $\tilde{r}_{i_j}$. Filtering accelerates the optimization because it avoids meaningless tuning of parameters caused by measurement noise.

Finally, another soft constraint is added for the identification to avoid unrealistic solutions. The typical Reynolds number distribution along a wind turbine blade is almost constant for the majority of its span but assumes smaller values close to the blade tip and root. The implementation of this work, improving on the work of [37], specifically considers that the airfoil polars depend on Re. The expected range of Reynolds numbers is discretized by linear shape functions and associated nodal values, and the local Reynolds number is computed at each spanwise station based on local geometry and flow conditions. The results presented later on consider scaled wind turbine models for wind tunnel testing. For these rotors, the chord-based Reynolds number is much lower than in typical full-scale applications, and ad hoc low-Reynolds airfoils [85] are used. Because of the special flow regime of these airfoils, the formulation is complemented by the conditions $\partial C_L/\partial \mathrm{Re} > 0$ and $\partial C_D/\partial \mathrm{Re} < 0$. The first condition accounts for the earlier reattachment of the laminar separation bubble on the suction side of the airfoil for increasing Re, and the second for the shorter chord extent of that same bubble [86]. They are enforced as soft penalty constraints in problem (2.5) by modifying the cost function as $J = J + J_p$, where

$$J_p = W \int_{\alpha_m}^{\alpha_M} \int_{\mathrm{Re}_m}^{\mathrm{Re}_M} \left(\max\left(0, -\frac{\partial C_L}{\partial \mathrm{Re}}\right) + \max\left(0, \frac{\partial C_D}{\partial \mathrm{Re}}\right) \right) \mathrm{dRe}\, \mathrm{d}\alpha, \tag{2.13}$$

where W is a penalty parameter, and $[\mathrm{Re}_m, \mathrm{Re}_M]$ and $[\alpha_m, \alpha_M]$ are the ranges of Reynolds and angle of attack of interest.

2.4 Nacelle and tower models

The nacelle and tower have a few minor effects on the aerodynamics. For a full-scale wind turbine, the impact of the nacelle and tower is usually neglected in CFD. The comparison study conducted here also supports the general practice of neglecting them, as their impact is sufficiently small. However, the effects should not be neglected for the scaled wind turbine models for two reasons. First, the relative nacelle and tower size of the scaled wind turbine model is bigger than in the full-scale wind turbine. A CAD model of the nacelle and tower in the G1 model is shown in Fig 2.3. The ratio between the height of the nacelle and the diameter of the rotor is about 0.091 for the G1 model, compared with about 0.056 for the DTU 10 MW reference wind turbine [87]. For smaller-scale turbine models, the ratio can be even higher. Second, the flow boundary layers on the surfaces of nacelle and tower are of similar sizes, typically several centimeters. This size, when compared to that of a full-size wind turbine, is small enough to be neglected. However, compared to the size of a scaled wind turbine, with a typical rotor diameter of about 1 m, the flow boundary layer does have some influence on turbine behavior.

One fundamental approach to modeling the nacelle and tower is to use body-conforming mesh. However, such an approach has at least two disadvantages. First, a structured mesh, as constituted by the complex geometry of the nacelle and tower, is difficult to generate. Second, the body-conforming mesh and transition region would experience mesh quality deterioration in the vicinity of the blades, significantly impeding the solution of the blade aerodynamics close to the root. To avoid these two issues, the immersed boundary method [88] was employed to model the nacelle and tower in this study. The immersed boundary method (IBM) was been implemented in foam-extend-4.0 [89, 90]. IBM solves the critical issue of mesh quality deterioration since the mesh does not have to be modified. A discrete forcing approach is used. The momentum equation is modified only in the stencil touching the IB to impose boundary conditions. The velocity inside the body of the nacelle and tower is set to zero to model the blockage of them.

Due to the large computation domain of wind farm CFD simulation, the cell size is comparable to that of the nacelle and tower. Typically, the height and width of the nacelle and the diameter of the

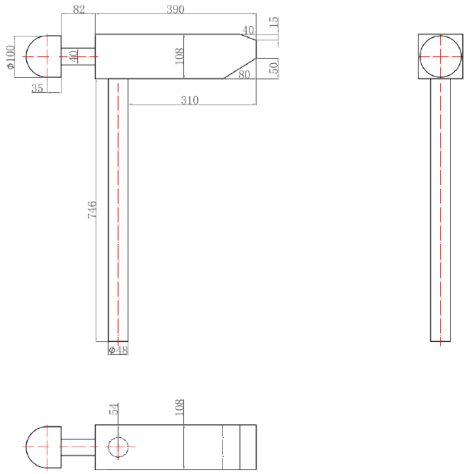

Figure 2.3: CAD model of the nacelle and tower of the G1 model.

tower are resolved by no more than two cells, both for the scaled and full-scale turbines. Therefore, all details in Fig 2.3 are filtered by the mesh, so the accuracy of the solution is limited. However, the most important effects of nacelle and tower on the wind turbine and wake can be captured. The existence of a tower model influences the turbine power and wake recovery. Every time a blade passes in front of the tower, the wind speed experienced by the blade decreases, leading to higher fatigue loads and noise emission. The eddies shed by the tower also enhance the wake recovery of the turbine. Compared to the tower model, the nacelle model has very little effect on the far wake, but it reduces wake center speed in the near wake.

2.5 Control in simulation

Wind farm control also requires a supervisory controller plus various turbine controllers. Both types of the controller were implemented in the CFD simulation framework. Each turbine controller communicates with its FAST module, while the supervisory controller communicates with the SOWFA module. The flow chart between different modules of the whole framework is shown in Fig.2.4.

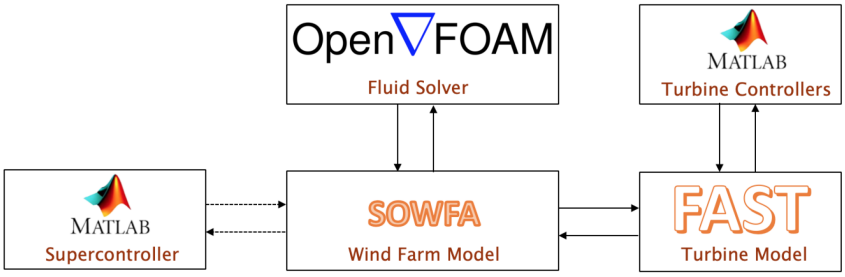

Figure 2.4: Control framework.

The turbine controllers are implemented with Matlab Simulink. The Simulink model is then converted to C-code before being compiled into a Dynamic Linked Library (DLL), which is then called by FAST through the Bladed-style [47] DLL-interface. The use of the DLL allows for a quick implementation of the controller, while the Simulink controller is the same one that was ported on-

board the scaled wind turbine model. This serves to guarantee the consistency of the controllers in the experiments and simulations.

The wind farm controller was implemented as an add-on module to SOWFA, in line with the concept proposed by [91]. The implementation allows for a wide range of control algorithms, which can be either coded in the module or linked through DLLs. A CFD simulation is usually executed in parallel with hundreds of processors. The computation tasks of multiple wind turbines are distributed to different processors. Typically, some processors are assigned with one turbine each, while the rest are not assigned to a turbine and just solve the fluid dynamics. Physically, the supervisory controller performs three tasks: collecting measurements from all wind turbines; computing control outputs according to the measurements; communicating control outputs to all wind turbines. Computationally, the process is similar but slightly more complicated. Fig. 2.5 illustrates the difference. For each processor that runs the FAST simulation pertaining to a wind turbine, there is a supervisory controller instance running at the same time. This controller, however, can only access the information elaborated by its associated processor. Therefore, the processors have to perform pairwise communication to exchange global information. Communication between processors is through the message passing interface (MPI) [92].

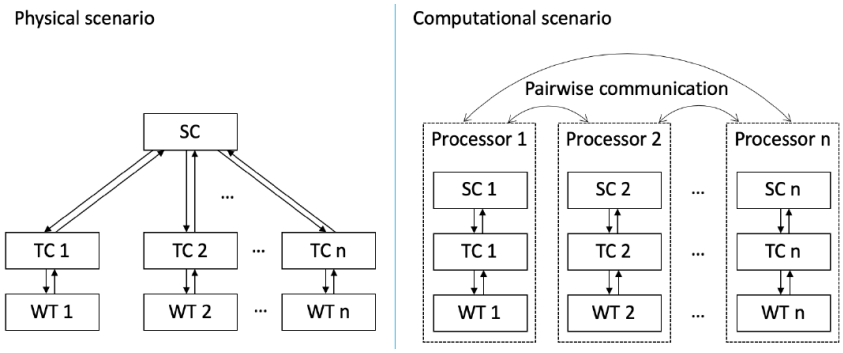

Figure 2.5: Implementation of the supervisory controller.

An example of the communication procedure with three wind turbines is shown in Table 2.1. P_1, P_2, P_3 are processors populated with one wind turbine instance each, while the other processors P_4 P_n are only involved in solving fluid dynamics. First, the supervisor controller collects input information from its only wind turbine instance. In the communication step that follows, the information is sent to all the other processors with a turbine instance. After communicating, each supervisory controller instance in the first three processors has complete knowledge of the status of the entire wind farm, enabling it to compute its control outputs. Finally, the control outputs are distributed to each wind turbine.

Operation	Collect inputs	Communication	Compute outputs	Send commands
P_1	Get u_1 from WT_1	Send x_1 to P_2, P_3	Compute y_1, y_2, , y_3	Send y_1 to WT_1
P_2	Get u_2 from WT_2	Send x_2 to P_1, P_3	Compute y_1, y_2, , y_3	Send y_2 to WT_2
P_3	Get u_3 from WT_3	Send x_3 to P_1, P_2	Compute y_1, y_2, , y_3	Send y_3 to WT_3
$P_4 - P_n$	Do nothing			

Table 2.1: The procedure of communication among processors in case of three wind turbines.

2.6 Large-eddy simulation

LES simulation [10,60,61] has been employed in the wind energy field for more than a decade. It is one of the most promising tools for studying the wakes and interactions of turbines. The principal of LES and the way it is employed in the CFD framework of this study is presented in detail in this section.

2.6.1 Momentum equation

The incompressible momentum equation in Einstein notation can be written as:

$$u_{i,t} + (u_j u_i)_{,j} = -\frac{1}{\rho_0} p_{,i} + \nu u_{i,jj} + \frac{1}{\rho_0} f_i, \tag{2.14}$$

where u_i is the velocity component in the ith direction, and i varies from 1 to 3; a comma in a subscript stands for a derivative, e.g. $(\cdot)_{,t}$ means a derivative regarding time, $(\cdot)_{,j}$ means a derivative regarding the jth spatial coordinate; f_j is the body force from in the jth spatial direction. For incompressible flow, the velocity field is divergence-free:

$$u_{j,j} = 0. \tag{2.15}$$

With this property, the diffusion term can be reformulated as follows

$$\nu u_{i,jj} = \nu(u_{i,jj} + u_{j,ij}) = \nu(u_{i,j} + u_{j,i})_{,j} = 2\nu S_{ij,j} = 2(\nu S_{ij})_{,j}, \tag{2.16}$$

where $S_{ij,j} = \frac{1}{2}(u_{i,j} + u_{j,i})$ is the rate-of-strain tensor. Replacing the original diffusion term with modified one, the momentum equation becomes:

$$u_{i,t} + (u_j u_i)_{,j} = -\frac{1}{\rho_0} p_{,i} + 2(\nu S_{ij})_{,j} + \frac{1}{\rho_0} f_i \tag{2.17}$$

The quantities are passed through a spatial filter. The LES in the foam-extend environment is implemented implicitly, i.e. filtered by the mesh. The filtered quantities are denoted by a tilde symbol placed above as in:

$$\tilde{u}_{i,t} + (\widetilde{u_j u_i})_{,j} = -\frac{1}{\rho_0} \tilde{p}_{,i} + 2(\nu \tilde{S}_{ij})_{,j} + \frac{1}{\rho_0} \tilde{f}_i \tag{2.18}$$

The filtered convection term can be split into:

$$\widetilde{u_i u_j} = \tau_{ij} + \tilde{u}_i \tilde{u}_j, \tag{2.19}$$

where τ_{ij} is an unclosed term that reflects Sub-Grid-Scale (SGS) fluxes. Replacing the original convection term, the equation becomes:

$$\tilde{u}_{i,t} + (\tilde{u}_j \tilde{u}_i)_{,j} = -\frac{1}{\rho_0} \tilde{p}_{,i} + 2(\nu \tilde{S}_{ij})_{,j} - \tau_{ij,j} + \frac{1}{\rho_0} \tilde{f}_i, \tag{2.20}$$

to solve the equation, τ_{ij} is modeled by the constant Smagorinsky model [93]:

$$\tau_{ij} - \frac{1}{3}\tau_{kk}\delta_{ij} = -2\nu_t \tilde{S}_{ij} = -2(C_s\Delta_g)^2 |\tilde{S}| \tilde{S}_{ij}, \tag{2.21}$$

where $|S| = \sqrt{2\tilde{S}_{ij}\tilde{S}_{ij}}$, and $\nu_t = (C_s\Delta_g)^2|\tilde{S}|$. Only the deviatoric part of the SGS model is relevant because the gradient of the trace can be absorbed into an effective pressure field.

$$\tilde{u}_{i,t} + (\tilde{u}_j \tilde{u}_i)_{,j} = -\frac{1}{\rho_0}(\tilde{p} + \frac{1}{3}\tau_{kk})_{,i} + 2(\nu \tilde{S}_{ij})_{,j} + (2\nu_t \tilde{S}_{ij})_{,j} + \frac{1}{\rho_0} \tilde{f}_i, \tag{2.22}$$

denote $p^e = \tilde{p} + \frac{1}{3}\tau_{kk}$ as the modified pressure. Typically, the value of $\frac{1}{3}\tau_{kk}$ is relatively small. Replacing the expression of S_{ij} by its definition, equation 2.22 becomes:

$$\tilde{u}_{i,t} + (\tilde{u}_j\tilde{u}_i)_{,j} = -\frac{1}{\rho_0}p^e_{,i} + [(\nu+\nu_t)(\tilde{u}_{i,j}+\tilde{u}_{j,i})]_{,j} + \frac{1}{\rho_0}\tilde{f}_i. \tag{2.23}$$

Again, the divergence-free property of the filtered velocity field is used, and equation 2.23 becomes:

$$\tilde{u}_{i,t} + (\tilde{u}_j\tilde{u}_i)_{,j} = -\frac{1}{\rho_0}p^e_{,i} + [(\nu+\nu_t)(\tilde{u}_{i,j}+\tilde{u}_{j,i}-\frac{1}{3}\tilde{u}_{k,k}\delta_{ij})]_{,j} + \frac{1}{\rho_0}\tilde{f}_i. \tag{2.24}$$

For a simulation involving wind turbines, the body force can be separated into two parts, the buoyancy force and the turbine body forces:

$$f_i = \frac{\rho}{\rho_0}g_i + b_i \tag{2.25}$$

where g_i is the constant gravity body force vector, b_i is the wind turbine body forces term. Using the Boussinesq approximation [94]

$$\rho = 1 - \beta(T - T_0) \tag{2.26}$$

Substitute equations 2.25 and 2.26 into equation:

$$\tilde{u}_{i,t} + (\tilde{u}_j\tilde{u}_i)_{,j} = -\frac{1}{\rho_0}p^e_{,i} + [(\nu+\nu_t)(\tilde{u}_{i,j}+\tilde{u}_{j,i}-\frac{1}{3}\tilde{u}_{k,k}\delta_{ij})]_{,j} + [1-\beta(\tilde{T}-T_0)]g_i + \frac{1}{\rho_0}\tilde{b}_i. \tag{2.27}$$

The momentum equation should hold everywhere in the domain, which means the integral of the equation should also hold for each cell. Therefore, the governing equation is integrated within the body of one cell:

$$\begin{aligned}\iiint_{V_c}\tilde{u}_{i,t}dV + \iiint_{V_c}(\tilde{u}_j\tilde{u}_i)_{,j}dV = -\frac{1}{\rho_0}\iiint_{V_c}p^e_{,i}dV + \\ \iiint_{V_c}[(\nu+\nu_t)(\tilde{u}_{i,j}+\tilde{u}_{j,i}-\frac{1}{3}\tilde{u}_{k,k}\delta_{ij})]_{,j}dV + \iiint_{V_c}[1-\beta(\tilde{T}-T_0)]g_i dV + \frac{1}{\rho_0}\iiint_{V_c}\tilde{b}_i dV.\end{aligned} \tag{2.28}$$

Applying the Gaussian theorem to the convection and diffusion terms, the equation transforms into:

$$\begin{aligned}\iiint_{V_c}\tilde{u}_{i,t}dV + \oiint_{\partial V_c}(\tilde{u}_j\tilde{u}_i)dS_j = -\frac{1}{\rho_0}\iiint_{V_c}p^e_{,i}dV + \\ \oiint_{\partial V_c}[(\nu+\nu_t)(\tilde{u}_{i,j}+\tilde{u}_{j,i}-\frac{1}{3}\tilde{u}_{k,k}\delta_{ij})]dS_j + \iiint_{V_c}[1-\beta(\tilde{T}-T_0)]g_i dV + \frac{1}{\rho_0}\iiint_{V_c}\tilde{b}_i dV\end{aligned} \tag{2.29}$$

The integral over the cell boundaries can be split into integrals over cell faces:

$$\begin{aligned}\iiint_{V_c}\tilde{u}_{i,t}dV + \Sigma_{f\in faces(V_c)}\iint_f(\tilde{u}_j\tilde{u}_i)dS_j = -\frac{1}{\rho_0}\iiint_{V_c}p^e_{,i}dV + \\ \Sigma_{f\in faces(\partial V)}\iint_f[(\nu+\nu_t)(\tilde{u}_{i,j}+\tilde{u}_{j,i}-\frac{1}{3}\tilde{u}_{k,k}\delta_{ij})]dS_j + \iiint_{V_c}[1-\beta(\tilde{T}-T_0)]g_i dV + \frac{1}{\rho_0}\iiint_{V_c}\tilde{b}_i dV\end{aligned} \tag{2.30}$$

Then, a one-point Gaussian integral is applied using volume center or surface center quantities, denoted by an over-line above the quantity. The face area and cell volume are denoted as S and V, respectively. Thus, the spatially discretized form of the momentum equation can be written as follows:

$$\begin{aligned}\overline{\tilde{u}}_{i,t}V + \Sigma_{f\in\partial V_c}(\overline{\tilde{u}_j}n_j\overline{\tilde{u}_i})S = -\frac{1}{\rho_0}\overline{\tilde{p}}^e_{,i}V + \\ \Sigma_{f\in faces(\partial V)}[(\nu+\overline{\nu_t})(\overline{\tilde{u}}_{i,j}+\overline{\tilde{u}}_{j,i}-\frac{1}{3}\overline{\tilde{u}}_{k,k}\delta_{ij})n_j]S + [1-\beta(\overline{\tilde{T}}-T_0)]g_i V + \frac{1}{\rho_0}\overline{\tilde{b}_i}V\end{aligned} \tag{2.31}$$

To enable easier time discretization analysis, the spatially semi-discretized equation 2.31 has to be simplified. Equation 2.31 can be rendered as:

$$U_{,t} = D + P + B(\psi_s, \psi_p, U), \tag{2.32}$$

where

$$U = \overline{\tilde{u}}_i,$$

$$D = \Sigma_{f \in faces(\partial V)}[(\nu + \overline{\nu_t})(\overline{\tilde{u}}_{i,j} + \overline{\tilde{u}}_{j,i} - \frac{1}{3}\overline{\tilde{u}}_{k,k}\delta_{ij})n_j - (\overline{\tilde{u}}_j n_j \overline{\tilde{u}}_i)]\frac{S}{V} + [1 - \beta(\overline{\tilde{T}} - T_0)]g_i,$$

$$P = -\frac{1}{\rho_0}\overline{\tilde{p}}^e_{,i},$$

$$B(\psi, U) = \frac{1}{\rho_0}\overline{\tilde{b}_i},$$

where the body force term is expressed as a function of three variables: ψ_s, the blade azimuth angle when velocities are sampled, ψ_p, the blade azimuth angle at which the forces are projected, and the velocity field U. The backward Euler time derivative scheme is employed:

$$\frac{1}{\Delta t}(U^{n+1} - U^n) = D^{n+1} + P^{n+1} + B(\psi^n, \psi^{n+1}, U^n), \tag{2.33}$$

where ψ is the blade azimuth angle, and the superscripts denote the timestep, with n the current timestep and $n+1$ the next timestep. The meaning of the body force term $B(\psi^n, \psi^{n+1}, U^n)$ can be explained together with the principle for calculating the force. First, the solver samples the flow velocity in the vicinity of the blade from the current known velocity field U^n when the azimuth angle of the blade is ψ^n, after which the blade body force is computed and projected around the blade when the azimuth angle is ψ^{n+1}. Velocity sampling and force projection, therefore, take place at different locations. This is also referred to as loose coupling since the body force term $B(\psi^n, \psi^{n+1}, U^n)$ is explicit. Although the blade azimuth angle ψ^{n+1} is indexed by the next timestep, this quantity is known ($\psi^n + \Omega\Delta t$ with Ω the rotor speed and Δt the timestep) before the solution of the next timestep since. The loose coupling of the body force is both a good approximation of the original solution and a good compromise between computation speed and accuracy. With the exception of the explicit body force term on the RHS, the terms are implicit. Equation 2.33 is thus solved iteratively.

The pressure-implicit with the splitting of operators (PISO) algorithm [95] is used to solve the equations. The algorithm consists of two steps: prediction and correction. The prediction step of equation 2.33 can be written in a generic form:

$$\mathbf{C}\mathbf{u}^* = \mathbf{r} - \nabla\mathbf{p}^n + \rho_k^n\mathbf{g} + \mathbf{b}^n, \tag{2.34}$$

where $\mathbf{r}$ is the right-hand side explicit source term excluding the pressure gradient, buoyancy force, and turbine body forces; $\mathbf{C}$ is the multiplying matrix for the vector of predicted velocity $\mathbf{u}^*$. The matrix $\mathbf{C}$ is influenced by the turbulence model, but the change of the turbulence model does not change the generic form of 2.34. The matrix $\mathbf{C}$ can be split into the diagonal part $\mathbf{A}$ and the off-diagonal part $\mathbf{H}'$. So the equation becomes:

$$\mathbf{A}\mathbf{u}^* + \mathbf{H}'\mathbf{u}^* = \mathbf{r} - \nabla\mathbf{p}^n + \rho_k^n\mathbf{g} + \mathbf{b}^n. \tag{2.35}$$

The predicted velocity $\mathbf{u}^*$ is obtained by solving equation 2.35. The predicted velocity field $\mathbf{u}^*$ is not necessarily divergence-free. Therefore, a corrector is used to guarantee this property. The corrector equation is written as follows:

$$\mathbf{A}\mathbf{u}^{**} + \mathbf{H}'\mathbf{u}^* = \mathbf{r} - \nabla\mathbf{p}^* + \rho_k^{n+1}g + \mathbf{b}^n, \tag{2.36}$$

where the corrected field $\mathbf{u}^{**}$ is forced to be divergence-free. Denote $\mathbf{H} = r - \mathbf{H}'\mathbf{u}^*$, left multiply $\mathbf{A}^{-1}$ with equation 2.36 and take its divergence. This will yield:

$$\nabla^2(\mathbf{A}^{-1}\mathbf{p}^*) = \nabla\cdot(\mathbf{A}^{-1}\mathbf{H} + \mathbf{A}^{-1}\rho_k^{n+1}\mathbf{g}^n + \mathbf{b}^n) \tag{2.37}$$

Equation 2.37 is called the Poisson equation, which gives the solution of the corrected pressure field $\mathbf{p}^*$. The solution of the Poisson equation is typically the most costly operation of the whole procedure. Having obtained the solution of the corrected pressure, the corrected velocity can be calculated explicitly as:

$$\mathbf{u}^{**} = \mathbf{A}^{-1}\mathbf{H} - \mathbf{A}^{-1}\nabla\mathbf{p}^* + \mathbf{A}^{-1}\rho_k^{n+1}g + \mathbf{A}^{-1}\mathbf{b}^n \tag{2.38}$$

Equation 2.37 and 2.38 can be iterated several times to obtain better convergence and stability. In all simulation cases presented in this work, the number of iterations was set to 3.

2.6.2 Temperature equation

Parallel to the momentum equation, the temperature is solved by the LES solver. The solution of temperature is mandatory to enable the buoyancy force to be predicted and is especially desirable for the atmospheric boundary layer (ABL) simulations [96, 97], which will also be presented in this work.

The temperature equation for an incompressible solver is written as follows:

$$(\rho_0 e)_{,t} + (\rho_0 e u_i)_{,i} = -q_{i,i}, \tag{2.39}$$

where ρ_0 is the reference density of the flow, and q_i the conductive heat flux leaving the control volume. The subscript $(\cdot)_{,t}$ indicates the time derivative while the subscript $(\cdot)_{,i}$ indicates the spatial derivative. The internal energy e can be calculated as:

$$e = c_p T, \tag{2.40}$$

where c_p is the specific heat capacity of the material and T is the absolute temperature. Apply an LES filter to Eq. 2.39 and use a tilde sign to indicate filtered quantities:

$$(\rho_0 \tilde{e})_{,t} + (\rho_0 \widetilde{eu_i})_{,i} = -\tilde{q}_{i,i}, \tag{2.41}$$

where the term $\widetilde{eu_i}$ can be modeled as $\tilde{e}\tilde{u}_i + q_{t_i}$, and q_{t_i} is the turbulent heat flux. $\tilde{q}_i$ can be calculated with the Fourier's law of heat:

$$\tilde{q}_i = -k\tilde{T}_i, \tag{2.42}$$

where k is the heat conductivity of the flow. The turbulent heat flux is modeled in a similar way:

$$\tilde{q}_{t_i} = -k_t\tilde{T}_i, \tag{2.43}$$

where k_t is the modeled turbulent heat conductivity. Substituting the expressions of the turbulent model and heat fluxes into the temperature equation 2.39:

$$\tilde{T}_{,t} + (\tilde{T}\tilde{u}_i)_{,i} = [\frac{k_t + k}{\rho_0 c_p}\tilde{T}]_{,i}. \tag{2.44}$$

the coefficient of $\tilde{T}$ on the right-hand-side of Eq. 2.44 can be calculated as follows:

$$\frac{k_t + k}{\rho_0 c_p} = \frac{\nu_t}{Pr_t} + \frac{\nu}{Pr}, \tag{2.45}$$

where ν_t is the turbulent viscosity modeled in the momentum equation, $Pr_t = \frac{c_p\rho_0\nu_t}{k_t}$ is the turbulent Prandtl number which can be approximated as a constant value, ν is the kinematic viscosity of the flow

and $Pr = \frac{c_p \rho_0 \nu}{k}$ is the Prandtl number of the flow, and it can be evaluated directly since all quantities are known. Finally, $\frac{\nu_t}{Pr_t} + \frac{\nu}{Pr}$ is denoted as the effective heat transfer coefficient κ_{eff} and Eq. 2.44 can be simplified as:

$$\tilde{T}_{,t} + (\tilde{T}\tilde{u}_i)_{,i} = (\kappa_{eff}\tilde{T})_{,i}. \tag{2.46}$$

The same finite volume method is employed to solve the temperature equation. In the solution of the equation, there is a predictor step, but no corrector step since no continuity condition is to be enforced. Therefore, no Poisson solution is required, which makes the process of solving the temperature much quicker than solving the velocity equation.

2.7 Precursor simulation

The turbulence generated in the wind tunnel is simulated with CFD to obtain a full digital copy of the experimental facilities. The goal of the precursor simulation is to resolve the passive turbulence generation process in the civil test chamber of the wind tunnel and save the turbulent inflow data. The inflow data can then be used for wind turbine simulations. Once the inflow data has been collected, it can be used repeatedly for different simulations of turbines.

The wind tunnel facility is a circuit, and the flow is generated by a cluster of fans. It is not necessary to model the whole circuit since only the most important and relevant phenomena are to be captured, i.e., the flow development in the civil test chamber. Therefore, only the civil test chamber is simulated, applying inflow and outflow conditions for both open sides. For the inflow slice, a time-invariant Dirichlet boundary condition that specifies a velocity distribution on the inflow slice is applied. This approach is feasible for two reasons: the inflow of the civil test chamber only has a turbulence intensity of about 1%, and the wind speed distribution on the slice does not change significantly in time. The flow along the closed-loop wind tunnel has been observed to occasionally undergo low-frequency oscillations, which cause only minor speed fluctuations that were not considered in the present work. The precursor simulation is computation-intensive. It is worthwhile to discard the circuit structure in exchange for a much lower computational cost.

The inflow of the civil test chamber can be modeled with a steady inflow with a distribution of velocity $U_0(y,z)$. The velocity distribution $U_E(y,z)$ at 19.1 m downstream of the inflow slice of the test chamber was measured with PIV. The aim of the precursor simulation is to match the velocity and turbulence intensity distribution at the measurement location. If this goal is achieved, the inflow of the wind farm in CFD will be very close to the inflow in the wind tunnel, which would aid further analysis. The match is achieved by iterative corrections of $U_0(y,z)$. In each iteration, the distribution $U_0(y,z)$ was superimposed with a different distribution $U_E(y,z) - U_S(y,z)$, where $U_S(y,z)$ was the velocity distribution obtained in the current iteration.

Precursor simulations were conducted for two different experimental setups to mimic onshore and offshore scenarios, respectively. For the onshore case, nine type-A spires and hundreds of roughness elements were used, as shown by Fig.2.6.

The type-A spire consists of a supporting board and an equilateral-triangular mainboard. The length of the bottom edge and the height of the equilateral triangle are 0.8 m and 2.5 m, respectively. The distance between two adjacent spires was 1.55 m. 24 rows of bricks were placed on the ground, symmetrically around the slice $y = 0$ m. The number of bricks in odd rows is 12, in even rows 13, resulting in a staggered brick distribution. The lateral distance between adjacent bricks and the longitudinal distance between adjacent rows were both 1.1 m. For the offshore case, 14 type-B spires and no bricks were used. The type-B spire consists of an equilateral trapezoid and a supporting board. The lengths of the bottom and top edges of the trapezoid are 0.26 m and 0.1 m, respectively, and the height of the trapezoid is 2.0 m. The distance between two adjacent spires was 1 m.

A body-conforming structured hexahedron mesh was generated in ANSYS-ICEM to resolve the spires. The cells close to walls, including the surfaces of spires and wind tunnel boundaries, are refined

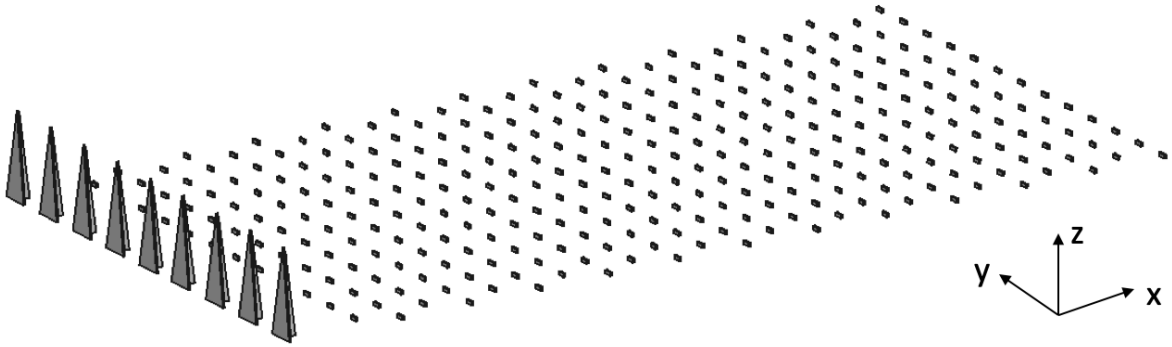

Figure 2.6: Type A spires and bricks in the wind tunnel.

such that the non-dimensional wall distance $y+$ is about 100, which is suitable for the application of wall functions. The non-slip wall boundary conditions with wall functions are applied to all walls. For the type-A spires, a Y-grid technology was used to resolve the mainboard triangular geometry. The roughness elements are modeled with immersed boundary methods [88] due to a large number of elements and the staggered layout. Using a structured mesh to model the roughness elements is not only too cumbersome but also not optimal for the quality of mesh in the free stream. In contrast, the immersed boundary method does not require modification of the mesh close to the elements and thus provides a high degree of freedom. The drawback of the immersed boundary method is its lack of accuracy. However, for small roughness elements, the negative impact is limited to a very small region, and the quality of simulation results is sufficiently high. For the type-B spires, an O-grid technology was used to confine the fine mesh to the close vicinity of the spires. The physical process of turbulence generation in the case of type-B spires is visualized by Fig. 2.7. Big eddies are shed after the spires, and the eddies consistently break down into smaller ones. Finally, an almost uniform turbulence field was generated for both types of spires.

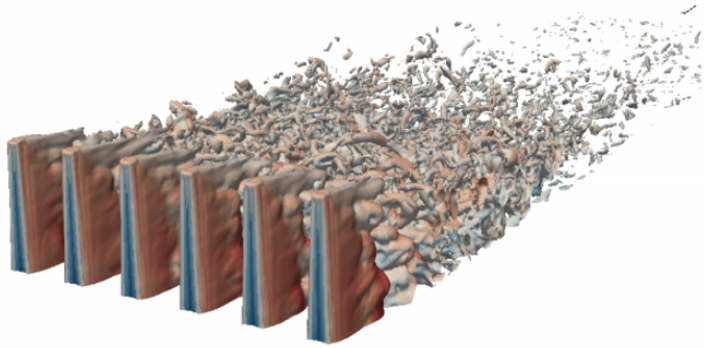

Figure 2.7: Visualization of iso-vorticity surfaces for the precursor simulation with type-B spires.

2.8 Full-scale turbine design

Full-scale turbine models were designed through a backward-engineering approach to match the characteristics of G1. The purpose is to compare the wake recovery, path, profile, Reynolds shear stresses, and available power downstream between full-scale and scaled models. This section mainly

introduces the characteristics and the approach to design the full-scale turbines.

The aerodynamic design of the rotor of the full-scale turbines was adapted to match the characteristics of the G1 in terms of TSR and circulation distribution. Three different versions of the full-scale models were designed, and they are termed as G178, G178-nRA, and G178-MC, respectively. All the models are based on the DTU 10 MW wind turbine [98]. G178 and G178-nRA both use the same airfoil as the DTU 10-MW turbine on the whole blade and match the circulation distribution of G1 partially from 25% to 100% blade span, while G178-MC matches the circulation distribution of G1 completely by using thinner airfoils close to the root as it was done for G1. Rotational augmentation correction that corrects for delayed stall according to [99] was applied to G178 but not to G178-nRA. The distributions of twist angle, lift coefficient chord, and circulation of the three models, as well as of G1, are shown in Fig. 2.8. The chord distributions are normalized by their respective arithmetic mean values c_0 over the span. Lift coefficient and circulation are evaluated at rated conditions using the BEM method implemented in the code `FAST` [47]. The lift coefficient of the G1 is significantly smaller than the one of the full-scale turbines, which is a result of the low-Reynolds regime of its airfoils. However, the lower lift is compensated by a larger chord and different twist distributions.

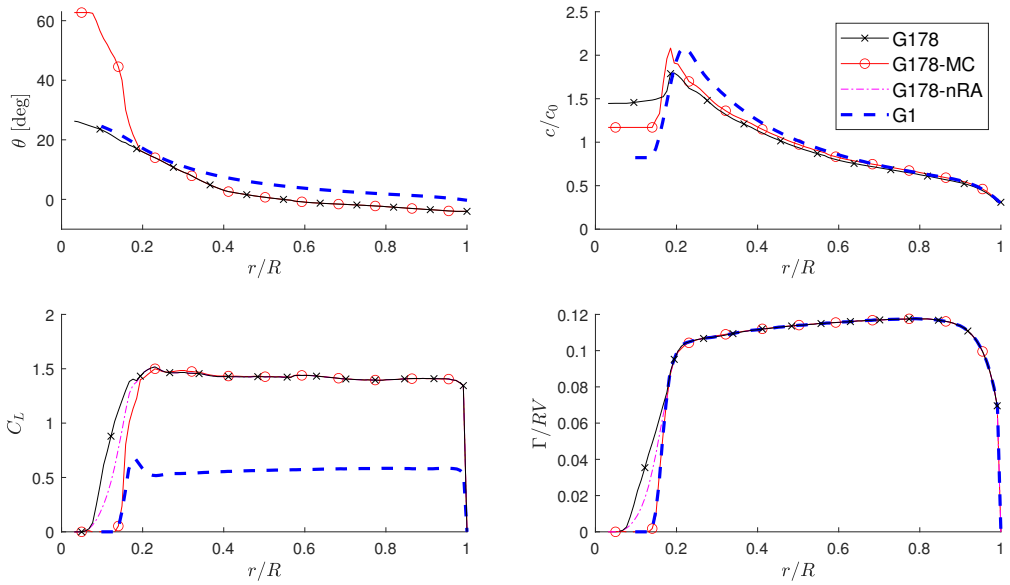

Figure 2.8: Twist θ, non-dimensional chord c/c_0, lift coefficient C_L and non-dimensional circulation Γ/RV distributions for the G1 and for the G178 and G178-MC full-scale turbines.

The full-scale turbines have a rotor diameter of 178.3 m and a hub height of 133.7 m. The hub height H of the full-scale machine was slightly adjusted to match the D/H ratio of the G1 turbine, where D is the rotor diameter, and H is the hub-height. The sizes of the nacelle and tower were kept the same as the DTU reference. In terms of non-dimensional quantities, the front area of the nacelle of G1 is 2.6 times bigger than the full-scale turbines, while the tower diameter of G1 is 49% larger than the full-scale ones.

The impacts of the mismatch of the turbine size, circulation, nacelle, and tower sizes and the integral length scale of the inflow on the wake are to be quantified and analyzed with CFD simulations of the turbines.

CHAPTER 3

Paper 1: Identification of Airfoil Polars from Uncertain Experimental Measurements

3.1 Summary

Both the low-fidelity BEM model and the high-fidelity CFD model use polars, i.e., the lift and drag coefficients at different angles of attack and Reynolds numbers, as inputs. The accuracy of model outputs is directly related to the accuracy of the polars. For scaled wind turbines, it is non-trivial to know the polars of the airfoils used on the blades precisely because many factors can make the actual polars of a specific blade differ from the nominal ones. As an important example, the polars of small-sized airfoils used for scaled turbines are much more sensitive to production imperfections than large ones used on full-scale turbines.

This paper describes a new procedure for the tuning of polars based on turbine operational data. The method is based on a maximum likelihood formulation that uses the power and thrust coefficients of a turbine under various operating conditions to identify the airfoil lift and drag coefficients. The maximum likelihood method formulation used in this paper includes both errors in the outputs and the inputs, generalizing the classical error-in-the-output-only formulation. The explicit consideration of the errors in inputs, including wind speed, air density, blade pitch angle, and rotor speed, plays a vital role in improving identification results. The new formulation requires the identification of both the model parameters and the model inputs, resulting in a massive coupled problem. This problem is broken into small ones and finally coupled again through an outer iteration. Since many parameters are required to describe the behavior of airfoil polars as functions of the angle of attack and Reynolds number, this paper uses a singular value decomposition to solve for a reduced set of observable parameters. The singular value decomposition method decreases the complexity level of the problem, accelerates the algorithm, and makes the identification problem better posed.

A filtering technique based on the a priori information about measurement uncertainties is proposed to give a better initial guess for the identification problem. Since the filtering technique requires additional computation, which becomes expensive when repeated in the iteration loop, an approach to significantly decrease the computational burden has been proposed and applied in this paper. This work also considers the dependency of airfoil polars on Reynolds number and corresponding constraints related to Reynolds number.

The new approach is demonstrated by identifying high-quality polars for scaled wind turbines used in wind tunnel experiments. With the identified polars, an excellent match between the blade element momentum simulations and wind tunnel measurements under a wide range of operating conditions has been achieved.

3.2 Contributions to the scientific literature

Various improvements of a previously published polars identification method have been proposed in this work. The improvements include the explicit consideration of system inputs errors. The wind

speed is one of the inputs with the most uncertainties, and the influence of the wind speed uncertainty can be significant for the outputs, i.e., the power and thrust coefficients. Therefore, the input errors are handled systematically in this paper, which improves results significantly. In addition, other improvements include the capability to apply constraints concerning Reynolds number, a filtering technique, and various methods to accelerate the identification algorithm. High-quality polars have been identified, and they are used for subsequent CFD simulations presented in other parts of this dissertation.

3.3 Authors' contribution

Chengyu Wang developed the a priori residual filtering method, wrote the software, performed the simulations, and analyzed the results. Filippo Campagnolo was responsible for the wind tunnel experiments and the analysis of the measurements. Carlo L. Bottasso devised the original idea of estimating polars from operational turbine data, developed the ML formulation with errors in inputs and outputs, and supervised the work. Chengyu Wang and Carlo L. Bottasso wrote the manuscript. All authors provided important input to this research work through discussions and feedback and by improving the manuscript.

3.4 Reference

C. Wang, F. Campagnolo, and C. L. Bottasso, "Identification of airfoil polars from uncertain experimental measurements," *Wind Energy Science*, vol. 5, pp. 1537–1550, 2020. doi: https://doi.org/10.5194/wes-5-1537-2020

CHAPTER 4

Paper 2: Wake behavior and control: comparison of LES simulations and wind tunnel measurements

4.1 Summary

This paper presents an LES-ALM simulation framework based on open-source software. The CFD numerical scheme, turbine model, and mesh setup are described in detail. The simulation framework is validated with a scaled wind turbine operated in a boundary layer wind tunnel with experimental measurements. A good match of wind turbine power, thrust, wake profile, and flow spectra has been achieved.

A precursor-successor simulation procedure is described in this work. The precursor simulation simulates the turbulent inflow generated with a cluster of spires in the wind tunnel. The spires are modeled by structured mesh. The precursor simulation is validated with experimental measurements of mean flow speed field and turbulence intensity distribution. The inflow data is sampled and used to simulate a wind farm of scaled wind turbines.

In experiments, the rotor speeds vary slightly during operation. In CFD simulations, the speeds are specified to the mean value measured from the experiments. Results indicate such an approach is good enough to capture the main characteristics of turbine power, thrust, and wake.

Two different wind farm control strategies, i.e., yaw misalignment control and cyclic pitch control, were applied in the simulation framework. For both situations, the simulation framework is still able to match experimental measurements well.

4.2 Contributions to the scientific literature

This contribution of this work is to validate the simulation framework for scaled wind turbines operated in a boundary layer wind tunnel. Results indicate that the phenomena in the wind tunnel and yaw and pitch control effectiveness can be modeled with reasonable accuracy with the simulation framework. The framework is used for all other CFD-relevant papers presented in this dissertation.

4.3 Authors' contribution

Chengyu Wang performed the precursor simulations that were used to generate the turbulent inflow data and analyzed the results. Chengyu Wang also participated in implementing the immersed boundary method used to model the nacelle and tower, especially regarding the parallel computation of the method and the CAD input files. Jiangang Wang and Chengyu Wang developed the simulation framework together. Jiangang Wang conducted the simulations of wind turbines and wrote the manuscript with Carlo L. Bottasso.

4.4 Reference

J. Wang, C. Wang, F. Campagnolo, and C. L. Bottasso, "Wake behavior and control: comparison of les simulations and wind tunnel measurements," *Wind Energy Science*, vol. 4, no. 1, pp. 71–88, 2019. doi: https://doi.org/10.5194/wes-4-71-2019

CHAPTER 5

Paper 3: Validation of large-eddy simulation of scaled waked wind turbines in different yaw misalignment conditions

5.1 Summary

Yaw-based control appears to be very effective despite its simplicity. Upstream wind turbines are yawed slightly out of the wind to steer their wakes away from downstream turbines. When the yaw angle is chosen appropriately, the power gain on downstream turbines exceeds the power loss on upstream ones, resulting in an increase of wind farm power.

This paper compares LES-ALM simulation results of scaled wind turbines against experimental measurements obtained in a boundary layer wind tunnel. This paper serves to validate the CFD code, the turbine model, and the implementation of wind turbine controllers. Three scaled wind turbine models were arranged in either wind-aligned or misaligned conditions. In the experiments, the wind turbine power and speed were measured by on-board sensors, while the flow was measured with two LiDARs. In two sets of simulations, wind turbine controllers were switched either on or off. The turbine controllers were based on a standard look-up table for torque and proportional-integral controller for pitch, so the turbines in simulations could adjust their rotor speeds according to the inflow conditions.

Simulation and experimental results are compared concerning flow characteristics, turbine states, and wake behavior. The analysis of the results shows a good match between simulations and experiments. When simulated without turbine controllers, the turbine power time series contains spurious oscillations, but they are eliminated when the torque controllers are properly integrated into the simulations. Therefore, it is important to include torque controllers in CFD simulations to capture the power spectrum correctly. Besides the verification, the numerical simulations are also used to explain a wake interference phenomenon observed in the experiments, which causes the secondary wake deflection in the path of the wake of shaded turbines. According to the simulation results, the secondary deflection is caused by a significantly non-zero lateral velocity component that mainly appears on one side of the turbine wake.

5.2 Contributions to the scientific literature

A framework to implement the wind farm controller and wind turbine controllers has been implemented in this work. In this work, the supervisory controller is tasked with collecting information from each wind turbine, while the turbine controller adapts the turbine to the inflow condition. The turbine controller's implementation is shown to be important in removing spurious oscillation of turbine power outputs. For the first time, a comparison of turbine wakes on a whole horizontal slice between experimental measurements and simulation results is demonstrated. The secondary wake deflection phenomenon is observed both in the experiment and the simulation, and its mechanism is explained by observing the simulation results.

5.3 Authors' contribution

Chengyu Wang implemented the turbine controller, performed the simulations, analyzed the results, and wrote the manuscript with Carlo L. Bottasso. Chengyu Wang and Jiangang Wang developed the simulation framework together. Filippo Campagnolo conducted wind tunnel experiments and provided data. Daniel B. Carreón Cortés submitted and monitored CFD simulations. Carlo L. Bottasso supervised the work.

5.4 Reference

C. Wang, J. Wang, F. Campagnolo, D. Carraón, and C. Bottasso, "Validation of large-eddy simulation of scaled waked wind turbines in different yaw misalignment conditions," in *Journal of Physics: Conference Series*, vol. 1037, no. 6. IOP Publishing, 2018, p. 062007. doi: 10.1088/1742-6596/1037/6/062007

CHAPTER 6

Paper 4: Code-to-code-to-experiment validation of LES-ALM wind farm simulators

6.1 Summary

Large-Eddy Simulation (LES) is actively researched and used to explain wind farm phenomena and predict effects that enable improved design and operation. However, notwithstanding the success of LES, there is still only a limited understanding of the actual accuracy of such numerical methods in representing the complex physical processes that govern wake-turbine interactions. The present paper presents a code-to-code-to-experiment comparison of two state-of-the-art LES-ALM (Actuator Line Method) codes with significantly different features. While one code is second-order accurate in space, the other is of sixth-order. Numerical results of both solvers for different mesh resolutions are compared in this work to study the effectiveness of convergence order. Corresponding experiments are used to validate the numerical results. The objective is to evaluate the accuracy and uncertainty of LES for wind farm flows. While the experiments provide benchmarks of integral quantities like power, thrust, and mean wake profile, the code-to-code comparison can also illustrate differences of other quantities like Reynolds shear stresses and integral time scale.

Results indicate that the second-order method is slightly more accurate and substantially cheaper in computational cost than the sixth order method. The higher accuracy of the second-order method is most likely due to the Smagorinsky model that was set to the same value in both solvers. However, the Smagorinsky constant was initially tuned for the second-order method. The second-order solver also has a lower computational cost, which is mainly because of the ability of mesh refinement. When the costs are normalized to the number of float operations per cell per code, the second-order method has a slightly lower cost.

6.2 Contributions to the scientific literature

A detailed comparison between the two codes has been conducted. The excellent match in the detailed code-to-code-to-experiment comparison increases the plausibility of both solvers. Results indicate that both the widely adopted second-order scheme and the sixth-order scheme are able to match experimental measurements well, while the second-order scheme matches experiments slightly better. The computational cost of the second-order scheme is also significantly lower, mainly due to the possibility of local mesh refinement. The match of Reynolds shear stresses and integral time scale between the two solvers serves an even stronger validation of the method used in this dissertation.

6.3 Authors' contribution

Chengyu Wang performed the simulations with the TUM code, analyzed the results, provided the experimental data to the ICL authors, supported them in its use and the analysis of the results, and wrote the manuscript with Carlo L. Bottasso and with the assistance of the ICL authors. The ICL

authors, Arturo Muñoz-Simón, Georgios Deskos, Sylvain Laizet conducted the simulations with the ICL code under Rafael Palacios's supervision. Filippo Campagnolo conducted wind tunnel experiments and provided data.

6.4 Reference

C. Wang, A. Muñóz-Simon, G. Deskos, S. Laizet, R. Palacios, F. Campagnolo, and C. Bottasso, "Code-to-code-to-experiment validation of les-alm wind farm simulators," in *Journal of Physics: Conference Series*, vol. 1618, no. 6. IOP Publishing, 2020, p. 062041. doi: 10.1088/1742-6596/1618/6/062041

CHAPTER 7

Paper 5: Effects of dynamic induction control on power and loads, by LES-ALM simulations and wind tunnel experiments

7.1 Summary

The dynamic induction control (DIC) strategy is a strategy to mitigate wake effects, and its primary goal is to increase wind farm power. DIC has been studied by the authors who proposed this strategy using LES-AD (actuator disk) simulations. DIC exploits the natural instabilities in the near-wake vortex structures to enhance wake recovery. The technique works by sinusoidally varying the rotor thrust in an open-loop; when performed at the right frequency, this perturbation speeds up the vortex breakdown and enhances wake recovery. This strategy increases the power of downstream turbines. The choice of DIC parameters is important for its performance. The parameters include the frequency, amplitude, and offset of the pitch motion.

The cyclic pitch motion tends to increase the loads for various components of the turbine, especially the tower. The first assessment of DIC effects on loads was attempted by aeroelastic simulations based on a blade-element momentum (BEM) method, i.e., without considering a complete CFD simulation of the system. In this paper, the effects of DIC on power and loads are demonstrated by CFD-ALM (actuator line method) simulations.

A thorough validation of an LES-ALM simulation tool was first conducted against experimental measurements, which shows the CFD tool's capability to accurately simulate the power, loads, and wake behaviors of a wind turbine operating with DIC. The validated CFD model was then employed to study the DIC parameters. It is shown that the frequency, amplitude, offset of the blade pitch motion all affect the wind farm power output. The optimal parameters were determined numerically, which are very close to the ones obtained experimentally. The fatigue loads of various components of the turbine were computed for the case with the baseline case without DIC and the optimal DIC case, i.e., the case with the maximal wind farm power. Results indicate that the slight power gain obtained with DIC is at the cost of an enormous increase in the fatigue loads. Therefore, this trade-off should be taken into account for the practical implementation of the DIC strategy.

7.2 Contributions to the scientific literature

This paper fills a gap in the literature by performing CFD-ALM simulations of the DIC strategy, which have a higher fidelity compared with CFD-AD simulations. The optimal DIC parameters are found through CFD simulations, which are very close to those obtained experimentally. This activity serves as an even more robust validation of the CFD framework, showing its capability to model blade aerodynamics and rotor speed response accurately in cyclic pitch scenarios. The simulation results reveal the trade-off between power gain and fatigue loading increase caused by DIC.

7.3 Authors' contribution

Chengyu Wang implemented the DIC controllers and improved the turbine model, especially regarding the moment of inertia. Chengyu Wang performed the simulations, analyzed the results, and wrote the manuscript with Carlo L. Bottaso. Filippo Campagnolo conducted wind tunnel experiments and provided data. Ashutosh Sharma participated in the simulation work. Carlo L. Bottasso supervised the work.

7.4 Reference

C. Wang, F. Campagnolo, A. Sharma, and C. Bottasso, "Effects of dynamic induction control on power and loads, by les-alm simulations and wind tunnel experiments," in *Journal of Physics: Conference Series*, vol. 1618, no. 2. IOP Publishing, 2020, p. 022036. doi: 10.1088/1742-6596/1618/2/022036

CHAPTER 8

Paper 6: Does the use of load-reducing IPC on a wake-steering turbine affect wake behavior?

8.1 Summary

Wind shear, wind misalignment, and partial wake impingement can cause nodding and yawing moments on the rotor, which cause periodic loads on the main shaft of a turbine during its operation. IPC is capable of reducing such periodic loads, resulting in significantly reduced fatigue damage. In a wind farm, some turbines are operated at high misalignment angles deliberately to steer their wakes, which has potential benefits for the total wind farm power. However, the high misalignment may induce an increase in fatigue loading through a yawing moment on the rotor, and IPC can be used to limit this negative effect of wake steering. The present paper uses CFD-ALM simulation to investigate the effects of IPC on the wake path, wake recovery, loads of turbines, and the impact on downstream turbines.

Experiments of either a single turbine or two aligned turbines were conducted with scaled wind turbines in a boundary layer wind tunnel. Baseline cases without IPC and cases with IPC have been conducted. Comparisons between the simulation and experiment concerning turbine power, loads, and wakes were presented for each case. A good match between simulation results and experimental measurements was achieved for various operating conditions, so all CFD results are backed by experimental evidence. After validation, the CFD tool was used to study the subtle effects of IPC on the turbine wake path and recovery and explain the impact of IPC on turbine power and loads.

Results show that IPC is an effective way of reducing loading for all considered operating conditions. The mechanisms by which IPC influences the turbine and its wake is discussed. Overall, no significant wake recovery enhancement is observed. The use of IPC on the upstream turbine is shown to generate a moderate power increase for positive yawing, both upstream and downstream, while induces power losses for negative yawing. IPC on the downstream turbine tends, in general, to always reduce power.

8.2 Contributions to the scientific literature

This paper validates the application of a CFD-ALM simulation tool to the IPC scenario and obtains a good match with experiments. The impact of IPC on the wake path, recovery, and turbine responses is quantified. For each observed phenomenon, a physical explanation is given. When load-reducing IPC is used, there is a preferable yaw direction, which is associated with higher expected power both on the upstream and downstream turbines.

8.3 Authors' contribution

Chengyu Wang implemented the IPC controllers, performed the simulations, analyzed the results, explained the mechanism of the physical phenomena, and wrote the manuscript with Carlo L. Bot-

tasso. Filippo Campagnolo conducted wind tunnel experiments and provided data. Carlo L. Bottasso supervised the work.

8.4 Reference

C. Wang, F. Campagnolo, and C. Bottasso, “Does the use of load-reducing IPC on a wake-steering turbine affect wake behavior?” in *Journal of Physics: Conference Series*, vol. 1618, no. 2. IOP Publishing, 2020, p. 022035. doi: 10.1088/1742-6596/1618/2/022035

CHAPTER 9

Paper 7: A POD reduced-order model for wake steering control

9.1 Summary

The design of control strategies can significantly benefit from models that can faithfully capture relevant physical processes playing a role in wind turbine wake interactions. However, the models also pose significant challenges. Existing engineering models are typically fast and consume a small amount of computation. They might often be not as accurate as desired. Also, these models typically depend on parameters that need to be calibrated. Inappropriate model parameters may strongly influence the accuracy of models. In contrast, CFD-based models are based on solving the Naiver-Stokes equations, which implies better accuracy and resolution than engineering models. In the meantime, CFD models rely less on parameter tuning.

On the other hand, CFD simulations are typically associated with very high computational cost. Therefore, the use of CFD simulations in the context of control synthesis is challenging or even impossible. Therefore, a model with both high fidelity and a lower computational cost is desired. This paper proposes an approach based on compressing high-fidelity CFD data into a reduced-order model (ROM). The model is obtained through a data-driven model-identification procedure, based on the proper orthogonal decomposition (POD). The resulting ROMs capture the dominant dynamics of wind turbine wakes and their interactions while showing at the same time a high degree of data compression. In this way, the computationally intensive part of the process is performed offline. The identification of ROM leads to a small-sized state-space model with high fidelity and a low computational cost, which is optimal for the design of model-based wind farm control strategies.

9.2 Contributions to the scientific literature

Reduced-order models of CFD simulations are obtained in this paper. The method has a low computational cost and good accuracy, both essential features for a tool-oriented tool for wind farm control. A Kalman filter that uses power as the feedback signal is used to improve the model's quality. The focus of this study is on yaw misalignment control with two turbines. The ROMs are identified with CFD simulations in which the yaw angle of the upstream turbine keeps changing with time. Results indicate that the ROMs can capture the main flow characteristics in a horizontal slice and a vertical slice, both through the rotor center. The power predicted by the ROMs is very close to the values obtained in CFD.

9.3 Authors' contribution

Chengyu Wang implemented the yaw controllers, performed the CFD simulations, and provided data to the first author, Alberto Fortes-Plaza. Jiangang Wang and Chengyu Wang developed the simulation framework together. Filippo Campagnolo conducted wind tunnel experiments and provided data.

Alberto Fortes-Plaza wrote the manuscript with Carlo L. Bottasso. Carlo L. Bottasso supervised the work.

9.4 Reference

A. Fortes-Plaza, F. Campagnolo, J. Wang, C. Wang, C. Bottasso *et al.*, "A POD reduced-order model for wake steering control," in *Journal of Physics: Conference Series*, vol. 1037, no. 3, 2018. doi: 10.1088/1742-6596/1037/3/032014

CHAPTER 10

Paper 8: How realistic are turbine wakes in wind tunnel tests?

10.1 Summary

Wind tunnel testing offers some unique advantages over full-scale field testing. In addition to its much lower costs compared to full-scale experiments, there are several other benefits. First, the ambient conditions are repeatable and controllable. Second, it is possible to obtain detailed flow measurements, for example, with hot-wire probes, PIV and LiDARs, whereas measurements of comparable accuracy are hardly possible at full scale. Third, turbine models can be designed ad hoc to achieve specific goals and can be extensively instrumented, while layouts and scenarios can be readily changed to explore different operating conditions of interest.

Notwithstanding these benefits, it is essential to quantify the level of realism of wakes of scaled wind turbines in wind tunnels. The aim of this paper is to identify what aspects of the wakes in wind tunnels faithfully represent the full-scale truth and what aspects do not. Several steps are taken to answer the question. First, detailed measurements of the TUM G1 scaled wind turbine wake are gathered in a boundary layer wind tunnel for different yaw misalignment and turbulent inflow conditions. Second, an LES-ALM (actuator line method) is used to simulate the wind tunnel experiments. The code is then validated with respect to the power, thrust coefficients, and wake profiles. Third, a dimensional analysis and wake physics are used to review the mechanism of wake formation and recovery. Next, full-scale turbines are designed that match some of the parameters of the scaled model. Various versions of these models are considered, ranging from a more realistic full-scale turbine to less realistic ones that better match the characteristics of the scaled model. The full-scale models are simulated with the same LES-ALM code, using the same algorithmic parameters. Finally, the numerically simulated scaled and full-scale wakes are compared, revealing which aspects of the wakes obtained in the wind tunnel are realistic and which aspects are not.

10.2 Contributions to the scientific literature

The non-dimensional mean flow speed and Reynolds shear stresses have been compared between the full-scale models and scaled models for both wind-aligned and wind-misaligned conditions. The match of all the quantities is good, especially in the far wake from 3D. Several factors result in slight mismatches between different scales, including the circulation mismatch close to the blade's root, the sizes of nacelle and tower, and the mismatch of the inflow integral length scale. The mismatches caused by these factors have been quantified using CFD simulations, and the impacts are very small or even negligible. In addition to the analysis of a single turbine, two wind farm control metrics have been evaluated, i.e., the available power ratio in the wake of a turbine and the amount of flow angle change in the wake of a yawed turbine. The scaled turbine model preserves these two metrics well compared to full-scale models. Overall, with very limited mismatches caused by various factors, the wakes in wind tunnels obtained with appropriately scaled wind turbine models have a very high degree

of realism. These results show that it is reasonable to research wake behavior in wind tunnels with appropriately scaled wind turbine models.

10.3 Authors' contribution

Chengyu Wang performed the simulations and analyzed the results; Carlo L. Bottasso devised the original idea of this research, performed the scaling analysis, and supervised the work; Filippo Campagnolo was responsible for the wind tunnel experiments and the analysis of the measurements, and co-supervised the work; Helena Canet designed the full-scale turbine models; Daniel J. Barreiro Clemente validated the full-scale turbine models with BEM and CFD codes. Chengyu Wang and Carlo L. Bottasso wrote the manuscript. All authors provided important input to this research work through discussions, feedback, and by improving the manuscript.

10.4 Reference

C. Wang, F. Campagnolo, H. Canet, D. J. Barreiro, and C. L. Bottasso, "How realistic are turbine wakes in wind tunnel tests?" *Wind Energy Science, in review*, 2020. doi: https://doi.org/10.5194/wes-2020-115

CHAPTER 11

Conclusions and discussion

In this dissertation, high-quality BEM and CFD models of a scaled turbine were built. The models were thoroughly validated with wind tunnel measurement in terms of turbine responses and wake profiles. The validated models were used to study various wind farm control strategies, and the physical mechanisms of each strategy were explained. Several full-scale wind turbine models that match the non-dimensional characteristics of the scaled wind turbine were designed, which were used to study the level of realism of turbine wakes obtained in the wind tunnel.

One critical aspect of building up high-quality digital models was to obtain accurate polars, which was achieved through a polars identification method. Then, the validated models were used to study three different sorts of wind farm control strategies, including yaw misalignment control, dynamic induction control, and individual pitch control. In addition, the models were also used to study the aerodynamics of floating offshore wind turbines installed on a multi-turbine platform and a reduced-order model that has the potential to reproduce CFD results with a much lower computational cost. Finally, the comparison between the full-scale and scaled turbine wakes indicates that it is reasonable to use appropriately scaled turbines and wind tunnel to study wake effects.

Polars identification

The aerodynamic parameters of airfoils used on scaled wind turbine models were identified from turbine operational data. The inputs include wind speed, air density, rotor speed, and blade collective pitch angle, while the outputs include power and thrust coefficients. The identification method is appropriate for a scaled wind turbine since its aerodynamic parameters can deviate from nominal values because of manufacturing imperfections [82].

A new maximum likelihood method [64] that accounts for errors in the outputs and inputs was proposed and employed to obtain the parameters. The new method is a generalization of the classical approach, which allows the model inputs to differ from the actual measured quantities because of noise. The newly expanded formulation uses an iteration between the standard parameter estimation and a series of decoupled and reasonable steps to compute the inputs. An SVD-based coordinate transformation was used to accelerate the algorithm and increase the posedness of the identification problem. The formulation is further improved by a filtering technique that utilizes the a priori information on the measurement uncertainties, which provides a better initial guess for the identification.

The new identification approach was applied to estimate aerodynamic characteristics of the blades of small-scale wind turbine models. Results also indicate that the current approach was able to cope with the ill-posedness of the problem caused by the low observability of many unknown parameters, which is essential for the practical applicability of the model for complex problems. The polars obtained had higher quality than the error-in-output-only method, indicating the necessity to account for input errors in the polars identification problem. For the first time, the identified parameters were able to correctly model derated operating conditions that were not included in the data for identification.

CFD framework

A digital copy [40] of the scaled experiments performed in a boundary layer wind tunnel was developed with a CFD approach. The digital copy includes both the turbulent inflow condition used in the wind tunnel and the wind turbine ALM (actuator line method) model.

The turbulent inflow was generated passively by using spires and roughness elements in the wind tunnel. With two different setups, turbulent inflows with a medium (5%) and high (10%) turbulence intensity were generated, corresponding to typical offshore and onshore conditions. Precursor simulations were conducted to obtain the digital copies of the two types of turbulent inflows. Structured body-conforming mesh resolves shapes of the spires, while the immersed boundary method models hundreds of roughness elements. The precursor simulation results were validated with constant temperature anemometry (CTA) measurements conducted in the wind tunnel [100], and an excellent match has been obtained for both the velocity and turbulence intensity profile. Among various approaches attempted during the dissertation, the one using body-conforming structured mesh gave the best results.

The ALM models [46] of turbines were validated with detailed wind tunnel measurements of the G1 model, including the power, thrust, and wake at different locations. Detailed comparisons between numerical and experimental results demonstrate the ability of LES to model a wide range of operating conditions. The comparison between experiments and simulations began with low-turbulence (1%) operating conditions, showing a good agreement. Then, the medium turbulence intensity case was considered, giving an even better agreement with the experiments. According to the validation findings, the requirement on mesh fineness if the ambient turbulence intensity is relatively high. The ambient turbulence fosters tip vortices break-down and decreases the mesh fineness requirement to resolve the break-down process. Overall, results indicate that the LES-ALM approach in this work is a reliable approach to model scaled wind turbine experiments, in the sense that CFD results match all wind tunnel measurements well.

As a further step of validation, a code-to-code-to-experiment [65] comparison was conducted for two LES-ALM codes. The main difference between the two codes is the discretization scheme: a second-order finite volume method and a sixth-order compact finite difference scheme. The second-order scheme is the primary methodology used for this dissertation, while partners at Imperial College London use the sixth order scheme.

Both codes were able to simulate the scaled wind farm with reasonable accuracy. A grid convergence study shows that the higher-order scheme converges at a coarser mesh resolution, as expected. The comparisons of power, thrust, mean wake profiles, Reynolds shear stresses, flow spectra, and velocity auto-correlations show a high level of similarity between the two codes. The sixth order scheme is moderately under-dissipative, while the second-order scheme is slightly over-dissipative. The second-order scheme had a better match with the experiments and also had a much lower computational cost. These results indicate that the second-order scheme used in this dissertation suits the need to simulate wind farm phenomena.

Yaw misalignment control

The validated CFD simulation framework is applied to various applications with different wind farm control strategies. The first wind farm control validated with CFD was the yaw misalignment control [44] of a cluster of three wind turbines [55]. Although it is not a new concept, the detailed flow measurement using LiDARs and a thorough comparison between experiments and simulations provided valuable insights.

Numerical simulations were performed for scaled waked wind turbines at different fixed yaw settings, including a greedy case and an optimal yaw case. For both cases, the flow in a horizontal slice

slightly above the hub-height was measured with two scanning LiDARs [30]. A good match between simulations and experiments in terms of flow velocity distribution and power was obtained. As a novel aspect, turbine torque controllers were implemented in the CFD simulations. The rotor speeds of all three turbines in the simulations matched well with experimental measurements, indicating the accuracy of the turbine model. For the wind farm layout used in this work, the wind farm power of the optimal yaw case is about 20% higher than the greedy case, confirming the potential of yaw control to increase wind farm power.

Besides the validation of the numerical model, the secondary deflection effect was demonstrated by both the experiment and the simulation. There is an observation that the wake of the second turbine was more deflected than the wake of the first turbine, although the yaw angle of the second is smaller than the one of the first. Therefore, it appears that the side wash caused by a deflected wake has non-negligible effects on the path of downstream wakes.

Dynamic induction control

The CFD-ALM framework was used to simulate the dynamic induction control (DIC) strategy [31]. This strategy uses cyclic blade pitch motions to enhance wake recovery. Although corresponding CFD-AD simulations were performed in the past, higher fidelity CFD-ALM simulations were still desired, and this part of the dissertation filled this gap.

In the wind tunnel, three aligned wind turbines models G1 were placed in the wind tunnel with a spacing of 5D, and the pitch angle of the first wind turbine changed with a sinusoidal signal to implement the DIC. An excellent match with experimental measurements was achieved [66].

The experimental and numerical results were both evidence for the power enhancement capability of DIC. CFD was used to scan the DIC parameter space and study their effects on the performance. A maximum wind farm power gain of 3.6% was determined with CFD simulations, which corresponds to a thrust coefficient oscillation amplitude of 0.274 at a Strouhal number of 0.3. However, this power increase was obtained at the cost of a high increase in fatigue loading.

Individual pitch control

The effects of load-reducing IPC [34] on the wake of turbines were studied with the CFD tool. Although it is already known that IPC can reduce the nodding and yawing moments on the rotor, the impact of IPC on the turbine wake was investigated in detail, and it was quantified experimentally and numerically [67]. A simulation model was first validated with experiments and then exploited to study differences caused by IPC on wake behavior, power, and loads.

Results show that IPC is an effective way of reducing loading for all considered operating conditions, including positive yaw, negative yaw, and zero yaw cases. The mechanisms by which IPC influences the turbine power and its wake was discussed. The IPC controller responds to lateral flow caused by yaw misalignment and vertical wind shear, which creates asymmetry for positive and negative yawing in terms of the impact on power. The response of the IPC controller directly influences the near wake profile, while the effects change as the wake propagates and rotates.

Overall, no significant enhancement of wake recovery has been observed. The use of IPC on the upstream turbine has been shown to generate a moderate power increase for positive yawing, both upstream and downstream, while it induces power losses for negative yawing. Therefore, the positive yaw direction is preferred when considering yaw misalignment wind farm control if other conditions are kept the same. IPC on the downstream turbine tends, in general, to always reduce power.

POD reduced-order model

Given the high computational cost of CFD, it is not practical to use it for real-time wind farm control with currently available computational resources. A reduced-order model (ROM) was developed [69] based on the proper orthogonal decomposition (POD) as an attempt to fill this gap. The model used flow data obtained from a CFD simulation with two aligned wind turbines with a spacing of 5D. While the yaw angle of the first wind turbine changed with a specified time series, the second turbine did not yaw. This simulation is termed the training simulation. Instantaneous velocity data at each time step on a vertical slice and a horizontal slice were sampled as inputs. The ROM was obtained by compressing the collected data into a standard state-space representation. By extraction of the most dominant features of the data, the degree of freedom of the ROM is significantly smaller than the original data. Instead of only using the velocity data, a Kalman filter is added by using the power signal to further improve the model performance.

After the model identification, a second simulation with a different yaw command was conducted to validate the model. Results indicate that the proposed method can represent the CFD results well, in terms of both flow and turbine power. The flow reconstructed by the ROM preserves the primary features of the original flow sampled from CFD, while some small fluctuations are filtered because of the model size reduction. The Kalman filter improves power prediction significantly. The ROM has a significantly reduced computational cost compared to CFD, so this method can potentially be used for real-time model-based wind farm control.

Level of realism of wind tunnel experiments

Although most research in this dissertation was conducted with scaled wind turbine models in the wind tunnel, the ultimate target is still to understand full-scale turbine aerodynamics. Therefore, it is important to quantify how faithful are the wakes of the scaled turbine compared to the actual ones in the field. A thorough validation of the assumption about the similarity of wakes between scaled and full-scale turbines was not conducted [68]. For this purpose, several full-scale turbines that match the characteristics of G1 were designed. While one model matches the circulation distribution of G1 completely, others only match it partially due to structural constraints. All turbine models were simulated with the same LES-ALM code with the same algorithmic parameters to study factors that lead to discrepancies between scaled and full-scale turbines, including the circulation mismatch.

Results indicate that the turbulence intensity and the non-dimensional velocity profiles are very similar between the full-scale and scaled turbines, especially in the far wake from 4D. Discrepancies mainly appear in the near wake, and they are caused by two main factors, i.e., the sizes of nacelle and tower of and the difference in power coefficient due to airfoil characteristics. The discrepancies decay as wakes propagates downstream. Other factors, like the influence of rotation augmentation effect, and the integral length scale of the inflow, are all shown to have limited effects on the mean wake profile. These results indicate that it is reasonable to research wake by conducting wind tunnel experiments.

Outlook

In the scope of this dissertation, high-quality numerical models that are thoroughly validated by experimental measurements were obtained. The numerical models were used to study various applications, wind farm control strategies, and the similarity between different scales. The ultimate goal of the efforts is to use numerical tools to help understand and explore effective wind farm control strategies.

While many works were done for the validation and the physical mechanism explanation for various scenarios, only a limited amount of work was conducted to explore and optimize wind farm

and turbine controllers. With high-quality numerical tools, further research can be done to explore future wind farm control technology. A list of possible future research directions is listed in the following.

Atmospheric boundary layer simulation

As described in the methods chapter, the current CFD framework models the buoyancy forces with the Boussinesq approximation [94], and a temperature equation is solved for each time step. These two features make the numerical simulations of atmospheric boundary layers (ABL) under different stability conditions possible. In fact, some initial tests with the current CFD framework already demonstrate its capability to model ABL with reasonable accuracy. Although all the wind tunnel experiments and simulations presented in this dissertation were conducted with stable to neutral ABL, it is valuable to check the situations with unstable ABL. An especially interesting research topic is exploring how does the stability of the atmosphere influence wake recovery. The numerical simulation tools can be exploited to give initial answers to this question. The approach is to use CFD to construct two ambient flows with the same turbulence intensity but different ABL stability conditions. When a turbine is operated in each ambient flow, the influence of ABL stability on wake recovery can be isolated and studied.

Advanced dynamic induction control

Although it is known that the mechanism of dynamic induction control is to trigger the natural instability of the wake, a more detailed explanation is desired. This goal can be achieved through more detailed visualization through CFD. Some initial results of the iso-vorticity surfaces indicate that the reason can be the collision between fast and slow concentric vortex rings. Once the DIC mechanism is better understood, some more advanced DIC strategies can be explored. For example, the DIC discussed in this dissertation was done with cyclic pitch motion, but it could also be done with yaw oscillations. Given the low sensitivity of power with respect to yaw when it is close to zero and low expectation of additional loads, yaw oscillations might result in better performance both for power and thrust. The CFD tool can be employed to study such effects.

Advanced individual pitch control

The effects of load-reducing IPC based on PI control have been studied, and all observed phenomena have been explained. However, the usage of IPC should not be only limited to load reduction, and it could also be used for wake recovery enhancement. Instead of eliminating nodding and yawing moments on the rotor, IPC can also be used to modify the frequencies and magnitudes of these two moments. Thus, artificial wake meandering can be generated, which results in a helix [101]. When conducted at the right frequency and magnitude, this strategy has the potential to enhance wake recovery.

Development and exploitation of the ROM

The POD reduced-order model can be further extended to improve its predictive capabilities. For example, local estimates of wind speed on the rotor speed obtained using blade load measurement can be an additional input for the model. In addition, the temperature, pressure, and vorticity of the flow can all be used as additional inputs to provide more abundant information, which can be handled collectively by the POD method.

While the reduced-order model was validated with out-of-set simulation data, it has not been applied for real-time wind farm control purposes yet. It is interesting to verify the effectiveness of such a model-based controller with closed-loop wind farm control.

Field testing

Pure numerical simulations were conducted to study the similarity of wakes between scaled and full-scale turbines. Although the results are relatively complete, it is undoubtedly beneficial to collect some evidence from experimental field measurements. With the validation of field testing data, the similarity will be confirmed with even better plausibility.

Wind Energ. Sci., 5, 1537–1550, 2020
https://doi.org/10.5194/wes-5-1537-2020

eawe european academy of wind energy
Open Access
WIND ENERGY SCIENCE

Identification of airfoil polars from uncertain experimental measurements

Chengyu Wang, Filippo Campagnolo, and Carlo L. Bottasso

Wind Energy Institute, Technische Universität München, 85748 Garching b. München, Germany

Correspondence: Carlo L. Bottasso (carlo.bottasso@tum.de)

Received: 17 July 2020 – Discussion started: 30 July 2020
Revised: 21 September 2020 – Accepted: 1 October 2020 – Published: 10 November 2020

Abstract. A new method is described to identify the aerodynamic characteristics of blade airfoils directly from operational data of the turbine. Improving on a previously published approach, the present method is based on a new maximum likelihood formulation that includes errors in both the outputs and the inputs, generalizing the classical error-in-the-outputs-only formulation. Since many parameters are necessary to meaningfully represent the behavior of airfoil polars as functions of angle of attack and Reynolds number, the approach uses a singular value decomposition to solve for a reduced set of observable parameters. The new method is demonstrated by identifying high-quality polars for small-scale wind turbines used in wind tunnel experiments for wake and wind farm control research.

1 Introduction

Most simulation models of wind turbine rotors, from the low to the high end of the fidelity spectrum, rely on polars, i.e., on the aerodynamic characteristics of the airfoils used on the blade. Clearly, irrespectively of its sophistication, the quality of the results that a simulation can deliver is bound to many details of the underlying mathematical model and numerical methods but also to the accuracy of the polars. Unfortunately, it is often difficult to have a precise knowledge of such a crucial ingredient. In fact, whereas polars are typically characterized by ad hoc experiments or simulations conducted on isolated airfoils, there are many reasons why the actual polars of a specific blade can differ from the nominal ones. To address this need, this paper describes a new procedure for the tuning of polars based on turbine operational data.

Airfoil polars are used for modeling the aerodynamics of rotors using lifting lines in conjunction with blade element momentum (BEM), free vortex wake (FVW), and computational fluid dynamic (CFD) models. BEM methods are routinely used for the aeroservoelastic analysis of wind turbines and provide most of today's industrial-level simulation capabilities for load analysis, design, and control development activities (Manwell et al., 2009; Burton et al., 2011; OpenFast, 2020). FVW methods (Sebastian and Lackner, 2012; Shaler et al., 2019) are not yet routinely used because of their higher computational costs but offer promising alternatives by removing some of the assumptions of BEM theory. On the higher end of the spectrum, the large-eddy simulation actuator line method (LES-ALM; Troldborg et al., 2007; Churchfield and Lee, 2012; Churchfield et al., 2012; Wang et al., 2019) is currently the main approach for the modeling of wakes, including the hot topic of wind farm control (Fleming et al., 2013; Gebraad et al., 2016).

In all of these approaches, a lifting line models the blade from the aerodynamic point of view. A generic lifting line is a three-dimensional curve running along the blade, which may be prebent and swept. The local chord, twist, airfoil type, and its relative position (for example, in terms of the chordwise offset of the aerodynamic center) are specified along the curve. The lifting line is attached to the structural model of the blade and moves with it following its travel around the rotor disk and its deformation. At each instant of time during a simulation, the local flow relative to a generic point of the lifting line can be computed. The local flow accounts for the wind inflow, for the motion of the blade, and for the local induction generated by the rotor, whose details depend on the specific aerodynamic model (BEM, FVW, or CFD). Given the local flow, the angle of attack of the airfoil and the Reynolds number can be readily obtained. This allows one

to compute the lift, drag, and moment aerodynamic coefficients at that location along the blade, typically by interpolating within look-up tables that store the aerodynamic properties of the airfoil. Possible corrections are applied to take into account tip and root losses, unsteady aerodynamics, dynamic stall, Coriolis-induced delayed stall, and other effects, in turn producing the local aerodynamic force exerted on the blade at that location. By the principle of action and reaction, an equal and opposite force is applied to the flow, and, again depending on the specific formulation, this closes the loop between blade motion and fluid flow. A new estimate of the local flow is therefore produced, and the process is repeated until convergence.

For several years, the group of the senior author has been developing scaled and controlled wind turbine models for wind tunnel testing (Bottasso et al., 2014b; Bottasso and Campagnolo, 2020). Applications have considered both wind turbine (Bottasso et al., 2014b) and wind farm control (Campagnolo et al., 2016, 2020; Frederik et al., 2019). In addition to the collection of valuable data sets in the known, repeatable, and controllable environment of the wind tunnel, the development and validation of digital copies of these experiments have been main ambitions of this research effort. Both aeroelastic BEM (Bottasso et al., 2014b) and LES-ALM (Wang et al., 2019) models of the experiments have been developed, in the latter case including not only the wind turbines but also the wind tunnel and the passive generation of a sheared and turbulent flow. Results collected to date demonstrate an excellent ability of the simulation models in reproducing the experiments, including multiple wake interactions and conditions relevant to wind farm control (Wang et al., 2019, 2020a,b,c).

One crucial component of the simulation chain has been a method for estimating the polars directly from operational data of the turbines (Bottasso et al., 2014a). In fact, the blades of scaled wind turbine models operate in low Reynolds regimes, where even relatively small changes in the operating conditions can cause significant changes in the aerodynamic characteristics of the blade sections. In addition, given the small size of these models, even modest manufacturing imperfections and normal wear of the blades can lead to deviations from their nominal shape. Using the method of Bottasso et al. (2014a), the nominal airfoil polars are augmented with parametric correction terms, which are identified using a maximum likelihood (ML) criterion based on operational power and thrust measurements. These data points are collected on the turbine at various operating conditions, selected in order to span a desired range of angles of attack and Reynolds numbers. Since a large number of free parameters are necessary to represent the correction terms, the resulting problem is ill-posed, and the parameters are collinear. To address this issue, the original parameters are transformed into a new orthogonal set by using the singular value decomposition (SVD). Because the new parameters are uncorrelated with each other, one can select an observability threshold, discard the unobservable set, and solve only for the observable one. After having solved the identification problem, which is now well posed, the solution is mapped back onto the space of the original physical parameters.

Although this method works well in practice, it still suffers from assumptions that limit its effectiveness. Indeed, the classical ML formulation is based on an input–output model and assumes errors in the outputs only (Klein and Morelli, 2006; Jategaonkar, 2015). Following this approach, outputs differ from available measurements because of measurement errors and model deficiencies. However, errors are not explicitly accounted for in the inputs, which are assumed to be equal to their measured values. In the present context, inputs represent the operating conditions of the turbines, which are expressed by the ambient air density and wind speed, the rotor angular velocity, and the blade pitch setting. Errors in such quantities have a non-negligible effect on the outputs and should be taken into account in a rigorous statistical sense.

To address this issue, the present paper proposes a new general formulation of ML identification that includes errors both in the outputs and in the inputs. This generalized formulation leads to an optimization problem in the model parameters and the unknown model inputs, which can now differ from their measured values. The proposed method is again cast within the SVD-based reformulation of the unknowns to deal with the ill-posedness and redundancy of the parameters. The new formulation is applied to the identification of the polars of small-scale controlled wind turbines, developed to support wind farm control and wake research (Wang et al., 2019; Campagnolo et al., 2020; Frederik et al., 2019; Bottasso and Campagnolo, 2020). Results indicate that the new formulation delivers polars of superior quality with respect to the original error-in-the-outputs-only formulation. Specifically, the new polars were able for the first time to correctly predict the turbine power outputs in derated conditions, which had always defied previous efforts.

The paper is organized according to the following plan. Section 2 describes first the classical ML approach in Sect. 2.1 and its reformulation in terms of uncorrelated parameters in Sect. 2.2; Sect. 2.3 presents the novel ML method with errors in both outputs and inputs, while Sect. 2.4 discusses a way to take into account a priori information on the errors. Section 3 specializes the general formulation of Sect. 2.3 to the identification of the polars of scaled wind turbines. Finally, Sect. 4 presents the results, and conclusions are drawn in Sect. 5.

2 Formulation

2.1 Classical maximum likelihood estimation with errors in the outputs

Consider a system described by the parametric model

$$\boldsymbol{y} = \boldsymbol{h}(\boldsymbol{p}, \boldsymbol{u}), \tag{1}$$

where $\boldsymbol{u} \in \mathbb{R}^l$ are the inputs (or, in the present context, the operating conditions), $\boldsymbol{p} \in \mathbb{R}^n$ the model parameters, and $\boldsymbol{y} \in \mathbb{R}^m$ the outputs. In correspondence to the N inputs $\mathcal{U} = \{\boldsymbol{u}_1^*, \boldsymbol{u}_2^*, \ldots, \boldsymbol{u}_N^*\}$, N experimental measurements of the outputs are available and noted $\mathcal{Y} = \{\boldsymbol{y}_1^*, \boldsymbol{y}_2^*, \ldots, \boldsymbol{y}_N^*\}$. Because of modeling and measurement errors, the experimental measurements are in general not identical to the outputs predicted by Eq. (1), a difference that can be quantified by the residual $\boldsymbol{r} = \boldsymbol{y}^* - \boldsymbol{y}$. The goal of the estimation problem is to find the model parameters $\boldsymbol{p}$ that minimize the residuals $\boldsymbol{r}$.

A classical approach to this parameter estimation problem is the ML method (Klein and Morelli, 2006). The idea of maximum likelihood estimation is to find the parameters $\boldsymbol{p}$ that maximize the probability J of obtaining the measurement sample $\mathcal{Y}$, where J is written as

$$J = \frac{Nm}{2}\ln(2\pi) + \frac{N}{2}\ln(\det\mathbf{R}) + \frac{1}{2}\sum_{i=1}^{N} w_i^2 \boldsymbol{r}_i^T \mathbf{R}^{-1}\boldsymbol{r}_i, \tag{2}$$

$\mathbf{R}$ being the residual covariance and w_i a weight assigned to the ith residual. In this work, weights are introduced to account for the fact that not all operating conditions appearing in the sample $\mathcal{U}$ might have the same importance. For example, it might happen that some $\boldsymbol{u}_i$'s represent frequent typical operating conditions of the system, whereas others are less frequent or relevant conditions. It might then be desirable to better match these more frequent conditions than the less frequent ones. One way to achieve this behavior from the ML estimator is to assign weights to the residuals. The weights could be proportional to the relative frequency of each operating condition in the lifetime of the system or be inversely proportional to the distance of that operating condition to some nominal behavior, a concrete example of this latter case being explained later in the results section.

A robust implementation of this optimization problem is obtained by the following iteration (Klein and Morelli, 2006).

1. Assuming temporarily frozen parameters equal to $\boldsymbol{p}$, minimize J with respect to $\mathbf{R}$, which yields the following expression for the covariance matrix (Jategaonkar, 2015):

$$\mathbf{R} = \frac{1}{NW}\sum_{i=1}^{N} w_i^2 \boldsymbol{r}_i(\boldsymbol{p})\boldsymbol{r}_i^T(\boldsymbol{p}), \tag{3}$$

   where $W = 1/N\,\Sigma_{i=1}^{N} w_i^2$.

2. Assuming a temporarily frozen error covariance $\mathbf{R}$, solve the minimization problem

$$\boldsymbol{p} = \mathrm{argmin}_{\boldsymbol{p}} \frac{1}{2}\sum_{i=1}^{N} w_i^2 \boldsymbol{r}_i^T(\boldsymbol{p})\mathbf{R}^{-1}\boldsymbol{r}_i(\boldsymbol{p}). \tag{4}$$

3. Return to step 1, and repeat until convergence.

In the following, alternating between steps 1 and 2 is termed a "major" iteration. The internal iterations necessary for the solution of the optimization problem at step 1 are termed in the following "minor" iterations.

2.2 Maximum likelihood estimation in terms of uncorrelated parameters

The estimation problem expressed by Eqs. (3) and (4) can be ill-posed because of low observability and collinearity of the unknowns. This is a classical difficulty in parameter estimation: on the one hand one would typically prefer a rich set of parameters that give ample freedom to adjust the behavior of a model in order to accurately match the measurements; on the other hand, it might be difficult – if not altogether impossible – to always guarantee that there is enough informational content in the measurements to correctly identify and distinguish the effects of each one of the unknown parameters.

Indeed, the well-posedness of the identification problem is associated with the curvature of the likelihood function with respect to changes in the parameters. Around a flat maximum, different values of the parameters yield similar values of the likelihood. A measure of the curvature of the solution space is provided by the Fisher information matrix (Jategaonkar, 2015). The inverse of this matrix is also useful because it bounds the variance of the estimates (Cramér-Rao bound) (Jategaonkar, 2015). Unfortunately, the Fisher information by itself does not offer a constructive way of reformulating a given ill-posed problem.

To overcome this difficulty, Bottasso et al. (2014a) proposed to transform the original physical parameters of the model into an orthogonal parameter space. This mapping is obtained by diagonalizing the Fisher matrix using the SVD. As the new variables are now statistically independent, one can readily select and retain in the analysis only the parameters that are associated with a sufficiently high level of confidence. Once the problem is solved, the uncorrelated parameters are mapped back onto the original physical space.

This approach enables one to solve an identification problem with many free parameters, some of which might be interdependent or not observable in a given data set. Furthermore, the SVD diagonalization reduces the problem size, retaining only the orthogonal parameters that are indeed observable. Finally, this approach reveals, through the singular vectors generated by the SVD, the interdependencies that may exist among some parameters of the model, which may provide useful insight into the problem itself.

A detailed description of the SVD-based version of ML identification is given in Bottasso et al. (2014a). The same formulation is used also in the present paper.

2.3 Maximum likelihood estimation with errors in the inputs and outputs

The standard formulation of the ML identification presented in Sect. 2.1 considers the presence of noise in the outputs $\boldsymbol{y}$. Indeed, outputs are affected by measurement errors but also, being computed through a model, by the deficiencies of the model itself. Although errors in the outputs are typically the primary source of uncertainty in a parameter estimation problem, there are situations where significant errors may also be associated with the inputs $\boldsymbol{u}$, which is the case of the present application. A formulation of ML that accounts for errors both in the outputs and inputs is presented next.

The parametric model described by Eq. (1) is expanded as

$$\widehat{\boldsymbol{y}} = \left\{ \begin{matrix} \boldsymbol{y} \\ \boldsymbol{u} \end{matrix} \right\} = \left\{ \begin{matrix} \boldsymbol{h}(\boldsymbol{p},\boldsymbol{u}) \\ \boldsymbol{u} \end{matrix} \right\}. \tag{5}$$

Because of modeling and measurement errors, the experimental output measurements $\boldsymbol{y}^*$ are in general not identical to the model-predicted outputs $\boldsymbol{y}$. Similarly, because of measurement errors and an imperfect realization of the operating conditions, the experimental inputs $\boldsymbol{u}^*$ are in general not identical to the nominal ones $\boldsymbol{u}$. These differences can be synthetically quantified by the residual $\widehat{\boldsymbol{r}} = \widehat{\boldsymbol{y}}^* - \widehat{\boldsymbol{y}}$, where now $\widehat{\boldsymbol{y}}^*$ is an expanded vector that contains measurements of both outputs and inputs:

$$\widehat{\boldsymbol{y}}^* = \left\{ \begin{matrix} \boldsymbol{y}^* \\ \boldsymbol{u}^* \end{matrix} \right\}. \tag{6}$$

The goal of the estimation problem is to find the model parameters $\boldsymbol{p}$ and system inputs $\boldsymbol{u}_i$ that maximize the probability of obtaining the measurements $\boldsymbol{y}^*$ and $\boldsymbol{u}^*$. According to the maximum likelihood criterion, Eq. (4) becomes

$$\begin{aligned} &\boldsymbol{p}, \boldsymbol{u}_1, \ldots, \boldsymbol{u}_N \\ &\quad = \operatorname{argmin}_{\boldsymbol{p},\boldsymbol{u}_i} \frac{1}{2} \sum_{i=1}^{N} w_i^2 \widehat{\boldsymbol{r}}_i^T(\boldsymbol{p},\boldsymbol{u}_i) \widehat{\mathbf{R}}^{-1} \widehat{\boldsymbol{r}}_i(\boldsymbol{p},\boldsymbol{u}_i), \end{aligned} \tag{7}$$

and Eq. (3) is now

$$\widehat{\mathbf{R}} = \frac{1}{NW} \sum_{i=1}^{N} w_i^2 \widehat{\boldsymbol{r}}_i(\boldsymbol{p},\boldsymbol{u}_i) \widehat{\boldsymbol{r}}_i^T(\boldsymbol{p},\boldsymbol{u}_i). \tag{8}$$

Instead of solving the problem in a monolithic fashion, the following iteration can be conveniently used:

1. Initialize $\boldsymbol{p}$ (see Sect. 2.4), and set $\boldsymbol{u}_i = \boldsymbol{u}_i^*$, $i = [1, N]$.
2. Calculate $\widehat{\mathbf{R}}$ from Eq. (8).
3. Assuming temporarily frozen inputs $\boldsymbol{u}_i$, solve

$$\boldsymbol{p} = \operatorname{argmin}_{\boldsymbol{p}} \frac{1}{2} \sum_{i=1}^{N} w_i^2 \widehat{\boldsymbol{r}}_i^T(\boldsymbol{p},\boldsymbol{u}_i) \widehat{\mathbf{R}}^{-1} \widehat{\boldsymbol{r}}_i(\boldsymbol{p},\boldsymbol{u}_i). \tag{9}$$

   This is formally identical to the classical error-in-the-outputs-only ML formulation, which can be solved by the SVD-based reformulation in terms of uncorrelated parameters (Bottasso et al., 2014a).

4. Assuming temporarily frozen parameters $\boldsymbol{p}$, solve

$$\begin{aligned} \boldsymbol{u}_j = &\operatorname{argmin}_{\boldsymbol{u}_j} \frac{1}{2} \sum_{i=1}^{N} w_i^2 \widehat{\boldsymbol{r}}_i^T(\boldsymbol{p},\boldsymbol{u}_i) \widehat{\mathbf{R}}^{-1} \widehat{\boldsymbol{r}}_i(\boldsymbol{p},\boldsymbol{u}_i), \\ &j = [1, N]. \end{aligned} \tag{10}$$

   These are N decoupled small sized problems, which return the values of the model inputs.

5. Return to step 2, and repeat until convergence.

This way the solution of the identification problem with input and output errors is obtained by using the classical error-in-the-outputs-only ML implementation (using Eq. 9), followed by a sequence of inexpensive optimizations to compute the model inputs (using Eq. 10). Notice that, as long as it converges, this iteration returns the same result as the monolithic solution of Eqs. (7) and (8).

2.4 Filtering of measurements based on a priori uncertainties

Often, a priori information on the expected uncertainties may be available. In such cases, the unknown true inputs $\boldsymbol{u}_i$ can be bounded as

$$\boldsymbol{u}_i^* - \Delta\boldsymbol{u} \le \boldsymbol{u}_i \le \boldsymbol{u}_i^* + \Delta\boldsymbol{u}, \tag{11}$$

where $\Delta\boldsymbol{u}$ are the expected uncertainty bounds. This a priori information can be used to retain in the cost function J only those measurements for which the corresponding residual cannot be simply explained by the uncertainties expressed in Eq. (11) but must be due to the model parameters $\boldsymbol{p}$.

To this end, notice first that the residual $\boldsymbol{r}_i$ is a function of $\boldsymbol{p}$ and $\boldsymbol{u}_i$, i.e.,

$$\boldsymbol{r}_i(\boldsymbol{p},\boldsymbol{u}_i) = \boldsymbol{y}_i^* - \boldsymbol{h}(\boldsymbol{p},\boldsymbol{u}_i). \tag{12}$$

Indicating the jth component of residual $\boldsymbol{r}_i$ as r_{i_j}, its maximum and minimum values for a given $\boldsymbol{p}$ are computed as

$$r_{i_j}^{\mathrm{M}} = \max_{\boldsymbol{u}_i} r_{i_j}(\boldsymbol{p},\boldsymbol{u}_i), \tag{13a}$$

$$r_{i_j}^{\mathrm{m}} = \min_{\boldsymbol{u}_i} r_{i_j}(\boldsymbol{p},\boldsymbol{u}_i), \tag{13b}$$

$$\text{subject to: } \boldsymbol{u}_i^* - \Delta\boldsymbol{u} \le \boldsymbol{u}_i \le \boldsymbol{u}_i^* + \Delta\boldsymbol{u}. \tag{13c}$$

If the maximum $r_{i_j}^{\mathrm{M}}$ and minimum $r_{i_j}^{\mathrm{m}}$ have different signs, then $r_{i_j} = 0$ lies somewhere within this range, and hence this

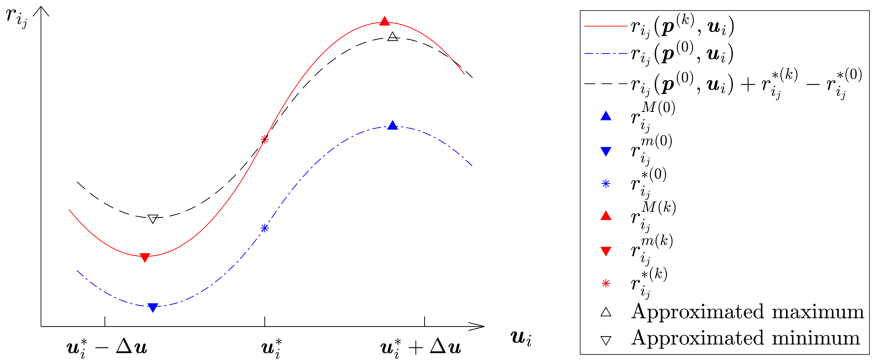

Figure 1. Approximation of the maximal and minimal residuals.

residual component can be fully explained by input uncertainties. Therefore, it cannot drive meaningful changes in the parameters and should be neglected. Otherwise, this residual carries valuable information and should be retained. To account for this, a filtered residual $\tilde{r}_{i_j}$ is defined as

$$\tilde{r}_{i_j} = \min\left(|r_{i_j}|\right). \tag{14}$$

The a priori estimates are used to initialize the parameters $\boldsymbol{p}$ at step 1 of the iterative algorithm formulated in Sect. 2.3. A standard ML method is used for the initialization, considering only errors in the outputs and using Eqs. (3) and (4) where the residual components r_{i_j} are replaced by the filtered ones $\tilde{r}_{i_j}$. Filtering accelerates the optimization because it avoids meaningless tuning of parameters caused by measurement noise. Once this initial estimate of the parameters is obtained, it is further refined by considering the a posteriori effects of noise in inputs and outputs by stepping through points 2–5 of the algorithm. Residual filtering is not used further because it is based on a priori assumptions relying on knowledge of the measurement chain, which can only estimate bounds and might not reflect the actual noise effectively experienced for any given measurement.

In practice, a naive implementation of filtering can be very expensive. In fact, as the residual $\boldsymbol{r}_i$ depends on $\boldsymbol{p}$, one would have to recompute the optimization problems expressed in Eq. (13) each time the parameters are updated, which becomes prohibitively expensive.

The cost of filtering can be drastically reduced with a simple approximation, as graphically illustrated in Fig. 1. The figure shows with a dotted blue line the residual component r_{i_j} as a function of the input $\boldsymbol{u}_i$ for a given value of the model parameters $\boldsymbol{p}^{(0)}$. The counter $(\cdot)^{(0)}$ refers to the values that the parameters assume at the beginning of each major iteration used to solve Eq. (4). The minimum and maximum of this curve, corresponding to $r_{i_j}^{\mathrm{m}}$ and $r_{i_j}^{\mathrm{M}}$, are respectively indicated with downward- and upward-pointing blue triangles. These stationary points are computed at the beginning of each major iteration by solving Eq. (13). For simplicity, this is obtained by a simple evaluation of the residuals over a regular subdivision of the unknowns.

At the kth minor iteration of the solution of Eq. (4), the model parameters have been updated, and they now assume the value $\boldsymbol{p}^{(k)}$. The corresponding function r_{i_j} is depicted in the figure with a solid red line, together with its new minimum and maximum points indicated by downward- and upward-pointing red triangles. To reduce the computational burden, these stationary points are not computed by solving Eq. (13) but are approximated.

The nature of the approximation is shown in the figure. The initial function r_{i_j} corresponding to $\boldsymbol{p}^{(0)}$ is shifted by the difference $r_{i_j}^{*(k)} - r_{i_j}^{*(0)}$, i.e., the difference in the residual evaluated at the nominal inputs $\boldsymbol{u}_i^*$ for the two parameter values $\boldsymbol{p}^{(k)}$ and $\boldsymbol{p}^{(0)}$. The shifted function is shown by the dashed black curve in Fig. 1. This is an inexpensive operation since it does not require any optimization. This nominal difference is then used for shifting the minimum and maximum residuals from their initial value at $\boldsymbol{p}^{(0)}$ to the new value at $\boldsymbol{p}^{(k)}$. By this approximation, the maximum and minimum residuals are readily and inexpensively updated at each iteration as

$$r_{i_j}^{\mathrm{M}(k)} = r_{i_j}^{\mathrm{M}(0)} + r_{i_j}^{*(k)} - r_{i_j}^{*(0)}, \tag{15a}$$

$$r_{i_j}^{\mathrm{m}(k)} = r_{i_j}^{\mathrm{m}(0)} + r_{i_j}^{*(k)} - r_{i_j}^{*(0)}. \tag{15b}$$

Based on these updated values, the residual filtering condition expressed by Eq. (13) can be readily updated.

This approximation works very well in practice since the interval $[\boldsymbol{u}_i^* - \Delta\boldsymbol{u}, \boldsymbol{u}_i^* + \Delta\boldsymbol{u}]$ is small. In addition, by a standard Taylor series analysis, one can show that this approximation entails neglecting terms that are quadratic in the changes in the parameters within a major iteration, which are typically small. Finally, the approximation does not affect the quality of the results as the true stationary points are recomputed at each new major iteration of the ML algorithm. In this sense, the approximation only speeds up the calculations of the minor iterations, but the results – at convergence of the major and minor loops – are the same that would have been

obtained by a straightforward (but more expensive) solution of Eq. (13).

3 Application to the identification of airfoil polars

The parameter identification problem setting described in the previous pages is completely general and could be used for a wide range of applications. However, for the specific problem at hand and with reference to Eq. (1), the outputs are defined as $\boldsymbol{y} = (C_\mathrm{P}, C_\mathrm{T})^T$, where $C_\mathrm{P} = 2P/(\rho A V^3)$ and $C_\mathrm{T} = 2T/(\rho A V^2)$ are respectively the rotor power and thrust coefficients, and P is power, T thrust, ρ air density, $A = \pi R^2$ the rotor swept area, R the rotor radius, and V the wind speed. The inputs describe the rotor operating conditions and are defined as $\boldsymbol{u} = (\rho, V, \Omega, \beta)^T$, where Ω is the rotor angular velocity and β the blade collective pitch angle. To obtain the power and trust coefficients, nominal values of the inputs are used for both the measured and predicted cases.

The airfoil lift and drag coefficients, respectively noted C_L and C_D, are now assumed to be in error, and the goal of the estimation problem is to calibrate them in order to match a given set of measurements. This is achieved by defining changes ΔC_L and ΔC_D with respect to nominal values C_{L_0} and C_{D_0}, i.e.,

$$\Delta C_\mathrm{L} = C_\mathrm{L} - C_{\mathrm{L}_0} = \Delta C_\mathrm{L}(\eta, \alpha, Re), \tag{16a}$$

$$\Delta C_\mathrm{D} = C_\mathrm{D} - C_{\mathrm{D}_0} = \Delta C_\mathrm{D}(\eta, \alpha, Re), \tag{16b}$$

where η is the spanwise location along the blade (because different airfoils are typically used at different stations along a rotor blade); α is the local angle of attack; and $Re = uc/\nu$ is the local Reynolds number, u being the relative flow speed, c the chord length, and ν the kinematic viscosity of air. The dependency of these functions on spanwise location, angle of attack, and Reynolds number is approximated using assumed shape functions and their associated nodal parameters $\boldsymbol{p}_{C_\mathrm{L}}$ and $\boldsymbol{p}_{C_\mathrm{D}}$, which therefore represent the tunable algebraic parameters of the model, i.e.,

$$\Delta C_\mathrm{L}(\eta, \alpha, Re) \approx \Delta C_\mathrm{L}\left(\boldsymbol{p}_{C_\mathrm{L}}\right), \tag{17a}$$

$$\Delta C_\mathrm{D}(\eta, \alpha, Re) \approx \Delta C_\mathrm{D}\left(\boldsymbol{p}_{C_\mathrm{D}}\right). \tag{17b}$$

Following Bottasso et al. (2014a), instead of working directly with $\boldsymbol{p} = (\boldsymbol{p}_{C_\mathrm{L}}; \boldsymbol{p}_{C_\mathrm{D}})$, which might not be all observable, these variables are first transformed by the SVD into an uncorrelated set of parameters, which are then truncated with a variance threshold, calibrated according to the ML criterion, and finally projected back onto the original functional space ΔC_L and ΔC_D.

The dependency of $\boldsymbol{y}$ on $\boldsymbol{p}$ and $\boldsymbol{u}$ is expressed through Eq. (1) using blade element momentum (BEM) theory (Manwell et al., 2009), as implemented in the code FAST (OpenFast, 2020).

The typical Reynolds number distribution along a wind turbine blade is almost constant for the majority of its span but assumes smaller values close to the blade tip and root. The implementation of this paper, improving on the work of Bottasso et al. (2014a), specifically considers that the airfoil polars depend on Re. The expected range of Reynolds numbers is discretized by linear shape functions and associated nodal values, and the local Reynolds number is computed at each spanwise station based on local geometry and flow conditions. The results presented later on consider scaled wind turbine models for wind tunnel testing. For these rotors, the chord-based Reynolds number is much lower than in typical full-scale applications, and ad hoc low-Reynolds airfoils (Lyon and Selig, 1998) are used. Because of the special flow regime of these airfoils, the formulation is complemented by the conditions $\partial C_\mathrm{L}/\partial Re > 0$ and $\partial C_\mathrm{D}/\partial Re < 0$. The first of these conditions accounts for the earlier reattachment of the laminar separation bubble on the suction side of the airfoil for increasing Re and the second for the shorter chord extent of that same bubble (Selig and McGranahan, 2004). They are enforced as soft penalty constraints in Eq. (4) by modifying the cost function as $J = J + J_p$, with

$$J_\mathrm{p} = W_\mathrm{p} \int_{\alpha_\mathrm{m}}^{\alpha_\mathrm{M}} \int_{Re_\mathrm{m}}^{Re_\mathrm{M}} \left(\max\left(0, -\frac{\partial C_\mathrm{L}}{\partial Re}\right) + \max\left(0, \frac{\partial C_\mathrm{D}}{\partial Re}\right)\right) \mathrm{d}Re\mathrm{d}\alpha, \tag{18}$$

where W_p is a penalty parameter, and $[Re_\mathrm{m}, Re_\mathrm{M}]$ and $[\alpha_\mathrm{m}, \alpha_\mathrm{M}]$ are the ranges of Reynolds and angle of attack of interest.

4 Results

4.1 Experimental setup

A scaled wind turbine model of the G1 type (Campagnolo et al., 2016) was operated in the boundary layer wind tunnel of the Politecnico di Milano in low turbulence (1 %) conditions. The rotor blade design is based on one single low-Reynolds airfoil of the RG14 type (Lyon and Selig, 1998). Measurements of the rotor thrust and power were obtained for 158 different operational conditions, chosen to span the range [5.87, 8.81] for the tip speed ratio (TSR) $\lambda = \Omega R/V$ and the range $[-5, 12]^\circ$ for the blade pitch angle β. The wind speed V was varied in the interval $[3.10, 7.86]\,\mathrm{m\,s^{-1}}$, resulting in a range of Reynolds equal to [10 000, 90 000].

Table 1 reports a priori estimates of the uncertainties associated with the various measured quantities. Given the uncertainties of the measurements, worst-case uncertainties of the power and thrust coefficients can be readily computed as

$$\Delta C_\mathrm{P} = \max\left|\frac{2(Q \pm \Delta Q)(\Omega \pm \Delta\Omega)}{(\rho \pm \Delta\rho)A(V \pm \Delta V)^3} - \frac{2Q\Omega}{\rho A V^3}\right|, \tag{19a}$$

$$\Delta C_\mathrm{T} = \max\left|\frac{2(T \pm \Delta T)}{(\rho \pm \Delta\rho)A(V \pm \Delta V)^2} - \frac{2T}{\rho A V^2}\right|. \tag{19b}$$

Table 1. A priori uncertainty estimates of measurements.

Quantity	ΔV	$\Delta\beta$	$\Delta\Omega$	$\Delta\rho$	ΔQ	ΔT
Uncertainty	$\pm 0.1\,\mathrm{m\,s^{-1}}$	$\pm 0.2°$	± 1.5 rpm	$\pm 0.01\,\mathrm{kg\,m^{-3}}$	± 0.005 Nm	± 0.03 N

The wind speed V was measured by a Mensor CPT-6100 pitot transducer (Mensor, 2016), which is affected by pressure and alignment errors. The pitot tube measures the dynamic pressure, i.e., the difference $\Delta p = 1/2\rho V^2$ between the total and the static pressures. Since the wind speed is computed by inverting the dynamic pressure expression, errors in Δp and ρ directly pollute V. Additionally, a yaw and tilt misalignment may exist between the pitot axis and the incoming wind vector, increasing the error in V. The uncertainty of the air density was estimated from the hygrometer and barometer installed in the wind tunnel. After considering all relevant factors, the uncertainty of the wind speed was determined using the guidelines described in Standard ISO 3354 (2008). The uncertainty in the blade pitch angle β was estimated by calibrating the actuator encoder with a Wyler Clinotronic Plus inclinometer (Campagnolo, 2013). Power was computed as $P = Q\Omega$, where Q is the torque, which was measured by strain gages at the rotor shaft. These sensors were calibrated by applying a known torque to the locked rotor. The rotor speed Ω was measured by an optical incremental encoder with a count per revolution $N_\mathrm{e} = 10000$ and an observation window $t_\mathrm{ow} = 4$ ms, which results in an error $\Delta\Omega = 1/N_\mathrm{e}t_\mathrm{ow} \approx 1.5$ rpm. The thrust T was obtained by measuring with a strain gage bridge the fore–aft bending moment at the tower base; here again, the strain gages were calibrated by applying a known load to the turbine by a pulley-and-weight system. The contribution to the bending moment due to the drag of nacelle and rotor was obtained by a dedicated experiment in the wind tunnel without the blades. Additional details on sensors and error quantification are discussed in Campagnolo (2013) and Bottasso et al. (2014b).

For each wind speed V, a turbine should operate at a specific TSR λ and blade pitch β, which are computed in region II to maximize power capture and in region III to limit power output to the rated value. On the other hand, for the task of identifying the airfoil polars, a broad range of conditions is necessary in order to span a sufficient range of angles of attack and Reynolds of interest. Although a broad range is necessary for the generality of the identified model, the conditions that are closer to the nominal operating points – according to the regulation trajectory of the machine – are also the ones most likely encountered during the actual operation of the turbine. To account for this fact, the weight w_i of each operational condition i (see Eq. 2) was assigned based on its distance to the nominal conditions, computed as

$$d_i = \min_\mathrm{s}\sqrt{\epsilon_1(V_i - V^*(s))^2 + \epsilon_2(\beta_i - \beta^*(s))^2 + \epsilon_3(\lambda_i - \lambda^*(s))^2}, \quad (20)$$

where $(\cdot)^*$ indicates a nominal value, and $\epsilon_{1/2/3}$ are scaling factors. All data points were divided into four groups according to their distance. Data points within each group were assigned the same weight, with longer mean distances corresponding to lower weights.

4.2 Identification results

Nominal values of the blade polars are defined as the ones previously computed with the method of Bottasso et al. (2014a). Although of a good quality, these polars are not always able to correctly represent the behavior of the turbine, for example in derated conditions. To improve on this situation, the method proposed here was used to further correct the polars and provide improved estimates.

The lift and drag coefficients were parameterized in terms of bilinear shape functions using seven nodal values for Reynolds and 21 for angle of attack for each one of the two coefficients. Since the G1 blades use one single airfoil type along their entire span, it was not necessary to introduce the dependency on η appearing in the general expressions of Eq. (16).

For the nominal polars, Fig. 2 plots the variance σ^2 (which is the inverse of the singular values produced by the SVD analysis) for the seven considered Reynolds numbers and the lowest 25 modes. The figure shows that modes of intermediate Reynolds number have better observability as most conditions do happen within this range. All modes with a variance above 1 (a threshold indicated in the figure by a dashed horizontal line) were discarded, reducing the number of degrees of freedom from the initial 294 to 117, which improves the well-posedness of the problem and also reduces the computational cost.

The identification first used nominal model inputs $\boldsymbol{u}^*$ and the residual filtering technique of Sect. 2.4 to identify an initial guess to the system parameters $\boldsymbol{p}$, a process that converged after nine major iterations of Eqs. (3) and (4). For the converged solution, Fig. 3 shows the nominal model inputs (two upper plots) and the output residuals (two lower plots), including the nominal residual $\boldsymbol{r}^*$, the maximal residual $\boldsymbol{r}^\mathrm{M}$, the minimal residual $\boldsymbol{r}^\mathrm{m}$, and the filtered residual $\tilde{\boldsymbol{r}}$ (see Eqs. 13 and 14) for each one of the measured data points. The filtered residuals $\tilde{\boldsymbol{r}}$ are 0 for most conditions, indicating that the information carried by these data points cannot be distinguished further from input measurement noise. In addition, all nonzero filtered residuals are small, indicating an almost singular $\widetilde{\mathbf{R}}$, which is in fact used as a termination criterion.

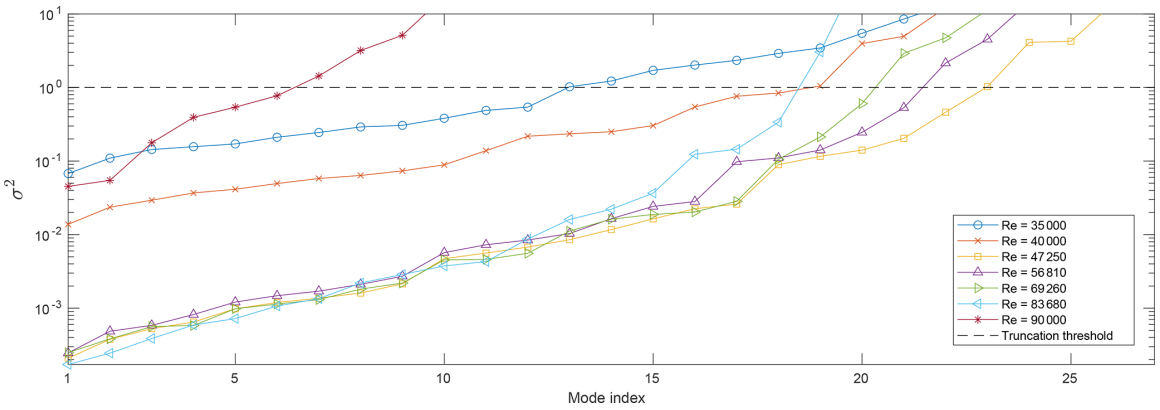

Figure 2. Variance of the lowest 25 modes for varying Reynolds.

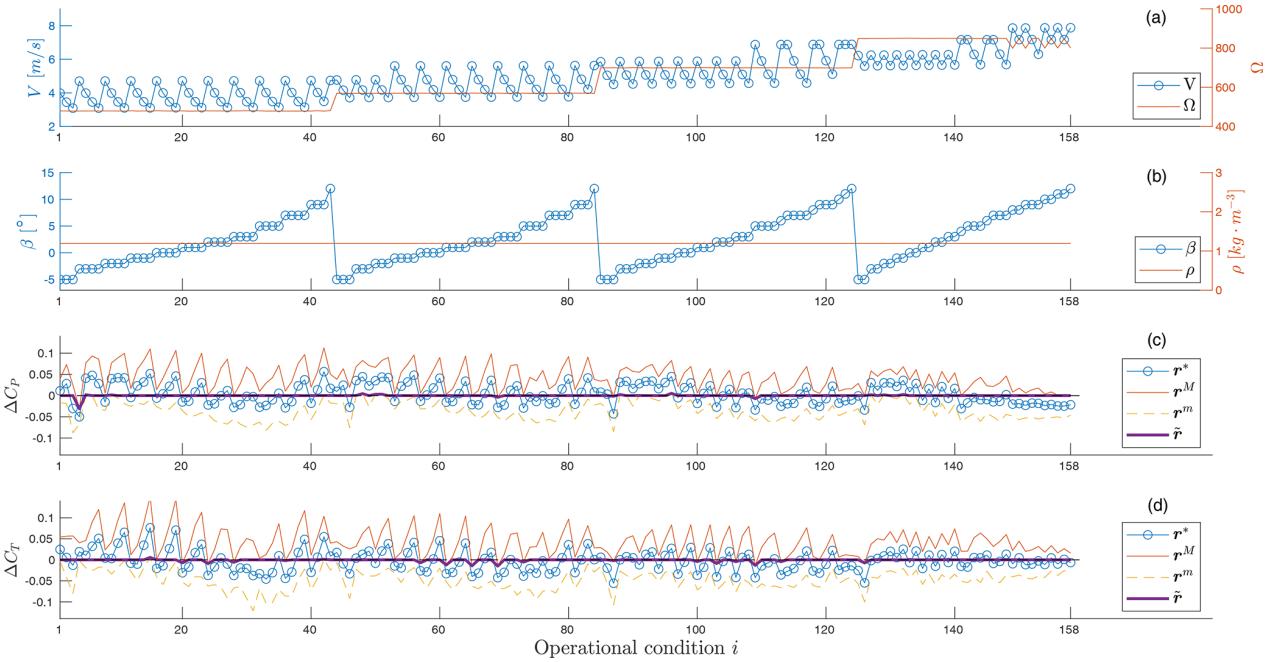

Figure 3. **(a, b)** Nominal model inputs V, Ω, β, ρ. **(c, d)** Nominal, maximal, minimal, and filtered residuals for the two outputs ΔC_P and ΔC_T. All quantities are plotted for each one of the 158 operating conditions in the measurement set.

An a priori estimate of the maximal uncertainties of the power and thrust coefficients can be computed based on Eq. (19) and Table 1, which yields

$$\sigma_\mathrm{P} = \sqrt{\frac{\sum_{i=1}^{N} w_i^2 \left(\Delta C_{\mathrm{P},i}\right)^2}{\sum_{i=1}^{N} w_i^2}} = 0.037, \tag{21a}$$

$$\sigma_\mathrm{T} = \sqrt{\frac{\sum_{i=1}^{N} w_i^2 \left(\Delta C_{\mathrm{T},i}\right)^2}{\sum_{i=1}^{N} w_i^2}} = 0.047. \tag{21b}$$

On the other hand, an a posteriori estimate of the uncertainties evaluated with nominal inputs $\boldsymbol{u}^*$ is available by the covariance matrix $\mathbf{R}$ of Eq. (3) that, using unfiltered residuals, gives

$$\sigma_\mathrm{P} = \sqrt{\widehat{R}_{11}} = 0.024, \tag{22a}$$

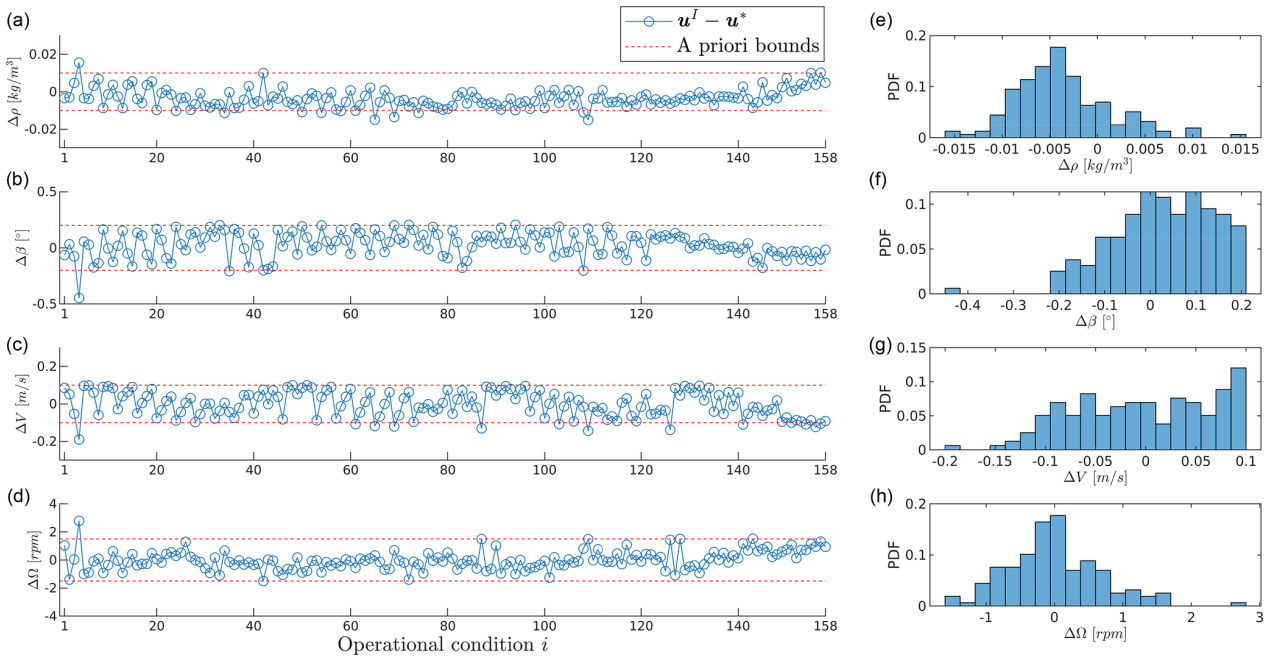

Figure 4. Differences between identified and nominal inputs for all operating conditions **(a–d)** and their corresponding distributions **(e–h)**.

$$\sigma_T = \sqrt{\widehat{R}_{22}} = 0.023. \tag{22b}$$

As expected, the a posteriori estimates are smaller than the a priori ones since the latter represent a worst-case scenario.

The process was then continued using the previously converged parameters as an initial guess. Now, however, the model inputs $\boldsymbol{u}$ were added to the identification to include the effects of their uncertainties. After three iterations, a converged solution was obtained. The final identified inputs are denoted in the following as $\boldsymbol{u}^I$. For all operational conditions, Fig. 4 shows the differences $\Delta\boldsymbol{u} = \boldsymbol{u}^{\mathrm{I}} - \boldsymbol{u}^*$ between identified and nominal values. In all subplots, two dashed horizontal lines indicate the a priori uncertainties reported in Table 1. It is interesting to observe that most estimated inputs are within the a priori bounds, indicating a good coherence between a priori and a posteriori statistics. The right part of the same figure reports the distributions of the errors that, except for wind speed, are close to normal. On the other hand, density appears to have a small bias, which violates one of the assumptions of ML estimation.

Figure 5 shows the nominal (dashed lines) and identified (solid lines) lift (left plot) and drag (right plot) coefficients as functions of angle of attack for various Reynolds numbers. Values outside of the angle of attack and Reynolds ranges of the plot are not identifiable with the available data set and therefore are not shown. The nominal coefficients tuned according to Bottasso et al. (2014a) cross each other, violating the consistency constraints on the laminar separation bubble expressed by Eq. (18). In contrast, the new identified results do comply with the constraints.

Table 2 reports the correlation coefficients, computed from the extended covariance matrix $\widehat{\mathbf{R}}$ at convergence, as $\varrho_{ij} = \widehat{R}_{ij}/(\sigma_i\sigma_j)$, where $\sigma_k = \sqrt{\widehat{R}_{kk}}$. Because of symmetry, only the upper triangle is shown.

The correlation coefficient between the two outputs, ΔC_{P} and ΔC_{T}, is negative. This means that, on average, at the end of the identification process the power and thrust residuals have opposite signs. This is expected since this behavior minimizes the cost function of Eq. (7). Additionally, each input induces same-sign variations in the two outputs; for example, a larger wind speed or density implies higher power and thrust coefficients, whereas a larger blade pitch implies lower power and thrust coefficients. Given that ΔC_{P} and ΔC_{T} have a negative correlation, the input–output correlation coefficients always have different signs for both outputs; e.g., $\varrho(\Delta C_{\mathrm{P}}, \Delta\beta)$ and $\varrho(\Delta C_{\mathrm{T}}, \Delta\beta)$ have opposite signs. The signs of the input–input correlations can be explained in similar terms. For example, the correlation between density and blade pitch is negative because these two inputs have correlations of opposite sign as the outputs, whereas the correlation between blade pitch and wind speed is positive because these two inputs have correlations of the same sign as the outputs.

From the extended covariance matrix at convergence, the mean absolute a posteriori uncertainties of the inputs $\overline{|u^{\mathrm{I}} - u^*|}$ were found to be $0.06\,\mathrm{m\,s^{-1}}$ for speed V, 0.09° for blade pitch angle β, 0.5 rpm for rotor speed Ω, and $0.005\,\mathrm{kg\,m^{-3}}$ for density ρ. By comparison with Table 1, all a posteriori uncertainties are smaller than the a priori ones, as expected.

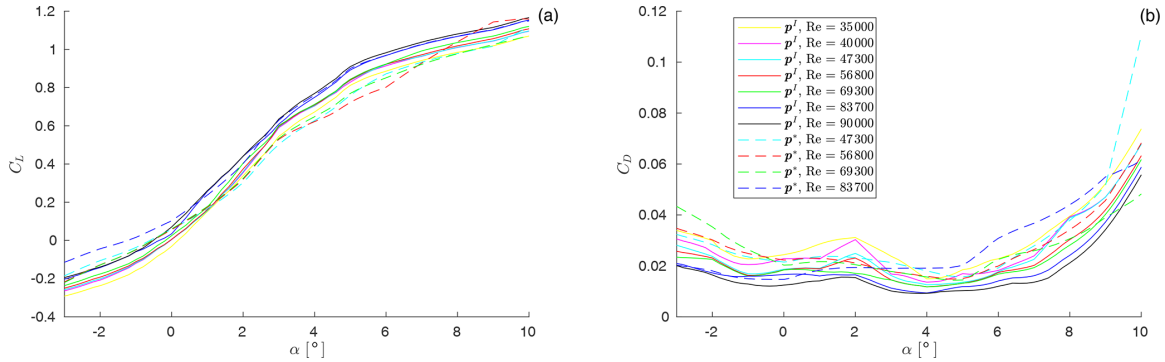

Figure 5. Lift C_L **(a)** and drag C_D **(b)** coefficients as functions of angle of attack α for various Reynolds numbers. Dashed lines: nominal values according to Bottasso et al. (2014a); solid lines: new identified values.

Table 2. Correlation coefficients among inputs and outputs.

	ΔC_P	ΔC_T	$\Delta\rho$	$\Delta\beta$	ΔV	$\Delta\Omega$
ΔC_P	1.0000	−0.8518	0.7084	−0.5550	−0.6206	0.7969
ΔC_T	–	1.0000	−0.8839	0.8540	0.1948	−0.6245
$\Delta\rho$	–	–	1.0000	−0.6661	−0.1100	0.2488
$\Delta\beta$	–	–	–	1.0000	0.0134	−0.4751
ΔV	–	–	–	–	1.0000	−0.5025
$\Delta\Omega$	–	–	–	–	–	1.0000

Table 3. Experimental conditions of the power-derating cases.

Power percentage	100 %	97.5 %	95 %	92.5 %
β (°)	0.42	1.02	1.43	1.79
λ (rpm)	8.31	8.23	8.16	8.10
V (m s^{-1})	5.87	5.88	5.88	5.88

4.3 Power-derating cases

To verify the quality of the identified polars, derated operational conditions were considered. It should be stressed that these conditions were not included in the identification data set and therefore provide for a verification of the generality of the results. These additional conditions are listed in Table 3 and correspond to values equal to 100 %, 97.5 %, 95 %, and 92.5 % of rated power.

Figure 6 shows the results in terms of power (on the left) and thrust (on the right) coefficients as functions of derating percentage. In all plots, the experimental results are shown using a solid blue line with $*$ symbols; whiskers indicate the uncertainties according to Eq. (19) and Table 1. Simulation results are computed with nominal measured inputs $\boldsymbol{u}^*$ for both the nominal polars $\boldsymbol{p}^*$ according to Bottasso et al. (2014a) and the newly identified polars $\boldsymbol{p}^{\mathrm{I}}$, and they are marked with $\times$ and $\circ$ symbols, respectively. The results indicate a marked improvement when using the newly identified polars, especially regarding the rotor power coefficient.

5 Conclusions

This paper has presented a new maximum likelihood identification method that, departing from the classical formulation, accounts for errors both in the outputs and the inputs. The new method is a generalization of the classical approach, where the system parameters are estimated together with the system inputs, which this way can differ from their actual measured quantities because of noise. The new expanded formulation is solved using a partitioned approach, resulting in an iteration between the standard parameter estimation and a series of decoupled and inexpensive steps to compute the inputs. To cope with the ill-posedness of the problem caused by low observability of the parameters, the formulation uses an SVD-based transformation into a new set of uncorrelated unknowns, which, after truncation to discard unobservable modes, are mapped back onto the original physical space. The formulation is further improved by an initialization step that accounts for a priori information on the errors affecting the measurements, discarding all data points whose residuals can be simply explained by uncertainties.

The new proposed formulation was applied to the estimation of the aerodynamic characteristics of the blades of small-scale wind turbine models. This is a particularly difficult problem because an extended set of parameters is necessary in order to give a meaningful description of the polars, taking into account their variability with blade span, angle of attack, and Reynolds number; invariably, this results in an

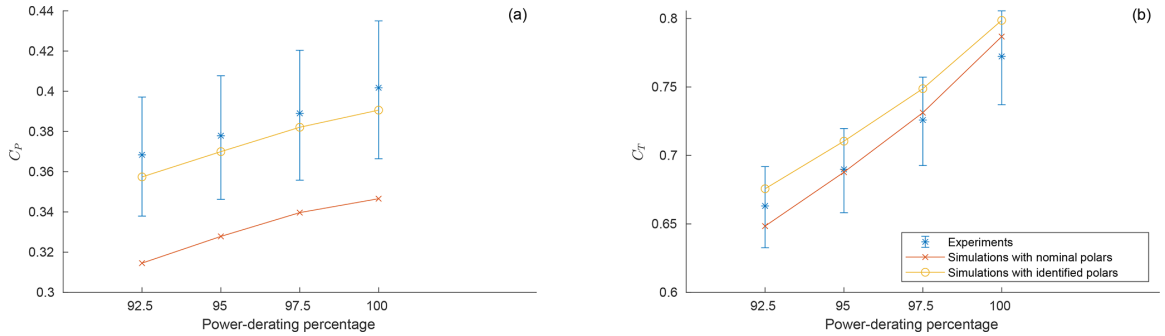

Figure 6. Results for the power-derating cases. **(a)** Power coefficient, **(b)** thrust coefficient. Solid blue line with $*$ symbols: experimental results, including uncertainties according to Table 1; solid orange line with $\circ$ symbols: simulation results with newly identified polars; solid red lines with $\times$ symbols: simulation results with nominal polars according to Bottasso et al. (2014a).

ill-defined problem because of the many unknown parameters and their possible collinearity. In addition, measurement errors affect both the outputs and the inputs, the latter being particularly relevant and representing the operating conditions of the turbines. On the other hand, good-quality estimates of the polars are of crucial importance for the accuracy of simulation models based on lifting lines.

Results indicate that a higher quality of the estimates is achieved by the proposed method compared to an error-in-the-outputs-only approach. Indeed, the estimated polars were able to correctly model derated operating conditions, which were not included in the parameter estimation process. All prior attempts at modeling these conditions failed to a various extent when using the standard maximum likelihood formulation. In addition, results indicate that the present approach was able to cope with the ill-posedness of the problem caused by the low observability of the many unknown parameters, which is an important aspect for the practical applicability of the method to complex problems as the one considered in this paper.

Appendix A: Nomenclature

A	Rotor-swept area
C_{D}	Drag coefficient
C_{L}	Lift coefficient
C_{P}	Power coefficient
C_{T}	Thrust coefficient
J	Cost function
p	Pressure
$\boldsymbol{p}$	Model parameters
P	Power
Q	Torque
$\boldsymbol{r}$	Residual
$\mathbf{R}$	Covariance matrix
Re	Reynolds number
T	Thrust
$\boldsymbol{u}$	Model inputs
V	Wind speed
w_i	Weight of the ith measurement
$\boldsymbol{y}$	Model outputs
α	Angle of attack
β	Blade collective pitch angle
η	Nondimensional blade span location
λ	Tip speed ratio
Ω	Rotor speed
ρ	Density
ϱ	Correlation coefficient
σ	Standard deviation
$\hat{(\cdot)}$	Expanded quantity
$\tilde{(\cdot)}$	Filtered quantity
$(\cdot)^{\mathrm{I}}$	Identified quantity
$(\cdot)^{*}$	Measured quantity
ALM	Actuator line method
BEM	Blade element momentum
CFD	Computational fluid dynamics
FVW	Free vortex wake
LES	Large-eddy simulation
ML	Maximum likelihood
SVD	Singular value decomposition
TSR	Tip speed ratio

Code and data availability. An implementation of the polar identification method and the data used for the present analysis can be obtained by contacting the authors.

Author contributions. CW developed the a priori residual filtering method, wrote the software, performed the simulations, and analyzed the results. FC was responsible for the wind tunnel experiments and the analysis of the measurements. CLB devised the original idea of estimating polars from operational turbine data, developed the ML formulation with errors in inputs and outputs, and supervised the work. CW and CLB wrote the manuscript. All authors provided important input to this research work through discussions and feedback and by improving the manuscript.

Competing interests. The authors declare that they have no conflict of interest.

Acknowledgements. The authors gratefully acknowledge Stefano Cacciola of Politecnico di Milano, who provided the outputs-only version of the code. The authors also express their appreciation to the Leibniz Supercomputing Centre (LRZ) for providing access and computing time on the SuperMUC-NG system.

Financial support. This work has been supported by the CL-WINDCON project, which receives funding from the European Union Horizon 2020 research and innovation program under grant agreement no. 727477.

Review statement. This paper was edited by Alessandro Bianchini and reviewed by two anonymous referees.

References

Bottasso, C. L. and Campagnolo, F.: Wind Tunnel Testing of Wind Turbines and Farms, in: Handbook of Wind Energy Aerod., edited by: Stoevesandt, B., Schepers, G., Fuglsang, P., and Sun, Y., Springer Nature, Switzerland, https://doi.org/10.1007/978-3-030-05455-7, 2020.

Bottasso, C. L., Cacciola, S., and Iriarte, X.: Calibration of wind turbine lifting line models from rotor loads, Wind Eng. Ind. Aerod., 124, 29-45, https://doi.org/10.1016/j.jweia.2013.11.003, 2014a.

Bottasso, C. L., Campagnolo, F., and Petrovic, V.: Wind tunnel testing of scaled wind turbine models: Beyond aerodynamics, J. Wind Eng. Ind. Aerodyn., 127, 11–28, https://doi.org/10.1016/j.jweia.2014.01.009, 2014b.

Burton, T., Jenkins, N., Sharpe, D., and Bossanyi, E.: Wind energy handbook, John Wiley & Sons, West Sussex, UK, 2011.

Campagnolo, F.: Wind tunnel testing of scaled wind turbine models: aerodynamics and beyond, PhD thesis, Politecnico di Milano, Milano, Italy, 2013.

Campagnolo, F., Petrović, V., Schreiber, J., Nanos, E. M., Croce, A., and Bottasso, C. L.: Wind tunnel testing of a closed-loop wake deflection controller for wind farm power maximization, J. Phys.: Conf. Ser., 753, 032006, https://doi.org/10.1088/1742-6596/753/3/032006, 2016.

Campagnolo, F., Weber, R., Schreiber, J., and Bottasso, C. L.: Wind tunnel testing of wake steering with dynamic wind direction changes, Wind Energ. Sci., 5, 1273–1295, https://doi.org/10.5194/wes-5-1273-2020, 2020.

Churchfield, M. and Lee, S.: NWTC design codes-SOWFA, NREL, available at: http://wind.nrel.gov/designcodes/simulators/SOWFA (last access: 4 November 2020), 2012.

Churchfield, M. J., Lee, S., Moriarty, P. J., Martinez, L. A., Leonardi, S., Vijayakumar, G., and Brasseur, J. G.: A large-eddy simulation of wind-plant aerodynamics, in: 50th AIAA, 9–12 January 2012, Nashville, Tennessee, https://doi.org/10.2514/6.2012-537, 2012.

Fleming, P., Gebraad, P., Churchfield, M., Lee, S., Johnson, K., Michalakes, J., van Wingerden, J.-W., and Moriarty, P.: SOWFA Super-controller User's Manual, National Renewable Energy Laboratory, Golden, Colorado, USA, 2013.

Frederik, J. A., Weber, R., Cacciola, S., Campagnolo, F., Croce, A., Bottasso, C., and van Wingerden, J.-W.: Periodic dynamic induction control of wind farms: proving the potential in simulations and wind tunnel experiments, Wind Energ. Sci., 5, 245–257, https://doi.org/10.5194/wes-5-245-2020, 2020.

Gebraad, P., Teeuwisse, F., Wingerden, J., Fleming, P. A., Ruben, S., Marden, J., and Pao, L.: Wind plant power optimization through yaw control using a parametric model for wake effects – a CFD simulation study, Wind Energy, 19, 95–114, 2016.

Jategaonkar, R. V.: Flight vehicle system identification: a time-domain methodology, American Institute of Aeronautics and Astronautics, Reston, VA, USA, 2015.

Klein, V. and Morelli, E. A.: Aircraft system identification: theory and practice, American Institute of Aeronautics and Astronautics, Reston, VA, USA, 2006.

Lyon, C. and Selig, M. S.: Summary of low speed airfoil data, SOARTECH Publications, Virginia Beach, VA, USA, 1997.

Manwell, J. F., McGowan, J. G. and Rogers, A. L.: Wind energy explained: theory, design and application, John Wiley & Sons, Hoboken, NJ, USA, 2010.

Mensor: Precision Pressure Transducer Models CPT6100, CPT6180, WIKA Alexander Wiegand SE & Co. KG, Klingenberg, Germany, available at: http://www.wika.rs/upload/DS_CT2510_en_co_34182.pdf (last access: 4 November 2020), 2016.

OpenFast: OpenFast documentation – Release v2.3.0, National Renewable Energy Laboratory, Golden, Colorado, USA, 2 April 2020.

Sebastian, T. and Lackner, M. A.: Development of a free vortex wake method code for offshore floating wind turbines, Renew. Energy, 46, 269–275, https://doi.org/10.1016/j.renene.2012.03.033, 2012.

Selig, M. S. and McGranahan, B. D.: Wind tunnel aerodynamic tests of six airfoils for use on small wind turbines, J. Sol. Energ. Eng., 126, 986–1001, https://doi.org/10.1115/1.1793208, 2004.

Shaler, K., Kecskemety, K. M., and McNamara, J. J.: Benchmarking of a free vortex wake model for prediction of wake interactions, Renew. Energy, 136, 607–620, https://doi.org/10.1016/j.renene.2018.12.044, 2019.

Standard ISO 3354: Measurement of clean water flow in closed conduits–Velocity-area method using current-meters in full con-

duits and under regular flow conditions, Inter. Org. for Standardization, UK, 2008.

Troldborg, N., Sørensen, J. N., and Mikkelsen, R.: Actuator line simulation of wake of wind turbine operating in turbulent inflow, J. Phys.: Conf. Ser., 75, 012063, https://doi.org/10.1088/1742-6596/75/1/012063, 2007.

Wang, J., Wang, C., Campagnolo, F., and Bottasso, C. L.: Wake behavior and control: comparison of LES simulations and wind tunnel measurements, Wind Energ. Sci., 4, 71–88, https://doi.org/10.5194/wes-4-71-2019, 2019.

Wang, C., Muñóz-Simon, A., Deskos, G., Laizet, S., Palacios, R., Campagnolo, F., and Bottasso, C. L.: Code-to-code-to-experiment validation of LES-ALM wind farm simulators, J. Phys.: Conf. Ser., 1618, 062041, https://doi.org/10.1088/1742-6596/1618/6/062041, 2020a.

Wang, C., Campagnolo, F., Sharma, A., and Bottasso, C. L.: Effects of dynamic induction control on power and loads, by LES-ALM simulations and wind tunnel experiments, J. Phys.: Conf. Ser., 1618, 022036, https://doi.org/10.1088/1742-6596/1618/2/022036, 2020b.

Wang, C., Campagnolo, F., and Bottasso, C. L.: Does the use of load-reducing IPC on a wake-steering turbine affect wake behavior, J. Phys.: Conf. Ser., 1618, 022035, https://doi.org/10.1088/1742-6596/1618/2/022035, 2020c.

Wind Energ. Sci., 4, 71–88, 2019
https://doi.org/10.5194/wes-4-71-2019

eawe european academy of wind energy
Open Access
WIND ENERGY SCIENCE

Wake behavior and control: comparison of LES simulations and wind tunnel measurements

Jiangang Wang, Chengyu Wang, Filippo Campagnolo, and Carlo L. Bottasso

Wind Energy Institute, Technische Universität München, Garching bei München, Germany

Correspondence: Carlo L. Bottasso (carlo.bottasso@tum.de)

Received: 28 May 2018 – Discussion started: 26 June 2018
Revised: 12 December 2018 – Accepted: 10 January 2019 – Published: 29 January 2019

Abstract. This paper applies a large-eddy actuator line approach to the simulation of wind turbine wakes. In addition to normal operating conditions, a specific focus of the paper is on wake manipulation, which is performed here by derating, yaw misalignment and cyclic pitching of the blades. With the purpose of clarifying the ability of LES methods to represent conditions that are relevant for wind farm control, numerical simulations are compared to experimental observations obtained in a boundary layer wind tunnel with scaled wind turbine models. Results indicate a good overall matching of simulations with experiments. Low-turbulence test cases appear to be more challenging than moderate- and high-turbulence ones due to the need for denser grids to limit numerical diffusion and accurately resolve tip-shed vortices in the near-wake region.

1 Introduction

Wind plants are collections of wind turbines often operating in close proximity of one another. Several complex phenomena take place within a wind farm. First, there is an interaction between the atmospheric boundary layer and the whole wind farm caused by the smaller-scale interaction between the atmospheric flow and each individual wind turbine. Second, within the power plant itself, there is an interaction among upstream and downstream wind turbines through their wakes. In turn, the wakes themselves interact with the atmospheric flow and other wakes, playing a central role in determining the overall behavior of the plant. Wakes produced by upstream wind turbines may have a profound influence on the performance of downstream operating machines. In fact, waked turbines experience lower power output and increased loading compared to clean isolated conditions. A thorough understanding of these complex phenomena is clearly indispensable for optimizing the layout and operation of wind plants. However, even an optimal layout will still incur negative effects due to wake interactions, at least in some wind and environmental conditions. To mitigate these effects, a number of control strategies are currently being investigated to optimize the operation of wind power plants, including power derating, wake deflection and enhanced wake recovery (Fleming et al., 2014; Knudsen et al., 2015).

The current research in this field is very active, covering a broad spectrum that ranges from high-fidelity numerical simulations to reduced order models, from scaled experiments in the wind tunnel to direct measurements in the field, all the way to control methods and various supporting technologies. Among the many studies reported in the literature, meteorological and performance data collected at the Horns Rev and Middelgrunden offshore wind farms have been systematically investigated (Barthelmie et al., 2007; Hansen et al., 2012). Moreover, scaled wind farm experiments were conducted in wind tunnels to study wake deficit and its impact on downstream wind turbines (Medici and Alfredsson, 2006; Chamorro and Porté-Agel, 2009; Bartl et al., 2012). These test campaigns have been actively used to validate several engineering and computational fluid dynamics (CFD) wake models in terms of power capture, velocity profiles and higher-order flow quantities (Barthelmie et al., 2006; Kennedy et al., 2011; Porté-Agel et al., 2011; Gaumond et al., 2014). Wake models can be classified on the basis of their complexity and fidelity to reality. The steady-state kinematic wake model of Jensen (1983) was among the first proposed analytical formulations, later extended by

Jiménez et al. (2010) to cover the case of yaw misalignment. Larsen et al. (2007) derived a more sophisticated dynamic wake meandering model. Higher-fidelity models have been developed by using CFD. For example, Carcangiu (2008) used the Reynolds-averaged Navier–Stokes (RANS) equations to simulate near-wake behavior, while Stovall et al. (2010) simulated wind turbine clusters and compared RANS to the higher-fidelity large-eddy simulation (LES) approach. Results indicated that RANS is not sufficiently accurate, as it typically overestimates diffusion.

With the significant increase in computational performance in recent years (thanks to advancements in hardware, software and algorithms), LES has gained an increasing adoption by the wind farm research community (Calaf et al., 2010; Porté-Agel et al., 2011; Churchfield et al., 2012). In fact, LES has the ability to better resolve the relevant flow features, leading to an improved insight on flow characteristics within a wind farm. In addition, several researchers (Jiménez et al., 2010; Fleming et al., 2014; Gebraad et al., 2016) have been using LES to investigate wake control strategies.

Although LES is an approach based on first principles, it is still not completely tuning-free. For example, when used in conjunction with an actuator line method (ALM) to represent wind turbine blades, there is a need to properly tune the procedure used for mapping lifting line aerodynamic forces onto the volumetric grid (Sørensen and Shen, 2002; Martinez et al., 2012). In addition to several algorithmic details, other important characteristics of the simulation are represented by the grid (Jha et al., 2014; Martínez-Tossas et al., 2017) and features of the model, including the presence of nacelle and tower. The effects of the tower have been investigated with different versions of the ALM by Churchfield et al. (2015) and Stevens et al. (2018), with an immersed boundary method by Santoni et al. (2017) and with an actuator surface approach by Yang and Sotiropoulos (2018).

In general, most of the published research focuses on the use of CFD to study wake behavior and control strategies, but pay relatively less attention to the problem of ensuring the fidelity of such simulations to reality. In fact, a comprehensive validation of LES methods for wind turbine wakes is still missing. This is clearly not due to a lack of attention to this problem, but rather to a lack of comprehensive high-quality data sets. Unfortunately, experiments in the field are not without hurdles: in fact, wind conditions cannot be controlled, and measurements at full scale are not always possible or complete. In this sense, testing at scale in a wind tunnel is gaining attention as a means to perform experiments with much more precise knowledge and control of the testing conditions.

As a contribution towards a better understanding of the capabilities and limits of LES for modeling wind turbine wakes, this paper applies a recently developed computational framework to the simulation of scaled wind turbines. These models were operated in a large boundary layer wind tunnel in a variety of conditions. A complete LES-based digital model of the experiments is developed in this work, including a model of the wind tunnel and of the passive generation of sheared and turbulent flows. The paper specifically focuses on operating conditions that are relevant to wind farm control. In fact, the existing literature either uses LES to study wind farm control conditions without comparing simulations against experiments (Jiménez et al., 2010; Fleming et al., 2014, 2015; Gebraad et al., 2016) or considers both numerical and experimental results but not in the context of wind farm control (Jiménez et al., 2010; Lu and Porté-Agel, 2011; Porté-Agel et al., 2011; Wu and Porté-Agel, 2011; Churchfield et al., 2012; Mo et al., 2013; Martínez-Tossas et al., 2015; Sørensen et al., 2015; Nilsson et al., 2015; Shamsoddin and Porté-Agel, 2017; Abkar and Dabiri, 2017; Sedaghatizadeh et al., 2018). The present paper tries to fill this gap by conducting a first preliminary study on the ability of LES to model the behavior of wakes in conditions that are relevant to wind farm control applications. This study is preliminary in the sense that only a limited set of conditions for one isolated wind turbine are analyzed. Wake interactions are analyzed in Wang et al. (2017b, 2018) and in forthcoming publications. The authors believe in the need to clarify to what degree wake modeling methods are indeed able to represent farm-control-relevant conditions, this work being a first limited-scope step in this direction.

The present LES framework is characterized by some distinguishing features. First, the tuning-free immersed boundary (IB) method of Jasak and Rigler (2014) is used to model the effects caused by the nacelle and tower. Second, the integral velocity sampling method (Churchfield et al., 2017) is employed, which reduces the sensitivity of the results – and especially of power – to the mapping of aerodynamic forces onto the fluid flow. Third, an ad hoc developed approach is used for tuning the airfoil polars. In fact, given the small scale of the experimental models, their blades operate at low Reynolds numbers and are therefore designed using special low-Reynolds airfoils. Clearly, the accuracy of the airfoil polars plays an important role in the accuracy of the overall LES simulation. Rotational augmentation, manufacturing imperfections and other effects may influence the behavior of the blade airfoils and alter it with respect to their nominal characteristics, which are typically obtained in 2-D dedicated wind tunnel tests. To address this issue, airfoil polars are tuned here by means of a specific identification method (Bottasso et al., 2014), which makes use of dedicated experimental measurements conducted with the scaled turbine (i.e., not with the single airfoils, but with the rotor on which the airfoils are used). Indeed, the airfoil Reynolds varies depending on the operating condition of the turbine. By accounting for the effects of Reynolds on the airfoil polars, which are particularly relevant at the low Reynolds numbers at which the scaled models operate, better accuracy in the results can be achieved.

The problem of computational cost is addressed in a companion paper (Wang et al., 2018), in which a scale-adaptive simulation (SAS) approach is used to model the unresolved scales, resulting in LES-like behavior at a cost similar to RANS with a roughly similar accuracy.

The paper is organized according to the following plan. The numerical method is described in Sect. 2. The computational setup is reported in Sect. 3, in which a precursor simulation mimicking the process that takes place in the wind tunnel is used for the passive generation of the turbulent flow, whose resulting outflow is used as an inlet for subsequent wind turbine wake simulations (called successor simulations). The experimental setup is presented in Sect. 4, including a short description of the wind tunnel, the scaled wind turbine model and the measurement equipment. Results are discussed in Sect. 5. First, an isolated flow-aligned wind turbine is considered, and the LES framework is tuned to match experimental measurements obtained in this baseline case. Next, the three wake manipulation strategies of derating, yaw misalignment and cyclic pitch control are considered. Here again, low-turbulence experimental results are compared with simulations, without any additional tuning with respect to the parameters chosen in the baseline case. Finally, a moderate-turbulent condition is considered, again without any additional tuning. Conclusions are drawn in Sect. 6.

2 Numerical simulation model

The present LES framework is developed within `SOWFA` (Churchfield and Lee, 2012; Fleming et al., 2013), a simulation tool based on a standard incompressible solver in the OpenFOAM repository.

The rotor is modeled in terms of actuator lines by direct coupling with the aeroservoelastic simulator `FAST` (Jonkman and Buhl Jr., 2005). The integral approach of Churchfield et al. (2017) is used to compute the flow conditions at each station along an actuator line and to project the calculated aerodynamic forces back onto the fluid domain using a single Gaussian width value. Aerodynamic forces at each station are computed by interpolating precomputed lift and drag aerodynamic coefficients, which are stored in lookup tables parameterized in terms of angle of attack and Reynolds number. Depending on the problem, the wind turbine model is either controlled in a closed loop by a pitch and torque controller based on the implementation described in Bottasso et al. (2014) or simply by using experimentally measured values of pitch and rotor speed.

Both the constant Smagorinsky (CS) (Deardorff, 1970) and the Lagrangian dynamic Smagorinsky (LDS) (Meneveau et al., 1996) models are implemented. However, results of extensive numerical experiments indicate that, for the present application, the performance of LDS is very similar to CS, as shown later in this work and already observed by Sarlak et al. (2015) and Martínez-Tossas et al. (2018) in turbulent conditions.

The IB formulation of Lai and Peskin (2000), Mittal and Iaccarino (2005), and Jasak and Rigler (2014) is used to model the wind turbine nacelle and tower, whose effects on the flow proved to be quite significant, at least in the near-wake region, and should therefore not be neglected (Wang et al., 2017b). The IB method is employed to avoid the use of surface-conforming meshes to represent the shape of such bodies (Mittal and Iaccarino, 2005). The present IB approach, based on a discrete forcing method, uses a direct imposition of the boundary conditions (Uhlmann, 2005), thus preserving the sharpness of the body shape. Boundary conditions and wall models can be directly imposed on the IB surfaces with this approach, yielding good solution quality for high-Reynolds viscous flows (Bandringa, 2010). Details on the formulation are reported in Wang et al. (2017b).

ALM-modeled blades and an IB-modeled nacelle and tower introduce local numerical dispersion and diffusion, which affect simulation stability and accuracy (Holzmann, 2016; Moukalled et al., 2016). The gamma-bounded high-resolution interpolation method is used here to address this issue (Jasak et al., 1999). The gamma scheme is parameterized in terms of β_m, a tunable constant that allows one to control the level of upwinding. In general, a larger value of β_m implies a lower dispersion and a higher diffusion (i.e., more upwinding) and vice versa. The value $\beta_m = 0.45$ is employed in the near-wake region to stabilize the simulation, since actuator line body forces and an immersed boundary possibly generate numerical dispersion, and $\beta_m = 0.05$ is used in the far wake to minimize numerical diffusion while retaining a minimum amount of necessary upwinding.

Table 1 shows the linear solvers used for the precursor and the wind turbine–wake simulations. The precursor problem has slightly less regular grids because of the need to mesh the large turbulence generators (termed spires) placed at the tunnel inlet, which requires a slightly different setup of the linear solvers. The PISO time-marching algorithm recursively solves (or corrects) the pressure flux equation to account for non-orthogonal grid elements (Greenshields, 2015). The number of iterations is fixed a priori and set equal to 1 and 0 for the precursor and successor simulations, respectively. Indeed, given the good quality of the grid in the latter case, non-orthogonal corrections are not indispensable, and their elimination lowers the computational cost by about 10 %.

Multi-airfoil table identification

Clearly, the accuracy of the sectional aerodynamic coefficients is a crucial ingredient of the ALM formulation. A method to tune the aerodynamic polars of lifting lines was described in Bottasso et al. (2014). In a nutshell, the method works by first measuring thrust and torque on a rotor at a number of different operating conditions that cover the angles of attack and Reynolds numbers of interest. Next, these

Table 1. Linear algebraic solvers used for the precursor and the wind turbine–wake simulations (CG: conjugate gradient; GAMG: geometric–algebraic multigrid; DIC: diagonal incomplete Cholesky; GS: Gauss–Seidel; DILU: diagonal incomplete LU factorization; NOC: non-orthogonal corrector).

Type	Precursor simulation	Wind turbine simulation
p solver	CG	CG
p preconditioner	GAMG	GAMG
p smoother	DIC-GS	GS
No. of p corrector steps	3	3
$\widetilde{\boldsymbol{u}}$ solver	bi-CG	bi-CG
$\widetilde{\boldsymbol{u}}$ preconditioner	DILU	DILU
No. of NOC steps	1	0

values are used to update some given baseline polars by using a maximum-likelihood criterion.

Nominal values of both the lift and drag coefficients C_k (where $k = \mathrm{L}$ or $k = \mathrm{D}$ for lift and drag, respectively) are corrected as

$$C_k(\eta, \alpha, Re) = C_k^0(\eta, \alpha, Re) + \Delta_k(\eta, \alpha, Re), \quad (1)$$

where $\eta \in [0, 1]$ is a span-wise location, α the angle of attack, Re the Reynolds number, C_k^0 the nominal coefficient value and Δ_k the unknown correction. This latter term is expressed by a linear interpolation as

$$\Delta_k(\eta, \alpha, Re) = \boldsymbol{n}^T(\eta, \alpha, Re)\boldsymbol{p}_k, \quad (2)$$

where $\boldsymbol{p}_k$ is the vector of unknown nodal values and $\boldsymbol{n}(\eta, \alpha, Re)$ is the vector of assumed multi-linear shape functions. To improve the well-posedness of the problem, the polar correction terms are transformed using a singular-value decomposition, which ensures the actual observability of the tuned parameters. Through this method, the corrections to the baseline lift and drag characteristics of the airfoils are recast in terms of a new set of statistically independent parameters. By analyzing their associated singular values, one can retain in the identification only those parameters that are observable with a desired level of confidence (Bottasso et al., 2014).

The unknown correction terms are computed by maximizing the likelihood function of a sample of N available experimental observations. This amounts to first minimizing the following cost function:

$$J = \frac{1}{2}\sum_i^N \boldsymbol{r}_i^T \mathbf{R}^{-1} \boldsymbol{r}_i, \quad (3)$$

where $\boldsymbol{r}$ is the discrepancy between power and thrust coefficients computed by a blade element momentum model as implemented in the `WT_Perf` code (Platt and Buhl, 2012) and the corresponding experimentally measured quantities. The optimization is performed for a fixed covariance $\mathbf{R}$ by using the gradient-based sequential quadratic programming approach. Next, the covariance is updated as $\mathbf{R} = 1/N\sum_i^N \boldsymbol{r}_i \boldsymbol{r}_i^T$, and the optimization is repeated. Iterations between the minimization and covariance update are continued until convergence (Bottasso et al., 2014).

More than 100 operating points were measured experimentally. The operating conditions were determined in order to cover a desired range of angles of attack and Reynolds numbers, and they were obtained by operating the scaled wind turbine model at different tip speed ratios (TSRs) and blade pitch angles. Experiments were then grouped in terms of average blade Reynolds number, and for each group a separate identification was performed, yielding a calibrated version of the polars at that specific Reynolds.

3 Computational setup

3.1 Precursor simulation

The LES-ALM numerical model was used to create a complete digital copy of the experiments, which were conducted in the 36 m × 13.84 m × 3.84 m boundary layer test section of the wind tunnel at Politecnico di Milano (Zasso et al., 2005; Bottasso et al., 2014).

A first simulation is used to generate the turbulent inflow (precursor) used as an inlet for successive wind turbine–wake (successor) simulations. The layout of the partially overlapped precursor and successor domains is represented in Fig. 1. The precursor domain has a size of 30 m × 6.92 m × 3.84 m. The reduced width of the domain with respect to the actual tunnel size is chosen to limit the computational cost. The turbulent inflow for the successor simulation is sampled 19.2 m downstream of the precursor inlet, as shown in the figure. The simulation mimics the passive turbulence-generating system adopted in this wind tunnel (Zasso et al., 2005). A structured body-conforming mesh discretizes the volume around the turbulence-generating spires at the wind tunnel inlet using a purely hexahedral O grid. The average stretching ratio for the volume mesh is 1.25, while the maximum skewness is equal to 2.7, which does not compromise the simulation stability. Mesh quality is limited by the sharp edges and abrupt surface changes in the spire geometry.

Dirichlet-type nonslip conditions are used for the resolved velocity vector $\widetilde{\boldsymbol{u}}$ on the tunnel side walls and the spire surfaces. Neumann-type conditions are imposed for pressure on the same boundary surfaces, while Dirichlet-type wall conditions are employed for temperature, which is assumed to be the same on all surfaces. Regarding the sub-grid-scale model, Dirichlet-type surface conditions are used for the eddy viscosity μ_t on the ceiling, with a fixed value equal to 1×10^{-5} m^2 s^{-1} on account of the negligible turbulence; a small positive nonzero value is used because μ_t is evaluated at cell centroids and not on the wall surface. A wall model

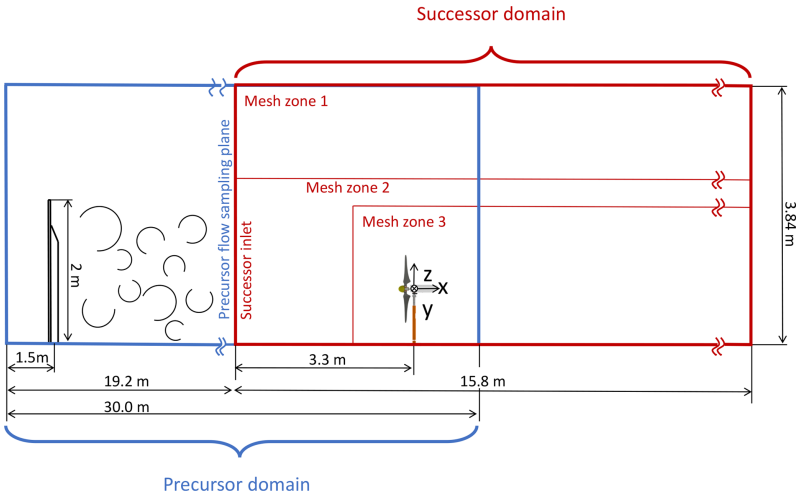

Figure 1. Layout of the partially overlapped precursor and successor computational domains.

is imposed on the other surfaces, including spires, left–right walls and floor, to adjust wall shear stresses.

The inflow speed at the inlet equals 4.7 m s^{-1}, as measured in the wind tunnel, and the maximum Courant number is limited to 1. The constant Smagorinsky sub-grid-scale model is used with its constant parameter C_s set to 0.13. In order to reach steady-state conditions, the simulation requires about 15 s of physical time. After achieving a steady mean speed, the precursor flow is collected at a sampling plane about 3 D in front of the turbines and stored to be used as input for subsequent successor simulations.

Figure 2 shows the normalized time-averaged streamwise velocity $\langle u_x \rangle$ and turbulence intensity $\sigma / \langle u_x \rangle$ profiles measured 20.85 m downstream of the tunnel inlet, which corresponds to 1.5 D upstream of the wind turbine rotor. A reference frame is located at the hub, as shown in Fig. 1 on the right. The two horizontal and vertical velocity profiles are in good agreement with the experimental data. The average velocity error $\langle \Delta u_x \rangle$ is around 1 %–2 % for both profiles. The horizontal velocity appears to be not exactly symmetric with respect to $y = 0$. This is due to the 16 fans of the tunnel (in two rows of eight side-by-side fans), stiffening transects upstream of the chamber inlet and the turbulence-generating spires. This slight horizontal shear was obtained in the numerical simulation by adjusting the prescribed inflow at the precursor domain inlet. Turbulence intensity also shows a reasonable agreement, with an average error of 7 % and 5 % for the horizontal and vertical profiles, respectively. The experimental results for $\sigma / \langle u_x \rangle$ along the horizontal profile show an unexpected discontinuity not observed in the simulations, which might be due to the effect of the traversing system used for holding and positioning the hot-wire probes.

Figure 3 shows the experimental and simulated turbulent kinetic energy spectrum $E(f)$ and autocorrelation $r(\tau)$ at hub height 1.5 D upstream of the rotor. The LES-computed spectrum appears to be in good agreement with the experimental one. The autocorrelation is computed as

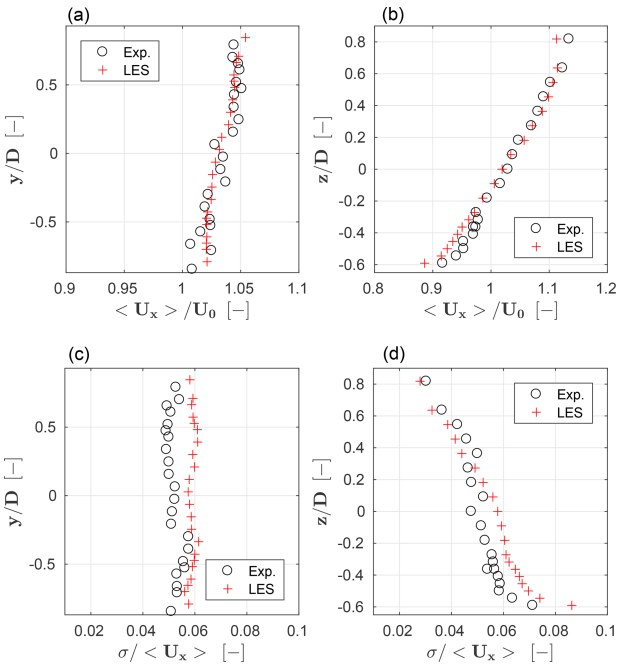

Figure 2. Normalized time-averaged streamwise velocity $\langle u_x \rangle$ **(a, b)** and turbulence intensity $\sigma / \langle u_x \rangle$ **(c, d)** 1.5 D downstream of the rotor. Left column: hub-height horizontal profile; right column: hub-centered vertical profile. Red + symbols: numerical results; black ∘ symbols: experimental measurements.

$$r^j(\tau) = \left\langle \left(u_x^j(t) - \left\langle u_x^j \right\rangle \right) \left(u_x^j(t+\tau) - \left\langle u_x^j \right\rangle \right) \right\rangle, \quad (4)$$

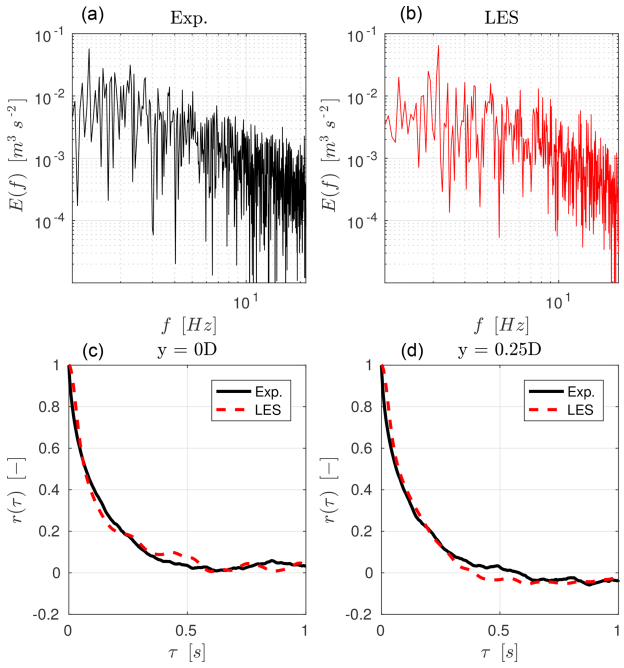

Figure 3. Turbulent kinetic energy spectrum $E(f)$ at hub height 1.5 D upstream of the rotor for the experiment (**a**, black line) and simulation (**b**, red line). Autocorrelation $r(\tau)$ at hub height 1.5 D upstream of the rotor **(c)** and 0.25 D to its left, looking downstream **(d)**.

where u_x^j is the streamwise component of the velocity at spatial point j. The integral timescale (O'Neill et al., 2004), defined as

$$T_\tau^j = \int_0^\infty \frac{r^j(\tau)}{\left\langle u_x^{j,2} \right\rangle} \mathrm{d}\tau, \tag{5}$$

is found to be 0.139 and 0.143 s for the experiment and simulation, respectively. These results indicate a good overall agreement between the simulation and experiment even at small scales, with a consequent correct estimation of flow mixture, wake recovery and other relevant features of the flow.

3.2 Successor simulation

The computational setup for the wind turbine–wake simulation follows Wang et al. (2017a). The domain layout is shown in Fig. 1. The domain width is reduced to 3.9 D, which is 3.4 times less than the actual test section width to minimize the computational cost without affecting the results due to wall blockage. Note that the precursor width is about twice the width of the successor domain, simply because the same precursor is also used for nonaligned multi-turbine configurations (not discussed here) that, having a larger frontal area, require a larger inflow. The mesh uses three zones of increasing density. Zone 1 is the base mesh, with cubic cells 0.08 m in size, while zones 2 and 3 have cubic cells of 0.04 m and 0.01 m, respectively. Less than 1 % of the total mesh is composed of polyhedral cells, while all others are cubic.

Two different flow conditions are considered in the present study. In the first case, the flow velocity is obtained from a lidar-scanned low-turbulence ($< 2\,\%$) inflow condition (van Dooren et al., 2017). Measurements also accounts for a slight nonuniformity of the flow within the wind tunnel (Wang et al., 2017a). In the second case, as previously explained, the output of the passively generated turbulent precursor simulation was instead used as an inlet for the successor simulation.

The treatment of the domain walls is as follows. Dirichlet-type nonslip wall conditions for $\widetilde{\boldsymbol{u}}$ are used for the tunnel ceiling and floor. Neumann-type conditions for pressure and temperature and mixed-type conditions for $\widetilde{\boldsymbol{u}}$ are used for the side walls, enforcing a null component of the velocity normal to the side surfaces to ensure mass conservation. The eddy viscosity μ_t is set with Neumann conditions on the left–right tunnel walls. For the ceiling and floor, μ_t is set with Dirichlet conditions to the fixed value $1 \times 10^{-5}\,\mathrm{m^2\,s^{-1}}$ in the low-turbulence case, while a wall model is used for the moderate-turbulence condition.

Dirichlet-type nonslip wall conditions are used for the IB-modeled nacelle and tower in the low-turbulence case, for which a laminar boundary layer (or, at least, a not fully developed turbulent boundary layer) is expected to extend over the entire IB surface due to the steadiness of the incoming flow. Despite the maximum y^+ being equal to 50 on the IB surfaces, a wall function cannot be used here, as it could properly model only a fully developed turbulent boundary layer. Due to the coarse grid, an overestimation of the boundary layer thickness on the IB-modeled bodies is expected, which in turn will lead to an overestimation of the blockage induced by the turbine nacelle and tower.

Slip wall IB surface conditions are used for the moderate-turbulence case in order to mitigate numerical stability issues. Although this neglects the boundary-layer-induced blockage and turbulence, results indicate a negligible impact on the downstream wake profile. This is probably explained by the background turbulence that, by enhancing mixing, diffuses the signature of the tower and nacelle on the downstream flow.

4 Experimental setup

Tests were performed with the G1 scaled wind turbine model, whose rotor diameter and optimal TSR are equal to 1.1 m and 8.25, respectively. The model, already used within other research projects (Campagnolo et al., 2016a, b, c), is designed to have realistic wake characteristics, with shape, deficit and recovery that are in good accordance with those of full-scale machines. The model features active individual pitch, torque and yaw control that, together with a comprehensive onboard sensorization (including measures of shaft and tower loads),

enables the testing of turbine and farm-level control strategies.

The flow within the wind tunnel was measured with hot-wire probes or stereo PIV. The latter technique was used to measure the flow characteristics in the near-wake (0.56 D) and far-wake (6 D) regions. The measurement planes cover a significant fraction of the wind turbine wake. In order to achieve a higher spatial resolution of the velocity field, the measurement area was divided into several windows with small overlaps between them. A rapid scanning of the entire measurement area was achieved by the use of an automated traversing system moving both the laser and the cameras. The measuring windows were divided into 32×32 pixel interpolation areas, which resulted in an approximate spatial resolution of 15 mm. For each measuring window, 200 pairs of images were acquired (per camera) without phase lock, resulting in time-averaged flow field measurements. Additional details concerning the PIV instrumentation are given in Campanardi et al. (2017).

5 Result and analysis

5.1 Baseline simulation and parameter tuning

The baseline simulation represents an isolated flow-aligned wind turbine. The machine is operated in a low-turbulence flow with a rotor-averaged inflow velocity equal to 5.9 m s^{-1}, which is slightly lower than the G1 rated speed (6.0 m s^{-1}).

This first case is used to determine the optimal values of the Smagorinsky constant C_s and the gamma scheme parameter β_m. The same tuned parameters are used for all other simulations in the rest of this work. This first test case is also used to verify the effects of the Gaussian width ϵ, which is used to project aerodynamic forces from the lifting lines onto the computational grid. In fact, it was observed that this projection may have a significant effect on the results, including rotor power and thrust. In principle, ϵ should be set to 2–3 times the cell size, i.e., $2h \leq \epsilon \leq 3h$ (Martinez et al., 2012). It was found that the dependency of the rotor aerodynamic power on ϵ is significantly reduced if the integral velocity sampling approach is used (Churchfield et al., 2017). For instance, if ϵ increases by 30 %, power will increase by 13 % if the traditional point-wise velocity sampling approach is used, but only by 5 % when using the integral velocity sampling method. In fact, in the point-wise approach a variation of ϵ reshapes the Gaussian curve, in turn changing the peak value and eventually affecting the calculated aerodynamic power, while the integral approach uses a weighted average that mitigates the reshaping effect (Churchfield et al., 2017).

Using a simple trial-and-error approach, the three parameters ϵ, C_s and β_m (in the near wake) were set to 0.025, 0.13 and 0.45, respectively. Given the low turbulence of the present case, the experimentally measured rotor speed was very nearly constant, and its average value was used in the simulation.

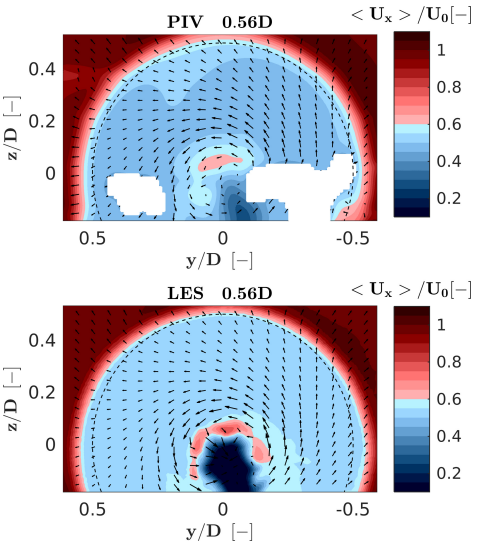

Figure 4. Streamwise velocity contours for the CS LES model and PIV experimental measurements, on a plane 0.56 D downstream of the rotor. Black arrows indicate the crosswind velocity component at a number of sampling points.

The rotor integral quantities of power and thrust are compared first by time averaging over 10 s. The wind turbine power was found to be equal to 45.79 W in the experiment and equal to 45.45 W for LES, showing a good agreement between these two values. A slightly larger discrepancy was obtained for the thrust, which was found to be 15.18 and 16.05 N for the experiment and simulation, respectively. This may be explained by the fact that thrust is directly measured at the shaft in the numerical simulation, while it is reconstructed from the fore–aft bending moment at the tower base in the experiment. This requires estimating the contribution of the nacelle and tower, which is done by a dedicated experiment performed on the wind turbine without the blades. As a result, this indirect calculation of the experimental thrust is affected by approximations, and it cannot be regarded to be as accurate as the measurement of rotor torque (and hence of power).

Next, the characteristics of the wake are compared between PIV measurements and the CS LES simulation. Figure 4 shows streamwise velocity contours on a plane 0.56 D downstream of the rotor. Measurements are missing from two areas left and right of the rotor disk; due to the close proximity of the measuring plane with the wind turbine, part of the nacelle (which is white) was in the background, leading to a wrong correlation between the PIV images. Apart from the two missing spots, the LES contours are similar to the PIV ones both in terms of wake width and deficit. The wake deficit for LES is on average 1.3 % higher than the experiment.

The figure also shows that the simulation overestimates the local wake deficit behind the nacelle and tower as a result of the enhanced blockage effect mentioned in Sect. 3.2. Indeed, the current mesh resolution (high y^+) implies a thicker boundary layer, which in turn produces a higher blockage with a consequent larger flow separation, tower shedding and induced turbulence. This problem could be mitigated by a suitable refinement of the mesh near the IB, which would come at the price of a significant increase in the computational cost.

Next, hot-wire probe measurements are used to compare wake profiles at 3, 4, 7 and 8 D downstream positions. Figure 5 shows horizontal (top row) and vertical (central row) profiles of the normalized time-averaged velocity, as well as horizontal profiles of turbulence intensity (bottom row). The plots report results for the CS model, the LDS model and experimental measurements. The CS case includes two sets of results, one obtained including the effects of the nacelle and tower in the model and one obtained neglecting these two components. Comparing these two curves with the experimental results clearly indicates that the near-wake profile is more accurately represented when the nacelle and tower are included in the model, as already noted by other authors (Santoni et al., 2017). This may be particularly true for the present scaled wind turbine, for which these two components are relatively bigger than in full-scale machines. Indeed, the sum of the frontal area of the nacelle and the portion of the tower located within the rotor swept area A is $0.037\,A$, while it is $0.023\,A$ for the NREL 5 MW wind turbine (Jonkman et al., 2009). Although this parameter is larger for the G1, it is expected that the effects of the nacelle and tower on wake evolution might not be negligible even for typical multi-MW wind turbines (Wang et al., 2017b). All other simulations reported in this work were performed including the nacelle and tower in the model.

Both CS and LDS show a good agreement with the experimental curves. Indeed, the temporally and spatially averaged streamwise velocity difference $\langle \Delta u_x \rangle = \left(\langle u_{x,\mathrm{LDS}} \rangle - \langle u_{x,\mathrm{CS}} \rangle\right) / \langle u_{x,\mathrm{CS}} \rangle$ between the CS and LDS models is consistently less than 1 % at all downstream distances. Results indicate that the LDS model does not provide significantly more accurate results than CS, while at the same time it requires a 20 % larger computational effort caused by the solution of its two extra transport equations. Moreover, turbulence intensity plots seem to indicate a slightly better match of CS to the experiments than LDS. Based on these results, all other simulations in the present paper were based on the CS model.

The rotor-averaged streamwise velocity difference between the simulation (with nacelle and tower) and experiment $\langle \Delta u_x \rangle = \left(\langle u_{x,\mathrm{sim}} \rangle - \langle u_{x,\mathrm{exp}} \rangle\right) / \langle u_{x,\mathrm{exp}} \rangle$ is equal to $-2.7\,\%$, $-1.6\,\%$ and $-1.3\,\%$ at 3, 4 and 8 D, respectively. The root mean square (RMS) error can be used to quantify the spatial fit between simulations and experiments, and it is defined as

$$\mathrm{RMS}(\cdot) = \sqrt{\frac{1}{N}\sum_{j=1}^{N}\left(\left\langle(\cdot)^j_{\mathrm{sim}}\right\rangle - \left\langle(\cdot)^j_{\mathrm{exp}}\right\rangle\right)^2}, \tag{6}$$

where $\left\langle(\cdot)^j\right\rangle$ is a generic time-averaged quantity at a given spatial point j. At the various downstream distances, $\mathrm{RMS}(u_x)$ equals 0.34, 0.33 and $0.15\,\mathrm{m\,s^{-1}}$, respectively. As expected, the matching of simulations with experimental measurements improves when moving downstream. Indeed, if rotor thrust is well predicted, flow mixture is properly resolved and numerical diffusion is suitably controlled, then the simulation results in a fully developed wake that correlates well with the experiment. The far-wake profile can be approximated by the single Gaussian distribution used in some engineering wake models (Larsen et al., 2007; Renkema, 2007).

LES underestimates the rotor-averaged turbulence intensity $\sigma / \langle u_x \rangle$ by 23 %, 12 % and 12 % at 3, 4 and 8 D, respectively, while the rotor-averaged root mean square error $\mathrm{RMS}\left(\sigma / \langle u_x \rangle\right)$ is 0.04, 0.02 and 0.02 at these same positions. The turbulence intensity profiles in Fig. 5 clearly show that matching is not as good as in the case of the streamwise velocity, especially in the near-wake region where tip vortices are not resolved enough and tower shedding is overpredicted. Here again, the problem could be mitigated with a finer grid, which would lead to increased computational costs.

Comparing the turbulence intensity results with and without the nacelle and tower shows that there is an increased turbulence in the wake of the former case, which causes an earlier vortex breakdown and produces a higher turbulence intensity at the far wake. In turn, this generates a faster wake recovery, as shown in the speed deficit plots. Here again, this confirms the need for including the nacelle and tower in the simulation.

5.2 Low-turbulence inflow simulation

In this section, the characteristics of the LES framework are assessed with reference to three wake control strategies, namely power derating (or axial induction control), wake steering by yaw misalignment and wake-enhanced recovery by cyclic pitch control (CyPC). The flow conditions and setup of the simulations are the same as described earlier in the baseline case.

5.2.1 Power derating

Power derating was accomplished in the experiment by providing the turbine power controller with modified values of the rotor speed and torque. Specifically, for a power partialization factor p_{f}, the reference rotor speed is modified as $\sqrt[3]{p_{\mathrm{f}}}\Omega$, while the torque is modified as $\sqrt[3]{p_{\mathrm{f}}^2}\,Q$. This corresponds to having set the rated wind speed to the value

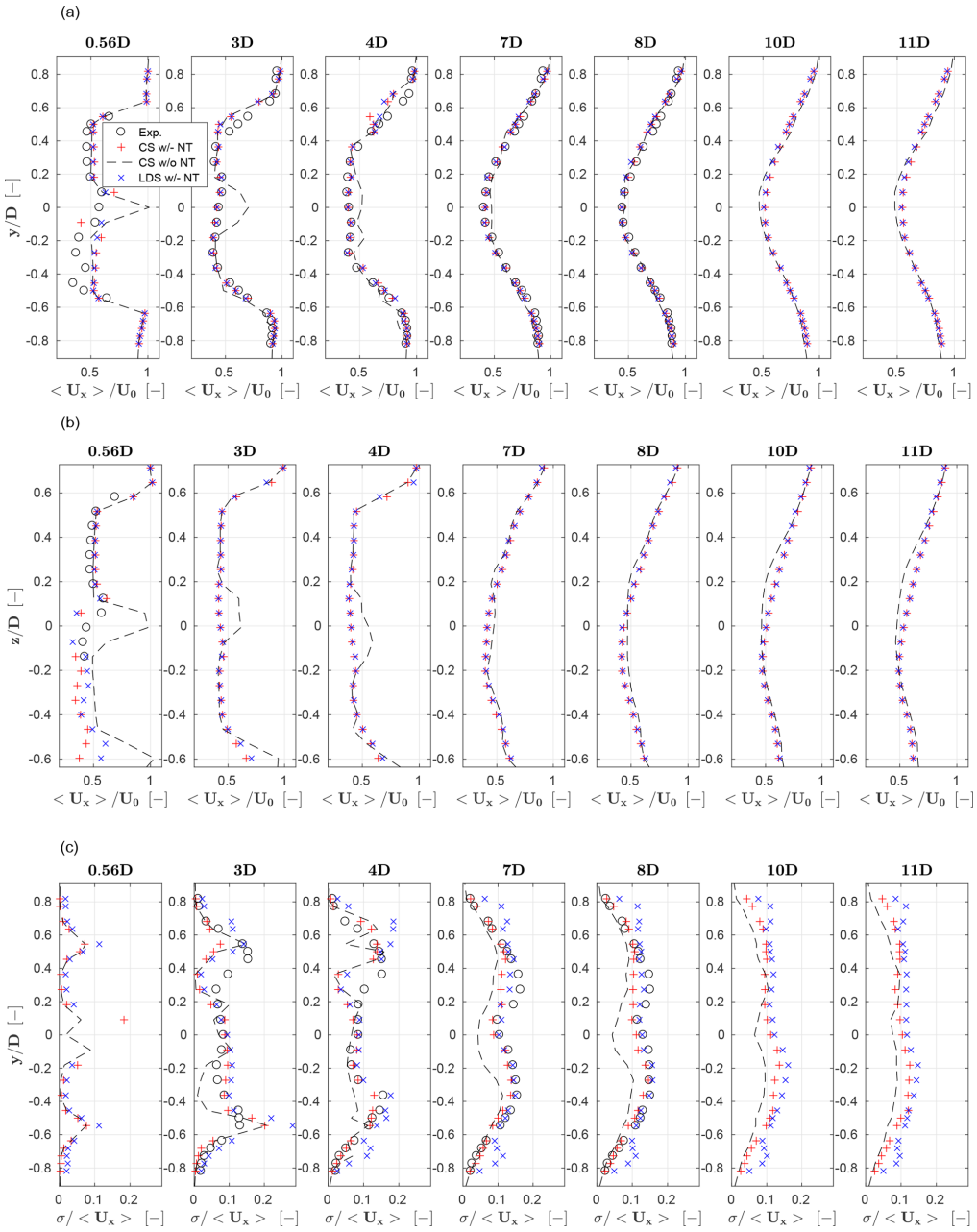

Figure 5. Profiles of normalized time-averaged streamwise velocity $\langle u_x \rangle / U_0$ along hub-height horizontal lines **(a)** and along vertical lines through the hub **(b)**. Turbulence intensity $\sigma / \langle u_x \rangle$ along hub-height horizontal lines **(c)**. Red + symbols: CS model with nacelle and tower; black dashed line: CS model without nacelle and tower; blue × symbols: LDS model with nacelle and tower; black ∘ symbols: experimental results.

$\sqrt[3]{p_f} U_\infty$; since this is lower than the current wind speed U_∞, the machine is now effectively operating in the full power region. Therefore, the collective blade pitch controller automatically adjusts the pitch setting to track the new reference rotor speed.

The resulting pitch and rotor speed changes modify the angle of attack and Reynolds number at the blade sections. Therefore, tests that include power derating are useful for evaluating the quality of the identified multi-airfoil tables. Indeed, to accurately estimate rotor power and thrust, the lifting line airfoil polars need to match the aerodynamic character-

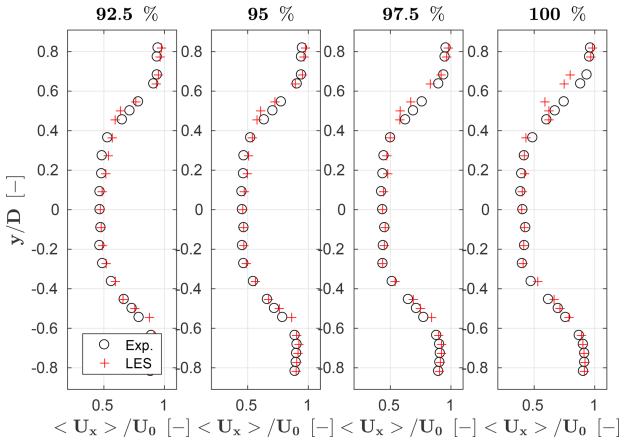

Figure 6. Normalized time-averaged streamwise velocity $\langle u_x \rangle / U_0$ profiles at 100 % and 92.5 % power settings, measured at hub height and 4 D downstream of the rotor. Red + symbols: LES; black ∘ symbols: experimental results.

istics of the corresponding blade sections in order to generate and project the proper body forces onto the fluid domain.

Simulations are conducted by prescribing the rotor speed and blade pitch measured in the experiment. Four power settings are considered, namely 100 %, 97.5 %, 95 % and 92.5 % of rated power. Figure 6 shows wake velocity profiles measured at hub height at a 4 D downstream position. For all cases, rotor-averaged speed error $\langle \Delta u_x \rangle$ and RMS(u_x) are about 1 % and 0.25 m s^{-1}, respectively. A quite satisfactory agreement between the simulation and experimental results can be noticed, although partialization seems to have only a modest effect on wake profile. Turbulence intensity profiles are not presented here, since the quality of the comparison is very similar to the one of the baseline case.

However, the situation is less satisfactory for rotor power and thrust, as shown in Table 2. Results indicate that power is particularly off, while thrust is affected by somewhat smaller errors. This might indicate a possible discrepancy in the behavior of the aerodynamic coefficients – especially of drag – with respect to the angle of attack. To verify that polars are indeed the culprit, several tests were conducted to check the effect of the Gaussian width ϵ. Indeed, one can tune ϵ to nearly exactly match the experimental results for each value of the curtailment factor. There is, however, not a single ϵ that is able to accommodate the investigated range of curtailments. On the other hand, keeping ϵ fixed, one can observe that the errors in power and thrust grow as the extent of power curtailment increases (and therefore as the angle of attack at the blade sections changes). These results seem to support the hypothesis that the slopes of the lift and drag coefficients with respect to the angle of attack are not calibrated well. To improve this aspect of the model, the polar calibration is being improved by a more sophisticated statistical weighting

Table 2. Power and thrust at 100 %, 97.5 %, 95 % and 92.5 % power settings.

		100 %	97.5 %	95 %	92.5 %
Power	Exp. (W)	45.79	44.36	43.20	42.11
	Sim. (W)	45.45	42.28	39.72	37.33
	ΔP %	−0.74	−4.69	−8.06	−11.35
Thrust	Exp. (N)	15.18	14.24	13.62	13.10
	Sim. (N)	16.05	14.57	13.56	12.70
	ΔT %	5.73	2.32	−0.44	−3.05

of the various experiments and by considering a span-wise variability of the Reynolds number.

5.2.2 Wake steering by yaw misalignment

Next, the LES model is verified in yaw misalignment conditions, which are relevant to wake deflection control. Hub-height wake profiles measured in low-turbulence conditions are used for the comparison for yaw misalignment angles of ±5, ±10 and ±20°.

Simulated and measured longitudinal speed profiles are presented at a downstream distance of 4 D in Fig. 7. Similar results were obtained at other distances, but are not reported for space limitations. The maximum rotor-averaged difference $\langle \Delta u_x \rangle$ between the simulation and experiment is 4.1 % and corresponds to the 20° case, while the maximum RMS(u_x) is 0.35 m s^{-1} at −10°. The average $\langle \Delta u_x \rangle$ and RMS(u_x) over the six yaw cases are equal to 1.6 % and 0.29 m s^{-1}, respectively. The results indicate a good agreement between the simulation and measurement, both in terms of wake deficit and pattern. Note, however, that the 1.6 % average speed error would correspond to a 4.8 % power error for a second wind turbine operating in full-wake shading at this downstream difference, a value that is small but not completely negligible.

5.2.3 Enhanced wake recovery by cyclic pitch control

A third wake control strategy in the same low-turbulence conditions is considered, in which the rotor blades are cyclicly pitched. The effect of cyclic pitching is changing the angle of attack of the blade sections cyclically over one rotor revolution. In turn, this results in an azimuthal change in the out-of-plane forces generated by the section, which then has the effect of correspondingly modifying the local induced velocity. A simple analytical model of the effects of cyclic pitching was developed in Wang et al. (2016). The analysis showed that, as already noticed by other authors (Fleming et al., 2014), CyPC has some effect on the speed of recovery of the wake, but results only in a very modest deflection of its path. In fact, wake deflection by yawing is driven by the tilting of the rotor thrust, which results in a significant lateral

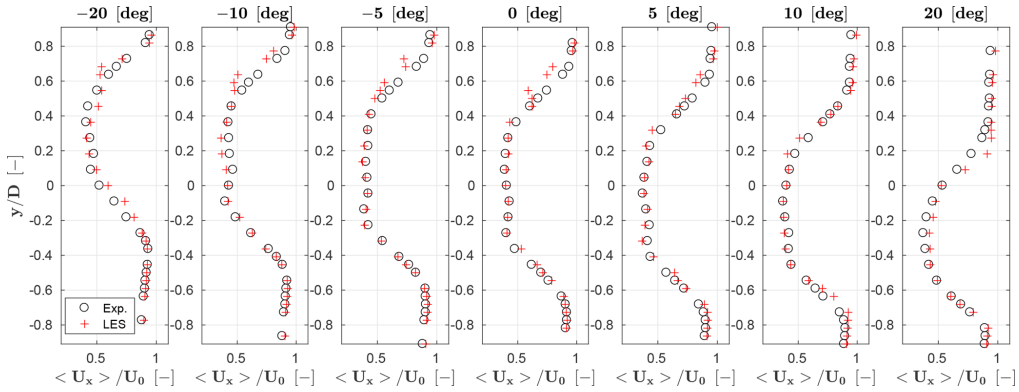

Figure 7. Normalized time-averaged streamwise velocity profiles at hub height for different yaw misalignments 4 D downstream of the rotor. Red + symbols: LES; black ∘ symbols: experimental results.

force being applied onto the flow. On the other hand, CyPC does modify the induced velocity, but only generates negligible lateral forces. In addition, it was observed that CyPC also results in large moments being generated in the rotor fixed frame, which further questions the practical applicability of this wake manipulation strategy. Nonetheless, CyPC is considered here to further verify the characteristics of the LES framework in operating conditions that differ significantly from the ones in the previous test cases.

Each blade is pitched according to $\theta_i = \theta_0 + \theta_c \cos(\psi_i + \gamma)$, where θ_0 is the collective pitch constant, θ_c the 1 P pitch amplitude, ψ_i the blade azimuth angle (clockwise looking downstream and null when the blade is pointing vertically up) and γ the phase angle (with the same origin and positive sense as ψ). The CyPC parameters were set as $\theta_0 = 0°$, $\theta_c = 5.3°$ and $\gamma = 270°$.

Given the effects of CyPC on the induced velocity and on the near-wake behavior, a more complete analysis can be performed by using the PIV measurements than considering the simple hub-height line scans obtained by hot-wire probes. Figure 8 reports, at left, the streamwise velocity just behind the rotor ($x/D = 0.56$), which is a distance for which few results have been previously reported. The images show that the use of CyPC has a strong effect on the wake structure, leading to a marked unsymmetrical shape. Indeed, the phase angle $\gamma = 270°$ implies that blades have maximum pitch and hence produce the minimal rotor-plane-normal force in the left part of the rotor, as shown in the figure, which in turn exhibits the lowest induction and highest resulting longitudinal flow speed. A comparison between experimental and numerical results shows that there is, in general, a good qualitative agreement and that the main distortion effects caused by CyPC are reasonably captured. The rotor-averaged error $\langle \Delta u_x \rangle$ between the simulation and measurement is 2.69 %, while RMS(u_x) is 0.79 m s^{-1}.

The discrepancy between the simulation and experiment is 2 times larger than in the baseline case. One possible reason for this is that unsteady aerodynamic effects of the airfoils are neglected. This could be improved by using unsteady aerodynamic models in the lifting line, including, for example, a Theodorsen correction and a dynamic stall model. Although the Beddoes–Leishman approach (Moriarty and Hansen, 2005) is implemented in `FAST` and therefore could be readily used in the present LES framework, the model requires the definition of several airfoil-dependent parameters, which would need to be specifically calibrated for the low-Reynolds airfoils used on the G1 scaled wind turbine.

The comparison of LES and the experiment in the far wake (6 D) is slightly better, as can be observed in the right part of Fig. 8. The wake recovery is reasonably good in terms of flow speed, although the slight tilting towards the right shown by the PIV measurements is not apparent in the LES results. Lastly, it should be remarked that CyPC leads to a faster recovery of the wake than in the baseline case, as already noted by Wang et al. (2016). In principle, this could be of interest for wind farm control, although, as previously mentioned, the large resulting loads exerted on the rotor probably limit the practical applicability of this control concept.

5.3 Moderate-turbulence inflow simulation

Next, a turbulent case is considered in which a flow characterized by a 6 % hub-height turbulence intensity is generated by the precursor simulation described in Sect. 3.1. The wind turbine model is aligned with the streamwise flow direction and the hub-height wind speed is equal to 4.76 m s^{-1} (partial load region). The simulated wind turbine operates in two different modes, namely with a fixed rotating speed of 720 RPM and blade pitch angle of 1.4° (which are the values measured on the scaled model in the experiment) or with a controller in the loop (Bottasso et al., 2014).

The aerodynamic power output, averaged over a 60 s time window, is equal to 31.0 W for the experiment and to 30.5 and 31.2 W for the prescribed speed and closed-loop torque simulations, respectively. In this latter case, the average ro-

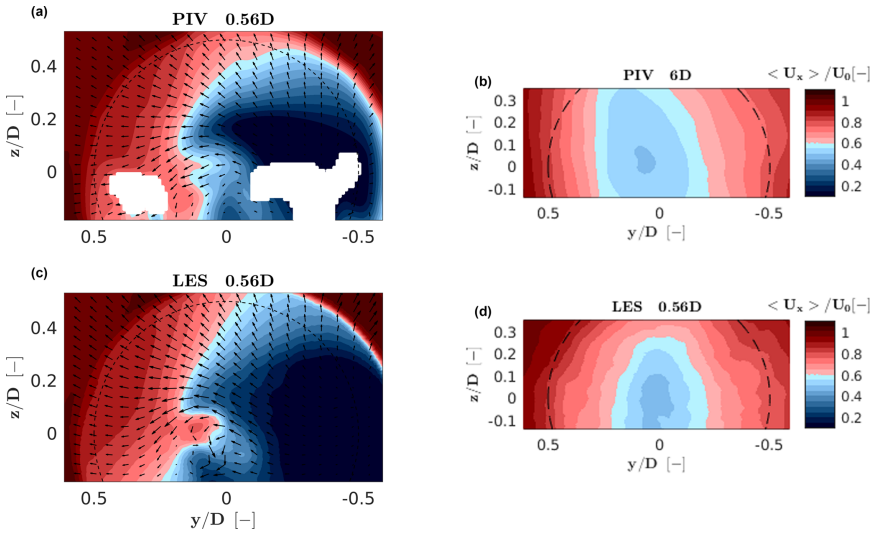

Figure 8. Streamwise velocity contour plots for the PIV measurements **(a, b)** and LES model **(c, d)** measured 0.56 D **(a, c)** and 6 D **(b, d)** downstream of the rotor. Black arrows indicate the crosswind velocity component at a number of sampling points.

tor speed was only 2.2 % higher than the one measured on the wind turbine, which clearly indicates a good overall match of the numerical model with the experiment. On the other hand, the power standard deviation was 0.2, 0.6 and 0.3 W, respectively, for the experiment, prescribed speed and closed-loop simulations. Clearly, prescribing a constant speed to the rotor in the numerical simulation induces significant torque oscillations because the rotor cannot adjust to the turbulent flow fluctuations. When loads are of interest, it is therefore essential to also use a closed-loop controller in the simulation. However, in this case the simulation might drift away from the operating condition realized in the experiment if the numerical model has a significant mismatch with respect to reality. Apparently, this is not the case here, and the numerical model seems to be well in line with the experimental one.

Figure 9 shows the normalized time-averaged velocity and turbulence intensity profiles for the LES model and experiment at distances of −1.5, 1.4, 1.7, 2, 3, 4, 6 and 9 D from the rotor. The position at −1.5 D is outside of the induction zone, and the flow can be regarded as the undisturbed free stream. The LES curves show, in general, a good agreement with the experimental ones. Only the case of the closed-loop regulation is reported here, as results are nearly identical to the prescribed speed case. The rotor-averaged simulation error $\langle \Delta u_x \rangle$ is less than 1 % on average across all distances. From the near-wake (1.4 D) to the far-wake (9D) regions, the root mean square error RMS(u_x) is gradually reduced from 0.2 to 0.1 m s^{-1}. The comparisons all indicate that the LES results are in good agreement with the experimental ones.

Contrary to the baseline low-turbulence simulation, the two turbulence intensity peaks induced by the blade tip vortices are well predicted in this case. To explain this phenomenon, we report in Fig. 10 for the low-turbulence (left) and moderate-turbulence (right) cases the instantaneous streamwise speed component u_x/U_0, the vorticity $\langle \nabla \times \boldsymbol{u} \rangle$ and the turbulence intensity $\sigma / \langle u_x \rangle$ on a horizontal plane at hub height. As previously observed, the turbulent structures induced by the nacelle and tower are different for the two cases on account of the different boundary conditions on their surfaces.

Vorticity shed by the tips in the near wake is quite similar for the low- and moderate-turbulence cases. Turbulence intensity is, on the other hand, very different in the blade tip region for these two different ambient turbulence cases. In fact, the higher background turbulence of the turbulent inflow case triggers the instability of the tip vortical structures (Sørensen, 2011), which rapidly break down. The contour plots of the turbulent simulation clearly show that, starting from 0.1 D downstream, the tip vortices generate significant turbulence intensity, while vorticity quickly diminishes from 2 D downstream, signalling that the coherent tip vortices have broken down into smaller and less coherent structures. Quite differently, the low-turbulence case shows a persistent modest turbulence intensity and high vorticity up to about 4 D downstream of the rotor. In this case, capturing the right amount of speed fluctuations – which are mostly caused here by the tip vortices in contrast to the other case that is predominantly dominated by turbulent fluctuations – probably requires a denser grid than the one used here, and this explains the poor match with the experiments in this case in the near-wake tip region. Apparently, the same grid is, however, capable of representing the simpler turbulent case well. An analysis of tip vortex breakdown is reported in Troldborg et al. (2015) using a blade-conforming approach, which therefore uses significantly denser grids than in the present case.

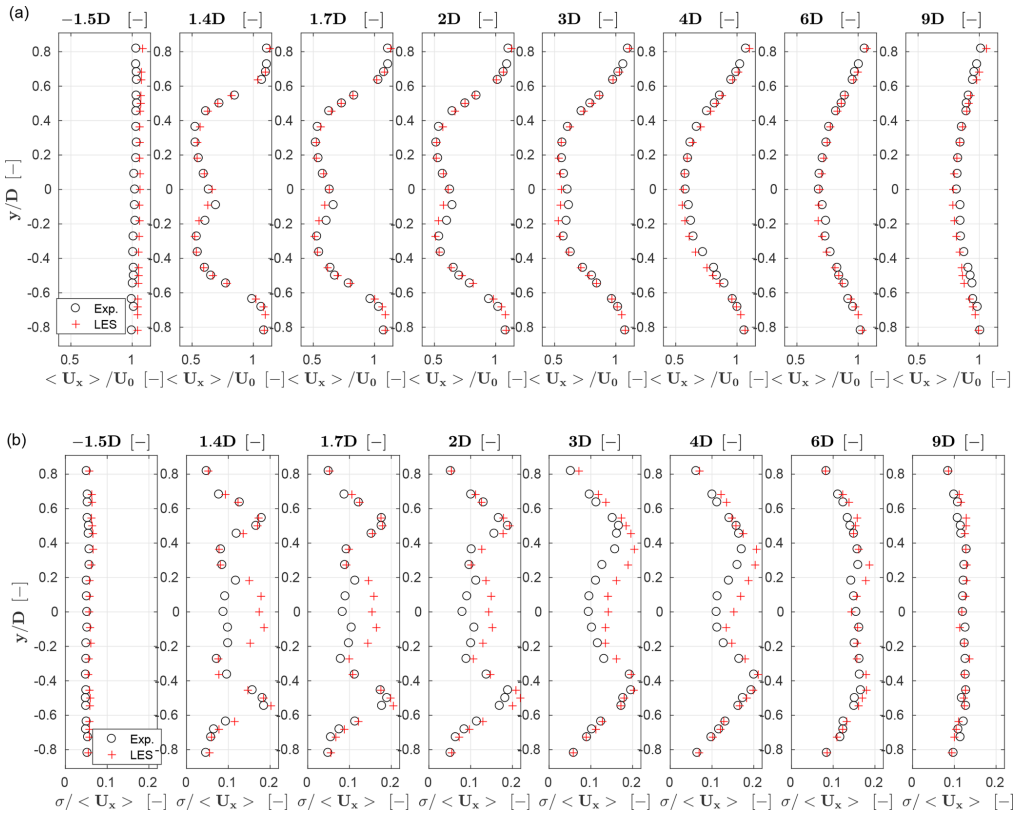

Figure 9. Normalized time-averaged streamwise velocity $\langle u_x \rangle / U_0$ **(a)** and turbulence intensity $\sigma / \langle u_x \rangle$ **(b)** profiles at hub height. Red + symbols: LES; black ∘ symbols: experimental results.

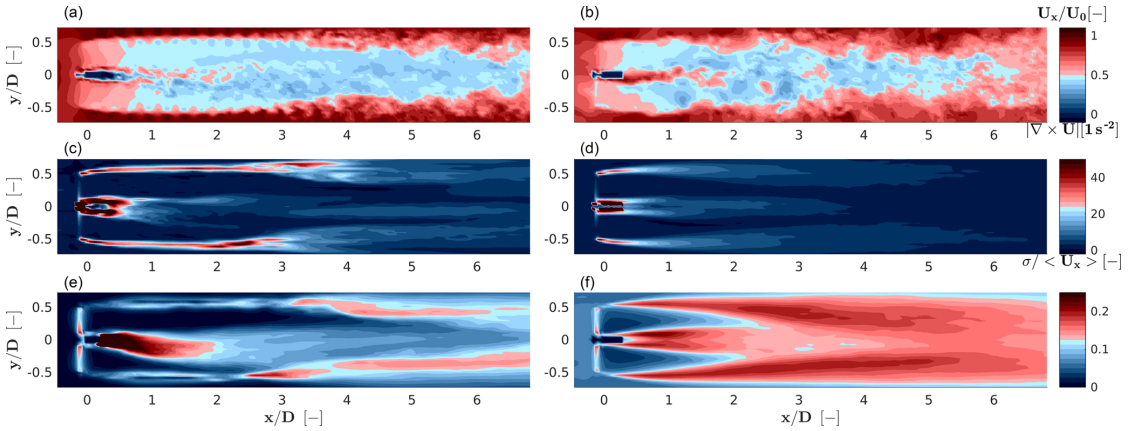

Figure 10. Instantaneous streamwise speed component u_x / U_0 **(a, b)**, vorticity $\langle \nabla \times \boldsymbol{u} \rangle$ **(c, d)** and turbulence intensity $\sigma / \langle u_x \rangle$ **(e, f)**. At left, low-turbulence case; at right: moderate-turbulence case.

6 Conclusions

This paper has employed an LES approach for the simulation of wind turbine wakes, obtaining a complete digital copy of scaled experiments performed in a boundary layer wind tunnel. The main goal of the paper was to try to quantify the ability of LES to represent operating conditions relevant to wind farm control. To this end, numerical results were compared to wind tunnel measurements of one single wind turbine, while multiple machines and wake interactions are studied in Wang et al. (2017b, 2018) and in other forthcoming papers. While

this work does not have the ambition to develop a comprehensive validation activity, it represents a step in the direction of a better understanding of the capabilities and limits of the current high-fidelity simulation technology for wakes.

A low-turbulence normal-operation problem is considered first, showing that simulations are in good agreement with experiments both in terms of rotor quantities (thrust and power) and wake behavior. Next, the three wake control strategies of power derating, wake steering by yaw misalignment and wake-enhanced recovery by cyclic pitch control are studied. Results show a good agreement of simulations with experiments for yaw misalignment, but are less satisfactory for derating, probably on account of inaccuracies in the airfoil drag. The wake turbulence intensity shows some discrepancies, which were here attributed to a lack of refinement of the grid that in turn affects the breakdown of the near-wake vortical structures. Slightly less accurate results are obtained for cyclic pitching, possibly due to un-modeled unsteady airfoil aerodynamics.

The paper continues by considering a moderately turbulent wind. The characteristics of the simulated turbulent flow are in good agreement with measurements. The average streamwise velocity is within 1 % of the experiments, and the average turbulence intensity within 5 %–7 %, while the turbulent kinetic energy spectrum and integral timescale also exhibit a good matching. The wake characteristics are in very good agreement with the experiments, since tip vortices break down earlier than in the low-turbulence condition, relaxing the need for very dense grids in the near-wake region. The use of a controller in the loop leads to a more realistic response of the model turbine to the turbulent flow, which is important if the load response of the machine is of interest. Remarkably, the model in the loop also operates at essentially the same rotor speed as the experiment, which demonstrates the overall fidelity of the digital model to the experimental one.

Results shown in this work indicate that the present LES-ALM approach is a viable way of simulating scaled wind tunnel experiments. Results are, however, not perfect, and areas of improvement include a more sophisticated and accurate calibration of the airfoil polars, the inclusion of airfoil unsteady aerodynamic effects (which also call for the calibration of these models with dedicated data sets), and a more efficient refinement of the grid where necessary by the use of unstructured meshing and adaption techniques.

These encouraging results motivate and justify the application of the present simulation framework to the analysis of clusters of wake-interacting wind turbines, for which we have gathered an ample collection of data sets in multiple operating conditions. Hopefully, this will lead to a better understanding of wake behavior, which is of crucial importance for the design and operation of wind turbines and wind power plants. The final validation of the present and similar simulation approaches can undoubtedly benefit from the use of scaled wind tunnel experiments, as attempted in this work, as an intermediate step towards their application to the full-scale case.

Data availability. Data can be provided upon request. Please contact the corresponding author Carlo L. Bottasso (carlo.bottasso@tum.de).

Appendix A: Nomenclature

A	Rotor swept area
D	Rotor diameter
C_{D}	Drag coefficient
C_{L}	Lift coefficient
C_k^0	Nominal coefficient
C_{s}	Smagorinsky constant
$E(f)$	Turbulent kinetic energy spectrum
J	Cost function
N	Number of available experimental observations
Q	Rotor torque
$\mathbf{R}$	Covariance matrix
T_τ	Integral timescale
U_∞	Free-stream wind speed
h	Grid size
p_{f}	Power partialization factor
$r(\tau)$	Autocorrelation
u_i	Velocity component
y^+	Dimensionless wall distance
α	Angle of attack
β_m	Tunable constant for gamma scheme
γ	Phase angle
ϵ	Gaussian width
η	Span-wise location
θ	Blade pitch angle
ψ	Blade azimuthal angle
ρ	Density
$\sigma/\langle u_x \rangle$	Turbulence intensity
τ	Time shift for autocorrelation analysis
Ω	Rotor speed
$\Delta\cdot$	Correction or difference
$\langle\cdot\rangle$	Averaged quantity
$\widetilde{(\cdot)}$	Resolved quantity
ALM	Actuator line method
bi-CG	Biconjugate gradient
CFD	Computational fluid dynamics
CG	Conjugate gradient
CS	Constant Smagorinsky
CyPC	Cyclic pitch control
DIC-GS	Gauss–Seidel smoothing with diagonal incomplete Cholesky factorization
DILU	Diagonal incomplete LU factorization
GAMG	Geometric–algebraic multigrid
IB	Immersed boundary
LES	Large-eddy simulation
LDS	Lagrangian averaging dynamic Smagorinsky
Lidar	Light detection and ranging
NOC	Non-orthogonal corrector
PISO	Pressure-implicit with splitting of operators
PIV	Particle image velocimetry
RANS	Reynolds-averaged Navier–Stokes
Re	Reynolds number
RMS	Root mean square
TSR	Tip speed ratio

Competing interests. The authors declare that they have no conflict of interest.

Acknowledgements. This work has been supported in part by the CL-WINDCON project, which receives funding from the European Union Horizon 2020 research and innovation program under grant agreement no. 727477. The first author was supported by the Chinese Scholarship Council. All tests were performed at the wind tunnel of the Politecnico di Milano, with the support of Alessandro Croce, Alex Zanotti, Gabriele Campanardi and Donato Grassi. The authors wish to thank Emmanouil M. Nanos of the Technische Universität München and Vlaho Petrović, now at the University of Oldenburg, for their contribution to the experimental work. The authors also express their appreciation to the Leibniz Supercomputing Centre (LRZ) for providing access and computing time on the SuperMUC Petascale System.

This work was supported by the German Research Foundation (DFG) and the Technical University of Munich (TUM) in the framework of the Open-Access Publishing Program.

Edited by: Luciano Castillo
Reviewed by: two anonymous referees

References

Abkar, M. and Dabiri, J. O.: Self-similarity and flow characteristics of vertical-axis wind turbine wakes: an LES study, J. Turbul., 18, 373–389, 2017.

Bandringa, H.: Immersed boundary methods, Masters thesis, University of Groningen, 2010.

Barthelmie, R. J., Larsen, G., Frandsen, S., Folkerts, L., Rados, K., Pryor, S., Lange, B., and Schepers, G.: Comparison of wake model simulations with offshore wind turbine wake profiles measured by SODAR, J. Atmos. Ocean. Tech., 23, 888–901, 2006.

Barthelmie, R. J., Frandsen, S. T., Nielsen, M., Pryor, S., Rethore, P.-E., and Jørgensen, H. E.: Modelling and measurements of power losses and turbulence intensity in wind turbine wakes at Middelgrunden offshore wind farm, Wind Energy, 10, 517–528, 2007.

Bartl, J., Pierella, F., and Sætrana, L.: Wake measurements behind an array of two model wind turbines, Enrgy. Proced., 24, 305–312, 2012.

Bottasso, C. L., Campagnolo, F., and Petrović, V.: Wind tunnel testing of scaled wind turbine models: Beyond aerodynamics, J. Wind Eng. Ind. Aerod., 127, 11–28, 2014.

Calaf, M., Meneveau, C., and Meyers, J.: Large eddy simulation study of fully developed wind-turbine array boundary layers, Phys. Fluids, 22, 015110, 2010.

Campagnolo, F., Petrović, V., Bottasso, C. L., and Croce, A.: Wind tunnel testing of wake control strategies, IEEE American Control Conference (ACC), 513–518, https://doi.org/10.1109/ACC.2016.7524965, 2016a.

Campagnolo, F., Petrović, V., Nanos, E. M., Tan, C. W., Bottasso, C. L., Paek, I., Kim, H., and Kim, K.: Wind tunnel testing of power maximization control strategies applied to a multi-turbine floating wind power platform, in: The 26th International Ocean and Polar Engineering Conference, International Society of Offshore and Polar Engineers, Rhodes, Greece, 2016b.

Campagnolo, F., Petrović, V., Schreiber, J., Nanos, E. M., Croce, A., and Bottasso, C. L.: Wind tunnel testing of a closed-loop wake deflection controller for wind farm power maximization, J. Phys. Conf. Ser., 753, 032006, https://doi.org/10.1088/1742-6596/753/3/032006, 2016c.

Campanardi, G., Grassi, D., Zanotti, A., Nanos, E. M., Campagnolo, F., Croce, A., and Bottasso, C. L.: Stereo particle image velocimetry set up for measurements in the wake of scaled wind turbines, J. Phys. Conf. Ser., 882, 012003, https://doi.org/10.1088/1742-6596/882/1/012003, 2017.

Carcangiu, C. E.: CFD-RANS study of horizontal axis wind turbines, PhD thesis, Università degli Studi di Cagliari, Via Università, 40, 09124 Cagliari CA, Italy, 2008.

Chamorro, L. P. and Porté-Agel, F.: A wind-tunnel investigation of wind-turbine wakes: boundary-layer turbulence effects, Bound.-Lay. Meteorol., 132, 129–149, 2009.

Churchfield, M. and Lee, S.: NWTC design codes-SOWFA, Tech. rep., National Renewable Energy Laboratory (NREL), Golden, CO, available at: http://wind.nrel.gov/designcodes/simulators/SOWFA (last access: 21 January 2018), 2012.

Churchfield, M. J., Lee, S., Moriarty, P. J., Martinez, L. A., Leonardi, S., Vijayakumar, G., and Brasseur, J. G.: A large-eddy simulation of wind-plant aerodynamics, AIAA paper, 537, https://doi.org/10.2514/6.2012-537, 2012.

Churchfield, M. J., Lee, S., Schmitz, S., and Wang, Z.: Modeling wind turbine tower and nacelle effects within an actuator line model, in: 33rd Wind Energy Symposium, 33rd Wind Energy Symposium, Kissimmee, Florida, p. 0214, https://doi.org/10.2514/6.2015-0214, 2015.

Churchfield, M. J., Schreck, S., Martınez-Tossas, L. A., Meneveau, C., and Spalart, P. R.: An Advanced Actuator Line Method for Wind Energy Applications and Beyond, in: 35th Wind Energy Symposium, 35th Wind Energy Symposium, Grapevine, Texas, p. 1998, https://doi.org/10.2514/6.2017-1998, 2017.

Deardorff, J. W.: A numerical study of three-dimensional turbulent channel flow at large Reynolds numbers, J. Fluid Mech., 41, 453–480, 1970.

Fleming, P., Gebraad, P., Churchfield, M., Lee, S., Johnson, K., Michalakes, J., van Wingerden, J.-W., and Moriarty, P.: SOWFA Super-controller User's Manual, National Renewable Energy Laboratory, EWEA 2013, Vienna, Austria, 2013.

Fleming, P., Gebraad, P. M., Lee, S., van Wingerden, J.-W., Johnson, K., Churchfield, M., Michalakes, J., Spalart, P., and Moriarty, P.: Simulation comparison of wake mitigation control strategies for a two-turbine case, Wind Energy, 18, 2135–2143, 2015.

Fleming, P. A., Gebraad, P. M., Lee, S., van Wingerden, J.-W., Johnson, K., Churchfield, M., Michalakes, J., Spalart, P., and Moriarty, P.: Evaluating techniques for redirecting turbine wakes using SOWFA, Renew. Energ., 70, 211–218, 2014.

Gaumond, M., Réthoré, P.-E., Ott, S., Pena, A., Bechmann, A., and Hansen, K. S.: Evaluation of the wind direction uncertainty and its impact on wake modeling at the Horns Rev offshore wind farm, Wind Energy, 17, 1169–1178, 2014.

Gebraad, P., Teeuwisse, F., Wingerden, J., Fleming, P. A., Ruben, S., Marden, J., and Pao, L.: Wind plant power optimization through yaw control using a parametric model for wake effects – a CFD simulation study, Wind Energy, 19, 95–114, 2016.

Greenshields, C. J.: Openfoam user guide, OpenFOAM Foundation Ltd, version 3, OpenCFD Ltd, ESI Group, 75015 Paris, France, 2015.

Hansen, K. S., Barthelmie, R. J., Jensen, L. E., and Sommer, A.: The impact of turbulence intensity and atmospheric stability on power deficits due to wind turbine wakes at Horns Rev wind farm, Wind Energy, 15, 183–196, 2012.

Holzmann, T.: Mathematics, Numerics, Derivations and OpenFOAM®, available at: https://holzmann-cfd.de (last access: 21 January 2018) 2016.

Jasak, H. and Rigler, D.: Finite volume immersed boundary method for turbulent flow simulations, in: 9th OpenFOAM Workshop, 9th International OpenFOAM Workshop, Zagreb, Croatia, 2014.

Jasak, H., Weller, H., and Gosman, A.: High resolution NVD differencing scheme for arbitrarily unstructured meshes, Int. J. Numer. Meth. Fl., 31, 431–449, 1999.

Jensen, N. O.: A note on wind generator interaction, Technical University of Denmark, Kgs. Lyngby, Denmark, 1983.

Jha, P. K., Churchfield, M. J., Moriarty, P. J., and Schmitz, S.: Guidelines for volume force distributions within actuator line modeling of wind turbines on large-eddy simulation-type grids, J. Sol. Energ.-T. ASME, 136, 031003, https://doi.org/10.1115/1.4026252, 2014.

Jiménez, Á., Crespo, A., and Migoya, E.: Application of a LES technique to characterize the wake deflection of a wind turbine in yaw, Wind Energy, 13, 559–572, 2010.

Jonkman, J., Butterfield, S., Musial, W., and Scott, G.: Definition of a 5-MW reference wind turbine for offshore system development, Tech. rep., National Renewable Energy Lab. (NREL), Golden, CO, USA, 2009.

Jonkman, J. M. and Buhl Jr., M. L.: FAST User's Guide-Updated August 2005, Tech. rep., National Renewable Energy Laboratory (NREL), Golden, CO, USA, 2005.

Kennedy, J. M., Fox, B., Littler, T., and Flynn, D.: Validation of fixed speed induction generator models for inertial response using wind farm measurements, IEEE T. Power Syst., 26, 1454–1461, 2011.

Knudsen, T., Bak, T., and Svenstrup, M.: Survey of wind farm control–power and fatigue optimization, Wind Energy, 18, 1333–1351, https://doi.org/10.1002/we.1760, 2015.

Lai, M.-C. and Peskin, C. S.: An immersed boundary method with formal second-order accuracy and reduced numerical viscosity, J. Comput. Phys., 160, 705–719, 2000.

Larsen, G. C., Madsen Aagaard, H., Bingöl, F., Mann, J., Ott, S., Sørensen, J. N., Okulov, V., Troldborg, N., Nielsen, N. M., Thomsen, K., Larsen, T. J., and Mikkelsen, R.: Dynamic wake meandering modeling, Tech. rep., Risø National Laboratory, 2007.

Lu, H. and Porté-Agel, F.: Large-eddy simulation of a very large wind farm in a stable atmospheric boundary layer, Phys. Fluids, 23, 065101, https://doi.org/10.1063/1.3589857, 2011.

Martinez, L. A., Leonardi, S., Churchfield, M. J., and Moriarty, P. J.: A comparison of actuator disk and actuator line wind turbine models and best practices for their use, AIAA Paper, 50th AIAA Aerospace Sciences Meeting including the New Horizons Forum and Aerospace Exposition Nashville, Tennessee, https://doi.org/10.2514/6.2012-900, 2012.

Martínez-Tossas, L. A., Churchfield, M. J., and Leonardi, S.: Large eddy simulations of the flow past wind turbines: actuator line and disk modeling, Wind Energy, 18, 1047–1060, 2015.

Martínez-Tossas, L. A., Churchfield, M. J., and Meneveau, C.: Optimal smoothing length scale for actuator line models of wind turbine blades based on Gaussian body force distribution, Wind Energy, 20, 1083–1096, 2017.

Martínez-Tossas, L. A., Churchfield, M. J., Yilmaz, A. E., Sarlak, H., Johnson, P. L., Sørensen, J. N., Meyers, J., and Meneveau, C.: Comparison of four large-eddy simulation research codes and effects of model coefficient and inflow turbulence in actuator-line-based wind turbine modeling, J. Renew. Sustain. Ener., 10, 033301, https://doi.org/10.1063/1.5004710, 2018.

Medici, D. and Alfredsson, P.: Measurements on a wind turbine wake: 3D effects and bluff body vortex shedding, Wind Energy, 9, 219–236, 2006.

Meneveau, C., Lund, T. S., and Cabot, W. H.: A Lagrangian dynamic subgrid-scale model of turbulence, J. Fluid Mech., 319, 353–385, 1996.

Mittal, R. and Iaccarino, G.: Immersed boundary methods, Annu. Rev. Fluid Mech., 37, 239–261, 2005.

Mo, J.-O., Choudhry, A., Arjomandi, M., and Lee, Y.-H.: Large eddy simulation of the wind turbine wake characteristics in the numerical wind tunnel model, J. Wind Eng. Ind. Aerod., 112, 11–24, 2013.

Moriarty, P. J. and Hansen, A. C.: AeroDyn theory manual, Tech. rep., National Renewable Energy Lab., Golden, CO, USA, 2005.

Moukalled, F., Mangani, L., and Darwish, M.: The finite volume method in computational fluid dynamics, Springer International Publishing, Switzerland, 2016.

Nilsson, K., Ivanell, S., Hansen, K. S., Mikkelsen, R., Sørensen, J. N., Breton, S.-P., and Henningson, D.: Large-eddy simulations of the Lillgrund wind farm, Wind Energy, 18, 449–467, 2015.

O'Neill, P., Nicolaides, D., Honnery, D., and Soria, J.: Autocorrelation functions and the determination of integral length with reference to experimental and numerical data, in: 15th Australasian Fluid Mechanics Conference, Vol. 1, 1–4, The University of Sydney, 2004.

Platt, A. D., and Buhl, M. L.: WT_Perf User Guide for Version 3.05.00., Golden, Colorado, National Renewable Energy Laboratory, available at: https://zh.scribd.com/document/166120851/WT-Perf-Users-Guide (last access: 22 January 2019), 2012.

Porté-Agel, F., Wu, Y.-T., Lu, H., and Conzemius, R. J.: Large-eddy simulation of atmospheric boundary layer flow through wind turbines and wind farms, J. Wind Eng. Ind. Aerod., 99, 154–168, 2011.

Renkema, D. J.: Validation of wind turbine wake models, Master of Science Thesis, Delft University of Technology, 93 pp., 2007.

Santoni, C., Carrasquillo, K., Arenas-Navarro, I., and Leonardi, S.: Effect of tower and nacelle on the flow past a wind turbine, Wind Energy, 20, 1927–1939, 2017.

Sarlak, H., Meneveau, C., and Sørensen, J. N.: Role of subgrid-scale modeling in large eddy simulation of wind turbine wake interactions, Renew. Energ., 77, 386–399, 2015.

Sedaghatizadeh, N., Arjomandi, M., Kelso, R., Cazzolato, B., and Ghayesh, M. H.: Modelling of wind turbine wake using large eddy simulation, Renew. Energ., 115, 1166–1176, 2018.

Shamsoddin, S. and Porté-Agel, F.: Large-eddy simulation of atmospheric boundary-layer flow through a wind farm sited on topography, Bound.-Lay. Meteorol., 163, 1–17, 2017.

Sørensen, J. N.: Instability of helical tip vortices in rotor wakes, J. Fluid Mech., 682, 1–4, 2011.

Sørensen, J. N. and Shen, W. Z.: Numerical modeling of wind turbine wakes, J. Fluids Eng.-T. ASME, 124, 393–399, 2002.

Sørensen, J. N., Mikkelsen, R. F., Henningson, D. S., Ivanell, S., Sarmast, S., and Andersen, S. J.: Simulation of wind turbine wakes using the actuator line technique, Philos. T. R. Soc. A, 373, https://doi.org/10.1098/rsta.2014.0071, 2015.

Stevens, R. J., Martínez-Tossas, L. A., and Meneveau, C.: Comparison of wind farm large eddy simulations using actuator disk and actuator line models with wind tunnel experiments, Renew. Energ., 116, 470–478, 2018.

Stovall, T., Pawlas, G., and Moriarty, P.: Wind farm wake simulations in OpenFOAM, AIAA Paper, 48th AIAA Aerospace Sciences Meeting Including the New Horizons Forum and Aerospace Exposition Orlando, Florida, https://doi.org/10.2514/6.2010-825, 2010.

Troldborg, N., Zahle, F., Réthoré, P.-E., and Sørensen, N. N.: Comparison of wind turbine wake properties in non-sheared inflow predicted by different computational fluid dynamics rotor models, Wind Energy, 18, 1239–1250, 2015.

Uhlmann, M.: An immersed boundary method with direct forcing for the simulation of particulate flows, J. Comput. Phys., 209, 448–476, 2005.

van Dooren, M. F., Campagnolo, F., Sjöholm, M., Angelou, N., Mikkelsen, T., and Kühn, M.: Demonstration and uncertainty analysis of synchronised scanning lidar measurements of 2-D velocity fields in a boundary-layer wind tunnel, Wind Energ. Sci., 2, 329–341, https://doi.org/10.5194/wes-2-329-2017, 2017.

Wang, J., Bottasso, C. L., and Campagnolo, F.: Wake redirection: comparison of analytical, numerical and experimental models, in: TORQUE 2016, The Science of Making Torque from Wind, IOP Publishing, Munich, Germany, 2016.

Wang, J., Foley, S., Nanos, E., Yu, T., Campagnolo, F., Bottasso, C., Zanotti, A., and Croce, A.: Numerical and experimental study for wake redirection techniques in a boundary layer wind tunnel, J. Phys. Conf. Ser., 854, 012048, https://doi.org/10.1088/1742-6596/854/1/012048, 2017a.

Wang, J., Mclean, D., Campagnolo, F., Yu, T., and Bottasso, C.: Large-eddy simulation of waked turbines in a scaled wind farm facility, J. Phys. Conf. Ser., 854, 012047, https://doi.org/10.1088/1742-6596/854/1/012047, 2017b.

Wang, J., Liu, y., Filippo, C., and Bottasso, C. L.: Verification of a Low Cost Scale-Adaptive CFD Formulation for Waked Wind Turbines, in: AIAA Science and Technology Forum and Exposition (SciTech 2018), Gaylord Palms, Kissimmee, Florida, 2018.

Wu, Y.-T. and Porté-Agel, F.: Large-eddy simulation of wind-turbine wakes: evaluation of turbine parametrisations, Bound.-Lay. Meteorol., 138, 345–366, 2011.

Yang, X. and Sotiropoulos, F.: A new class of actuator surface models for wind turbines, Wind Energy, 21, 285–302, 2018.

Zasso, A., Giappino, S., Muggiasca, S., and Rosa, L.: Optimization of the boundary layer characteristics simulated at Politecnico di Milano Boundary Layer Wind Tunnel in a wide scale ratio range, in: Proceedings of the 6th Asia-Pacific Conference on Wind Engineering, Seoul, Korea, 2005.

The Science of Making Torque from Wind (TORQUE 2018) IOP Publishing
IOP Conf. Series: Journal of Physics: Conf. Series **1037** (2018) 062007 doi:10.1088/1742-6596/1037/6/062007

Validation of large-eddy simulation of scaled waked wind turbines in different yaw misalignment conditions

C Wang[1], J Wang[1], F Campagnolo[1], D B Carreón[2] and C L Bottasso[1,3]

[1] Wind Energy Institute, Technische Universität München, Boltzmannstraße 15, D-85748 Garching bei München, Germany
[2] Instituto de Energías Renovables, Universidad Nacional Autónoma de México, Priv. Xochicalco s/n Temixco, Morelos 62580, Mexico
[3] Dipartimento di Scienze e Tecnologie Aerospaziali, Politecnico di Milano, Via La Masa 34, I-20156 Milano, Italy

E-mail: cy.wang@tum.de

Abstract.
This paper compares lifting-line large-eddy simulations (LES) of scaled wind turbines against experimental measurements obtained in a boundary layer wind tunnel. The final goal of this effort is to develop a verified digital copy of the experimental facility, in support of wind farm control research. Three scaled wind turbine models are arranged in different waked configurations and yaw misalignment conditions. In the experiments, the wind turbine response is measured in terms of various operational parameters, while the flow is measured with two scanning LiDARs. Simulation and experimental results are compared with respect to flow characteristics, turbine states and wake behavior. The analysis of the results shows a good match between simulations and experiments. Besides this important verification, the numerical simulations are also used to explain a wake interference phenomenon observed in the experiments, which causes a modification in the path of the wake of shaded turbines.

1. Introduction

Among existing wind farm control strategies, yaw-based control appears to be very promising in spite of its apparent simplicity [1]. Using this control approach, upstream wind turbines are yawed slightly out of the wind with the goal of steering their wakes away from downstream turbines. A wind farm super-controller is then tasked with the goal of finding the optimal yaw angles for each wind turbine, which optimize some performance index while satisfying desired operational constraints.

In support of wind plant control research, our group has developed scaled wind turbines [2] that can be operated in a boundary layer wind tunnel. The wind turbines are governed by their individual controllers, but are also optionally managed in a collective manner by a wind farm super-controller.

A first goal of the present paper is to compare the results of a LES model of the scaled test facility with experimental measurements at different constant-in-time yaw misalignment angles. Various operational conditions are considered, which correspond to different overlaps of the shed

The Science of Making Torque from Wind (TORQUE 2018) IOP Publishing
IOP Conf. Series: Journal of Physics: Conf. Series **1037** (2018) 062007 doi:10.1088/1742-6596/1037/6/062007

wakes with the downstream wind turbines. The present static validation is an intermediate step towards the validation of the dynamic case, where the yaw angles change in time.

A second goal of the paper is to explain a wake interference effect observed in the experiments. Specifically, it appears that one of the downstream wake-shaded turbines exhibits a larger wake deflection than expected by its nominal misalignment angle with the free stream. Numerical simulations are used to show that this phenomenon can be qualitatively explained by the sidewash caused by the shading wake, which has the effect of modifying the flow direction at the downstream turbine rotor disk and of translating its wake path sideways.

2. Experimental setup

A cluster of three wind turbines is operated in the wind tunnel. The wind turbine rotors have a diameter of 1.1 m, and were designed to match the TSR and circulation distribution of a full-scale reference machine, resulting in a realistic wake behavior [2]. Spires are placed at the tunnel inlet and work as turbulence generators. Vortices shed by the spires result in quasi-isotropic turbulence where the wind turbine models are located. The longitudinal distance between each wind turbine is 4D, while the lateral distance is 0.5D. The static experiments are conducted at different yaw settings of the various machines. Figure 1 shows a top view of the wind tunnel when the wind turbines are optimally yawed for overall power capture, which corresponds to 20 deg and 16 deg of the first and second machine, respectively. The optimal yaw angles were determined experimentally. A more detailed description of the experiments is given in Refs. [2,3].

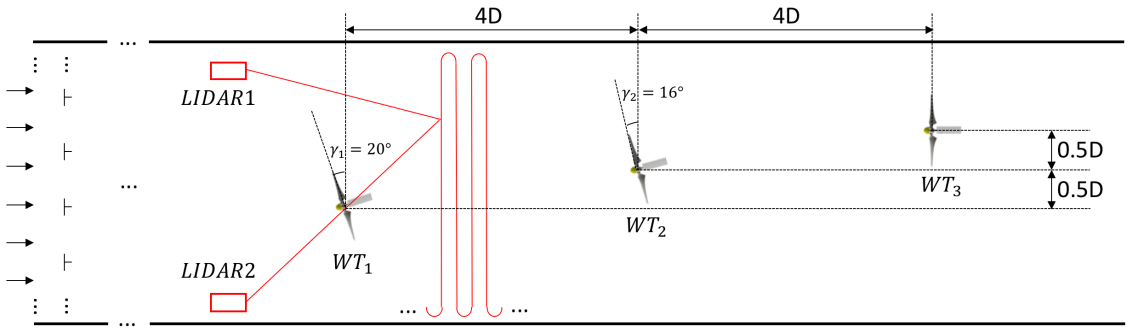

Figure 1: Top view of the wind tunnel experiment: from left to right, chamber inlet, turbulence generating spires, scanning LiDARs, upstream wind turbine WT1, example of LiDAR scanning path, downstream turbine WT2, and downstream turbine WT3.

One of the highlights of the experiment is the measurement of the flow with two scanning LiDARs [3]. The velocity field at a horizontal plane 0.09D above hub height is measured, neglecting the vertical velocity component. The red curve in Fig. 1 depicts the scanning path of the LiDARs, which takes 18.48 sec to be completed. An average flow field is obtained by averaging the LiDAR data over 30 passes [3].

3. Numerical model

The numerical simulation environment is based on the open-source code `Foam-extend-4.0`. The model is based on a finite-volume LES formulation, implemented in the code `SOWFA` [4], coupled with a lifting line model of the blades, whose implementation is based on `FAST v8` [5]. The turbine nacelle and tower are modelled by an immersed boundary method [6]. The airfoil polars are determined by a singular-value-decomposition-based system identification procedure [7]. By

The Science of Making Torque from Wind (TORQUE 2018) IOP Publishing
IOP Conf. Series: Journal of Physics: Conf. Series **1037** (2018) 062007 doi:10.1088/1742-6596/1037/6/062007

this method, the aerodynamic characteristic of the airfoils are obtained using experimental measurements of the rotor thrust and torque at various operating points [2]. This same simulation environment has been previously compared to scaled experimental measurements in Refs. [8–10] in wind aligned conditions. The present paper extends that analysis to yaw misaligned conditions, which are relevant to the problem of wind farm control.

The simulation model includes the wind tunnel walls and the passive generation of turbulence obtained by the use of spires placed at the tunnel inlet. The simulation of the flow around the spires is particularly expensive, as it must faithfully represent the breakdown of the spire-shed vortices into a sheared and turbulent flow. In fact, a high-quality dense mesh —obtained by the mesh generator `ANSYS/ICEM`— is used to resolve the flow around the spires. Since the same turbulent flow can be used for several simulations characterized by different operating conditions of the wind turbines, the overall wind tunnel chamber is split into two separate computational domains. One models the tunnel inlet, the spires and the development of the turbulent flow, up to a distance of 36 m downstream of the inlet. The outflow of this first "precursor" simulation is then used as inflow of a second computational domain, which models the wind turbines and their wake interactions all the way to the tunnel outlet.

The wind turbines are operated in closed-loop in the CFD simulations, using the same controller implemented in the experiments. The controller receives as inputs power demand P_d, measured power P, measured pitch β and measured rotor speed Ω, and it outputs the pitch command β_{cmd} and torque command T_{cmd}. The implementation is based on a standard look-up table for torque and proportional-integral controller for pitch [12].

The inclusion of the turbine controller in the simulations is important for generating realistic solutions. In fact, the turbulent flows in the experiment and simulation can only be similar in terms of average speed, shear and turbulence intensity, but cannot clearly match instantaneously. Therefore, one can not use in the simulations the blade pitch, rotor speed and azimuthal position measured in the experiments. Even the use of constant values of these quantities would lead to discrepancies, as shown later on in this work.

4. Results and analysis

Iso-vorticity surfaces of the precursor and of the wind turbine cluster simulations are visualized together in Fig. 2. The figure shows the generation of large vortical structures by the spires placed at the tunnel inlet. Such structures break down into a sheared and turbulent flow that becomes the inflow of the downstream turbines.

Figure 3 shows the stream-wise velocity field at a horizontal plane 0.09D above hub height. The images on the top report LiDAR measurements, the ones in the center are the corresponding numerical simulations, while the ones in the bottom part show the difference between measurements and simulations. The rotor planes are drawn using thick black lines. Figures to the left correspond to the case of greedy control, in which all turbines point into the wind. Figures to the right correspond to the case where the two upwind machines have been optimally yawed out of the wind to deflect their wakes and reduce the shading of the downstream turbines. For the LiDAR visualizations, fluctuations in the colors are due to data resolution limits, and to the fact that the number of passes was probably not sufficient to completely eliminate the effects of turbulence and wake meandering. For both the greedy and the optimal yaw cases, the figures show a good qualitative accordance between experiments and simulations. A significant wind farm power increase can be achieved by yaw control in this particular turbine layout and operating conditions. In fact, compared with the baseline greedy case, the optimally-yawed turbine cluster produces 17.6% more power.

The Science of Making Torque from Wind (TORQUE 2018) IOP Publishing
IOP Conf. Series: Journal of Physics: Conf. Series **1037** (2018) 062007 doi:10.1088/1742-6596/1037/6/062007

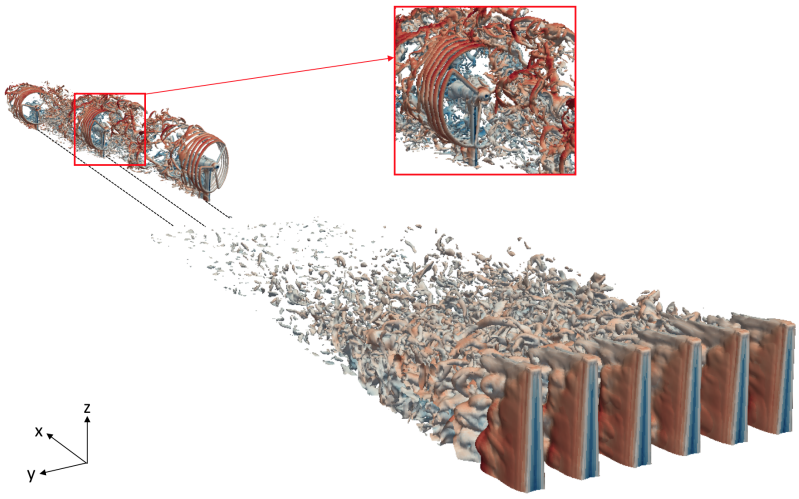

Figure 2: Visualization of iso-vorticity field for the precursor and turbine cluster simulations.

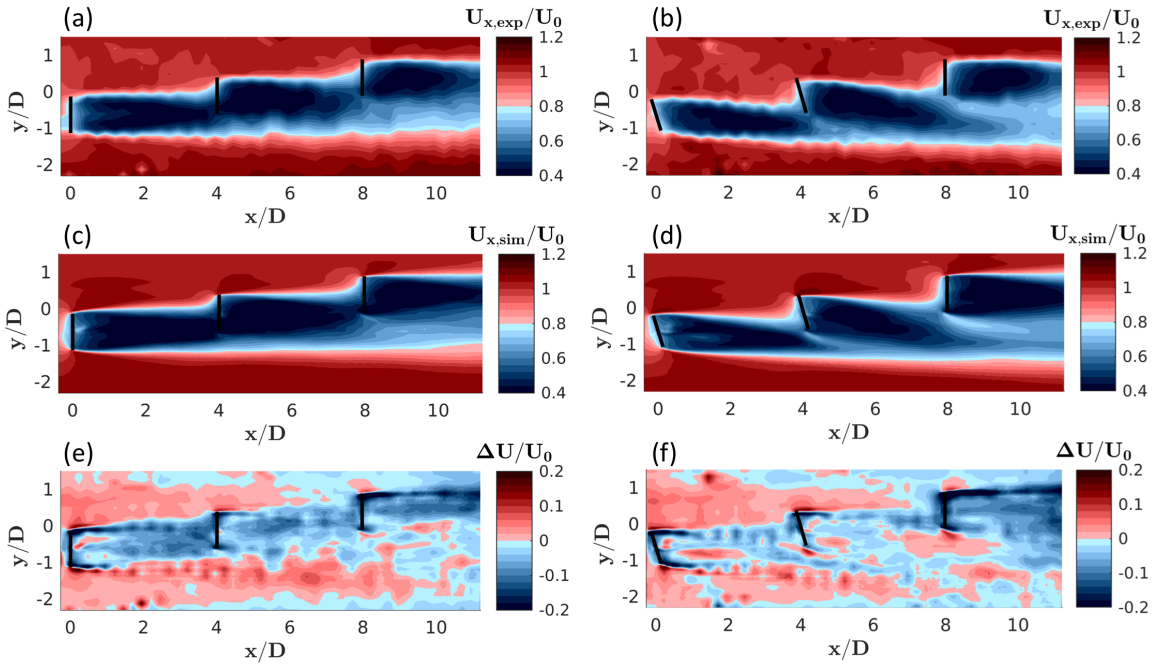

Figure 3: Stream-wise velocity field 0.09D above hub height. (a) Experiment, greedy policy; (b) Experiment, optimal yaw; (c) Simulation, greedy policy; (d) Simulation, optimal yaw; (e) Difference simulation-measurement, greedy policy; (f) Difference simulation-measurement, optimal yaw.

The Science of Making Torque from Wind (TORQUE 2018) IOP Publishing
IOP Conf. Series: Journal of Physics: Conf. Series **1037** (2018) 062007 doi:10.1088/1742-6596/1037/6/062007

For the optimally-yawed case with turbine controllers in the loop, Fig. 4 shows the time histories of mean power $\bar{P}$ and power standard deviation σ_P defined as:

$$\bar{P}_j = \frac{1}{j}\sum_{i=1}^{j} P_i, \tag{1a}$$

$$\sigma_{P_j} = \sqrt{\frac{1}{j}\sum_{i=1}^{j}(P_i - \bar{P}_j)}, \tag{1b}$$

where P_i is the instantaneous power at the ith step. Goal of these plots is to indicate the necessary time horizon over which one should average in order to compute from instantaneous noisy signals converged mean values and standard deviations for quantities of interest. In both experiments and simulations, the heads of the data streams have been removed to eliminate the effects of initial transients. In the experiments, it takes about 120 sec for the statistics to converge, while it appears that the convergence of the same quantities in simulations takes a much shorter time of about 40 sec. This is because the wind tunnel inflow exhibits moderate low frequency fluctuations due to its closed-loop arrangement. These effects are not reproduced by simulations, which only model the tunnel chamber and not the return flow. Due to their large computational cost, simulations were run for a shorter duration than the experiments. Nonetheless, as shown by the figure, this is still enough to allow for the near converge of the statistics of power. A similar behavior was observed for rotor speed and other quantities of interest.

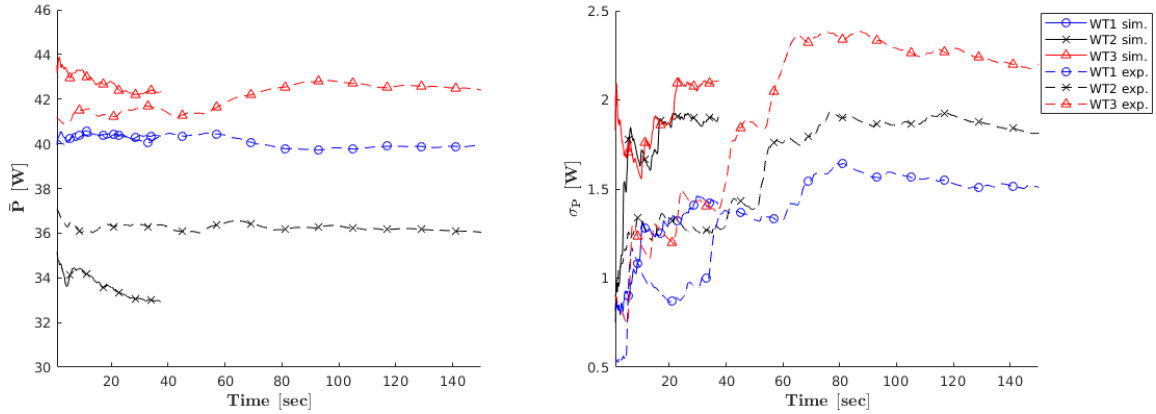

Figure 4: Time histories of mean power $\bar{P}$ and power standard deviation σ_P, indicating that data streams are long enough to compute converged statistics of quantities of interest.

A quantitative comparison between experiments and simulations is obtained by considering wake measurements performed by the scanning LiDARs along sampling lines at various downstream distances, shown in Fig. 5. The sampling lines are orthogonal to the tunnel flow and are located at 0.09D above hub height. The centers of the rotor planes of the three wind turbines are located respectively at 0D, 4D and 8D. Three lines downstream of each machine were measured, resulting in the wake profiles shown in the figure. The top part of the figure reports the greedy case, where all machines point into the wind, while the bottom part of the same figure shows the optimal yaw case.

The Science of Making Torque from Wind (TORQUE 2018) IOP Publishing
IOP Conf. Series: Journal of Physics: Conf. Series **1037** (2018) 062007 doi:10.1088/1742-6596/1037/6/062007

Although the overall accordance between experiments and simulations is good, there are areas where some small discordancies are indeed present. For the greedy case, the wake deficit of the first wind turbine is overestimated at 2D and 3D, although the wake at 1D is very precisely predicted. This implies a non-exact wake recovery, probably due to an underestimated momentum exchange between free stream and wake. In turn, this is probably due to the blade tip vortices [13], possibly because of an insufficiently refined mesh. An additional reason might be due to inaccuracies in the lifting line formulation at the blade tips, both in terms of angle of attack calculation and distribution of the computed aerodynamic forces back onto the CFD grid. The exact determination of the sources of such discrepancies requires further work. The wake deficit 1D downstream of the second wind turbine is slightly overestimated because of the underestimated inflow wind speed. The wake recovery on the upper side of the figure (i.e., to the left when looking downstream towards the wind turbine cluster) is underestimated. On the other hand, it is interesting to observe that the wake is well predicted in the lower side of the figure because that region interacts with the wake of the upstream wind turbine. Therefore, at 6 and 7D the wake deficit is only underestimated in the left part of the wake. A similar analysis holds for the wake of the third wind turbine.

For the optimally-yawed case, the wakes of the first and second wind turbines are very well predicted, with a very good match between experiments and numerical results. When the turbines are yawed, the inclination of the rotor thrust with respect to the incoming flow induces the generation of two counter rotating vortices in the near wake, that interact with the wake swirling caused by the rotor torque reaction onto the flow. The resulting complex flow pattern contributes to the momentum exchange between free stream and wake, reducing the role of the tip vortices in this process. Because of this, a better match between experiment and simulation is observed in the present case. As expected, since the third wind turbine is not yawed, wake recovery is again slightly underestimated.

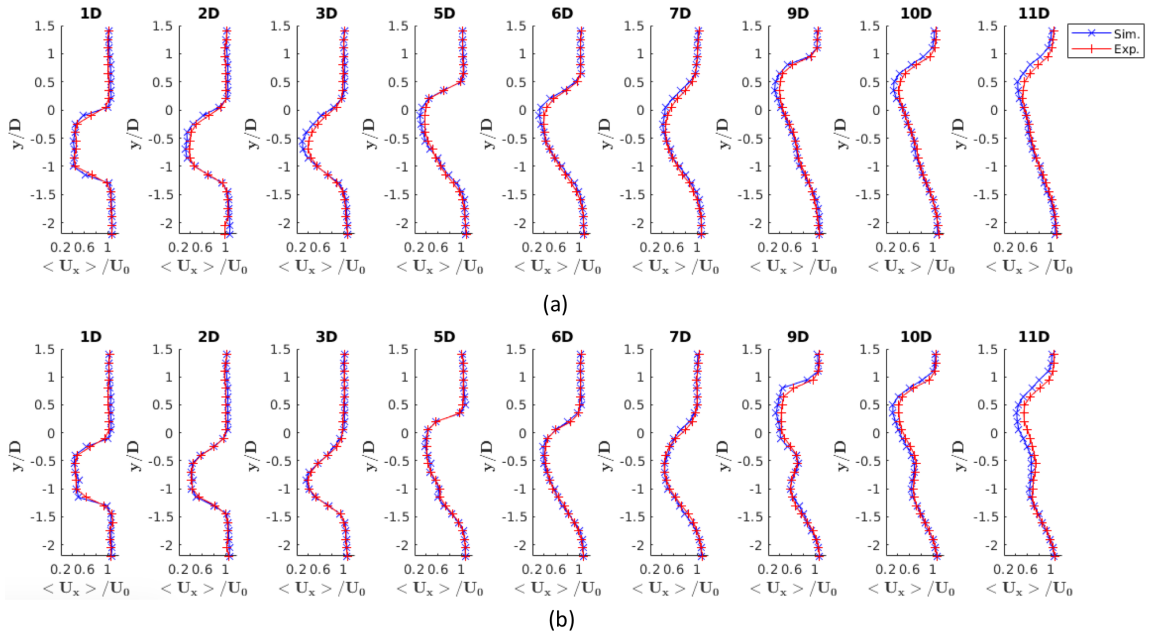

Figure 5: Wake profiles for the greedy (a) and optimally-yawed (b) cases.

Figure 6 shows the time histories of turbine speed and power for the simulations and

The Science of Making Torque from Wind (TORQUE 2018) IOP Publishing
IOP Conf. Series: Journal of Physics: Conf. Series **1037** (2018) 062007 doi:10.1088/1742-6596/1037/6/062007

experiments in the optimally-yawed case. The figures on the left show the case of the simulation with the controller in the loop; the central plots correspond to the case when the controller is off, and the rotor speed of each machine is constant in time and equal to the average of the experimentally measured one; finally, the plot to the right shows the experimental case. The case with the controller in the loop exhibits a behavior similar to the experimental one, although clearly the instantaneous values cannot match as the two flows are only statistically similar. On the other hand, when the rotors are driven at constant speed, power shows significant and non-physical fluctuations.

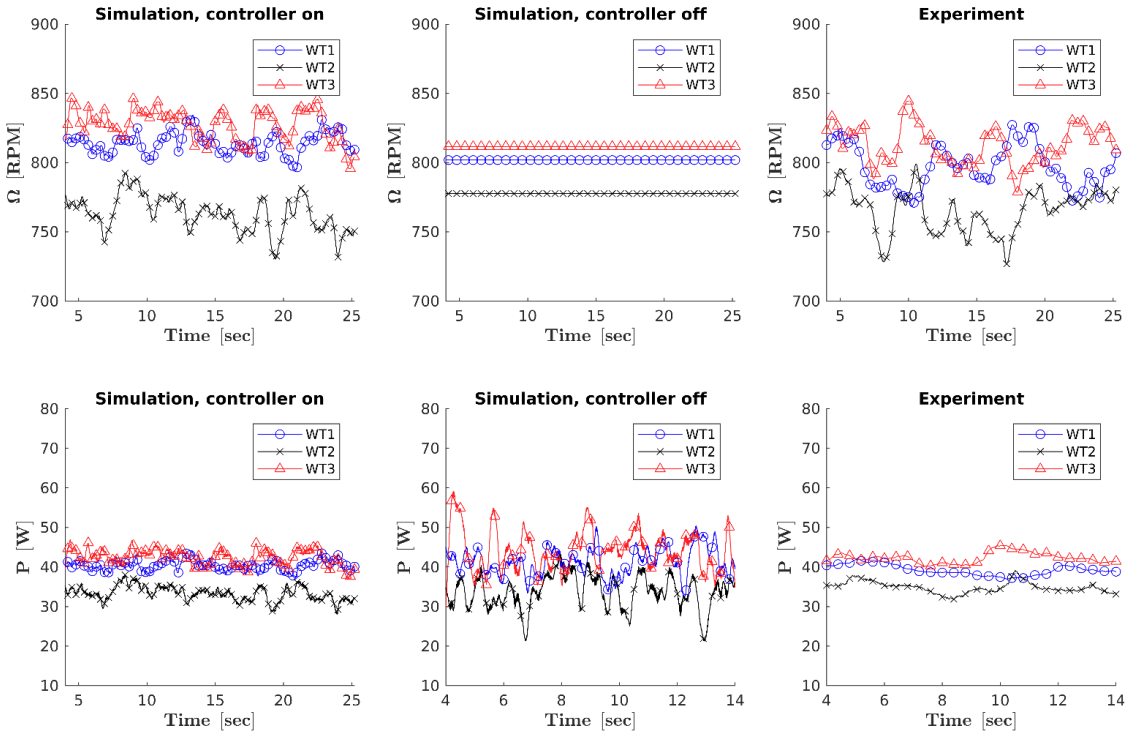

Figure 6: Speed and power time histories for the optimally-yawed case.

For the same three cases (controller in the loop, controller off, and experiment), Table 1 shows the time-averaged means (noted $\overline{(\cdot)}$) and non-dimensional standard deviations σ of rotor speed Ω and power P. Based on the results of Fig. 4, means and standard deviations were computed over 120 sec for the experiments, and over 40 sec for the simulations, which is enough to ensure convergence. The relative error in the average rotor speed for the three turbines is smaller than 2%. Speed variations in the simulations are underestimated, probably because of the assumed constant inflow velocity of the wind tunnel. The average power is predicted quite accurately for both simulations, with and without turbine controllers in the loop. However, as expected, the power standard deviation is much higher when the machines are driven at constant rotor speed.

Table 2 shows the results for the greedy case. The average rotor speed of the second wind turbine is slightly (5%) underestimated because of its underestimated inflow speed. The average speed of the other two wind turbines is very precisely predicted. Speed and power standard deviations for the first wind turbine are underestimated because of the assumption of a constant wind tunnel inflow. The standard deviations of the second and third wind turbines are relatively well predicted because they are more affected by upstream wakes rather than wind tunnel free

The Science of Making Torque from Wind (TORQUE 2018) IOP Publishing
IOP Conf. Series: Journal of Physics: Conf. Series **1037** (2018) 062007 doi:10.1088/1742-6596/1037/6/062007

stream. For average power, the accordance is in general good, except for the second wind turbine. This situation is visually summarized by the histograms of normalized power shown in Fig. 7 for the various cases and turbines.

Wind turbine	WT1			WT2			WT3		
Case	on	off	exp	on	off	exp	on	off	exp
$\bar{\Omega}$ [RPM]	814	802	802	764	778	778	828	812	812
$\sigma_\Omega/\bar{\Omega}$ [%]	0.9	0	2.1	1.7	0	2.5	1.6	0	2.5
$\bar{P}$ [W]	40.4	41.0	40.5	32.9	33.8	36.4	42.5	43.2	42.0
$\sigma_P/\bar{P}$ [%]	3.2	8.5	4.0	5.5	13.6	5.5	4.7	12.5	4.5

Table 1: Power and speed comparisons for the optimally-yawed case.

Wind turbine	WT1			WT2			WT3		
Case	on	off	exp	on	off	exp	on	off	exp
$\bar{\Omega}$ [RPM]	840	830	830	672	710	710	734	736	736
$\sigma_\Omega/\bar{\Omega}$ [%]	0.5	0	2.0	1.7	0	2.7	1.9	0	3.0
$\bar{P}$ [W]	44.5	45.7	44.3	22.8	21.5	26.5	29.5	29.1	30.3
$\sigma_P/\bar{P}$ [%]	1.8	9.0	3.1	6.6	28.8	7.1	7.1	26.8	6.9

Table 2: Power and speed comparisons for the greedy case.

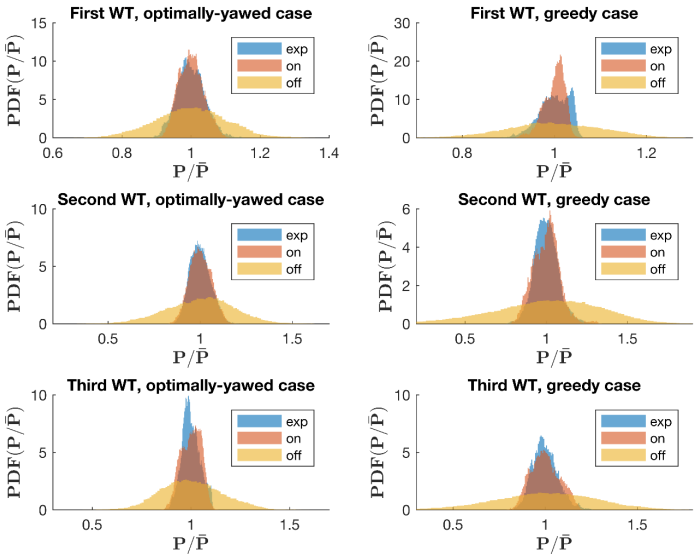

Figure 7: Wind turbine power histogram for simulations and experiments.

The Science of Making Torque from Wind (TORQUE 2018) IOP Publishing
IOP Conf. Series: Journal of Physics: Conf. Series **1037** (2018) 062007 doi:10.1088/1742-6596/1037/6/062007

5. Effects of wake shading on wake deflection

An interesting phenomenon can be observed in Fig. 3 for both the experimental and the simulation results. In fact, for the optimally-yawed case, it appears that the wake of the second wind turbine is more deflected than the wake of first machine, although the yaw angle of the second (16 deg) is smaller than the one of the first (20 deg).

This phenomenon is caused by the changed inflow conditions for the second shaded wind turbine, caused by the presence of the wake shed by the upstream machine. To better illustrate this phenomenon, a simulation was run with one single wind turbine operating exactly in the same conditions of the first upstream machine (the effects of the two downstream machines on the inflow of the first one being negligible). For this single turbine simulation, Fig. 8 shows the stream-wise and lateral velocity components, respectively to the left and to the right of the picture. Although the second and third turbines are not present in this simulation, their rotor planes are still plotted in dotted lines to indicate their location within the cluster.

When looking at the stream-wise velocity component, it appears that the wake of the first turbine has only a modest overlap with the rotor disk of the second machine. On the other hand, the analysis of the lateral velocity component reveals a very different situation. In fact, the rotor disk of the second turbine is immersed in a region of significant sidewash caused by the wake of the upstream machine. This sidewash component, combined with the incoming free stream, generates a tilting of the local wind vector of about 3.6 deg. Therefore, while the misalignment angle of the second wind turbine with the free stream is nominally equal to 16 deg, its *actual* misalignment with the *local* wind vector is about 19.6 deg. This value is quite close to the misalignment angle of the first wind turbine, which is equal to 20 deg.

Therefore, the additional deflection of the wake observed for the second machine can be justified based on the sidewash velocity of the impinging wake. Indeed, this additional lateral wind component causes two effects: a) it tilts the local wind vector, which has the effect of modifying the actual misalignment angle of the turbine, and b) it carries the wake shed by the second machine sideways, further incrementing its deflection. In present engineering wake models, little attention has been paid so far to the changed ambient velocity outside of the central wake region. Indeed, according to the authors' knowledge, published engineering wake models only represent what happens inside the wake, but not outside of it. However, the current results seem to indicate that the induced lateral velocity outside of a deflected wake should be taken into due account for an accurate prediction of the wake path of shaded wind turbines.

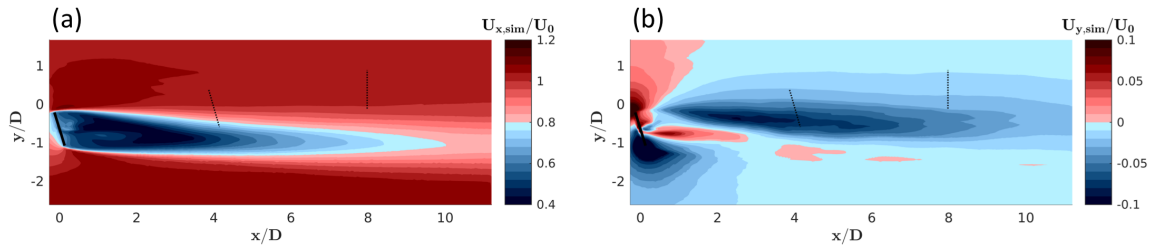

Figure 8: Wake of a single yawed wind turbine: (a) stream-wise velocity (b) lateral velocity. Dashed lines indicate position and orientation of the downstream machines in the cluster. Negative values of the lateral velocity indicate a velocity directed downwards in the picture.

6. Conclusion

In this paper, numerical simulations were performed for scaled waked wind turbines at given fixed yaw settings. The flow within the scaled wind turbine cluster and the operational response

of the machines show a good match between simulations and measurements. In particular, the simulation model appears to be capable of predicting with good accuracy the wake behavior and power output of the various wind turbines. The tool appears to be mature enough to consider the dynamic case where yaw angles change in time, which will be the subject of future work.

Besides the validation of the numerical method, this paper also exploits the numerical model to interpret and explain wake interference effects. Specifically, it appears that the sidewash caused around a deflected wake has non-negligible effects on the path of downstream wakes, effects that are currently not accounted for in engineering wake models.

7. Acknowledgements

This work has been supported by the CL-WINDCON project, which receives funding from the European Union Horizon 2020 research and innovation program under grant agreement No. 727477. The authors also express their appreciation to the Leibniz Supercomputing Centre (LRZ) for providing access and computing time on the SuperMUC Petascale System.

References

[1] Churchfield M J, Fleming P, Bulder B, et al. 2015 *Wind Turbine Wake-Redirection Control at the Fishermen's Atlantic City Windfarm* Preprint OTC-25644-MS
[2] Campagnolo F, et al. 2016 Wind tunnel testing of a closed-loop wake deflection controller for wind farm power maximization *J. Phys. Conf. Seri.* **753**(3) 032006
[3] Dooren M F, Campagnolo F, Sjholm M, Angelou N, Mikkelsen T and Khn M, 2017 Demonstration and uncertainty analysis of synchronised scanning LiDAR measurements of 2-D velocity fields in a boundary-layer wind tunnel *Wind Energy Science* **2**(1) 329
[4] Fleming, Paul A, et al. 2014 Evaluating techniques for redirecting turbine wakes using SOWFA *Renewable Energy* **70** 211–218
[5] Guntur S, Jonkman J, et al. 2016 FAST v8 verification and validation for a MW-scale Wind turbine with aeroelastically tailored blades *Wind Energy Symp.* (San Diego, USA) p. 1008
[6] Peskin, Charles S. 2002 The immersed boundary method *Acta numerica* **11** 479–517.
[7] Bottasso C L, Stefano C, et al. 2014 Calibration of wind turbine lifting line models from rotor loads *J. Wind Engineering and Industrial Aerodynamics* **124** 29-45.
[8] Wang J, Mclean D, et al. 2017 Large-eddy simulation of waked turbines in a scaled wind farm facility *J. Phys. Conf. Seri.* **854**(1) 012047
[9] Wang J, Bottasso C L, et al. 2016 Wake redirection: comparison of analytical, numerical and experimental models *J. Physics: Conf. Seri.* **753**(3) 032064
[10] Wang, J., et al. 2017 *Numerical and experimental study of wake redirection techniques in a boundary layer wind tunnel* J. of Phys. Conf. Seri. **854**(1) 012048
[11] Foti D, Yang X, Campagnolo F, et al. Wake meandering of a model wind turbine operating in two different regimes *Physical Review Fluids* under review
[12] Bottasso C L, Campagnolo F, et al. 2014 Wind tunnel testing of scaled wind turbine models: beyond aerodynamics *J. Wind Engineering and Industrial Aerodynamics* **127** 11–28
[13] Wang J, Chengyu W, Campagnolo F and Bottasso C L 2018 A large-eddy simulation approach for wind turbine wakes and its verification with wind tunnel measurements *Wind Energy Science* under review

The Science of Making Torque from Wind (TORQUE 2020) IOP Publishing
Journal of Physics: Conference Series **1618** (2020) 062041 doi:10.1088/1742-6596/1618/6/062041

Code-to-code-to-experiment validation of LES-ALM wind farm simulators

C Wang[1], A Muñoz-Simón[2], G Deskos[3], S Laizet[2], R Palacios[2], F Campagnolo[1], C L Bottasso[1]

[1] Wind Energy Institute, Technische Universität München, Boltzmannstraße 15, D-85748 Garching bei München, Germany
[2] Department of Aeronautics, Imperial College London, SW7 2AZ, London, UK
[3] National Renewable Energy Laboratory, CO 80401, Golden, USA

E-mail: carlo.bottasso@tum.de

Abstract.
The aim of this work is to present a detailed code-to-code comparison of two Large-Eddy Simulation (LES) solvers. Corresponding experimental measurements are used as a reference to validate the quality of the CFD simulations. The comparison highlights the effects of solver order on the solutions, and it tries to answer the question of whether a high order solver is necessary to capture the main characteristics of a wind farm. Both solvers were used on different grids to study their convergence behavior. While both solvers show a good match with experimental measurements, it appears that the low order solver is more accurate and substantially cheaper in terms of computational cost.

1. Introduction

Large-Eddy Simulation (LES) is actively researched and used because it has the potential to explain wind farm phenomena and to predict effects that enable improved design and operation [1]. However, notwithstanding the success of LES, there is still only a limited understanding of the actual accuracy of such numerical methods in representing the complex physical processes that govern wake-turbine interactions. The present paper presents a code-to-code comparison of two state-of-the-art LES-ALM (Actuator Line Method) codes with significantly different features. Numerical results of both solvers for different mesh resolutions are compared in this work. Corresponding experiments are used to validate the numerical results. The objective is to evaluate the accuracy and uncertainty of LES for wind farm flows and possibly obtain indications for the future evolution of the numerical procedures. While the experiments provide benchmarks of integral quantities like power, thrust and mean wake profile, the code-to-code comparison can also illustrate differences of other quantities like Reynolds shear stresses.

2. Methodology

2.1. Experimental setup

Three laterally-misaligned scaled wind turbines of the G1 type [2], with a rotor diameter of 1.1 m, were operated in the boundary layer wind tunnel of the Politecnico di Milano, which

The Science of Making Torque from Wind (TORQUE 2020) IOP Publishing
Journal of Physics: Conference Series **1618** (2020) 062041 doi:10.1088/1742-6596/1618/6/062041

has a cross-section of 3.8 × 13.8 m^2 and a length of 36 m. The longitudinal distance between each wind turbine was 4D, while the lateral distance was 0.5D, resulting in a partial wake impingement on the two downstream turbines. An inflow condition with 5% turbulence intensity was generated passively with spires positioned close to the inlet of the wind tunnel. All wind turbines were operated in region II with constant pitch and were governed by a standard look-up-table generator torque controller. First, a greedy case was considered, in which the yaw angles of all turbines were set to zero. Then, a yaw misalignment case was tested, in which the yaw angles of the three turbines were set to optimal values with respect to total wind farm power output. In all considered conditions, the power and thrust of each turbine were measured. Additionally, two scanning LiDARs measured the horizontal mean wake profile of all turbines on a horizontal slice 0.1D above hub height [3]. A previous code-to-experiment validation with the same measurement data has been reported in [4].

2.2. Numerical models

The TUM solver [1] is based on OpenFoam [6] and SOWFA [7], and it is described in [1]. The ICL Winc3D solver is described in [5]. Table 1 summarizes the differences between the two solvers. LES with constant Smagorinsky model and the same Smagorinsky constant of 0.16 has been used for both codes.

Item	TUM	ICL
Spatial discretization	Finite volume	Compact finite difference scheme
Time marching scheme	Backward Euler scheme	Third order Runge-Kutta scheme
Pressure-velocity decoupling	Rhie-Chow interpolation	Half-staggered grid
Continuity enforcement	Pressure correction	Pressure correction
Turbine model	ALM, FAST	In-house ALM code
Mesh	Cartesian mesh with refinement	Uniform Cartesian mesh
Spatial convergence order	Second order	Sixth order
Turbulence model	Constant Smagorinsky	Constant Smagorinsky
LES filter	Implicit	Explicit

Table 1: Comparison of the main characteristics of the two codes.

One of the critical differences between the two codes is the different temporal and spatial discretizations. The backward Euler time marching scheme of the TUM code has a lower order compared to the Runge-Kutta scheme used by ICL. The second-order finite volume spatial discretization method adopted by the TUM code also has a lower order compared to the sixth order compact finite difference scheme used by ICL [5]. The ICL code also has better scalability than OpenFOAM. In contrast, the finite volume method of the TUM code allows for mesh refinement, while the ICL code is limited to a uniform Cartesian mesh because of its spectral formulation. The TUM code used fine meshes only at necessary locations and a coarse mesh for other regions of the domain, while the ICL code used the same fine mesh for the whole computational domain. This results in significantly different cell numbers and computational costs. To avoid staggered solutions, the TUM code adopts the Rhie-Chow interpolation method [8], while the ICL code uses a half-staggered grid. The ALM approach has been used by both codes to model the rotor.

The Science of Making Torque from Wind (TORQUE 2020) IOP Publishing
Journal of Physics: Conference Series **1618** (2020) 062041 doi:10.1088/1742-6596/1618/6/062041

2.3. Simulation setup

In contrast to the quite different numerical schemes, the inputs to both codes are exactly the same, including all the turbine setup, the inflow data, initial conditions, boundary conditions, smearing length scales ϵ and time steps for each mesh resolution. To guarantee the same rotor operating condition, a prescribed constant rotor speed and blade pitch angle were used. The values of rotor speed are identical to the mean values measured in the experiments. In reality, the rotor speed oscillates in response to the turbulent fluctuations in the experiments. However, specifying an average rotor speed is sufficiently accurate to capture mean quantities, as shown in previous work [4]. Furthermore, to avoid subtle differences that could be caused by the models of the nacelle, tower and tip and hub loss models, all these features were switched off. The mesh resolutions were the same upstream, downstream and around all rotors.

3. Results

3.1. Impact of mesh refinement

The impact of mesh refinement on the inflow should be quantified since turbine power is very sensitive to inflow conditions. Figure 1 shows the inflow profile and turbulence intensity along a horizontal line slightly above hub-height and 2.55D in front of the first rotor. This location is about 1.4 D behind the inlet plane of the domain. The vertical dashed lines in both plots of Fig. 1 indicate the bounds of mesh refinement used for the TUM code. Within the bounds, the grid size is 2 cm (55 cells per rotor diameter); outside the bounds, the grid size is 4 cm. This results in a total number of cells of 10.3 million, which is significantly less than the 111 million cells used by the ICL code for a globally uniform Cartesian mesh. The values of mean velocity and turbulence intensity show little difference within the refinement bounds, while the turbulence intensity predicted by the TUM code is slightly lower than that of the ICL code because of the coarse mesh outside of the bounds. A drop of turbulence intensity due to a coarser mesh is an expected effect, while the good match in the fine mesh region indicates little adverse impact of mesh refinement on the results.

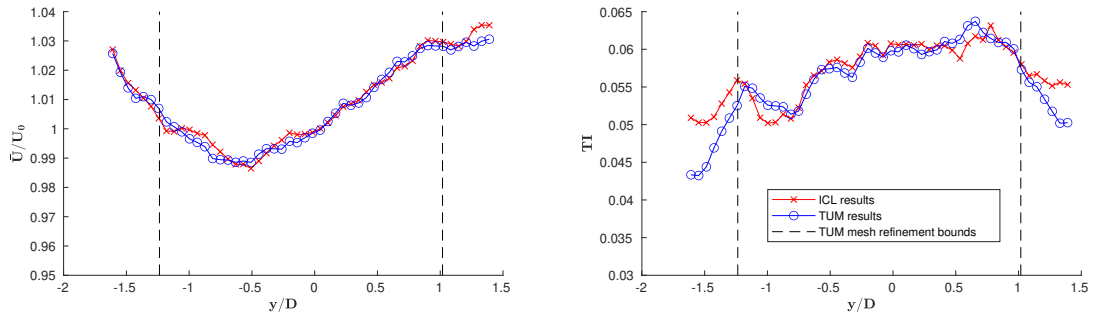

Figure 1: Lateral inflow profile and turbulence intensity along a horizontal line 2.55D in front of the first rotor.

3.2. Comparison and convergence of mean quantities

Figure 2 shows the mean velocity fields slightly above hub-height measured in the experiments and simulated by the codes with a 2 cm grid resolution. Table 2 shows the mean power and thrust and the relative errors of both codes in percentage with respect to the experiments for different grid resolutions.

The Science of Making Torque from Wind (TORQUE 2020) IOP Publishing
Journal of Physics: Conference Series **1618** (2020) 062041 doi:10.1088/1742-6596/1618/6/062041

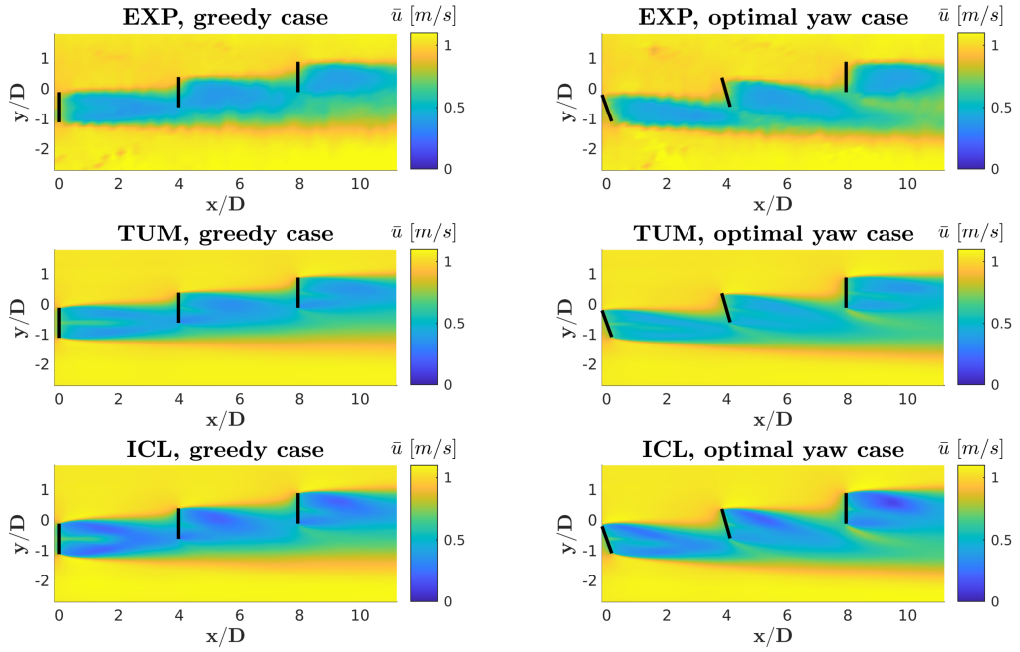

Figure 2: Top view of the mean velocity fields on a plane 0.1D above hub height. The black lines represent the rotor planes. The grid resolution is 2 cm.

Mesh (cm)		4		3	2		1.5	-
Time step (ms)		1.000		0.750	0.500		0.375	
ϵ (cm)		6		5	4		3	
Case		TUM	ICL	TUM	TUM	ICL	TUM	EXP
$\gamma_1 = 20°$ $\gamma_2 = 16°$ $\gamma_3 = 0°$	$\bar{P}_1$	+1.2%	0.0%	+0.5%	+0.7%	-0.7%	-1.7%	40.4 W
	$\bar{P}_2$	-25.5%	-20.6%	-16.5%	-6.6%	-18.4%	-8.2%	36.4 W
	$\bar{P}_3$	-21.9%	-16.6%	-15.9%	-4.6%	-17.0%	-7.1%	45.2 W
	$\bar{T}_1$	-7.2%	-6.6%	-7.2%	-7.2%	-6.6%	-8.4%	16.6 N
	$\bar{T}_2$	-21.9%	-18.7%	-17.4%	-13.5%	-18.7%	-14.2 %	15.5 N
	$\bar{T}_3$	-8.8%	-5.7%	-5.0%	+0.6%	-5.7%	-0.6%	15.9 N
$\gamma_1 = 0°$ $\gamma_2 = 0°$ $\gamma_3 = 0°$	$\bar{P}_1$	+1.1%	-1.4%	+1.1%	0.5%	-2.3%	-2.0%	44.3 W
	$\bar{P}_2$	-27.9%	-23.4%	-21.5%	-10.9%	-24.9%	-12.1%	26.5 W
	$\bar{P}_3$	-16.5%	-12.2%	-10.2%	-1.0%	-11.2%	-3.6%	30.3 W
	$\bar{T}_1$	-4.5%	-4.0%	-4.5%	-4.5%	-4.5%	-5.1%	17.6 N
	$\bar{T}_2$	-23.5%	-22.1%	-20.6%	-16.4%	-23.0%	-17.2 %	12.2 N
	$\bar{T}_3$	-11.8%	-11.0%	-9.4%	-6.3%	-10.2%	-7.1 %	12.7 N

Table 2: Grid convergence and comparisons among the two codes and measurements. Percentage errors are computed with respect to the experimental results.

The Science of Making Torque from Wind (TORQUE 2020) IOP Publishing
Journal of Physics: Conference Series **1618** (2020) 062041 doi:10.1088/1742-6596/1618/6/062041

Figure 2 shows that the expansion, deflection and recovery of the wakes are captured by both codes, although the ICL one somewhat underestimates wake speed. While the TUM code was used on four different meshes, the ICL code was run only on two of them. The time step is strictly proportional to the mesh size, giving almost the same CFL number for all simulations. The basic uniform Gaussian body force projection method [10] was used for both solvers. The projection parameter ϵ was chosen to match the power of the first turbine. As ϵ does not exactly scale with grid size Δ, the ratio ϵ/Δ is between 1.5 and 2 for all cases.

As the grid is refined, the errors of the TUM code drop significantly. Differences between the results on the 2 cm and 1.5 cm grids are small enough to indicate a final convergence of the solution. In contrast, the ICL code, thanks to its higher order discretization, converges much earlier, since the differences between results on the 4 cm and 2 cm grids are already very small.

For a grid resolution of 2 cm, both the TUM and ICL codes predict the power and thrust of the first turbine with almost the same accuracy for both the greedy and the optimal yaw cases. However, the TUM code moderately underestimates the power and thrust of the two downstream turbines, while the ICL code significantly underestimates these quantities. The larger error of the ICL code is expected, since Fig. 2 already shows that the wakes computed by this solver are too slow. Note that all simulations were conducted without nacelle and tower models. On the one hand, the wakes shed by the tower and nacelle decelerate the flow in the near wake region, but on the other hand, the stronger turbulence intensity caused by the wakes of nacelle and tower enhances wake recovery. These two phenomena have opposite effects on the wake. As indicated in [11], ambient turbulence intensity also contributes to making one prevail over the other. For the 5% turbulence intensity considered here, the two effects almost cancel each other. Therefore, the errors of the 2 cm grid resolution case are close to the errors reported in [4], in which CFD-ALM simulations were conducted with nacelle and tower models for the same scenario as in this paper.

3.3. Comparison of wake and Reynolds shear stresses

Figure 3 shows the mean velocity and two components of the Reynolds shear stress $\overline{u'u'}$ and $\overline{u'v'}$ for the optimal yaw case, while Fig. 4 shows the same quantities for the greedy case. Data has been sampled on nine horizontal crossflow lines 0.1D above hub-height. Each column of the figure corresponds to different longitudinal downstream distances as in Fig.2. The positions of the three turbines are 0D, 4D, and 8D, so there are three sample lines 1D, 2D and 3D behind each turbine. The quantity $\overline{u'u'}$ is the square of turbulence intensity along the longitudinal direction, and $\overline{u'v'}$ reflects the lateral turbulent flux that drives wake recovery.

A high-velocity region is visible behind the center of each rotor, since there is no nacelle model. Except for this difference, the wakes simulated by the TUM code have a good match with the experiments from 1D to 10D. However, the wakes at 11D are significantly slower than the measured ones, for both the optimal yaw and the greedy cases. Consistently with the observation from Fig. 2, the near wakes simulated by the ICL code are slower than the experiments. The situation improves for the far wakes (3D, 7D), although the flow speed is still slower than for the TUM code and the experiments, which explains the larger power underestimation shown in Table 2. The Reynolds shear stress $\overline{u'u'}$ simulated by the ICL code is significantly higher than for the TUM code, which indicates a stronger turbulence intensity. Similarly, $\overline{u'v'}$ computed by the ICL code is moderately higher than for the TUM code in absolute value terms. Both components indicate a stronger wake recovery for the ICL code, which is consistent with the observed wake characteristics. Although experiments and simulations are both subject to errors, the shapes of the curves shown in Fig. 4 and Fig. 3 are very similar and the differences of various physical quantities are within an acceptable range. The wake recovery is simulated better by the TUM code probably because of the Smagorinsky constant, since its value has been calibrated for second order schemes.

The Science of Making Torque from Wind (TORQUE 2020) IOP Publishing
Journal of Physics: Conference Series **1618** (2020) 062041 doi:10.1088/1742-6596/1618/6/062041

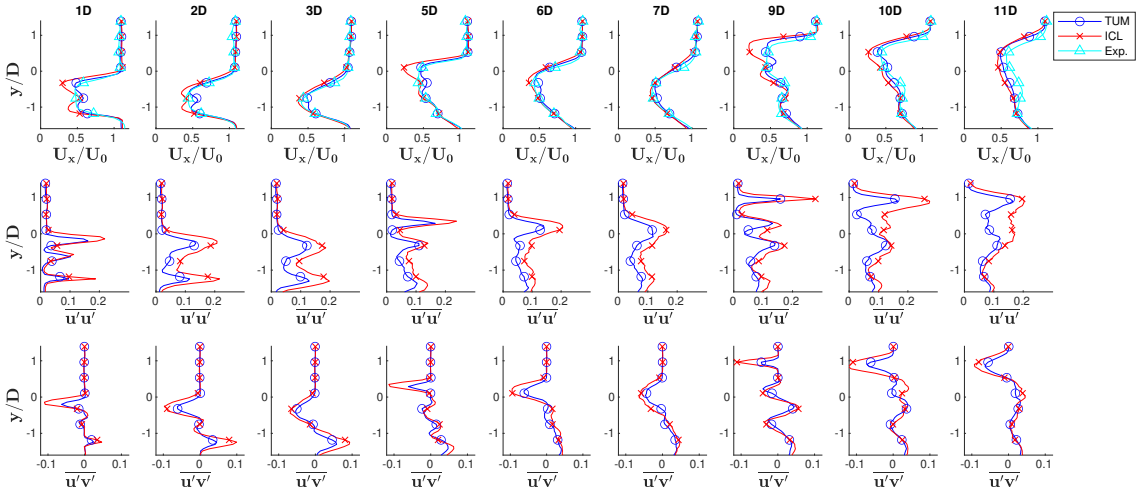

Figure 3: Wake profiles slightly above hub-height at three downstream stations behind each turbine for the optimal yaw case.

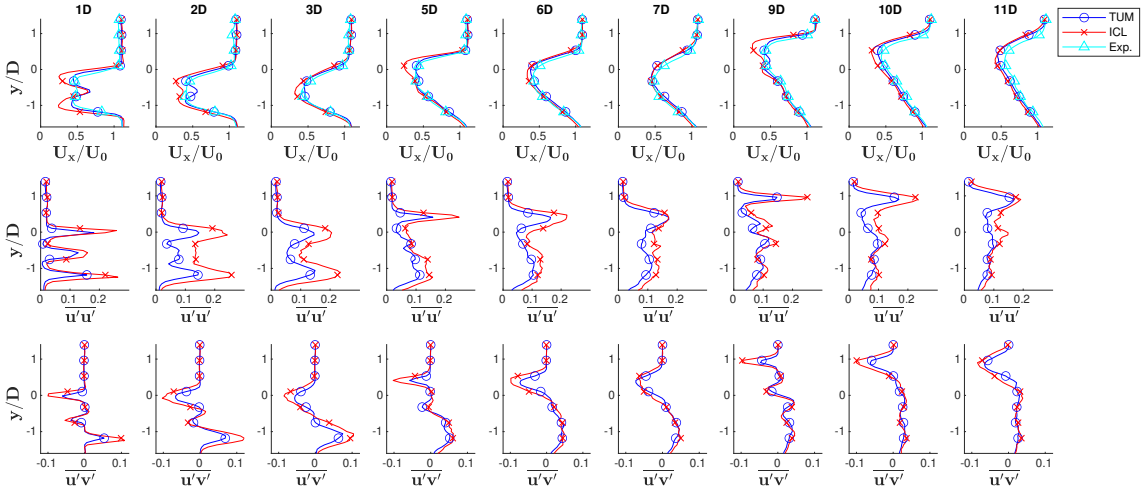

Figure 4: Wake profiles slightly above hub-height at three downstream stations behind each turbine for the greedy case.

Useful information can be extracted from the differences. First, the excessively slow near wake of the ICL code indicates that the axial induction factor is overestimated; in comparison, the TUM code seems to better resolve this quantity. Second, the higher-order scheme of the ICL code predicts stronger Reynolds shear stresses because it is less dissipative. However, it appears that wake recovery in this case is significantly quicker than in the experiment, which partially offsets the overestimated axial induction factor. In both simulation cases, the wake recovery of the first and second turbines are closer to the experiments for the TUM code, while the wake of the third turbine recovers too slowly. This indicates that the TUM second order scheme is slightly over-dissipative and the ICL sixth order scheme is moderately under-dissipative.

The Science of Making Torque from Wind (TORQUE 2020) IOP Publishing
Journal of Physics: Conference Series **1618** (2020) 062041 doi:10.1088/1742-6596/1618/6/062041

3.4. Turbulence spectra and autocorrelation

The turbulence spectrum and autocorrelation of the longitudinal velocity component were computed at a number of points in the wakes of the turbines. The match of these two quantities between the two codes is very good for all considered points. As a representative example, Fig. 5 shows the spectra and autocorrelations at a point 1D downstream of the center of the second rotor for the greedy case. The corresponding simulations have a grid resolution of 2 cm. A linear decay slope of -5/3 can be seen in both spectra in the inertial range. The TUM code predicts lower energy compared to the ICL code for most frequencies, which is consistent with the lower $\overline{u'u'}$ shown in Fig. 4. The autocorrelation curves of TUM and ICL have a good match for both mesh resolutions, thus giving a very similar integral time scale.

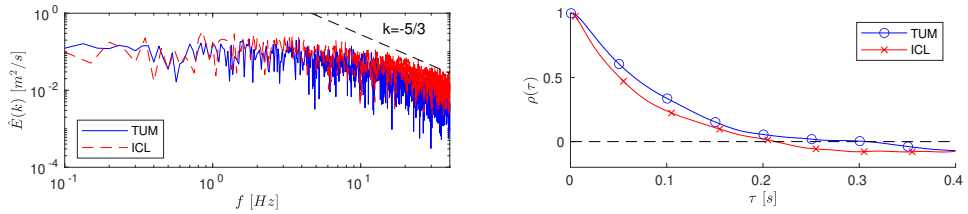

Figure 5: Turbulence spectra and autocorrelation of the longitudinal velocity component.

3.5. Computational efficiency

Table 3 shows a comparison between computation efficiency between the two codes for a grid size of 2 cm. For both codes, the number of cells N_c, the time consumption per time step Δt, the number of processors used N_p and the High Performance Conjugate Gradients (HPCG) benchmark [12] are listed. The last column of the table, $N_p N_s \Delta t / N_c$, is an estimation of the number of floating-point operations per time step per cell, where N_s is the number of floating point operations of the processor per second. This value is slightly higher for the ICL code, which makes intuitive sense because there is a computational cost to implement a high order scheme.

Code	Number of cells N_c	Time per time step Δt (s)	Number of processors N_p	Cluster HPCG N_s (GFlop/s)	$\frac{N_p N_s \Delta t}{N_c}$ (Flop)
TUM	10.3×10^6	1.789	192	0.680	2.27×10^4
ICL	111×10^6	2.085	2208	0.684	2.84×10^4

Table 3: Comparison of the computational efficiency of the TUM and ICL code

4. Conclusions

A code-to-code-to-experiment comparison has been conducted for the two LES-ALM codes and wind tunnel experiments of three wake-interacting wind turbines. The main difference between the two codes is the discretization scheme (with its implications on the grid), which is of the second and sixth order, respectively. Both codes are able to simulate this small wind farm with reasonable accuracy. A grid convergence study shows that the higher order scheme converges at a coarser mesh resolution, as expected. The comparison of power, thrust, mean wake profiles, Reynolds shear stresses, flow spectra and velocity autocorrelations show a high level of similarity

between the two codes. The sixth order scheme is moderately under-dissipative, while the second order scheme is slightly over-dissipative. The second order scheme has a better match with the experiments and also has a much lower computational cost. This indicates that the second order CFD is a good choice for wind energy applications. The reasons for the better matching of the lower order scheme might be due to the calibration of the Smagorinsky constant, which was set to 0.16 for both codes in this work. It is possible that this constant should be recalibrated for the high order spectral method. Future work will try to clarify whether this is indeed the case, or whether other reasons can explain the better results of the lower order scheme.

5. Acknowledgements

This work is supported by the TUM Global Incentive Fund 2019 and Imperial-Technische Universität München Collaboration Fund. This work has also been partially supported at TUM by the CL-WINDCON project, which receives funding from the European Union Horizon 2020 research and innovation program under grant agreement No. 727477. This research has received funding at ICL from the European Unions Horizon 2020 research and innovation program under the Marie Sklodowska-Curie grant agreement No. 765579 (CONFLEX project). The TUM authors express their appreciation to the Leibniz Supercomputing Centre (LRZ) for providing access and computing time on the SuperMUC Petascale System. The authors would like to thank the UK turbulence consortium (grant number EP/R029321/1) for the computational time on the UK Supercomputing facility ARCHER.

References

[1] Wang J et al. 2019 Wake behavior and control: comparison of LES simulations and wind tunnel measurements *Wind Energy Sci.* **4**(1) 71-88
[2] Campagnolo F et al. 2016 Wind tunnel testing of a closed-loop wake deflection controller for wind farm power maximization *J. Phys. Conf. Seri.* **753**(3) 032006
[3] Dooren M F et al. 2017 Demonstration and uncertainty analysis of synchronised scanning LiDAR measurements of 2-D velocity fields in a boundary-layer wind tunnel Wind Energy Sci. **2** 329
[4] Wang C et al. 2018 Validation of large-eddy simulation of scaled waked wind turbines in different yaw misalignment conditions *J. Phys.: Conf. Series.* **1037**(6) 062007
[5] Deskos G, Laizet S and Palacios R 2020 WInc3D: A novel framework for turbulence-resolving simulations of wind farm wake interactions *J. Wind Energy* **23**(3) 779-794
[6] Jasak H 2009 OpenFOAM: open source CFD in research and industry *Int. J. Nav. Arch. Ocean* **1**(2) 89-94
[7] Fleming P et al. 2014 Evaluating techniques for redirecting turbine wakes using SOWFA *Renewable Energy* **70** 211-218
[8] Rhie C M, Chow W L 1983 Numerical study of the turbulent flow past an airfoil with trailing edge separation *AIAA J.* **21**(11) 1525-1532
[9] Guntur S et al. 2016 FAST v8 verification and validation for a MW-scale Wind turbine with aeroelastically tailored blades Wind Energy Symp. (San Diego, USA) 1008
[10] Troldborg N, Sørensen J N and Mikkelsen R 2007 Actuator line simulation of wake of wind turbine operating in turbulent inflow *J. Phys.: Conf. Ser.* **75**(1) 012063
[11] Wang J et al. 2018 High-fidelity Simulation for Wind Turbine Wake Interaction Research. Technische Universität München
[12] Dongarra J, Michael A H and Luszczek P 2016 High-performance conjugate-gradient benchmark: A new metric for ranking high-performance computing systems *Int. J. High Perform. C.* **30**(1) 3-10

The Science of Making Torque from Wind (TORQUE 2020) IOP Publishing
Journal of Physics: Conference Series **1618** (2020) 022036 doi:10.1088/1742-6596/1618/2/022036

Effects of dynamic induction control on power and loads, by LES-ALM simulations and wind tunnel experiments

C Wang[1], F Campagnolo[1], A Sharma[2] and C L Bottasso[1]

[1]Wind Energy Institute, Technische Universität München, Boltzmannstraße 15, D-85748 Garching bei München, Germany
[2]Fraunhofer IWES, Fraunhofer Institute for Wind Energy Systems, Am Seedeich 45, D-27572 Bremerhaven, Germany

E-mail: carlo.bottasso@tum.de

Abstract.
Dynamic Induction Control (DIC) has the potential of boosting wind farm power by enhancing wake recovery, whereby periodic pitch motions are used to exploit the natural instabilities of wind turbine wakes. This work studies DIC both experimentally and numerically. A thorough validation of an LES-ALM (Actuator Line Method) simulation tool is first conducted against experimental measurements. This shows that the CFD model is able to accurately simulate the power, loads and wake behavior of a wind turbine operating with DIC. The validated CFD model is then employed to study the effects of some DIC parameters. Results indicate an increase in the fatigue loads caused by the pitch activity that enhances wake recovery.

1. Introduction

Wake effects reduce power output and increase loading in wind farms. Various strategies have been proposed and explored to mitigate the adverse impacts of wakes. Recently, a novel Dynamic Induction Control (DIC) strategy has been proposed and studied by LES-AD (Actuator Disk) simulations [1, 2]. The strategy exploits the natural instabilities in the near-wake vortex structures to enhance wake recovery. The technique works by sinusoidally varying the rotor thrust in open-loop; when performed at the right frequency, this perturbation has the effect of speeding up vortex breakdown and the recovery of the wake. This strategy results in a power increase for the downstream turbine that exceeds the power loss on the upstream one, so that the combined upstream-downstream power increases. The potential of DIC has been demonstrated in [3] through wind tunnel experiments and CFD-AD simulations, although the observed increase in wind farm power was not as high as the one found in [1, 2]. In addition, a first assessment of the effects of DIC on loads was attempted by aeroelastic simulations [3] based on a Blade-Element Momentum (BEM) method, i.e., without considering a complete CFD simulation of the system.

To the present date, it appears that the effects of DIC on power and loads have not yet been demonstrated by a CFD-ALM simulation. The present paper aims to fill this gap.

This work first verifies the accuracy of an LES-ALM solver when applied to DIC. The underlying idea is that the more accurate representation of the rotor and near wake behavior offered by ALM, when compared to AD, might lead to a better and more detailed representation

The Science of Making Torque from Wind (TORQUE 2020) IOP Publishing
Journal of Physics: Conference Series **1618** (2020) 022036 doi:10.1088/1742-6596/1618/2/022036

of the physical processes that govern dynamic induction. The verification of the simulation model is here accomplished with the help of wind tunnel experiments performed with scaled wind turbines [3]. After showing a good match between CFD and the experimental data, the validated LES-ALM tool is exploited to further characterize and optimize dynamic induction control in terms of wind farm power. Finally, loads of the optimized DIC case are compared to the ones of the baseline case without DIC, showing a significant impact of this control strategy on fatigue.

2. Methodology

2.1. Experimental setup

A cluster of three aligned wind turbines of the G1 type [4, 5] was operated in the boundary layer wind tunnel of the Politecnico di Milano, with a longitudinal spacing of 5D. The inflow turbulence intensity was about 5%. Turbulence was generated passively by using spires close to the inlet of the wind tunnel test section. The wind tunnel has a cross-section of 3.8×13.8 m^2, sufficient to avoid significant blockage effects [6]. A pitot probe was placed 2.3 D upstream of the first turbine to record the inflow conditions.

2.2. Numerical model

The LES flow solver is based on Foam-extend [7], while the wind turbine and farm models are implemented in FAST [8] and SOWFA [9], respectively. The software has been validated in previous work [10]. Both LES and faster scale adaptive simulation (SAS) [11] methods have been used for the various cases considered here. Although the results of both turbulence models are very close, SAS can be used on coarser meshes, hence reducing the computational time. A passive turbulence generation method with a cluster of spires was applied in the wind tunnel. This physical process was simulated with CFD using a structured body-conforming mesh of the spires [12]. The mean wind speed, turbulence intensity and vertical shear were validated with hot-wire measurements performed in the tunnel. The turbulent flow was sampled on a plane 3.8 D in front of the first turbine for every time-step, and then used as inflow for the subsequent LES-ALM wind turbine simulations. The same inflow data has been used for all CFD cases.

2.3. Wind turbine control

In all experiments and simulations, DIC is only applied to the first turbine since there is apparently no gain when also applied to the intermediate one [2]. The collective blade pitch angle β is the sinusoidal function

$$\beta = \alpha + A\sin(ft), \tag{1}$$

where α is the steady pitch angle, A is the dynamic pitch amplitude, and f is its frequency. Changing α corresponds to the classical axial induction control, in which the thrust of upstream turbines is decreased in order to increase the power of downstream machines. The frequency f is related to the Strouhal number $St = fD/U_\infty$, which has a significant effect on the recovery of the wake and, hence, on wind farm power [3]. The two downstream turbines are governed by standard PI torque controllers, and their pitch angles are always equal to the fine pitch angle, which is 0.4° for the G1 turbine.

3. Results

3.1. CFD validation: single-turbine cases

Comparisons between CFD and experiments are conducted with respect to the wake profile of the first turbine, to the power and thrust of both the upstream and downstream turbines and their sensitivity to DIC parameters. For the purpose of wake comparison, only the first turbine was operated in the wind tunnel, and its wake 5D downstream was measured with hot-wire probes in different operating conditions. Figure 1 shows the hub-height time-averaged lateral wake profiles. The static pitch angle α and dynamic amplitude A cover a fairly wide range,

The Science of Making Torque from Wind (TORQUE 2020) IOP Publishing
Journal of Physics: Conference Series **1618** (2020) 022036 doi:10.1088/1742-6596/1618/2/022036

and for each operating condition, the agreement between experiments and simulations is good. Case 1, shown on the left of Fig. 1, has a relatively high pitch amplitude, and it is termed "the reference case" in the following.

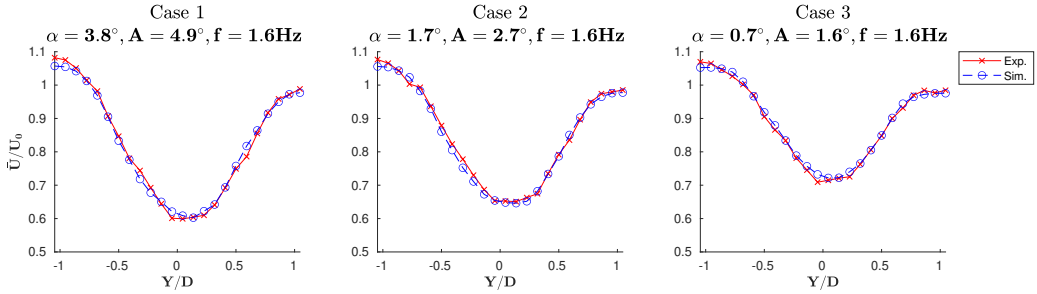

Figure 1: Turbine wake at a 5D downstream distance, for different DIC parameters.

The simulation model can capture both steady-state average values and the dynamic response of the turbines. To correctly model the oscillation of the rotor speed, the rotor moment of inertia was measured by a trifilar method [13]. The Fourier transforms of power and thrust of the first turbine for experiments and simulations were calculated, as shown in Fig. 2 for the reference case. There are peaks at multiples of the pitch excitation frequency of 1.6 Hz both for the simulation and the experiment, and the values of the peaks are in a very good agreement. Experimental measurements of both power and thrust contain high-frequency noise, which is not present in the simulations. The measured power has some low-frequency oscillations as a result of a slightly varying inflow speed, which is not modeled by CFD. However, these mismatches are at least one order of magnitude smaller compared to the peak of the response at the excitation frequency. Therefore, the CFD simulations should be able to capture turbine fatigue loads with good accuracy.

The harmonic amplitudes of power P and thrust T at the excitation frequency 1.6 Hz are shown in Table 1. These quantities are the most important contributor to fatigue loads. Here again, an excellent match between experiments and simulations can be appreciated.

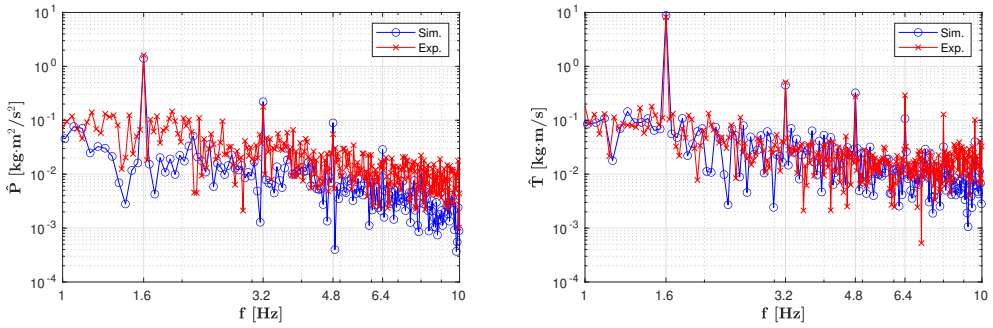

Figure 2: Power and thrust spectra of the first turbine for the reference case: $\alpha = 3.8°$, $A = 4.9°$, $f = 1.6Hz$.

The Science of Making Torque from Wind (TORQUE 2020) IOP Publishing
Journal of Physics: Conference Series **1618** (2020) 022036 doi:10.1088/1742-6596/1618/2/022036

Case	$A[^\circ]$	$\hat{P}_E(f_0)$ $[J]$	$\hat{P}_S(f_0)$ $[J]$	$\hat{T}_E(f_0)$ $[J]$	$\hat{T}_S(f_0)$ $[J]$
1	4.9	1.61	1.4	8.18	8.8
2	2.7	0.95	0.9	5.16	6.14
3	1.6	0.49	0.53	2.98	3.84

Table 1: Amplitudes of the power and thrust harmonics at the pitch excitation frequency $f_0 = 1.6$ Hz, for experiments (subscript E) and simulations (subscript S).

3.2. CFD validation: the reference case

Next, DIC was applied to the first turbine in a cluster of three aligned machines. This subsection shows the results for the reference DIC case. Figure 3 shows the time histories of the various quantities. Table 2 shows the mean values and the harmonic amplitudes at the excitation frequency of power, rotor speed and thrust for the same case. The match of all quantities between experiments and simulations is good. The aforementioned low frequency oscillation of power on the first turbine is clearly visible. For all other cases with different DIC parameters, a comparable match was achieved, similarly to the case presented here.

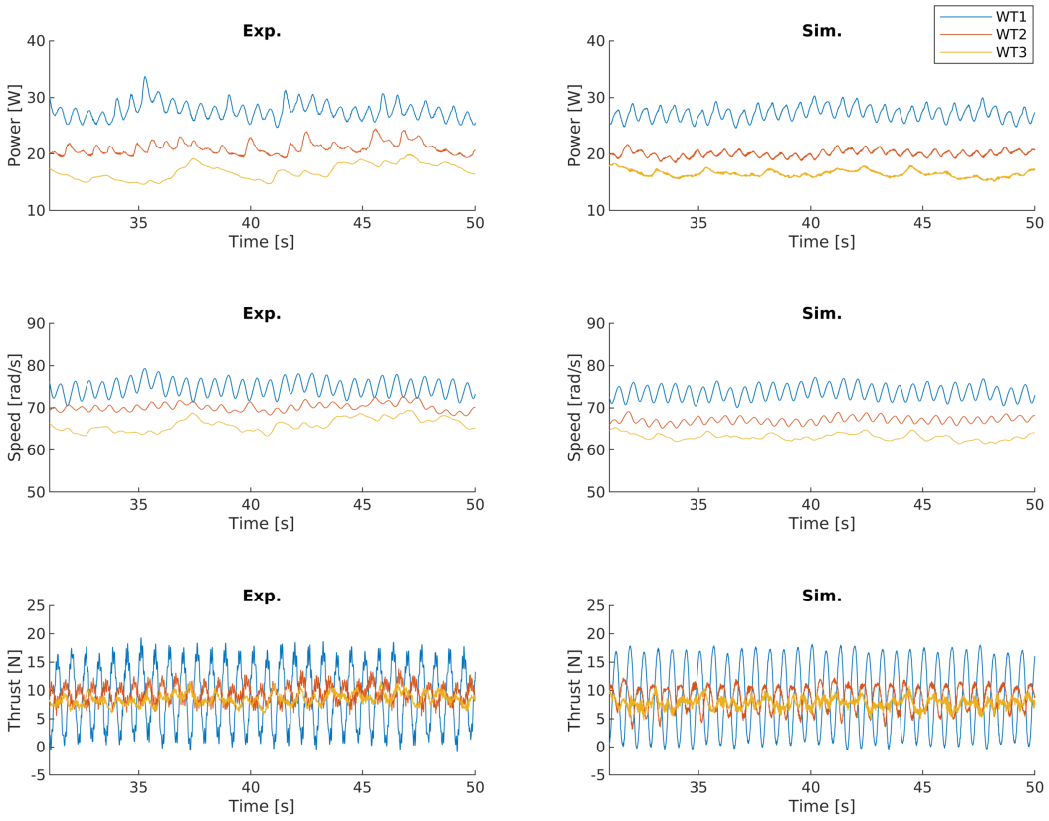

Figure 3: Power, speed and thrust time histories of the three turbines for the reference case ($\alpha = 3.8^\circ$, $A = 4.9^\circ$, $f = 1.6Hz$).

The Science of Making Torque from Wind (TORQUE 2020) IOP Publishing
Journal of Physics: Conference Series **1618** (2020) 022036 doi:10.1088/1742-6596/1618/2/022036

Quantity	Unit	WT1		WT2		WT3	
		Exp.	Sim.	Exp.	Sim.	Exp.	Sim.
$\bar{P}$	W	28.0	27.3	21.1	20.0	16.2	16.7
$\hat{P}(f_0)$	J	1.61	1.40	0.64	0.55	0.12	0.09
$\bar{\Omega}$	rad/s	74.8	73.7	70.1	67.1	65.3	63.4
$\hat{\Omega}(f_0)$	rad	2.39	2.19	0.69	0.91	0.18	0.13
$\bar{T}$	N	9.05	8.99	9.49	8.70	8.27	7.85
$\hat{T}(f_0)$	$kg \cdot m/s$	8.17	8.80	1.8	2.82	0.5	0.41

Table 2: Comparison between experiments and simulations of the mean power $\bar{P}$, speed $\bar{\Omega}$ and thrust $\bar{T}$ and harmonic amplitudes $\hat{P}$, $\hat{\Omega}$, $\hat{T}$ at $f_0 = 1.6$ Hz for the reference case. WT1, WT2 and WT3 denote the first, intermediate and last turbines, repectively.

3.3. CFD validation: frequency sweep

A group of experiments with the same collective pitch angle $\alpha = 0.7°$, similar pitch amplitude A (between 1.5° and 2.0°) but different frequencies f was then analyzed. The wind farm power coefficient ΣC_P, defined as the sum of the individual wind turbine power coefficients, is plotted as a function of pitch frequency f in Fig. 4. Results are normalized with the wind farm power coefficient without DIC, noted ΣC_{P0}. Except for one experimental outlier at 1 Hz, the trends of simulations and experiments match well, and the optimal frequency is shown to be between 1.5 Hz and 2.3 Hz, since such frequency triggers the natural instability in the wake [2].

A large number of experimental observations was conducted for varying frequencies and amplitudes. Considering all cases, the correlation coefficient between the simulated and experimental wind farm power coefficients is 0.86. Based on this extensive set of results, the CFD model appears to be capable of representing the physical phenomena at play with a good level of fidelity.

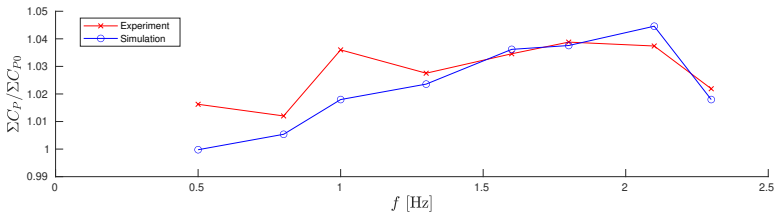

Figure 4: Wind farm power coefficient as a function of dynamic pitch frequency.

The gain obtained by employing DIC is a relatively small quantity of around 3% for the current wind farm layout. It is difficult to precisely investigate such a small difference only with experiments because of measurement uncertainties. Although the inflow condition in the wind tunnel can be controlled, each test could have slightly different mean inflow speed and wind shear. This effect is mitigated by using a pitot tube 2.3 D in front of the first-row turbine. The maximal difference of the mean flow speed measured by the pitot is about 0.7% among all tests, which indicates an excellent control of the inflow condition. However, even such a small difference results in a roughly 2% power difference, which is comparable to the maximal power gain of DIC. Hence, instead of using power, the power coefficient is used to study the effects

The Science of Making Torque from Wind (TORQUE 2020) IOP Publishing
Journal of Physics: Conference Series **1618** (2020) 022036 doi:10.1088/1742-6596/1618/2/022036

of DIC. Nevertheless, this relies on the measurement of a single pitot tube, which is only a single-point measurement and is itself subject to measurement errors, which could explain the small scatter of the experimental results shown in Fig. 4.

3.4. CFD exploitation: power optimization

In contrast to experiments, all CFD simulations are performed with exactly the same inflow condition for all cases, so that any change in wind farm performance in CFD can only be due to changes of DIC parameters. Hence, once the CFD tool is validated, it can be readily used to optimize the DIC parameters, which are the frequency f, collective pitch α and pitch motion amplitude A. More than 30 CFD simulations were conducted for optimization. The number of simulations is limited by their high computational cost. However, the number of data points is more than ten times the number of free variables, and as shown later, they seem sufficient to capture the behavior of the solution.

A gradient-based method was used to find the optimal parameters. The three DIC variables and the wind farm power coefficient span a 4-D space. Figure 5 shows projections of all results on three cross-sections to visualize the behavior of the normalized wind farm power coefficient $\Sigma C_P/\Sigma C_{P0}$. The maximum envelope on each plot is shown as a black curve. Although only a limited number of data points were used, the identification of the optimum should be relatively accurate since the distribution of points is relatively dense close to it.

Regarding the frequency f, there is a relatively flat peak that ranges from 1.5 Hz to 2.0 Hz, which is consistent with observations from experiments and corresponds to the natural instability of the wake, as explained in [2]. The sensitivity of the wind farm power coefficient with respect to the dynamic pitch amplitude seems to be the highest among all three DIC variables. The pitch amplitude is directly correlated with the change in thrust coefficient, and either a too large or too small value appears to be detrimental for the overall power. The collective pitch angle is optimal around the fine pitch angle 0.4° of region 2. Applying a higher collective pitch angle than the fine pitch is similar to the axial induction control, which usually does not increase wind farm power [14]. In fact, wind farm power decreases almost monotonically with respect to α.

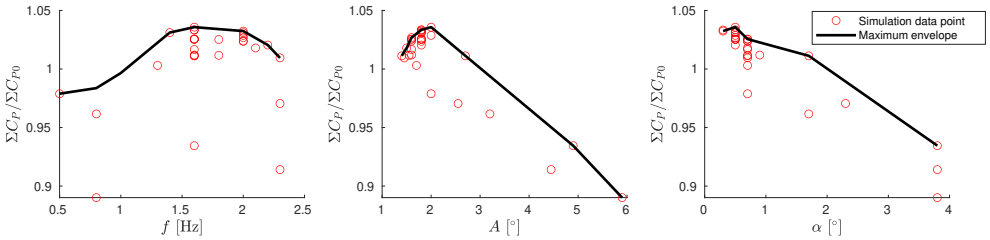

Figure 5: Behavior of wind farm power with respect to DIC parameters.

The optimal DIC parameters obtained by CFD optimization are $f = 1.6$ Hz (corresponding to a Strouhal number of 0.3), $A = 2.0°$, $\alpha = 0.5°$. The wind farm power is 3.6% higher than the baseline case. While the pitch angle is turbine-specific, the thrust coefficient has probably a more generic sense, and its amplitude is 0.274.

3.5. CFD exploitation: load analysis

The significant changes of C_T of the optimal DIC case raise concerns about fatigue loads. Damage Equivalent Loads (DELs) were computed by the rainflow algorithm [15]. Table 3 shows the DELs at blade root, at the shaft just behind the hub and at tower base for the optimal

The Science of Making Torque from Wind (TORQUE 2020) IOP Publishing
Journal of Physics: Conference Series **1618** (2020) 022036 doi:10.1088/1742-6596/1618/2/022036

DIC case and the baseline one. Compared to the baseline case, DIC has little influence on shaft DELs. In contrast, the DEL of the blades and tower of the front turbine increase significantly by 106% and 216% respectively, due to the periodic oscillation of thrust. For the second turbine, the increase in blade and tower DELs are 16% and 65%, caused by fluctuations in the wake speed induced by the thrust on the front turbine. Little influence is observed for the third turbine. The most critical additional loading caused by DIC is the tower fatigue of the first turbine, although this is clearly not the only problematic spot.

Case	Item	Blade DEL (Nm) or relative increase	Tower DEL (Nm) or relative increase	Shaft DEL (Nm) or relative increase
$f = 0.0Hz$	WT1	1.30	5.37	1.49
$A = 0.0°$	WT2	1.68	7.23	2.47
$\alpha = 0.4°$	WT3	1.87	7.40	2.44
$f = 1.6Hz$	WT1	+106%	+216%	+4%
$A = 2.0°$	WT2	+16%	+65%	-2%
$\alpha = 0.5°$	WT3	+3%	+11%	+9%

Table 3: DELs of some turbine components for the baseline case and their relative increase for the optimal DIC case.

4. Conclusions

LES-ALM simulations have been performed for various operating conditions of DIC, demonstrating an excellent match with experimental measurements. The experimental and numerical results are both evidence for the power enhancement capability of DIC. CFD has been used to scan the DIC parameter space and study their effects on performance. A maximum wind farm power gain of 3.6% has been determined with CFD simulations, which corresponds to a C_T oscillation amplitude of 0.274 at a Strouhal number of 0.3. However, this power increase was obtained at the cost of an extremely significant increase in fatigue loading. A continuation of this work should verify if such a large fatigue penalty is also observed for full-scale turbines, rather than the scaled models considered here.

5. Acknowledgements

This work has been supported by the CL-WINDCON project, which receives funding from the European Union Horizon 2020 research and innovation program under grant agreement No. 727477. The authors also express their appreciation to the Leibniz Supercomputing Centre (LRZ) for providing access and computing time on the SuperMUC Petascale System.

References

[1] Munters W and Meyers J 2017 An optimal control framework for dynamic induction control of wind farms and their interaction with the atmospheric boundary layer *Phil. Trans. R. Soc. A: Math., Phys. and Engineering Sci.* **375**(2091)

[2] Munters W and Meyers J 2017 Towards practical dynamic induction control of wind farms: analysis of optimally controlled wind-farm boundary layers and sinusoidal induction control of first turbines *Wind Energy Sci.* **3**(1) 409-425

[3] Frederik J et al. 2020 Periodic dynamic induction control of wind farms: proving the potential in simulations and wind tunnel experiments *Wind Energy Sci.* 245-257

[4] Campagnolo F et al. 2016 Wind tunnel testing of a closed-loop wake deflection controller for wind farm power maximization *J. Phys.: Conf. Ser.* **753** 032006

[5] Bottasso C L et al. 2014 Wind tunnel testing of scaled wind turbine models: beyond aerodynamics *J. Wind Eng. Ind. Aerodyn.* **127** 11-28

[6] West G S and Apelt C J 1982 The effects of tunnel blockage and aspect ratio on the mean flow past a circular cylinder with Reynolds numbers between 10^4 and 10^5 *J. of Fluid Mech.* **114** 361-377
[7] Jasak H 2009 OpenFOAM: open source CFD in research and industry *Int. J. Nav. Arch. Ocean* **1**(2) 89-94
[8] Guntur S et al. 2016 FAST v8 verification and validation for a MW-scale Wind turbine with aeroelastically tailored blades *Wind Energy Symp.* 1008
[9] Fleming P et al. 2014 Evaluating techniques for redirecting turbine wakes using SOWFA *Renewable Energy* **70** 211-218
[10] Wang J et al. 2019 Wake behavior and control: comparison of LES simulations and wind tunnel measurements *Wind Energy Sci.* **4**(1) 71-88.
[11] Menter F and Yury E 2005 A scale adaptive simulation model using two-equation models 43rd *AIAA Aeros. Sci. M. and Exhibit*
[12] Wang C et al. 2018 Validation of large-eddy simulation of scaled waked wind turbines in different yaw misalignment conditions *J. Phys.: Conf. Ser.* **1037**(6) 062007
[13] Hinrichsen P F 2018 Bi and trifilar suspension centering correction *Meccanica* **53**(1-2) 21-32
[14] Bartl J and Sætran L 2016 Experimental testing of axial induction based control strategies for wake control and wind farm optimization *J. Phys: Conf. Ser.* **753**(3) 032035
[15] Amzallag C et al. 1994 Standardization of the rainflow counting method for fatigue analysis *Int. J. Fatigue* **16**(4) 287-293

The Science of Making Torque from Wind (TORQUE 2020) IOP Publishing
Journal of Physics: Conference Series **1618** (2020) 022035 doi:10.1088/1742-6596/1618/2/022035

Does the use of load-reducing IPC on a wake-steering turbine affect wake behavior?

C Wang, F Campagnolo, and C L Bottasso

Wind Energy Institute, Technische Universität München, Boltzmannstraße 15, D-85748 Garching bei München, Germany

E-mail: carlo.bottasso@tum.de

Abstract.

This paper aims at quantifying and explaining the effects of Individual Pitch Control (IPC) on the wake of a wake-steering wind turbine. As the machine is intentionally misaligned with respect to the wind, IPC can be used to mitigate the resulting extra loading. However, while IPC reduces loads, it also affects the wake, which influences the power of downstream turbines. The question is therefore whether the IPC activity has any other appreciable effect at the wind farm level, in addition to its original turbine-level load reduction goal. In this work, experiments and CFD simulations of scaled wind turbines in a boundary layer wind tunnel are considered. The CFD model is first validated with measurements, and then used to show subtle changes in the wake, power and loads caused by IPC. It is observed that IPC does indeed have some non-negligible effects, and that these effects differ for positive and negative yawing.

1. Introduction

Although IPC increases pitch activity and affects the duty cycle, it reduces the periodic loads caused by shear and wind misalignment, resulting in reduced fatigue damage [1]. Furthermore, blade-passing 3P loads [2, 3] and aerodynamic or mass imbalances of the rotor can also be mitigated by IPC [4]. Today, operation at high misalignment angles is actively investigated as a way to control the wake path, with potential benefits in terms of power capture and loading of downstream wind turbines [5, 6]. However, the high misalignment angles at which a wake-steering machine must operate may induce an increase in fatigue loading, and IPC can be used to limit this negative effect of wake steering. The present paper tries to answer the following questions: if IPC is used to reduce the loads on a wake-steering turbine, what is the effect on the wake? Are path and/or recovery affected? Are these effects beneficial or detrimental for the downstream machine? And are the loads on the wake-steering turbine significantly reduced?

2. Methodology

2.1. Experimental setup

The questions posed above are investigated in this paper by using both ad hoc wind tunnel experiments and a simulation model. Two scaled wind turbines of the G1 type [7,8] were installed in the large boundary layer wind tunnel of the Politecnico di Milano, one 5D downstream of the other. Both turbines were equipped with a standard collective pitch-torque controller, with an optional IPC loop. A sheared inflow with a 5% turbulence intensity was generated in the

The Science of Making Torque from Wind (TORQUE 2020) IOP Publishing
Journal of Physics: Conference Series **1618** (2020) 022035 doi:10.1088/1742-6596/1618/2/022035

wind tunnel by passive means using a cluster of spires, resulting in a shear power coefficient of about 0.12. One test was conducted by removing the downstream turbine, with the goal of characterizing at its location the wake of the upstream machine using hot wire probes.

2.2. Simulation model

The simulation model is developed with a Large Eddy Simulator (LES) coupled with an Actuator Line Method (ALM), described in [5, 9]. While ALM is used to model blades, the Immersed Boundary Method (IBM) is used to model the nacelle and tower. To reduce the computational cost, a Scale Adaptive Simulation (SAS) was also often used, with practically the same results as LES. The turbulent inflow was obtained by LES precursor simulations conducted with Foam-extend [11] using a structured body-conforming mesh of the spires and the wind tunnel, as described in greater detail in [6].

2.3. Turbine control

The IPC implementation is based on fixed-frame loads, obtained by transforming rotating-frame measurements provided by strain gages installed on the shaft of the G1 machines. The pitch inputs in the d-q coordinate system are computed by a proportional-integral controller. The reference angles in the d-q coordinate system β_d, β_q are governed by a PI controller:

$$\beta_d = K_I \int_0^t M_n(\tau) d\tau + K_P M_n(t), \tag{1a}$$

$$\beta_q = K_I \int_0^t M_y(\tau) d\tau + K_P M_y(t), \tag{1b}$$

where K_I , K_P are integral and propotional gains, respectively, and M_n and M_y are the fixed frame nodding and yawing moments. The inverse Coleman transformation is then used to obtain the blade pitch angles from the d-q frame [1]:

$$\beta_i(\psi_i) = \beta_d \cos(\psi_i) + \beta_q \sin(\psi_i), \tag{2}$$

where ψ_i is the azimuth angle of each blade, $\psi = 0^\circ$ corresponding to the blade pointing vertically up, and ψ increases clockwise when looking downstream. The total pitch angle of each blade is the sum of its individual pitch angle β_i and the collective pitch angle β_c.

The baseline generator torque controller is based on a standard look-up table, while the collective pitch angle is constant since turbines only operate in region 2. The same controllers have been implemented in simulations and experiments.

3. Results

3.1. Validation of CFD

To digitally duplicate the experiments, it is necessary to accurately simulate the inflow in the wind tunnel. In fact, turbulence intensity influences wake recovery, while wind shear affects the IPC behavior. In the tunnel, turbulence was generated passively with an array of spires. The generated turbulent flow field has both a vertical and a small lateral wind shear. The turbulence intensity of 5% and the vertical wind shear equal to 0.12 obtained by the precursor simulation are both very close to the measurements.

Figure 1 illustrates the flow at hub height for two simulations considering only the upstream turbine, at 30° yaw (left plot) and 0° yaw (right plot). The dashed lines indicate the position of the downstream wind turbine that is 5D away from the upstream one.

The Science of Making Torque from Wind (TORQUE 2020) IOP Publishing
Journal of Physics: Conference Series **1618** (2020) 022035 doi:10.1088/1742-6596/1618/2/022035

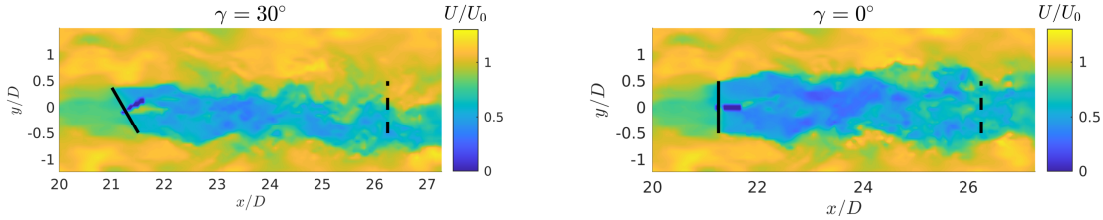

Figure 1: Top view of the instantaneous longitudinal flow speed at hub height. Solid lines indicate the upstream rotor, while dashed lines the downstream one.

Figure 2 shows the pitch angle of the first blade as a function of its azimuth for the $\gamma = 0°$ case. The pitch angle is not a single-valued function of the azimuth because of turbulence and rotor dynamics. However, the data points form a sinusoidal shape with its lowest value around $\psi_1 = 180°$. The scatter of the experimental data points is slightly bigger than the one of the simulations, which is probably mainly caused by measurement noise in the experiments or by having neglected the elasticity of the blades in the simulations.

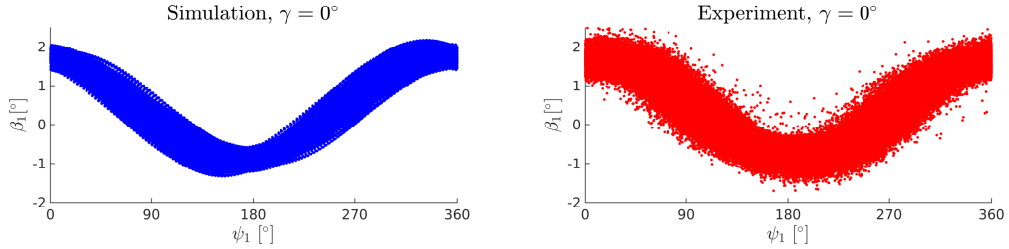

Figure 2: Comparison of the pitch angle of the first blade between simulation and experiment for the zero-yaw case.

To obtain a clearer view of the pitch-azimuth relationship, the mean pitch value corresponding to each azimuthal angle was calculated for each operating condition, as shown in Fig. 3. Table 1 shows the mean values of β_d, β_q and also the changes in loads and power caused by IPC.

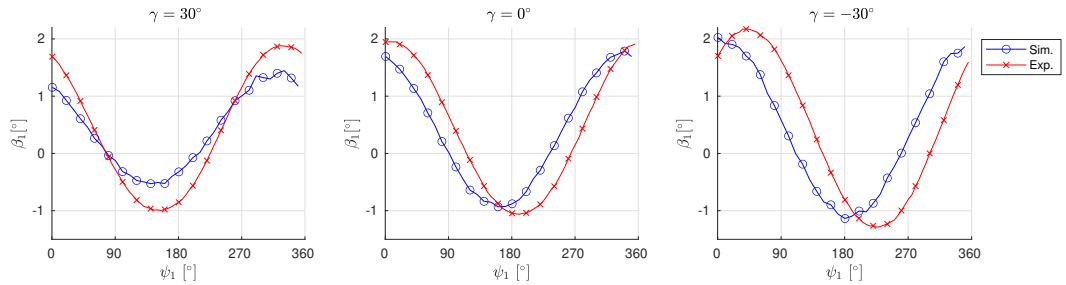

Figure 3: Comparison of average individual pitch behavior for different yaw misalignment cases.

The Science of Making Torque from Wind (TORQUE 2020) IOP Publishing
Journal of Physics: Conference Series **1618** (2020) 022035 doi:10.1088/1742-6596/1618/2/022035

	$\gamma = 30°$		$\gamma = 0°$		$\gamma = -30°$	
Data source	CFD	EXP	CFD	EXP	CFD	EXP
$\Delta\lvert\bar{M}_n\rvert/\lvert\bar{M}_n\rvert$	-99%	-94%	-99%	-99%	-99%	-99%
$\Delta\lvert\bar{M}_y\rvert/\lvert\bar{M}_y\rvert$	-97%	-95%	-81%	-88%	-98%	-98%
β_d [°]	0.90	1.27	1.28	1.36	1.45	1.21
β_q [°]	-0.67	-0.55	0.09	0.34	0.40	1.19
$\Delta C_P/C_P$	+1.0%	+1.5%	-3.0%	-0.4%	-2.6%	-1.8%

Table 1: Pitch angles and changes in power and fixed frame (nodding and yawing) moments for different yaw misalignment cases.

Note that IPC is not typically used in region 2 in aligned ($\gamma = 0°$) conditions, because of its impact on actuator duty cycle. However, here it is assumed that IPC is used in region 2 to mitigate the extra fatigue caused by yaw misalignment for wake-steering wind farm control.

There are some differences between simulations and experiments in the mean values of β_d and β_q, which are mainly driven by the differences in the vertical and horizontal local wind shears, respectively. In fact, although the inflow speed distribution in the simulation is very similar to the one of the experiments, the two are still not exactly identical. Notwithstanding these small differences, the experimental measurements can still be used as references for the simulations, since the goal of this work is to investigate changes caused by IPC rather than a precise match between experiments and simulations. Indeed, experiments and simulations show many similar trends.

In fact, changes in the yaw angle γ influence the phase of the $\beta - \psi$ curve. For positive yaw angles, the curve shifts to the right, and vice versa. This phenomenon is mainly driven by the change of β_q and it has an aerodynamic explanation. For a zero-yaw turbine with IPC, the pitch angle is smallest when the blade is close to the lower part of the rotor ($\psi = 180°$). When the turbine is yawed by $\gamma = 30°$, the left side ($\psi = 270°$) of the rotor moves upstream, while the right side ($\psi = 90°$) moves downstream. This tends to decrease the angle of attack and loads of the right side of the rotor, because the blade moves into the induction zone of the rotor, where the flow speed is lower. The opposite happens for the left side of the rotor. At this point, IPC intervenes to increase pitch on the left side and decrease pitch on the right side, which results in a negative value of β_q and a left shift of the $\beta - \psi$ curve. The analysis is similar for the other yaw direction ($\gamma = -30°$) and it results in a positive value of β_q and a right shift of the curve. For the zero yaw case, a non-zero β_q is only caused by the local horizontal wind shear, which is slightly larger in the experiment than in the simulations.

Changes in the yaw angle also influence the amplitude of the $\beta - \psi$ curve: the amplitude decreases as γ increases, and vice versa. Although the sensitivity is stronger in simulations, this phenomenon is visible from both simulation and experimental results, as shown in Fig. 3. In the simulation, the difference of β_q in absolute value terms is significant between the $\gamma = 30°$ and $\gamma = 0°$ cases, while the difference is small for the experiment, which is consistent with the significant change of amplitude between these two yaw misalignment cases for the simulation and a smaller change for the experiment. These differences might be caused by a slightly different horizontal shear.

The change in β_q is already understood, the task here is to explain the change in β_d, which can be done with the help of the schematic sketches of Fig. 4. In the figure, the airfoil profile at different azimuthal locations has been shown. The speed of the airfoil caused by the rotor rotation is ΩR. When the turbine is yawed, the incoming flow includes both a normal component $U\cos(\gamma)$ and a tangential component $U\sin(\gamma)$, so that the direction of the flow depends on the yaw direction and magnitude. For the cases with $\gamma = 30°$, $\psi = 0°$ (blade highest position) and

The Science of Making Torque from Wind (TORQUE 2020) IOP Publishing
Journal of Physics: Conference Series **1618** (2020) 022035 doi:10.1088/1742-6596/1618/2/022035

$\gamma = -30°$, $\psi = 180°$ (blade lowest position), the effect of yaw misalignment is to decrease the relative speed V_{Rel} with respect to the airfoil and increase the angle of attack α. In contrast, for the cases with $\gamma = 30°$, $\psi = 180°$ and $\gamma = -30°$, $\psi = 0°$, V_{Rel} increases and α decreases due to yaw. For both yaw misalignment cases, the changes in relative speed and angle of attack have opposite effects on loads. For the operational conditions considered here, the dominant factor is the effect of the relative speed, whose relative change is about 15% between $\psi = 0°$ and $\psi = 180°$, resulting in a 32% relative change of lift. The difference of α between the two azimuthal positions caused by yaw is about 1.0°, which results in only a 13% relative change of lift.

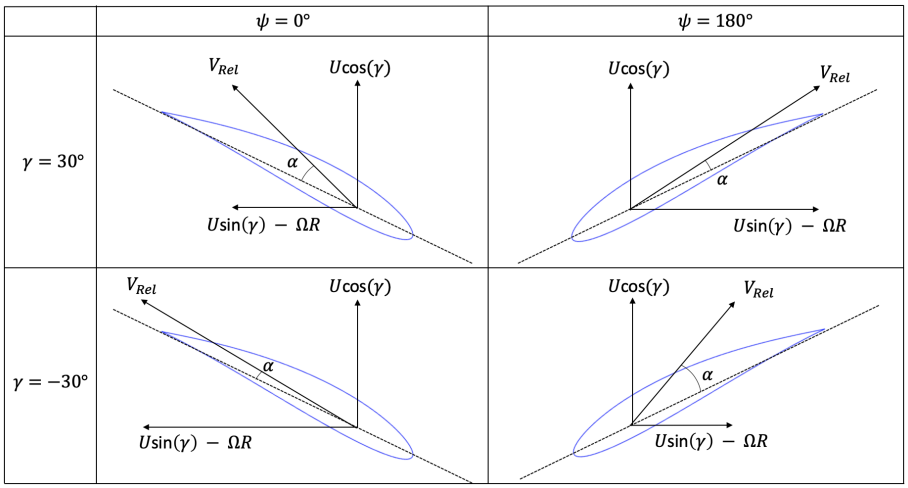

Figure 4: Velocity triangles at different azimuthal positions for different yaw angles. U is the flow speed at the rotor disk; V_{Rel} is the relative speed of the flow with respect to the airfoil; α is the angle of attack.

The presence of a vertical wind shear breaks the symmetry between positive and negative yaw angles. Further analysis of the triangle of velocities shows that a positive vertical shear increases the relative flow speed and angle of attack around $\psi = 0°$, and decreases both quantities around $\psi = 180°$. Considering a negative yaw angle, the effects of yaw and shear both increase the relative speed for $\psi = 0°$, and both decrease it for $\psi = 180°$; on the other hand, the effects on the angle of attack are of an opposite sign and tend to cancel each other. Exactly the opposite happens for a positive yaw angle, where the relative speed changes caused by yaw and shear have opposite signs, while the changes of angle of attack are in the same direction.

These changes in the operating conditions of the airfoils induce an effect of IPC also on power. Indeed, IPC affects power even for $\gamma = 0°$, as shown in Table 1. This is due to the fact that IPC, by aggressively targeting loads, generates an excessively low loading in the top part of the rotor, and an excessively high one in the bottom part. This moves the induction away from the optimal value of 1/3, leading to a loss of power. A similar effect is present when the machine is yawed. However, due to the lack of symmetry and the lower loading for positive yaw angles, IPC leads to a slight power improvement for $\gamma = 30°$ (Table 1).

This lack of symmetry has several effects. In fact, since lift in the top and bottom parts of the rotor changes more for negative than for positive yaw, a higher β_d is required for $\gamma = -30°$ than for $\gamma = 30°$ (cf. Table 1).

In the experiment, horizontal (at hub-height) and vertical wake profiles 5D downstream of the rotor were measured with hot-wire probes. Figure 5 reports the results for the 30° (top

The Science of Making Torque from Wind (TORQUE 2020) IOP Publishing
Journal of Physics: Conference Series **1618** (2020) 022035 doi:10.1088/1742-6596/1618/2/022035

plots), 0° (middle plots) and −30° (bottom plots) yaw misalignment cases. The first and third columns show speed profiles for the case IPC on and off, and for both CFD and experiments. The vertical wake profiles are located at the wake center, which was determined experimentally to be at $Y = -0.405$ m, $Y = 0$ m, and $Y = 0.437$ m for the yaw angles 30°, 0° and -30°, respectively. The match between experiments and simulations is acceptable, and small differences are caused by slight changes in inflow. The second and fourth columns of Fig. 5 show the differences between IPC on and off. Looking at the vertical profiles, it appears that IPC accelerates the flow above hub height and decelerates it below hub height. This effect is proportional to the direct pitch amplitudes β_d, coherently with Table 1. In contrast, the effect of IPC on the horizontal wake profile is not significant, as shown by the fourth column of Fig. 5.

The validation of CFD has been shown from different perspectives, indicating that the numerical model is able to capture the effects of IPC with reasonable accuracy. As the inflow conditions in CFD can be exactly the same for different operating conditions of the turbines, numerical simulations can be used to evaluate subtle differences in power, loading and wake behavior.

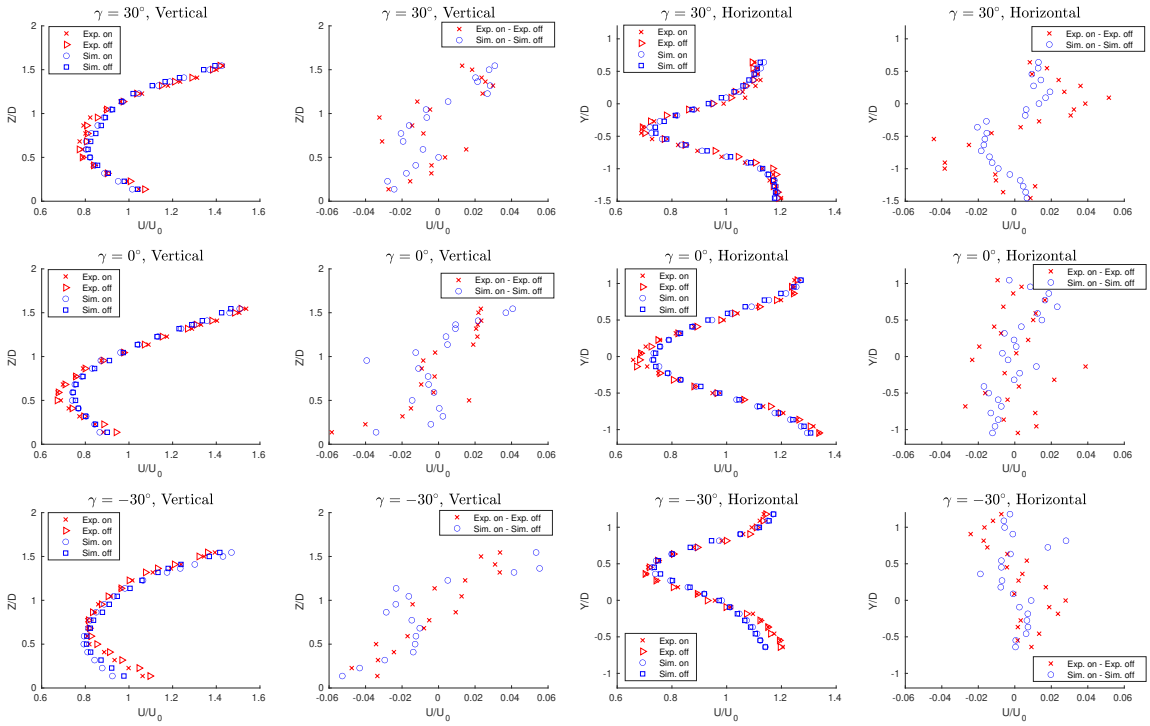

Figure 5: Vertical and horizontal wake profiles with and without IPC, at a 5D downstream location.

3.2. Effects of IPC on wake behavior

Figure 6 shows the difference in the wake longitudinal speed between IPC on and off at a 5D downstream distance, as computed by the simulation model. Looking at the case $\gamma = 0°$, IPC generates an acceleration close to the top of the rotor and a deceleration close to its bottom. This is consistent with the previously noted effect on induction, due to the aggressive targeting of blade loads, which causes a drop in power. As the wake propagates downstream and

The Science of Making Torque from Wind (TORQUE 2020) IOP Publishing
Journal of Physics: Conference Series **1618** (2020) 022035 doi:10.1088/1742-6596/1618/2/022035

swirls clockwise when looking upstream, the acceleration and deceleration regions are convected clockwise around the wake center, as visualized by the high-speed (yellow) and a low-speed (blue) bubbles present in all plots in Fig. 6. For a yawed turbine, a kidney-shaped wake is formed [10], caused by two counter-rotating vortices and the wake swirl. This system of vortices causes a small lateral velocity component on the leeward side of the wake, as shown by Fig. 7. This lateral wind component, indicated with a black arrow in Fig. 6, breaks the high-speed bubble for the $\gamma = 30°$ case and the low-speed bubble for the $\gamma = -30°$ case.

This influences the velocity field, and the resulting changes in the rotor effective wind speeds at the downstream turbine are 0.3%, -1.0% and -0.3% for the 30°, 0° and −30° yaw cases, respectively. By these results, the use of IPC on the upstream turbine is expected to have a positive effect on the power of the downstream turbine for $\gamma = 30°$, while it should have a negative effect for $\gamma = 0°$ and $\gamma = -30°$. These effects are indeed observed in the next subsection, where two turbines are simulated. Notice also that IPC does not seem to have any noticeable effect on wake recovery, as its frequency is not in the neighborhood of typical near-wake unstable modes.

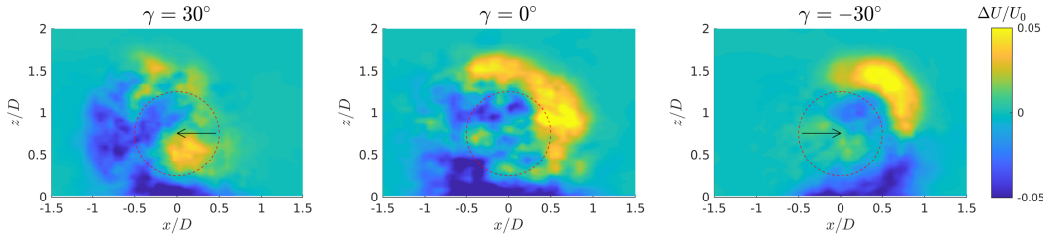

Figure 6: Difference in wake mean longitudinal speed between IPC on and off, 5D downstream of the rotor. The rotor planes are viewed from downstream. The red dashed circles show the location of the downstream rotor.

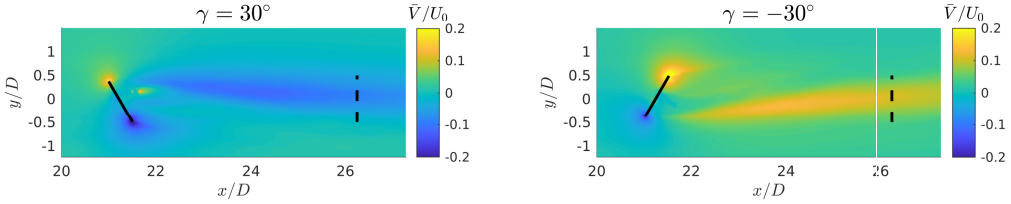

Figure 7: Mean lateral velocity component $\bar{V}$. The lateral velocity is significant only on the leeward side of the wake.

3.3. Effects of upstream turbine IPC

As shown, the activation of IPC on the upstream turbine has effects on both the upstream and downstream machines. Table 2 shows simulation results obtained with two turbines, and reports percentage changes of power coefficient and bending moments. The influence of IPC on the power coefficient C_{P1} of the upstream turbine is consistent with the results of single-turbine simulations shown in Table 1. When $\gamma = 30°$, IPC has a positive effect on the power for both turbines, showing potential for some moderate wind farm power boost. When $\gamma = 0°$, IPC

The Science of Making Torque from Wind (TORQUE 2020) IOP Publishing
Journal of Physics: Conference Series **1618** (2020) 022035 doi:10.1088/1742-6596/1618/2/022035

decreases power of both turbines. This is however not an issue, as IPC is not expected to be used in non-misaligned conditions, due to its negative effect on the actuator duty cycle. When $\gamma = -30°$, power decreases for the first turbine and remains almost constant for the second one.

The mean nodding and yawing moment of the upstream turbine, $|\bar{M}_{y1}|$ and $|\bar{M}_{z1}|$, are reduced to almost zero. The bending moments of the downstream turbine $|\bar{M}_{y2}|$ and $|\bar{M}_{z2}|$ are also slightly influenced, but only to a limited extent.

Case	1	2	3
γ_1 [°]	30	0	-30
WT1 IPC	on	on	on
WT2 IPC	off	off	off
$\Delta C_{P1}/C_{P1}$	+1.7%	-3.0%	-3.9%
$\Delta C_{P2}/C_{P2}$	+1.6%	-4.2%	-0.1%
$\Delta\lvert\bar{M}_{n1}\rvert/\lvert\bar{M}_{n1}\rvert$	-99%	-100%	-100%
$\Delta\lvert\bar{M}_{y1}\rvert/\lvert\bar{M}_{y1}\rvert$	-99%	-94%	-97%
$\Delta\lvert\bar{M}_{n2}\rvert/\lvert\bar{M}_{n2}\rvert$	-6%	-9%	-8%
$\Delta\lvert\bar{M}_{y2}\rvert/\lvert\bar{M}_{y2}\rvert$	+11%	-14%	-2%

Table 2: Effects of the upstream turbine IPC on power and loads. The relative changes of power and mean bending moments with respect to the benchmark cases without IPC are shown. Subscripts 1 and 2 indicate the upstream and downstream turbines, respectively.

3.4. Effects of downstream turbine IPC

Next, the IPC on the downstream turbine is also switched on. The simulated wake profiles at the location of the downstream rotor for both yaw misalignment cases are shown in Fig. 8. Two kidney-shape wakes pointing in opposite directions can be seen in the figure, triggering the response of the IPC controller on the downstream turbine. Table 3 shows the effects of IPC, which, as expected, brings all mean bending moments almost to zero.

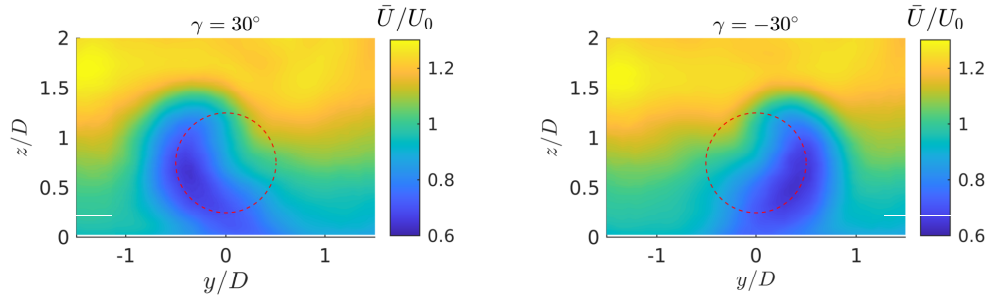

Figure 8: Longitudinal flow speed at the location of the downstream turbine, showing the typical kidney shape of a deflected wake.

When the upstream turbine is not yawed, the downstream turbine is exposed to a full wake. In this case, its power decreases only moderately when IPC is activated, which is the penalty for a high β_d. When the upstream turbine is yawed, there is a partial wake impingement on the downstream turbine, which results in high lateral wind shear. IPC reacts with a high β_q that has a detrimental effect on power; this differs from the beneficial effect of a small β_q discussed in

subsection 3.1. Case 6 indicates a more severe power loss on the downstream turbine than case 4 because of its higher β_d, which is caused by the direction of yaw and can still be explained by the analysis reported in subsection 3.1.

Case	4	5	6
γ_1 [°]	30	0	-30
γ_2 [°]	0	0	0
WT1 IPC	on	on	on
WT2 IPC	on	on	on
β_d [°]	1.5	1.3	1.9
β_d [°]	-2.3	0.2	2.4
$\Delta C_{P2}/C_{P2}$	-8.9%	-3.2%	-13.1%
$\Delta\lvert\bar{M}_{n2}\rvert/\lvert\bar{M}_{n2}\rvert$	-92%	-100%	-96%
$\Delta\lvert\bar{M}_{y2}\rvert/\lvert\bar{M}_{y2}\rvert$	-90%	-90%	-98%

Table 3: Effects on power and loads caused by the use of IPC on the downstream turbine. The relative changes of power and mean bending moments are computed with respect to the corresponding cases 1, 2, 3 of Table 2.

4. Conclusions

The effects caused by the use of IPC on a wake-steering turbine are quantified experimentally and numerically. A simulation model is first validated with experiments and then exploited to study differences caused by IPC on wake behavior, power and loads. The results show that indeed IPC is an effective way of reducing loading for all considered operating conditions. The mechanisms by which IPC influences the turbine and its wake has been discussed. Overall, no significant enhancement of wake recovery has been observed. The use of IPC on the upstream turbine has been shown to generate a moderate power increase for positive yawing, both upstream and downstream, while it induces power losses for negative yawing. IPC on the downstream turbine tends, in general, to always reduce power.

5. Acknowledgements

This work has been supported by the CL-WINDCON project, which receives funding from the European Union Horizon 2020 research and innovation program under grant agreement No. 727477, and by the CompactWind II project (FKZ: 0325492G), which receives funding from the German Federal Ministry for Economic Affairs and Energy (BMWi). The authors also express their appreciation to the Leibniz Supercomputing Centre (LRZ) for providing access and computing time on the SuperMUC-NG System.

References

[1] Bossanyi E A 2003 Individual blade pitch control for load reduction *J. Wind Energy* **6**(2) 119-128
[2] Bossanyi E A 2005 Further load reductions with individual pitch control *J. Wind Energy* **8**(4) 481-485
[3] Selvam K et al. 2009 Feedbackfeedforward individual pitch control for wind turbine load reduction *Int. J. Robust Nonlin.* **19**(1) 72-91
[4] Kanev Stoyan and Van Engelen T G 2009 Exploring the limits in individual pitch control *Pro. of Euro. Wind Energy Conf.* 1-10
[5] Fleming P et al. 2014 Evaluating techniques for redirecting turbine wakes using SOWFA *Renewable Energy* **70** 211-218
[6] Wang C et al. 2018 Validation of large-eddy simulation of scaled waked wind turbines in different yaw misalignment conditions *J. Phys.: Conf. Ser.* **1037**(6) 062007

[7] Campagnolo F et al. 2016 Wind tunnel testing of a closed-loop wake deflection controller for wind farm power maximization *J. Phys.: Conf. Ser.* **753**(3) 032006
[8] Bottasso C L et al. 2014 Wind tunnel testing of scaled wind turbine models: beyond aerodynamics J. Wind Eng. and Ind. Aerodyn. **127** 1128
[9] Wang J et al. 2019 Wake behavior and control: comparison of LES simulations and wind tunnel measurements *Wind Energy Sci.* **4**(1) 71-88.
[10] Bastankhah M and Port-Agel F 2016 Experimental and theoretical study of wind turbine wakes in yawed conditions *J. Fluid Mech.* **806** 506-541
[11] Jasak H 2009 OpenFOAM: open source CFD in research and industry *Int. J. Nav. Arch. Ocean* **1**(2) 89-94

The Science of Making Torque from Wind (TORQUE 2018) IOP Publishing
IOP Conf. Series: Journal of Physics: Conf. Series **1037** (2018) 032014 doi:10.1088/1742-6596/1037/3/032014

A POD reduced-order model for wake steering control

A Fortes-Plaza[1], F Campagnolo[1], J Wang[1], C Wang[1] and CL Bottasso[1,2]

[1] Wind Energy Institute, Technische Universität München, Garching bei München, Germany
[2] Dipartimento di Scienze e Tecnologie Aerospaziali, Politecnico di Milano, Milano, Italy

E-mail: carlo.bottasso@tum.de

Abstract. Wake steering by active yawing of upstream wind turbines is a promising wind plant control technique. To enable the development of model-based wind plant control methods, there is a need for models that can marry the contrasting requirements of good fidelity and low computational cost. This paper presents a reduced-order model (ROM) obtained by directly compressing high-fidelity computational fluid dynamics (CFD) simulation data using the proper orthogonal decomposition (POD) method. At first, simulations of wake-interacting wind turbines are obtained for time-varying yaw settings using the lifting-line large-eddy simulation (LES) code `SOWFA`. Next, a ROM is synthesized from the CFD transient simulations, obtaining a discrete-time state-space model that captures the dominant dynamics of the underlying high-fidelity model with only a reduced number of states. The ROM is optionally augmented with a Kalman filter, which feeds back turbine power measurements from the plant to the model, enhancing its accuracy. Results obtained in realistic turbulent conditions show a good agreement between high-fidelity CFD solutions and the proposed POD-based ROM in terms of wake behavior and power output of waked turbines. Additionally, the ROM presents acceptable results when compared to wind tunnel experiments, including the capability of the model to partially correct for an intentionally built-in model mismatch.

1. Introduction

Wind turbines are typically installed in clusters, in order to lower construction, maintenance and commissioning costs. However, turbines within a farm are often in close proximity of each other, which has the effect of creating aerodynamic interactions between downstream turbines and the wakes shed by upstream machines. In fact, wakes, which are characterized by a lower wind speed and higher turbulence intensity than the free stream, have a negative impact on the performance of wake-impinged downwind turbines, in turn increasing their loading and reducing their power output. Wind farm control is a newly emerging technology that tries to mitigate these effects.

The central idea of wind farm control is to move away from the current individual optimization of the set point of each single machine, and operate instead the turbines within the plant in a collective (cooperative) manner. This means that machines may be operated at set points that are sub-optimal at the single turbine level, if this creates a benefit at the collective wind plant level. Wake steering, or wake redirection, is a promising technique to implement wind farm control. The idea is in this case to alter the wake path with the goal of reducing the

The Science of Making Torque from Wind (TORQUE 2018) IOP Publishing
IOP Conf. Series: Journal of Physics: Conf. Series **1037** (2018) 032014 doi:10.1088/1742-6596/1037/3/032014

shading of downstream turbines. Among various possible ways of affecting wake behavior, yaw misalignment —where the rotor is intentionally misaligned with respect to the incoming wind— is the method that is currently more actively being investigated. For example, Refs. [1–3] study wake steering with the help of computational fluid dynamics (CFD) simulations, while Refs. [4,5] use scaled wind turbine models in a boundary layer wind tunnel.

The design of control strategies for wake steering can greatly benefit from models that can faithfully capture all relevant physical processes playing a role in wind turbine wake interactions. This, however, poses significant challenges. In fact, existing engineering models —although typically very fast and using only a limited number of degrees of freedom— might not always be as accurate as desired. In addition, they depend on parameters that need to be calibrated. Although the existence of model parameters offers the possibility of model tuning and adaption, it is also clear that mistuning may hamper the accuracy of the model. On the other hand, CFD-based models are based on first principles. This means that they should have better accuracy and resolution than engineering models, while at the same time they will also have no (or very few) tunable parameters. Unfortunately, they will also come at a very high computational cost. Because of this, their use in the context of control synthesis is extremely challenging, or can actually typically be altogether ruled out [6].

In order to marry the contrasting requirements of high-fidelity and low computational cost, this paper proposes an approach that is based on the idea of compressing high-fidelity CFD data into a reduced-order model (ROM). This is obtained through a data-driven model-identification procedure, based on the proper orthogonal decomposition (POD). The resulting ROMs capture the dominant dynamics of wind turbine wakes and their interactions, while showing at the same time a high degree of data compression. This way, the computationally intensive part of the process is performed offline and, once a ROM has been identified, one is left with a small size state-space model that is ideally suited for the design of model-based control laws.

The paper is organized according to the following structure. Section 2 discusses the characteristics of the simulation environment and considered wind farm control setup. Then, Sect. 3 formulates the methods used for ROM generation. Next, Sect. 4 reports and discusses results, comparing ROM-generated predictions with high-fidelity CFD simulations and wind tunnel experiments. Lastly, conclusions and an outlook towards further developments end the paper in Sect. 5.

2. Simulation environment

2.1. CFD model

First, high-fidelity CFD simulations are performed in order to generate detailed flow data, which is then used to obtain a compressed model (described in Sect. 3). Simulations are run here using a simulation tool based on `SOWFA` (Simulator fOr Wind Farm Applications) [7], which is a lifting-line-based large-eddy simulation (LES) tool developed at the National Renewable Energy Laboratory (NREL), using `OpenFOAM` and coupled with NREL's `FAST` wind turbine structural-dynamics model [8]. The implementation used here features an immersed boundary formulation [9] to model the effects of nacelle and tower, which may have a significant influence on wake development and behavior. Typical simulations last for several days, and were run on the 'SuperMUC' cluster of the Leibniz Supercomputing Centre (LRZ, Germany).

2.2. Simulation setup

The simulations considered here reproduce experiments conducted in the boundary layer wind tunnel of the Politecnico di Milano in Italy, using the G1 (Generic 1 m diameter rotor) scaled wind turbine models [5, 10]. The LES CFD environment was validated with respect to experimental data in previous studies [11]. Table 1 reports the main characteristics of the G1 scaled wind turbine models.

The Science of Making Torque from Wind (TORQUE 2018) IOP Publishing
IOP Conf. Series: Journal of Physics: Conf. Series **1037** (2018) 032014 doi:10.1088/1742-6596/1037/3/032014

Table 1: Main characteristics of the G1 scaled wind turbine model [10].

Rotor diameter (D)	1.1 m
Hub height	0.825 m
Rated rotor speed	850 rpm
Control	Variable speed, pitch, and yaw

The simulation setup considers a two-turbine cluster, where the machines are longitudinally spaced at a distance of 4D and aligned with the prevailing wind flow direction. The free stream flow has an average speed of 5.7 m/s with a turbulence intensity (TI) of about 6 % at hub height. Simulations were run with a time step of 0.0004 s and data was collected in snapshots sampled every 0.01 s (snapshot frequency of 100 Hz). The stored data includes the power output of both wind turbines, the prescribed upwind turbine yaw control input, and the three velocity components recorded at all grid points on two planes: the first one is a horizontal plane at hub height (termed XY), while the second is a vertical plane going through the center of the two turbine towers (termed XZ). Clearly, although data was collected only at these two planes, simulations consider the full 3D computational domain. A finer mesh was used closer to the turbines and in their wakes, while a coarser one was used elsewhere to reduce computational cost. A description of the grid characteristics on the two planes is provided in Table 2.

Table 2: Grid resolution on the two planes used for data collection.

Plane	Dimensions	Fixed coord.	Resolution	Total points
XY	$\Delta x = 6.2D$, $\Delta y = 1.8D$	$z = 0.825\,\mathrm{m}$	$\delta x = \delta y \approx 0.015D$	$\approx$ 53,000
XZ	$\Delta x = 6.2D$, $\Delta z = 3.5D$	$y = 3.500\,\mathrm{m}$	$\delta x = \delta z \approx 0.016D$	$\approx$ 80,000

Data at the generic ith snapshot is collected into column vectors: the three velocity components at each grid point on the two planes (for a total of $N_x \approx 400{,}000$ values) are stored in the state vector $\boldsymbol{x}_i$, the $N_y = 2$ wind turbine powers in the output vector $\boldsymbol{y}_i$, while the $N_u = 1$ upwind turbine yaw angle in the input $\boldsymbol{u}_i$. Next, the various vectors are grouped into snapshot matrices, which are defined as:

$$\mathcal{X} = \begin{bmatrix} \boldsymbol{x}_1 & \boldsymbol{x}_2 & \dots & \boldsymbol{x}_{n_s-1} \end{bmatrix} \in \mathbb{R}^{N_x \times (n_s-1)}, \tag{1a}$$

$$\mathcal{X}' = \begin{bmatrix} \boldsymbol{x}_2 & \boldsymbol{x}_3 & \dots & \boldsymbol{x}_{n_s} \end{bmatrix} \in \mathbb{R}^{N_x \times (n_s-1)}, \tag{1b}$$

$$\mathcal{U} = \begin{bmatrix} \boldsymbol{u}_1 & \boldsymbol{u}_2 & \dots & \boldsymbol{u}_{n_s-1} \end{bmatrix} \in \mathbb{R}^{N_u \times (n_s-1)}, \tag{1c}$$

$$\mathcal{Y} = \begin{bmatrix} \boldsymbol{y}_1 & \boldsymbol{y}_2 & \dots & \boldsymbol{y}_{n_s-1} \end{bmatrix} \in \mathbb{R}^{N_y \times (n_s-1)}, \tag{1d}$$

where n_s is the number of snapshots.

3. Methods

3.1. Model identification signal

In the present approach, ROMs are obtained by a data-driven model-identification procedure. Clearly, any ROM can only include information that is present in the data used for identifying it. Therefore, it is important to excite the system in a proper way during the data generation phase. The excitation signal, which is in this case the yaw input of the upstream turbine, should consider a number of requirements [12,13]: its spectrum should be such that the system response frequencies of interest are properly excited, it should account for limitations in the range of yaw angles and in the yaw rates, and it should be generated with an acceptable length based on

The Science of Making Torque from Wind (TORQUE 2018) IOP Publishing
IOP Conf. Series: Journal of Physics: Conf. Series **1037** (2018) 032014 doi:10.1088/1742-6596/1037/3/032014

a tradeoff between accuracy and computational time. To account for these characteristics, an APRBS (Amplitude-modulated Pseudo-Random Binary Sequence) signal [12, 13] was chosen to excite the system. Such a signal is based on the PRBS signal, a deterministic approximation of white noise in discrete time, which in turn results in a broad-band excitation of the system. Following the recommendations in Refs. [12–14], different values in the range of interest (yaw angles between $\pm 30°$) are assigned to different segments of the signal. This allows for the system to be excited in a wider range of values. Lastly, an APRBS-like yaw input signal is generated by inserting ramps to realistically connect the different steps of the APRBS. A ramp slope (yaw rate) of $30\,°\mathrm{s}^{-1}$ was chosen in agreement with the wind tunnel scaled model characteristics.

3.2. POD-based ROM

From the different ROM formulations proposed in the literature, the approach chosen for the present study is an I/O, data-driven, equation-free, POD-based approach, inspired by the formulation reported in Refs. [15–17]. This modeling procedure is intended to fit and compress the collected data into a standard state-space representation, in order to obtain models of a low computational cost, but also of sufficient quality. A considerable data reduction is obtained by extracting the most dominant features of the simulated system.

The reduced-order system is modeled as an explicit discrete-time time-invariant linear system in state-space form, which writes

$$\begin{cases} \tilde{\boldsymbol{x}}_{k+1} &= \tilde{\boldsymbol{A}}\tilde{\boldsymbol{x}}_k + \tilde{\boldsymbol{B}}\boldsymbol{u}_k, \\ \boldsymbol{y}_k &= \tilde{\boldsymbol{C}}\tilde{\boldsymbol{x}}_k + \tilde{\boldsymbol{D}}\boldsymbol{u}_k, \end{cases} \tag{2}$$

where k is the generic time instant, $\tilde{\boldsymbol{x}}_k \in \mathbb{R}^r$ is the reduced-order state vector, $\boldsymbol{u}_k \in \mathbb{R}^{n_u}$ is the input vector (i.e. the yaw angle of the upstream wind turbine; see Eq. (3)), and $\boldsymbol{y}_k \in \mathbb{R}^{n_y}$ is the output vector (i.e. the power outputs of the two turbines). Scalar r represents the order —or number of states— of the ROM. Matrices $\tilde{\boldsymbol{A}}$, $\tilde{\boldsymbol{B}}$, $\tilde{\boldsymbol{C}}$ and $\tilde{\boldsymbol{D}}$ have the appropriate dimensions.

In order to address non-linearities in the system and to improve the accuracy of the model, the input vector $\boldsymbol{u}_k$ was enriched so as to better capture the effects of yaw angle variations on the flow states $\tilde{\boldsymbol{x}}_k$ and power output $\boldsymbol{y}_k$. To this end, the input vector is defined as

$$\boldsymbol{u}_k = \boldsymbol{f}(\gamma_k) = (\gamma_k, \gamma_k^2, \gamma_k^3, \gamma_k^4, \cos^p(\gamma_k) - 1)^T, \tag{3}$$

where γ_k is the prescribed yaw angle. The non-linear relationship between yaw input and the variations of flow states and power outputs is modeled by the combination of a fourth order polynomial and a $\cos^p$ term. The latter is included considering the experimentally-derived relationship between yaw angle and power output [18], using the value $p = 1.787$. Regarding the system non-linearities that the polynomial fit partially handles, it should be noted that power is largely independent on the sign of the yaw angle misalignment. For this reason, even functions are required for properly modeling the relationship between yaw misalignment and power. Odd terms are also needed to match the behavior of the flow velocity components, and to handle any lack of symmetry in power output for positive and negative yaw angles.

The reduced-order state vector is obtained by projecting the full-order state vector $\boldsymbol{x}_k \in \mathbb{R}^{n_x}$ onto a lower-dimensional subspace of dimension r (typically, $n_x \gg r$). The relation between the full-order state vector and the reduced-order one is defined as:

$$\tilde{\boldsymbol{x}}_k = \boldsymbol{P}\boldsymbol{x}_k, \tag{4}$$

where $\boldsymbol{P} \in \mathbb{R}^{r \times n_x}$ is the projection subspace matrix. A suitable choice for the projection subspace matrix [15–17] is obtained by performing a singular value decomposition (SVD) of the snapshot matrix $\mathcal{X}$ of Eq. (1), which writes

$$\mathcal{X} = \boldsymbol{U}\boldsymbol{\Sigma}\boldsymbol{V}^T, \tag{5}$$

The Science of Making Torque from Wind (TORQUE 2018) IOP Publishing
IOP Conf. Series: Journal of Physics: Conf. Series **1037** (2018) 032014 doi:10.1088/1742-6596/1037/3/032014

where $\boldsymbol{U} \in \mathbb{R}^{n_x \times (n_s-1)}$ contains the left-singular vectors, $\boldsymbol{\Sigma} \in \mathbb{R}^{(n_s-1)\times(n_s-1)}$ the singular values and $\boldsymbol{V} \in \mathbb{R}^{(n_s-1)\times(n_s-1)}$ the right-singular vectors of $\mathcal{X}$. The left-singular vectors are, indeed, the so-called POD modes (POMs) of the system [19,20]. Using such modes for the generation of the subspace projection provides for major benefits, since POMs represent a series of intrinsic patterns of the flow (specifically, spatial and non-temporal ones). The temporal description, i.e. the evolution of the POMs over time, can be extracted from the right-singular vectors. Finally, the energy, or the weight, of each one of the POMs is given by the corresponding singular value.

The advantage of this decomposition is that, by only retaining a subset r of the POD modes, a high degree of compression of the original data can be obtained while still preserving a satisfactory modeling accuracy. In fact, the approximation of $\mathcal{X}$ can be written as

$$\mathcal{X} = \boldsymbol{U}\boldsymbol{\Sigma}\boldsymbol{V}^T = \begin{bmatrix}\boldsymbol{U}_r & \boldsymbol{U}_{n_s-1-r}\end{bmatrix} \begin{bmatrix}\boldsymbol{\Sigma}_r & \boldsymbol{0} \\ \boldsymbol{0} & \boldsymbol{\Sigma}_{n_s-1-r}\end{bmatrix} \begin{bmatrix}\boldsymbol{V}_r & \boldsymbol{V}_{n_s-1-r}\end{bmatrix}^T \simeq \boldsymbol{U}_r\boldsymbol{\Sigma}_r\boldsymbol{V}_r^T, \tag{6}$$

where $(\cdot)_r$ and $(\cdot)_{n_s-1-r}$ indicate a partitioning of the SVD matrices $\boldsymbol{U}$, $\boldsymbol{\Sigma}$ and $\boldsymbol{V}^T$. As previously stated, the projection subspace matrix that relates full- and reduced-order states is represented by the POD modes of the original system. In particular, a selection is used of the first r POD modes, i.e. the most energetic ones (characterized by higher singular values), which are also the ones typically associated with lower frequencies (and that are hence better resolved). This results in the following projection subspace matrix:

$$\boldsymbol{P} := \boldsymbol{U}_r^T. \tag{7}$$

Since $\boldsymbol{U}_r$ is a real orthogonal matrix formed by orthogonal unit vectors arranged in columns, the following relation holds

$$\boldsymbol{P}\boldsymbol{P}^T = \boldsymbol{I}_r, \tag{8}$$

where $\boldsymbol{I}_r$ is the $r \times r$ identity matrix.

Finally, consider the system of Eq. (2) expressed in compact form, i.e.

$$\begin{bmatrix}\tilde{\mathcal{X}}' \\ \mathcal{Y}\end{bmatrix} = \begin{bmatrix}\tilde{\boldsymbol{A}} & \tilde{\boldsymbol{B}} \\ \tilde{\boldsymbol{C}} & \tilde{\boldsymbol{D}}\end{bmatrix} \begin{bmatrix}\tilde{\mathcal{X}} \\ \mathcal{U}\end{bmatrix}, \tag{9}$$

where $\tilde{\mathcal{X}}'$ and $\tilde{\mathcal{X}}$ are the projections of $\mathcal{X}'$ and $\mathcal{X}$, respectively, onto the lower-dimensional subspace via matrix $\boldsymbol{P}$. Substituting the expressions of Eq. (4) and Eq. (7) into Eq. (9), the matrices defining the reduced-order state-space system can be readily obtained as:

$$\begin{bmatrix}\tilde{\boldsymbol{A}} & \tilde{\boldsymbol{B}} \\ \tilde{\boldsymbol{C}} & \tilde{\boldsymbol{D}}\end{bmatrix} = \begin{bmatrix}\boldsymbol{U}_r^T\mathcal{X}' \\ \mathcal{Y}\end{bmatrix} \begin{bmatrix}\boldsymbol{U}_r^T\mathcal{X} \\ \mathcal{U}\end{bmatrix}^{\dagger}. \tag{10}$$

4. Results

The model-compression procedure explained in the previous section was applied to raw CFD data in order to obtain the desired ROM. To this end, an APRBS signal was designed to excite the system by changing the upwind turbine yaw angle. The length of the training simulation was set to 60 s, which was considered long enough to appropriately excite the system within the range of $\pm 30°$, while limiting the computational costs. Then, the procedure explained in Sect. 3 was applied, resulting in a ROM with 22 POD modes. The order of the model was chosen as a best compromise between model size and error between high-fidelity and reduced-order-reconstructed flow and power outputs.

The Science of Making Torque from Wind (TORQUE 2018) IOP Publishing
IOP Conf. Series: Journal of Physics: Conf. Series **1037** (2018) 032014 doi:10.1088/1742-6596/1037/3/032014

Subsequently, a second CFD simulation was performed with a different input signal to validate the prediction capabilities of the previously obtained ROM. The ROM was verified for this validation test case in two different variants: in conjunction with a Kalman filter (KF) state observer [21], which uses the power measured at the two machines to estimate and update the model state vector, and in open loop. The process noise covariance matrix of the KF (Q_k) was tuned by differently weighting each element of the reduced-order state, i.e. each POD mode. Specifically, modes with higher energies and better resolution (low frequency spectra) were assigned smaller covariances. The measurement noise covariance matrix R_k was set to a low value, since power measurements can be assumed to be highly accurate.

A few of the POD modes of the system are displayed in Fig. 1. Each POM includes the three velocity components for the two planes of data collection; however, only the horizontal plane and the streamwise velocity component are plotted in Fig. 1. The low-index POD modes exhibit patterns that are consistent with the expected behavior resulting from an excitation by yawing of the upwind turbine, and indicate large spatial variations of the flow. High-index POMs (e.g. number 200 in Fig. 1) preserve, on the other hand, the high-fluctuating spatial behavior of the underlying high-fidelity data, and are therefore associated with lower energies. As explained in Sect. 3, POMs are also associated to a specific frequency content, stored in the right-singular vectors of the SVD. Commonly, POMs with low indices present also low-frequency spectra, and vice versa. Indeed, a frequency analysis (discrete Fourier transform, DFT) was performed for the POMs retained in the ROM. Their frequency spectrum was found to be below 15 Hz. Given that the Nyquist frequency associated with the sampling frequency is 50 Hz, this result ensures that the sampling is large enough to capture the mode dynamics.

A comparison of the power outputs of the validation case CFD simulation and ROM reconstruction is shown in Fig. 2. The power variations of both turbines predicted by the model is given directly in the model output vector, as stated in Eq. (2). The use of the Kalman filter —which feeds power measurements from the plant back to the ROM— improves the quality of predictions. Indeed, the time-averaged percentage error between CFD and ROM-predicted power outputs reduced from 3.83%, 6.68% and 3.64% for the case without KF, to 1.81%, 3.98% and 1.89% for the case with KF, where the three values refer to the upstream turbine (WT1), the downstream one (WT2) and the whole cluster, respectively. In open-loop, the model does not receive any information from the plant regarding power changes due to flow fluctuations. This appears clearly in the figure where, for constant yaw angles, the model cannot accurately predict the fluctuating behavior of power other than the intrinsic dynamics contained in the ROM.

The reconstructed full-order flow produced by the ROM can be approximated combining Eqs. (4) and (7). A comparison between CFD high-fidelity data and ROM-based reconstructed flow is shown in Figs. 3 and 4 for a given instant in time. ROM predictions, with and without state observer, match the average wake shape and position. On the other hand, smaller scale fluctuations and wake meandering are not captured. Notice further that the Kalman filter is capable of enhancing the behavior of the model in terms of power predictions, without visually substantially affecting the macroscopic flow behavior in the wake.

Finally, the behavior of the model was also tested with data from a wind tunnel experiment [5], under very similar conditions in terms of yaw dynamic changes, inflow and turbulent intensity of the numerical test conducted so far. However, crucially, in the wind tunnel experiments the two turbines were spaced 5D, while the simulations used to generate the ROM used a spacing of only 4D. In other words, the ROM was created on purpose with a significant built-in model mismatch. The ROM predictions are compared with the experimental data in terms of turbine power outputs in Fig. 5. It is observed, indeed, that the predicted power for the downwind turbine is always smaller than the actual one. This is expected, since in the experiment the wake recovered further before impinging onto the downstream wind turbine, due to the larger

The Science of Making Torque from Wind (TORQUE 2018) IOP Publishing
IOP Conf. Series: Journal of Physics: Conf. Series **1037** (2018) 032014 doi:10.1088/1742-6596/1037/3/032014

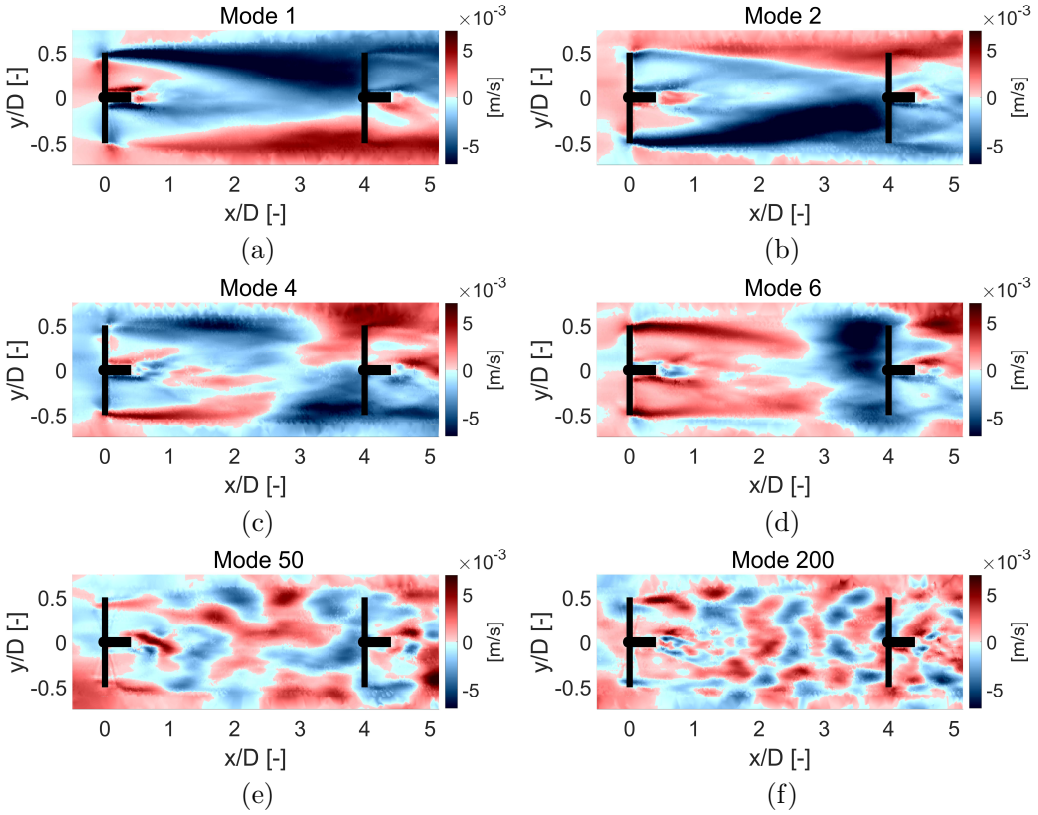

Figure 1: Selection of POD modes of the simulated system (only the mode streamwise velocity components in the XY plane are shown).

distance between the two machines. The KF is able to partially correct for this model defect. For the upwind turbine, the prediction fluctuates but does not present a systematic bias, as there is not a model mismatch in this case. Even considering the error due to the different wind farm layout, the ROM seems to be capable of predicting the power outputs with acceptable accuracy.

5. Conclusions and outlook

In this paper, a compression technique based on the POD is applied to obtain ROMs with very low computational cost and good accuracy, suitable for model-based wind farm control. The present study has focused on a two-turbine cluster, where yaw misalignment of the front machine is used for wake steering. To further improve the quality of predictions, the resulting ROM has been optionally equipped with a KF, which feeds power measurements from the plant back onto the model. Results indicate that the proposed method is able to represent well, when compared to high-fidelity CFD-simulated data, the wake characteristics of both turbines and their respective power outputs. Regarding flow predictions, a proper deflection and development of the wake is observed. With respect to power outputs, the predictions are also accurate and correlate well with changes in the upwind turbine yaw angle. When compared to wind tunnel experiments, acceptable results are also obtained, including the capability of the model to partially correct for an intentionally built-in model mismatch.

The present work will be expanded in multiple directions. Regarding model updating, it

The Science of Making Torque from Wind (TORQUE 2018) IOP Publishing
IOP Conf. Series: Journal of Physics: Conf. Series **1037** (2018) 032014 doi:10.1088/1742-6596/1037/3/032014

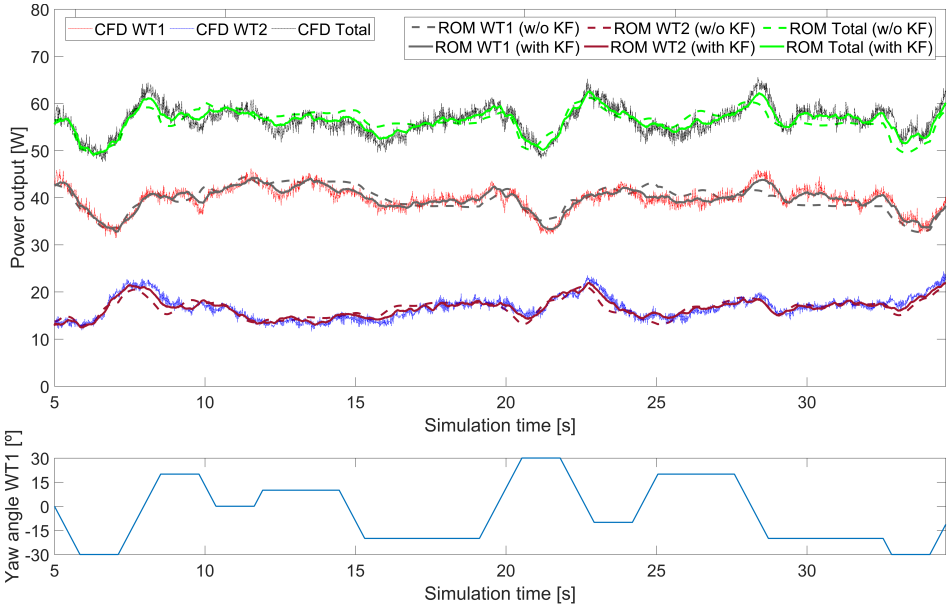

Figure 2: Comparison between CFD data and ROM-predicted power outputs (top); yaw angle time history for the upstream wind turbine (bottom).

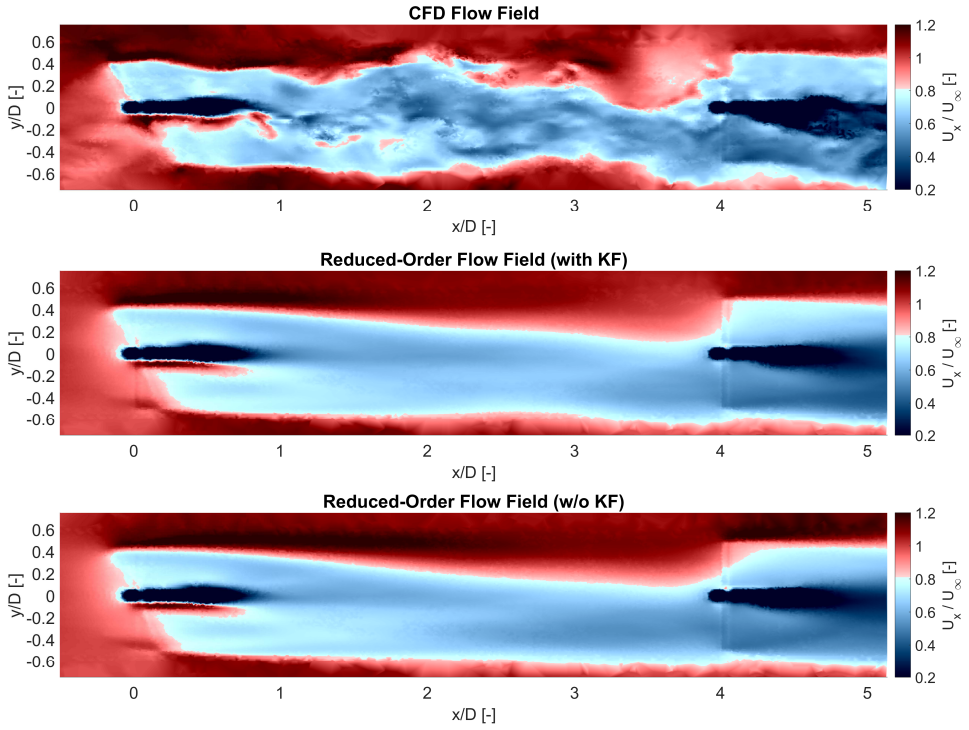

Figure 3: Comparison of the streamwise velocity component on the horizontal plane between the CFD flow (top), ROM-predicted flow with KF state observer (middle), and ROM-predicted flow without state observer (bottom) at one instant in time ($\gamma = 23°$).

The Science of Making Torque from Wind (TORQUE 2018) IOP Publishing
IOP Conf. Series: Journal of Physics: Conf. Series **1037** (2018) 032014 doi:10.1088/1742-6596/1037/3/032014

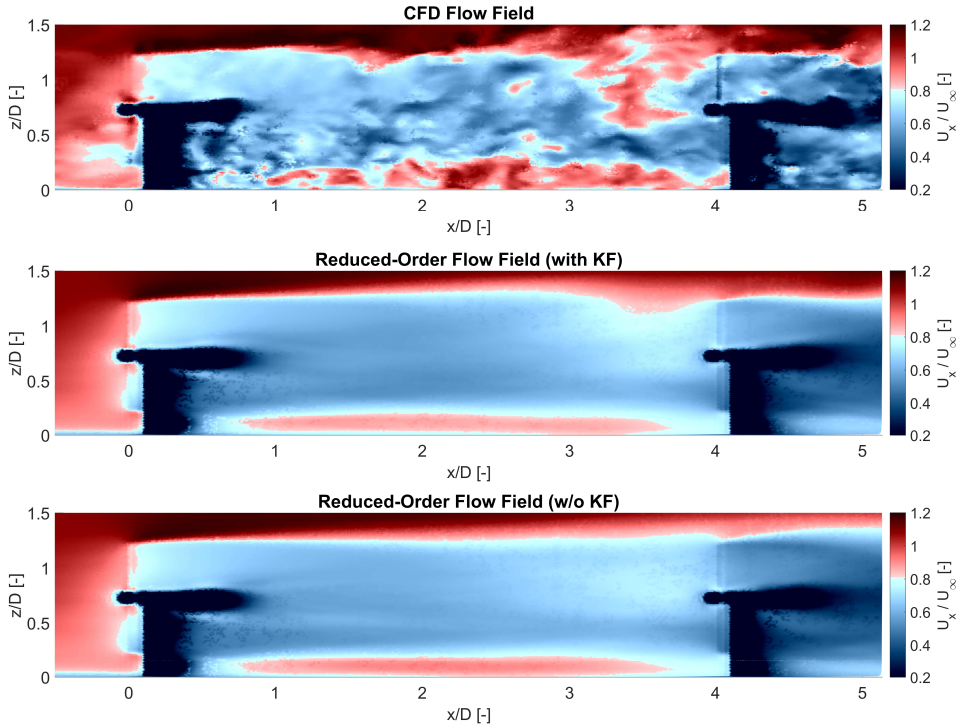

Figure 4: Comparison of the streamwise velocity component on the vertical plane between the CFD flow (top), ROM-predicted flow with KF state observer (middle), and ROM-predicted flow without state observer (bottom) at one instant in time ($\gamma = 23°$).

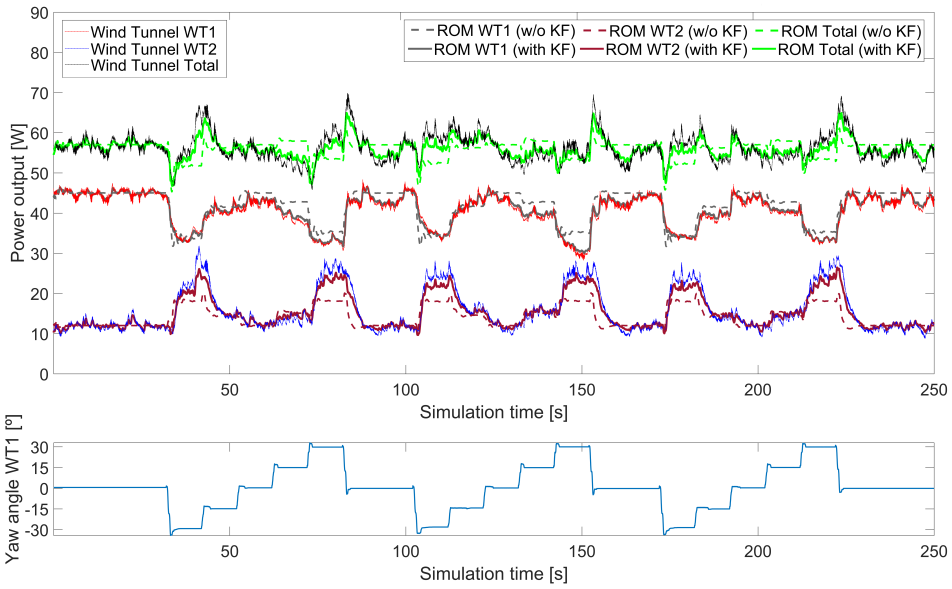

Figure 5: Comparison between wind tunnel and ROM-predicted power outputs considering a model mismatch (top); yaw angle time history for the upstream wind turbine (bottom).

should be mentioned that, in addition to power, other plant measurements can be used to improve the predictive capabilities of the method. For example, Ref. [22] uses local estimates of the wind speed on the rotor disk, obtained by using blade load measurements. Additional work will try to improve the generality of the approach. In fact, since the method is based on system identification, ROMs are derived for a particular configuration and operating condition (wind farm layout, wind speed, TI, etc.). If other conditions are desired, additional high-fidelity CFD simulations are required (cf. [23]). While this problem cannot be completely bypassed, there are techniques that we are currently exploring to reduce the complexity of the approach and its associated computational effort.

Acknowledgments
This work has been partially supported by the CL-Windcon project, which receives funding from the European Union Horizon 2020 research and innovation program under grant agreement No. 727477. The authors express their appreciation to the Leibniz Supercomputing Centre (LRZ) for providing access and computing time on the SuperMUC Petascale System under Projekt-ID pr84be.

References

[1] Fleming P A, Gebraad P M O, Lee S, van Wingerden J-W, Johnson K, Churchfield M, Michalakes J, Spalart P and Moriarty P 2014 *Renew. Energ.* **70** 211-8
[2] Gebraad P M O, Teeuwisse F W, van Wingerden J-W, Fleming P A, Ruben S D, Marden J R and Pao L Y 2014 *American Control Conference (ACC), 2014* 3128–34
[3] Gebraad P M O, Teeuwisse F W, van Wingerden J-W, Fleming P A, Ruben S D, Marden J R and Pao L Y 2016 *Wind Energ.* **19** 95–114
[4] Wang J, Bottasso C L and Campagnolo F 2016 *J. Phys.: Conf. Series* **753** 32064
[5] Campagnolo F, Petrović, Schreiber J, Nanos E M, Croce A and Bottasso C L 2016 *J. Phys.: Conf. Series* **753** 32006
[6] Munters W and Meyers J 2017 *Phil. Trans. R. Soc. A.* **375** 20160100
[7] Churchfield M and Lee S 2012 NWTC design codes-SOWFA `URL: https://nwtc.nrel.gov/SOWFA`
[8] Jonkman J M and Buhl Jr. M L 2005 FAST User's Guide-Updated August 2005 *National Renewable Energy Laboratory (NREL), Golden, CO (United States)*
[9] Mittal R and Iaccarino G 2005 *Annu. Rev. Fluid Mech.* **37** 239–61
[10] Bottasso C L, Campagnolo F and Petrović V 2014 *J. Wind Eng. Ind. Aerod.* **127** 11–28
[11] Wang J, Foley S, Nanos E M, Yu T, Campagnolo F, Bottasso C L, Zanotti A and Croce A 2017 *J. Phys.: Conf. Series* **854** 012048
[12] Isermann R and Münchhof M 2010 *Identification of Dynamic Systems: an Introduction with Applications* (Springer Science & Business Media)
[13] Nelles O 2013 *Nonlinear System Identification: from Classical Approaches to Neural Networks and Fuzzy Models* (Springer Science & Business Media)
[14] Deflorian M and Zaglauer S 2011 *IFAC Proc. Vol.* **44** 13179–84
[15] Annoni J, Gebraad P M O and Seiler P 2016 *American Control Conference* 506–12
[16] Proctor J L, Brunton S L and Kutz J N 2016 *SIAM J. Appl. Dyn. Syst.* **15** 142–61
[17] Annoni J, Nichols J and Seiler P 2016 *34th Wind Energy Symposium* 2201
[18] Schreiber J, Nanos E M, Campagnolo F and Bottasso C L 2017 *J. Phys.: Conf. Series* **854** 012041
[19] Holmes P 2012 *Turbulence, Coherent Structures, Dynamical Systems and Symmetry* (Cambridge University Press)
[20] Kerschen G and Golinval J-C 2002 *J Sound Vib.* **249** 849–65
[21] Kalman R E 1960 *J. Basic Eng.* **82** 35–45
[22] Bottasso C L, Cacciola S and Schreiber J 2018 *Renew. Energ.* **116** 155–68
[23] Annoni J and Seiler P 2017 *Int. J. Robust Nonlinear Control* **4** 582–97

https://doi.org/10.5194/wes-2020-115
Preprint. Discussion started: 10 November 2020

eawe european academy of wind energy
Open Access WIND ENERGY SCIENCE DISCUSSIONS

How realistic are the wakes of scaled wind turbine models?

Chengyu Wang[1], Filippo Campagnolo[1], Helena Canet[1], Daniel J. Barreiro[1], and Carlo L. Bottasso[1]
[1]Wind Energy Institute, Technische Universität München, D-85748 Garching b. München, Germany
Correspondence: Carlo L. Bottasso (carlo.bottasso@tum.de)

Abstract.

The aim of this paper is to analyze to which extent wind tunnel experiments can represent the behavior of full-scale wind turbine wakes. The question is relevant because on the one hand scaled models are extensively used for wake and farm control studies, whereas on the other hand not all wake-relevant physical characteristics of a full-scale turbine can be exactly matched by a scaled model. In particular, a detailed scaling analysis reveals that the scaled model accurately represents the principal physical phenomena taking place in the outer shell of the near wake, whereas differences exist in its inner core. A large eddy simulation actuator line method is first validated with respect to wind tunnel measurements, and then used to perform a detailed comparison of the wake at the two scales. It is concluded that, notwithstanding the existence of some mismatched effects, the scaled wake is remarkably similar to the full-scale one, except in the immediate proximity of the rotor.

1 Introduction

The simulation of wind turbine wakes in wind tunnels has been gaining an increasing interest in recent years. In fact, since wakes represent a major form of coupling within a wind plant, understanding their behavior and accurately simulating their effects are today problems of central importance in wind energy science, with direct practical implications on design, operation and maintenance. Recent studies include the analysis of single and multiple interacting wakes (see, for example, the review in Bottasso and Campagnolo (2020) or, among others, Whale et al. (1996); Chamorro and Porté-Agel (2009, 2010); Bartl and Sætran (2016); Bastankhah and Porté-Agel (2016); Tian et al. (2018); Campagnolo et al. (2016); Bottasso et al. (2014a); Campagnolo et al. (2020); Wang et al. (2020c) and references therein).

Wind tunnel testing offers some unique advantages over full-scale field testing:

- The ambient conditions are repeatable and —at least to some extent— controllable.
- Detailed flow measurements are possible with a plethora of devices, from standard pressure and hot-wire probes, to PIV (Meinhart, 1999) and scanning lidars (van Dooren et al., 2017), whereas measurements of comparable accuracy are today hardly possible at full scale. Additionally, time flows faster in a scaled experiment than at full scale (Bottasso and Campagnolo, 2020; Canet et al., 2020; Campagnolo et al., 2020), which means that a large informational content can be accumulated over relatively short periods of time.

https://doi.org/10.5194/wes-2020-115
Preprint. Discussion started: 10 November 2020

eawe european academy of wind energy
Open Access WIND ENERGY SCIENCE DISCUSSIONS

- Models can be designed ad hoc to achieve specific goals, and can be extensively instrumented (Bottasso and Campagnolo, 2020), while layouts and scenarios can be readily changed to explore different operating conditions of interest.
- Costs are limited, even for highly sophisticated models, also because there are no energy production losses as it is often the case in the field, whereas the costs of sophisticated wind tunnel facilities are typically amortized by their use for several different applications over long periods of time.
- Open datasets can be shared within the research community and collaborations are facilitated, since there are no —or fewer— constraints from intellectual property than when real wind turbine data is used.

Testing in the controlled and repeatable environment of the wind tunnel is today contributing to the understanding of the physical processes at play, generates valuable data for the validation and calibration of mathematical models, and offers opportunities for the verification of control technologies.

However, notwithstanding these and other unique advantages, a major question still hovers over the wind tunnel simulation of wakes: *how faithful are these wakes to the actual ones in the field?* In fact, in private conversations these authors have often been questioned on the actual usefulness of wind tunnel testing, based on a perceived lack of realism of these scaled tests. Indeed, some skepticism is justified and completely understandable: simulation codes are being calibrated and validated with respect to wind tunnel measurements, and wind farm control techniques are being compared and evaluated in wind tunnel experiments. Therefore, it is important to quantify the level of realism of wind tunnel simulated wakes, and to identify with better clarity what aspects faithfully represent the full-scale truth and what aspects do not.

A thorough and complete answer to this question is probably still out of reach today. In fact, detailed inflow and wake measurements of a full-scale turbine would be necessary, with a level of detail comparable to the ones achievable in the tunnel. Lidar technology is making great progress (Zhan, 2020), and might soon deliver suitable datasets. It should be a goal of the scientific and industrial communities to completely open such future datasets to research, which would surely greatly favor the scientific advancement of the field. In the meanwhile, however, some partial answers to the question of wake realism can still be given. This is the main goal of the present paper.

This study considers the TUM G1 scaled wind turbine (Bottasso and Campagnolo, 2020), and a dataset obtained with this machine in the boundary layer wind tunnel of the Politecnico di Milano in Italy. A large eddy simulation (LES) actuator line method (ALM) (Wang et al., 2019) is used to simulate the wind tunnel experiments, including the passive generation of a sheared turbulent inflow. The code has been validated with respect to the present and other similar measurements.

Following Bottasso and Campagnolo (2020) and Canet et al. (2020), dimensional analysis and wake physics are used to review the main factors driving wake behavior. The same analysis also reveals which physical aspects of full-scale wakes cannot be matched at the reduced scale and with the considered experimental setup. A first analysis of scaling was performed by Chamorro et al. (2016), considering the effects caused by the mismatch of the rotor-based Reynolds. Experimental results based on a miniature wind turbine showed that wake behaviour is unaffected by this parameter when it is larger than circa 10^5. However, in reality the behavior of the blades and, as a consequence, of the wake is much more strongly affected by the chord-based Reynolds number, as initially discussed in Bottasso et al. (2014a). In fact, the much lower Reynolds regime of a

https://doi.org/10.5194/wes-2020-115
Preprint. Discussion started: 10 November 2020

eawe european academy of wind energy
Open Access WIND ENERGY SCIENCE DISCUSSIONS

small-scale model blade compared to a full-scale machine implies very different aerodynamic characteristics of the airfoils, which in turn drive a number of specific design choices of the scaled model (Bottasso and Campagnolo, 2020; Canet et al., 2020). Notwithstanding the differences caused by the chord-based Reynolds mismatch, it is relatively easy —as shown more in detail later on— to match the main processes taking place in the outer shell of the near wake, as well as the ones that govern its breakdown and the characteristics of the far wake. On the other hand, several mismatched effects do exist in the central core of the near wake. Dimensional analysis also expresses the scaling relationships that allow the mapping of scaled quantities into equivalent full-scale ones, and viceversa.

Based on the understanding provided by dimensional analysis and wake physics, full-scale turbines are designed in this work to match some of the G1 scaled-model parameters. Various versions of these models are considered, ranging from a more realistic full-scale turbine —with a larger number of mismatched effects— to less realistic ones that however match a larger set of quantities of the scaled model.

The full-scale models are then simulated with the LES-ALM code, using the same exact numerical methods and algorithmic parameters used for the scaled simulations. These wind turbine models are also exposed to the same identical ambient turbulent inflow used for the scaled model. The underlying assumption is that, since the code was found to be in very good agreement with measurements obtained in the scaled experiments, the same code based on the same numerical setup should deliver results of similar accuracy even at full scale. This assumption cannot be formally proven at this stage, but it seems to be very reasonable and it is probably the only possible approach that can be pursued in the absence of a detailed full-scale dataset.

Finally, the numerically simulated scaled and full-scale wakes are compared. The analysis considers wind-aligned and misaligned conditions, typical of wake steering control applications, and various metrics, including wake shape, path, speed profile, Reynolds shear stresses, power available and wind direction modification due to the curled wake in misaligned conditions. This detailed comparison is used to quantify the degree of similarity among the different models and across the various metrics. Since the models differ by known mismatched effects, this also helps pinpoint and explain any source of discrepancy.

The paper is organized according to the following plan. Section 2 uses dimensional analysis and wake physics to identify the quantities that can be exactly matched between scaled and full-scale models, the ones that can only be partially matched, the ones that are unmatched, and those that are neglected from the present analysis. Next, Section 3 describes the scaled experimental wind turbine and its full-scale counterparts, which include various modifications to highlight the effects of specific mismatches. Section 4 describes the numerical simulation model, including the generation of the turbulent inflow in the wind tunnel. Results and detailed comparisons among the scaled and the full-scale models are reported in Section 5. Finally, Section 6 summarizes the main findings of this work.

2 Scaling

The matched, partially matched, unmatched and neglected physical effects of the scaled and full-scale models are reviewed next. Quantities referred to the scaled model are indicated with the subscript $(\cdot)_M$, while quantities referred to the full-scale physical system with the subscript $(\cdot)_P$. Scaling is defined by two parameters (Bottasso and Campagnolo, 2020; Canet et al.,

https://doi.org/10.5194/wes-2020-115
Preprint. Discussion started: 10 November 2020

eawe european academy of wind energy
Open Access WIND ENERGY SCIENCE DISCUSSIONS

2020): the length scale factor $n_l = l_M/l_P$, where l is a characteristic length (for example the rotor radius R), and the time compression ratio $n_t = t_M/t_P$, where t is time. In the present case $n_l = 1/162.1$ and $n_t = 1/82.5$. A more complete treatment of scaling for wind turbine rotors is given in Bottasso and Campagnolo (2020) and Canet et al. (2020).

2.1 Matched quantities

- Inflow. The ambient flow is obtained by simulating the passive generation of turbulence in the wind tunnel, as explained in §4.2; the developed flow is sampled on a rectangular plane, which becomes the inflow of the scaled turbine simulations. For the full-scale turbine simulations, the sides of the inflow rectangular area are geometrically scaled by n_l, while time is scaled by n_t and speed V as $V_M/V_P = n_l/n_t$, resulting in a flow with exactly the same identical characteristics (e.g., shear, turbulence intensity, integral length scale, etc.) at the two scales.

- Tip speed ratio (TSR) $\lambda = \Omega R/V$, where Ω is the rotor speed. TSR determines not only the triangle of velocity at the blade sections, but also the pitch of the helical vortex filaments shed by the blade tips.

- Non-dimensional circulation $\Gamma(r)/(RV) = 1/2\,(c(r)/R)\,C_L(r)(W(r)/V)$, where C_L is the lift coefficient, c the local chord, W the local flow speed relative to the blade section, and r is the spanwise blade coordinate (Burton et al., 2011). Each blade sheds trailing vorticity that is proportional to the spatial (spanwise) gradient $\mathrm{d}\Gamma/\mathrm{d}r$. Therefore, matching the non-dimensional spanwise distribution of Γ (and, hence, also its non-dimensional spanwise gradient) ensures that the two rotors shed the same trailing vorticity.

  The root of the G1 blade is located further away from the rotor axis than a typical full-scale machine, due to the space required for housing the pitch actuation system. The resulting effects caused on the wake were investigated by developing two different full-scale models, one with the exact same non-dimensional circulation of the G1 and one with more typical full-scale values, as discussed later.

- Rotor vortex shedding. The rotor Strouhal number $\mathrm{St} = f2R/V$ is matched, where f is the rotor vortex-shedding characteristic frequency, which ensures the correct periodic release of vortices behind the rotor.

2.2 Approximatively matched quantities

The following quantities or effects are very nearly, but not exactly, matched:

- Thrust coefficient $C_T = T/(1/2\rho A V^2)$, where T is the thrust force, ρ is air density and $A = \pi R^2$ the rotor swept area. The thrust characterizes to a large extent the speed deficit in the wake. In misaligned conditions, it is also the principal cause for the lateral deflection of the wake. The thrust coefficient is very nearly matched whereas the power coefficient is not (as discussed later), because the latter strongly depends on airfoil efficiency, which is affected by the Reynolds mismatch between the two models. On the other hand, drag has only a limited effect on thrust, which as a result is very similar in the two models.

https://doi.org/10.5194/wes-2020-115
Preprint. Discussion started: 10 November 2020

eawe european academy of wind energy
Open Access WIND ENERGY SCIENCE DISCUSSIONS

– Dynamic spanwise vortex shedding. During transients, spanwise vorticity is shed that is proportional to the temporal gradient of the circulation. To match the spanwise vortex shedding of a rotor, the matching of $(1/RV)\mathrm{d}\Gamma/\mathrm{d}\tau$ should be ensured (Bottasso and Campagnolo, 2020; Canet et al., 2020), where τ is a non-dimensional time (for example, $\tau = \Omega_r t$, Ω_r being a reference rotor speed), equal for both the full and scaled models.

  Rewriting the circulation as

$$\frac{\Gamma}{RV} = \frac{1}{2}\frac{c}{R}C_{L_\alpha}\frac{W}{V}\left(\frac{U_P U_T}{W^2} - \theta\right), \tag{1}$$

  C_{L_α} being the lift curve slope, the dynamic spanwise vortex shedding condition implies the matching of the non-dimensional time rates of change of the sectional tangential and perpendicular flow components U_P and U_T, with $W^2 = U_P^2 + U_T^2$, and of the pitch angle θ. The flow speed component tangential to the rotor disk is $U_T = \Omega r + u_T$, where u_T contains terms due to wake swirl and yaw misalignment. The flow speed component perpendicular to the rotor disk is $U_P = (1-a)V + u_P$, where a is the axial induction factor, and u_P the contribution due to yaw misalignment and vertical shear. A correct similitude of dynamic vortex shedding is ensured if the non-dimensional time derivatives λ', a', u_P', u_T' and θ' are matched, where $(\cdot)' = \mathrm{d}\cdot/\mathrm{d}\tau$.

  Matching of λ' is ensured here by the fact that the two rotors operate at the same TSR in the same inflow; additionally, the simulations were conducted by prescribing the rotor rotation (i.e. without a controller in the loop), so that $\Omega' = 0$. The term a' accounts for dynamic changes in the induction, which are due to the speed of actuation (of torque and blade pitch) and by the intrinsic dynamics of the wake. The speed of actuation is not relevant in this case, due to the absence of a pitch-torque controller. The intrinsic dynamics of the wake, as modelled by a first order differential equation (Pitt and Peters, 1981), is also automatically matched thanks to the matching of the TSR (Bottasso and Campagnolo, 2020; Canet et al., 2020). Finally, u_P' and u_T' are matched because the inflow is the same, with the exception of the contribution of wake swirl, which is not exactly the same because of the different torque coefficient, as noted below.

– Inflow size. The cross section of the wind tunnel has a limited size, resulting in the blockage phenomenon, i.e. in an acceleration of the flow between the object being tested and the sides (lateral walls and ceiling) of the tunnel (Chen and Liou, 2011). Although this problem is not strictly related to the scaling laws discussed here, it is still an effect that needs to be accounted for, especially if the ratio of the frontal area of the tested objected and the cross sectional area of the tunnel is not negligible. Simulations in domains of increasingly larger cross sections are conducted to quantify the blockage affecting the experimental setup considered here.

– Integral length scales (ILS). For the size of the TUM G1 turbines, the wind tunnel used in this research (located at Politecnico di Milano, Italy) generates a full-scale ILS of approximately 142 m at hub height, which is respectively about 16% and 58% smaller that the lengths specified by Ed. 2 (IEC 61400-1, 1999) and Ed. 3 (IEC 61400-1, 2005) of the IEC 61400-1 international standards. To understand the effects of this mismatch on wake behavior, different simulations are conducted in turbulent inflows differing only in their integral scales.

https://doi.org/10.5194/wes-2020-115
Preprint. Discussion started: 10 November 2020

eawe european academy of wind energy
Open Access WIND ENERGY SCIENCE DISCUSSIONS

2.3 Unmatched quantities

The following quantities cannot be matched based on the current experimental setup and scaling choices:

- The chord-based Reynolds number $\mathrm{Re} = \rho W c/\mu$, where μ is the fluid viscosity. The Reynolds mismatch is $\mathrm{Re}_M/\mathrm{Re}_P = n_l^2/n_t$, which is equal to 318.5 in the present case. This implies that the blades of the G1 model operate in a very different regime than the ones of the full-scale blade (Lissaman, 1983). To mitigate these effects, the G1 blade has a larger chord than the full-scale one, and uses ad hoc low-Reynolds airfoils (Bottasso and Campagnolo, 2020; Lyon and Selig, 1996). Additionally, noting that the scaling relationship of the rotor speed is $\Omega_M/\Omega_P = 1/n_t$, the time compression ratio n_t was chosen to further increase Reynolds on the scaled blade and reduce its mismatch (Bottasso and Campagnolo, 2020).

- The power coefficient $C_P = P/(1/2\rho A V^3)$, where P is the aerodynamic power. The power coefficient of the scaled model is lower than the one of the full-scale machine, because of the smaller efficiency of the airfoils at low-Reynolds regimes. Since the torque coefficient is $C_Q = C_P/\lambda$, then also C_Q is unmatched and lower for the small-scale model than for the full-scale one, resulting in reduced wake swirling (Burton et al., 2011).

- Tower and nacelle vortex shedding. The tower Strouhal number $\mathrm{St} = fd/V$ is matched when the tower diameter d is geometrically scaled. However, as noted later, the diameter of the G1 tower is 49% larger than the one of the full-scale machine, so that frequency and size of the shed vortices is accordingly affected. An even larger mismatch applies to the nacelle, which has a frontal area that is 2.6 times larger in the scaled model.

- Stall delay due to rotational augmentation (Dowler and Schmitz, 2015). Matching these effects requires the matching of the blade chord and twist distributions, of the non-dimensional circulation and of the Rossby number $\mathrm{Ro} = \Omega r/(2W)$ (Bottasso and Campagnolo, 2020). While the latter two quantities are indeed matched, the former two are not to compensate for Reynolds mismatch. The G1 simulations were conducted without correcting the inboard airfoils for rotational augmentation. To quantify the effects of rotational augmentation on wake behavior, two versions of the full-scale turbine were developed, as explained later on.

- The chord-based Mach number $\mathrm{Ma} = W/s$, where s is the speed of sound. However compressibility effects are irrelevant for the full and scaled models considered here, as for virtually all present-day wind turbines.

- Boundary layer stability and wind veer due to the Coriolis force. The wind tunnel used in the present research can only general neutrally stable boundary layers. Although atmospheric stability has a profound effect on wakes (Abkara and Porté-Agel, 2015), this problem has already been studied elsewhere, and it is considered to be out of scope for the present investigation. Similarly, Coriolis effects on the inflow and wake behavior are not represented in a wind tunnel, although they are known to have non-negligible effects on capture, loading and also on wake path (van der Laan and Sørensen, 2007).

https://doi.org/10.5194/wes-2020-115
Preprint. Discussion started: 10 November 2020

eawe european academy of wind energy
Open Access WIND ENERGY SCIENCE DISCUSSIONS

2.4 Neglected quantities

The following effects could be matched with a different experimental setup and scaling choices, but were neglected in the present work:

- All gravo-aeroelastic effects. Since the blades of the G1 turbine are not aeroelastically scaled (and are very stiff), also the full-scale model was simulated without accounting for flexibility. Aeroelasticity could have some effects on near-wake behavior for very flexible rotors, but would probably have only a negligible role on the characteristics of the far wake. Therefore, aeroelastic effects were excluded from the scope of the present investigation.
- Unsteady airfoil aerodynamics, including linear unsteady corrections (for example, according to Theodorsen's theory (Bisplinghoff and Ashley, 2002)), and dynamic stall. It was verified that the mildly misaligned operating conditions analyzed here would not have triggered dynamic stall, except than in a few instances, similarly to what was found in Shipley (1995). Here again, these effects would hardly have any visible effects on far-wake behavior.

2.5 Remarks

Wake stability analysis shows that the vortical structures released by the blade tips and root interact in the near wake (Okulov and Sørensen, 2007).

In the outer shell of the near wake, the mutual interaction of the tip vortices —triggered by turbulent fluctuations and vortex shedding— lead to vortex pairing, leapfrogging, and eventually to the breakdown of the coherent wake structures (Sørensen, 2011). The scaled and full-scale rotors are exposed to the same inflow (including the same turbulent fluctuations), experience the same vortex shedding (due to a matched Strouhal), the tip vortices have the same geometry (due to a matched TSR) and strength (due to a matched circulation), and the speed deficit is also essentially the same (because of the very nearly matched thrust coefficient). Hence, it is reasonable to assume a nearly identical near wake behavior of the external wake shell, given that all main processes are matched between scaled and full-scale models (with the exception of the effects that the unmatched tower may have).

The situation is different in the near wake inner core. Here the root vortices combine with the effects caused by the presence of the nacelle and tower. In particular, the nacelle has a much larger frontal area, creating a different blockage (radial redirection), nacelle wake and vortex shedding. Additionally, in the 20% inboard portion of the blade, both the circulation and rotational augmentation effects are unmatched. Finally, the mismatch of power induces a mismatch of torque that reduces wake swirl; as it is well known from blade element momentum (BEM) theory, swirl is mostly concentrated in the inner core of the wake, and decays rapidly with radial position (Burton et al., 2011). Hence, the near wake inner core is expected to behave differently in the scaled and full-scale models. However, some of the results reported here, in addition to evidence from other sources (Wu and Porté-Agel, 2011), indicate that the inner core near wake has only a modest effect on far-wake behavior. For example, it is common practice to simulate far-wake behavior with LES codes without even representing the turbine nacelle and tower (Martínez-Tossas et al., 2015).

https://doi.org/10.5194/wes-2020-115
Preprint. Discussion started: 10 November 2020

eawe european academy of wind energy
Open Access WIND ENERGY SCIENCE DISCUSSIONS

As a consequence, thanks to the employed scaling and matching criteria, the far-wake behavior is expected to be extremely similar between the wind tunnel generated wake and the full-scale one. The results section will more precisely support this claim.

3 Wind turbine models

3.1 The TUM G1 scaled wind turbine

The TUM G1 is a three-bladed clockwise-rotating (looking downstream) wind turbine, with a rotor diameter D of 1.1 m, a hub height H of 0.825 m, and rated rotor and wind speeds of 850 rpm and 5.75 ms^{-1}, respectively. The G1 was designed based on the following requirements (Bottasso and Campagnolo, 2020):

- A realistic energy conversion process and wake behavior;
- A sizing of the model obtained as a compromise between Reynolds mismatch, miniaturization constraints, limited wind tunnel blockage and ability to simulate multiple wake interactions within the size of the test chamber;
- Active individual pitch, torque and yaw control in order to test modern control strategies at the turbine and farm levels;
- A comprehensive on-board sensorization.

The turbine has been used for several research projects and numerous wind tunnel test campaigns (Campagnolo et al., 2016, 2020). The main features of the G1 rotor and nacelle are shown in Fig. 1a.

A brushless motor equipped with a precision gearhead and a tachometer is installed in the rear part of the nacelle and provides for the rotor torque, which is in turn measured by a torque sensor located behind the two shaft bearings. An optical encoder, located between the slip ring and the rear shaft bearing, measures the rotor azimuth, while two custom-made load cells measure the bending moments at the foot of the tower and in front of the aft bearing. Thrust is estimated from the tower base fore-aft bending moment, correcting for the drag of the tower and rotor-nacelle assembly.

Each wind turbine model is controlled by its own dedicated real-time modular Bachmann M1 system, implementing supervisory control functions, pitch-torque-yaw control algorithms, and all necessary safety, calibration and data logging functions. Measurements from the sensors and commands to the actuators are transmitted via analogue and digital communication. The Bachmann M1 system is capable of acquiring data with a sample rate of 2.5 kHz, which is used for acquiring aerodynamic torque, shaft bending moments and rotor azimuth position. All other measurements are acquired with a sample rate of 250 Hz.

3.2 Full-scale wind turbine

A full-scale wind turbine was designed through a backward-engineering approach to match the characteristics of the G1 scaled machine. The DTU 10 MW wind turbine (Bak et al., 2013), shown in Fig. 1b, was used as a starting design for this purpose. This turbine has a rotor diameter of 178 m and a hub height of 119 m, and the modified version used here is termed G178.

https://doi.org/10.5194/wes-2020-115
Preprint. Discussion started: 10 November 2020

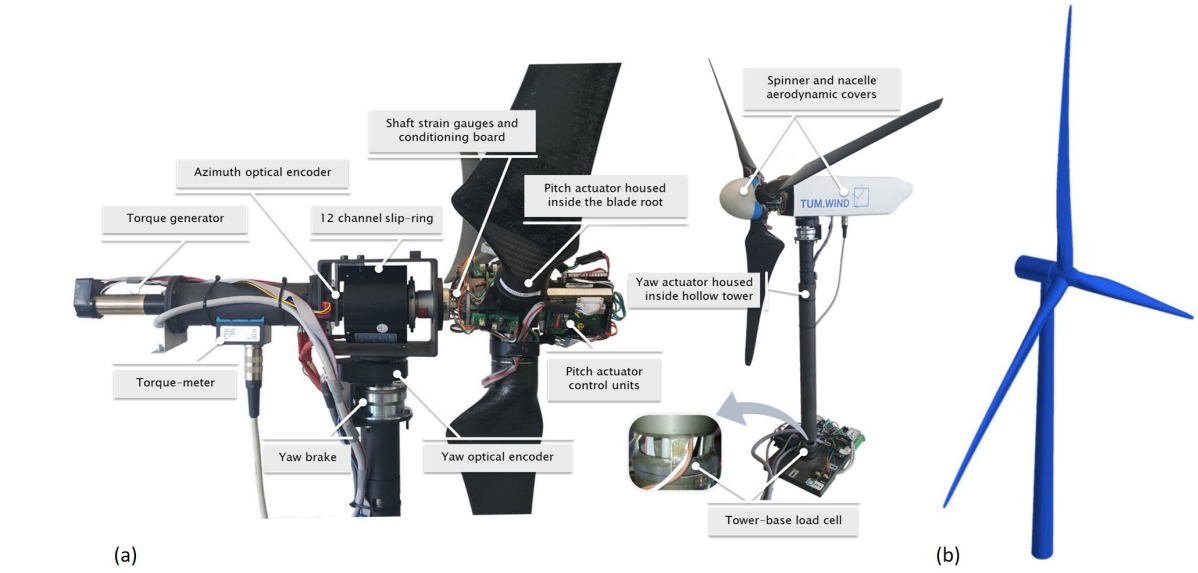

Figure 1. Left: the TUM G1 turbine (Campagnolo et al., 2016). Right: the full-scale DTU 10 MW turbine (from Bak et al. (2013)).

The ratio of the rotor diameter D of the G1 and DTU turbines was used to define the geometric scaling factor n_l. The hub height H of the full-scale machine was slightly adjusted to match the ratio D/H of the G1 turbine.

The shape of nacelle and tower were kept the same as the DTU reference, creating a mismatch with the G1 turbine. In fact, the scaled model —due to miniaturization constraints— has a frontal area of the nacelle that is 2.6 times larger than the DTU turbine; similarly, the tower diameter of the G1 turbine is 49% larger than the DTU machine. This creates a mismatch in the drag of the nacelle and tower, in their local blockage and vortex shedding.

The aerodynamic design of the rotor of the DTU turbine was modified, in order to match the characteristics of the G1 in terms of TSR and circulation distribution (and, as a consequence, also of the thrust). Three versions of the rotor were realized. The standard G178 uses the same airfoils of the DTU turbine over the entire blade span, while chord and twist distributions were modified to satisfy the matching criteria. As the root of the G1 blade is located further away from the rotor axis than in the case of the G178, the circulation is matched only between 20% and 100% of blade span. To account for the effects of rotational augmentation, the inboard airfoils were corrected for delayed stall according to the model of Snel (1994).

A second rotor was designed to investigate the effects of the mismatched circulation on wake behavior. To this end, the twist angle close to the root was modified to decrease the lift inboard and match the circulation of the G1 turbine even in this part of the blade; all the other parameters of the model were kept the same of the G178 turbine. This second turbine is termed G178-MC, where MC stands for ‘matched circulation’.

A third version of the rotor was obtained by eliminating from the G178 the rotational augmentation model, to investigate its effects. The resulting rotor is termed in the following G178-nRA, where nRA stands for ‘no rotational augmentation’.

https://doi.org/10.5194/wes-2020-115
Preprint. Discussion started: 10 November 2020

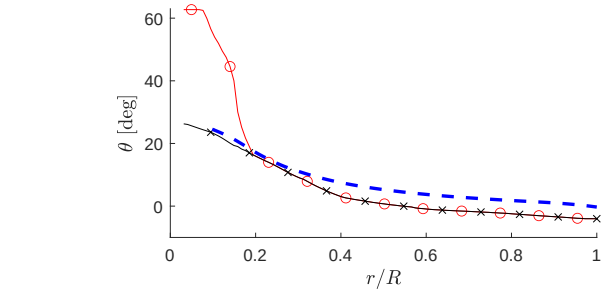

eawe european academy of wind energy
Open Access WIND ENERGY SCIENCE DISCUSSIONS

Distributions of the twist, chord, lift coefficient and non-dimensional circulation of the G1 and of the full-scale rotors are shown in Fig. 2. Chord distributions are normalized by their respective arithmetic mean values c_0 over the span. Lift coefficient and circulation are evaluated at rated conditions using the BEM method implemented in the code FAST 8 (Jonkman and Jonkman, 2018). The lift coefficient of the G1 is significantly smaller than the one of the full-scale turbines, which is a result of the low-Reynolds regime of its airfoils. The lower lift is however compensated by a larger chord and different twist distributions, resulting in a matched circulation from 20% span to the blade tip for the G178 turbine. For the G178-MC model, the circulation is matched over the whole blade span. The difference in lift and circulation between G178 and G178-nRA are due to rotational augmentation.

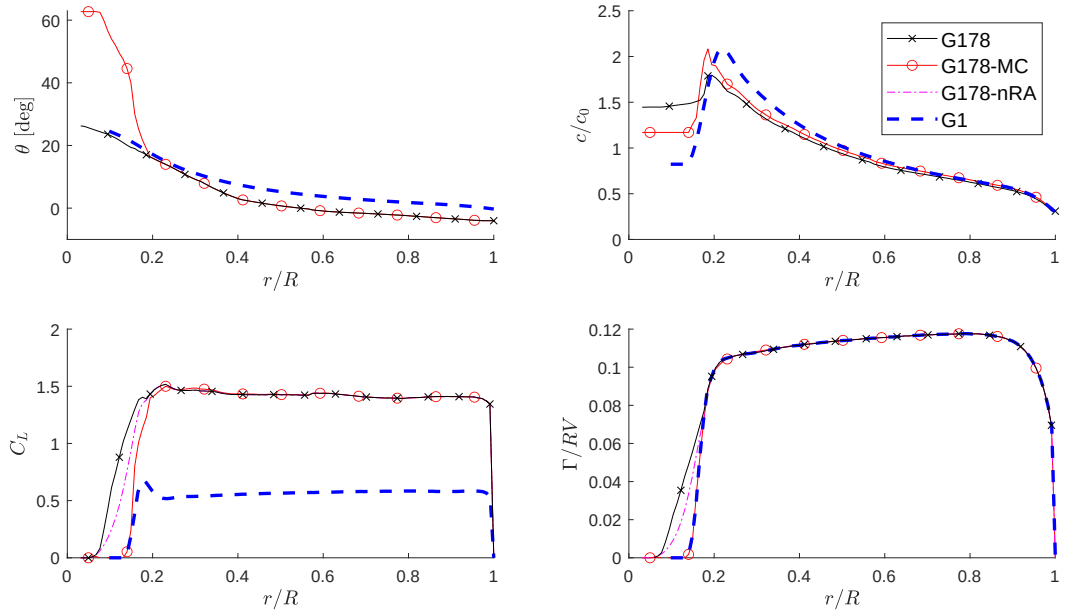

Figure 2. Twist θ, non-dimensional chord c/c_0, lift coefficient C_L and non-dimensional circulation Γ/RV distributions for the G1 and for the G178, G178-MC and G178-nRA full-scale turbines.

4 Simulation model

4.1 LES-ALM CFD code

Numerical results were obtained with a TUM-modified version of SOWFA (Fleming et al., 2014), more completely described in Wang et al. (2018, 2019). The code has been used extensively to numerically replicate wind tunnel tests conducted with G1

https://doi.org/10.5194/wes-2020-115
Preprint. Discussion started: 10 November 2020

eawe european academy of wind energy
Open Access WIND ENERGY SCIENCE DISCUSSIONS

turbines, achieving an excellent correlation with the experimental measurements in a wide range of conditions, including full and partial wake overlaps, wake deflection, static and dynamic induction control, and individual pitch control (for example, see Wang et al. (2019, 2020b, c)).

The finite volume LES solver is based on the standard Boussinesq PISO (Pressure Implicit with Splitting of Operator) incompressible formulation, and is implemented in OpenFOAM (Jasak, 2009). Spatial differencing is based on the Gamma method (Jasak et al., 1999), where a higher level of upwinding is used in the near wake region to enhance stability. Time marching is based on the backward Euler scheme. The pressure equation is solved by the conjugate gradient method, preconditioned by a geometric-algebraic multi-grid, while a bi-conjugate gradient is used for the resolved velocity field, dissipation rate and turbulent kinetic energy, using the diagonal incomplete-LU factorization as preconditioner. The turbulence model is based on the Constant Smagorinsky method (Smagorinsky, 1963).

An actuator-line method (ALM) (Troldborg et al., 2007) is used to represent the effects of the blades, according to the velocity sampling approach of Churchfield et al. (2017). The implementation of the actuator lines is obtained by coupling the CFD solver with the aeroservoelastic simulator FAST 8 (Jonkman and Jonkman, 2018). For improved accuracy, the airfoil polars of the G1 are tuned based on experimental operational data (Bottasso et al., 2014b; Wang et al., 2020a).

Finally, an immersed boundary (IB) formulation method (Mittal and Iaccarino, 2005; Jasak and Rigler, 2014) is employed to model the effects of the turbine nacelle and tower.

4.2 Turbulent inflow

Experiments with the G1 turbine took place in the large boundary layer test section of the wind tunnel at the Politecnico di Milano, where a turbulent flow is generated passively by the use of trapezoidal spires. Without the spires, the flow at the inlet has a turbulence intensity (TI) of about 1-2% and a small horizontal variability caused by the presence of 14 fans and internal transects upstream of the chamber. The non-uniform blockage caused by the spires decelerates the flow close to the wind tunnel floor, generating an initial vertical shear; furthermore, large vortical structures develop around the edges of the spires, which then break down as the flow evolves moving downstream.

Two setups are considered, with two different TI levels. To mimic a typical medium-turbulence offshore condition, 14 type-B spires were placed side by side 1 m from each other, 1 m downstream of the test chamber inlet. A type-B spire consists of an equilateral trapezoid and a supporting board. The height of the trapezoid is 2.0 m, while the widths of the bottom and top edges are 0.26 m and 0.1 m, respectively. The developed turbulent flow where the turbine is located (19.1 m downstream of the inlet) has a vertical shear with a power coefficient equal to 0.12, a small horizontal shear and hub-height speed and TI of 5.75 ms^{-1} and 5%, respectively. A second higher-turbulence inflow was generated using 9 spires of 2.5 m of height, a base of 0.8 m, placed at a distance of 1.55 m from each other. In addition, 24 rows of $0.23 \times 0.23 \times 0.1$ m bricks were placed on the ground, with 12 bricks in odd rows and 13 bricks in even ones, resulting in a staggered brick distribution. This second configuration resulted in a vertical shear with a power coefficient equal to 0.19, a small horizontal shear, and hub-height speed and TI of 5.75 ms^{-1} and 14%, respectively.

https://doi.org/10.5194/wes-2020-115
Preprint. Discussion started: 10 November 2020

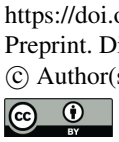

eawe european academy of wind energy
Open Access WIND ENERGY SCIENCE DISCUSSIONS

The same process of passive turbulence generation was simulated by using the LES code. The mesh was generated with ANSYS-ICEM, obtaining a structured body-conforming grid around the spires (Wang et al., 2019), while the bricks placed on the floor for the higher turbulence case were modelled by the IB method. Figure 3 shows the mean streamwise velocity distribution at the chamber cross-section 3.57 D in front of the rotor. The plots on the left report the results of an experimental mapping of the flow performed with triple hot wire probes, while the ones on the right report the numerical results for the medium (top row) and high (bottom row) turbulence cases; notice that measurements are available only 0.2 m above the floor. A good match between experimental measurements and simulation results can be observed over the whole cross-section of the test chamber, including not only the vertical shear but also the slight horizontal non-uniformities.

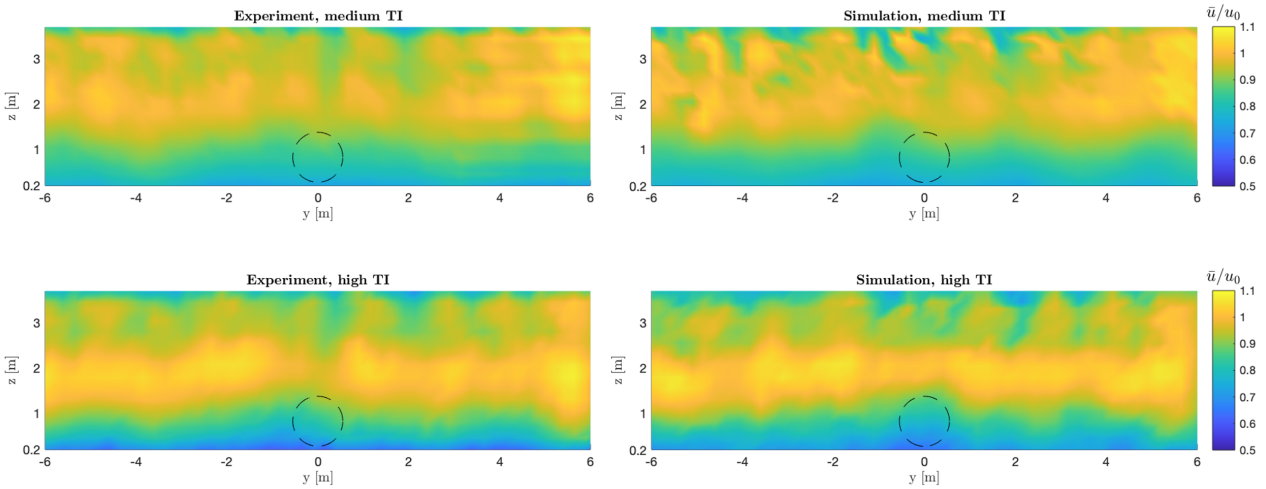

Figure 3. Streamwise velocity distribution on a cross section of the test chamber 3.57 D in front of the rotor. Left: experimental measurements; right: numerical simulation; top: medium TI case; bottom: high TI case.

For the same plane, Fig. 4 shows the mean (i.e., time-averaged) speed and TI profiles along a vertical line directly in front of the rotor center. Here again, a good match between experimental measurements and simulation can be observed, except in the immediate proximity of the floor.

The results of the passive turbulence-generating precursor simulations were sampled on the plane 3.57 D upstream of the turbine, and used as inlet for the simulations of the turbine and its wake, including the side walls and the ceiling of the tunnel. The chamber cross section has a width of 13.84 m and a height of 3.84 m, resulting in some vertical blockage, whose effects were quantified by running various simulations for increasing values of the chamber height, as reported later. The wind tunnel grid uses three zones of increasing density, the smallest cells having a size of 0.015 m (i.e., $1.4 \cdot 10^{-2}$ D). The ALM discretization used 108 points over the blade span, i.e. a spacing equal to $4.7 \cdot 10^{-3}$ D.

For the full-scale machine, each inflow was scaled in space and time, as previously explained, resulting in flows with the same identical characteristics at the two scales. Similarly, the same LES and ALM grids were geometrically upscaled and used

https://doi.org/10.5194/wes-2020-115
Preprint. Discussion started: 10 November 2020

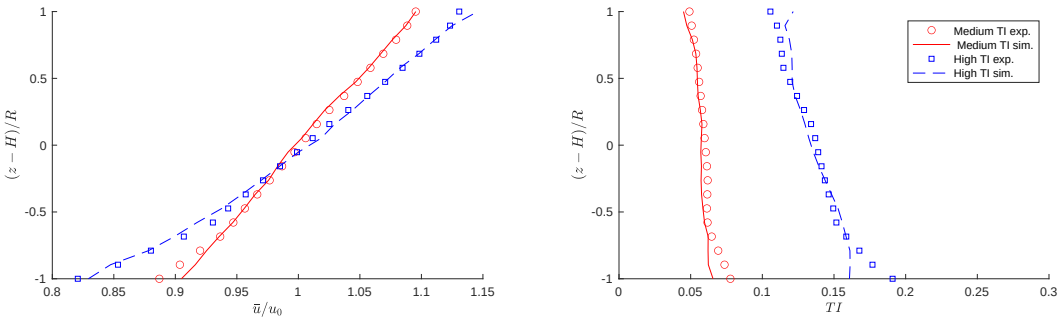

Figure 4. Mean velocity (left) and turbulence intensity (right) distributions along a vertical line 3.57 D in front of the rotor.

for the full-scale simulations; this means that also the full-scale simulations have the same slight anisotropic blockage effects of the wind tunnel case.

5 Results

5.1 Code to experiment verification

First, experimental measurements obtained with triple hot wire probes are compared with the corresponding numerical simulations. Two operating conditions in the partial load regime (region II) are considered: one aligned with the flow and one with a misalignment angle γ of 20 deg. Table 1 reports the experimental and simulated power and thrust coefficients in the two cases, in medium TI conditions. Figure 5 reports a comparison of horizontal scans of the wake (Wang et al., 2019) for the aligned case at various downstream distances for both the medium and high TI cases.

Table 1. Experimental and simulated power and thrust coefficients for the G1 turbine, in the medium TI Case.

Coefficient	C_P		C_T	
Case	Experiment	Simulation	Experiment	Simulation
$\gamma = 0$ deg	0.416	0.420	0.881	0.851
$\gamma = 20$ deg	0.364	0.358	0.810	0.742

The figure shows hub-height horizontal time-average streamwise velocity (top panel) and turbulence intensity (bottom panel) profiles. While the match of the wake profile is excellent for all locations, the numerical results slightly overestimates turbulence intensity in the center of the near wake region. Overall, simulation and experimental results are in very good agreement.

https://doi.org/10.5194/wes-2020-115
Preprint. Discussion started: 10 November 2020

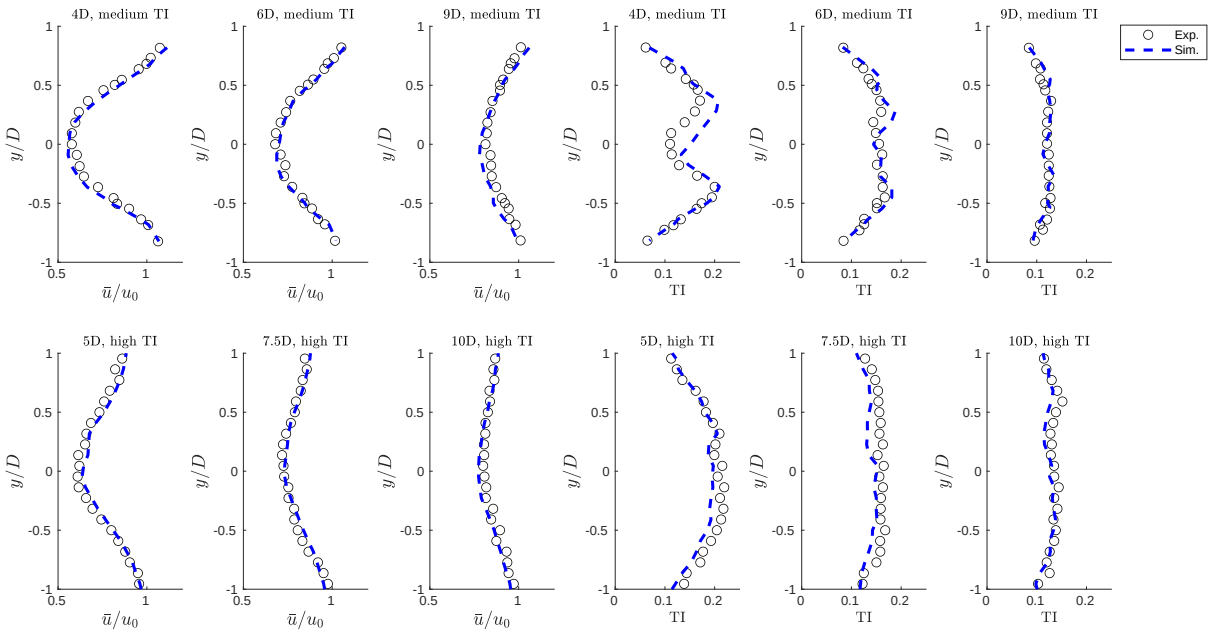

Figure 5. Horizontal hub-height profiles of normalized time-average streamwise velocity and turbulence intensity, for the medium (top) and high (bottom) inflow TI cases. Black *o* symbols: experimental results; blue dashed line: G1 simulations.

5.2 Scaled to full-scale comparisons

Next, having established a good correspondence between the numerical results and experimental measurements, simulations were conducted with the full-scale turbines to understand the effects of mismatched quantities.

Table 2 shows the turbine power and thrust coefficients for the different cases, considering the G1 and three G178 turbine models. As expected, the power coefficient of the G1 turbine is lower than the one of all full-scale G178s, because of the lower efficiency caused by the different Reynolds regime. On the other hand, there is a good match of the thrust coefficient, especially for G178; the nRA and MC versions produce a slightly lower lift in the inboard section of the blade, and hence have a marginally lower C_T.

Figure 6 gives a qualitative overview of the wakes of the G1 and G178 turbines for the aligned and misaligned cases. The wake deficits are similar, except for the central region of the near wake, as expected. Even this qualitative view shows a significant effect of the much larger nacelle of the G1. This difference however disappears moving downstream, and the far wakes of two turbines appear to be almost identical.

https://doi.org/10.5194/wes-2020-115
Preprint. Discussion started: 10 November 2020

eawe european academy of wind energy
Open Access WIND ENERGY SCIENCE DISCUSSIONS

Table 2. Power and thrust coefficients for the different turbine models in the two considered operating conditions.

Coefficient	C_P				C_T			
Turbine model	G1	G178	G178-nRA	G178-MC	G1	G178	G178-nRA	G178-MC
$\gamma = 0$ deg	0.420	0.475	0.472	0.470	0.851	0.831	0.827	0.822
$\gamma = 20$ deg	0.358	0.421	0.418	0.417	0.742	0.731	0.727	0.723

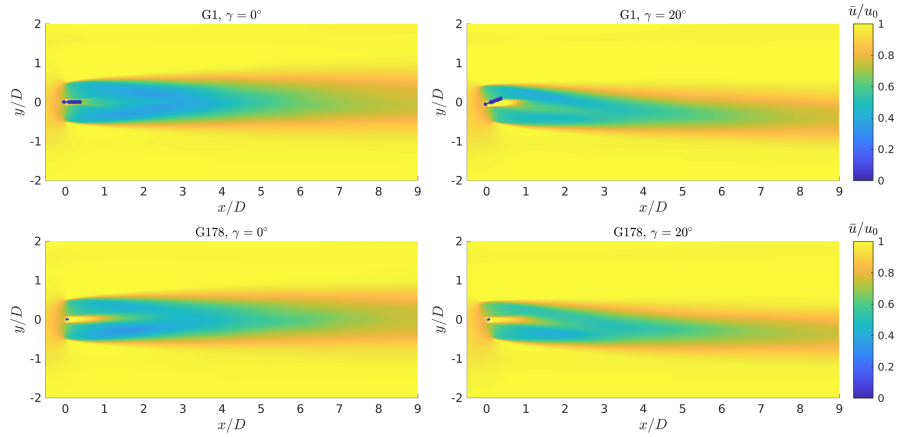

Figure 6. Wakes of the scaled G1 and full-scale G178 turbines. Left: aligned case; right: yaw misaligned case.

A more precise characterization of the differences between the scaled G1 model and the realistic full-scale G178 turbine is given by Fig. 7 (medium TI) and 8 (high TI), considering the misaligned case. For both figures, the first row shows the mean speed in the longitudinal direction, while the second and third rows show the Reynolds shear stress components $\overline{u'u'}/u_0^2$ and $\overline{u'v'}/u_0^2$, respectively, where the prime here indicates a fluctuation with respect to the mean.

Results indicate an excellent match between the scaled and full-scale wakes, for both TI levels. Some differences only appear in the peaks of $\overline{u'u'}/u_0^2$ immediately downstream of the rotor. However, the velocity profiles are remarkably similar already at 3 D, notwithstanding the differences around the hub and blade inboard sections between the two machines. Similar conclusions are obtained for the aligned case.

5.3 Effects of unmatched inboard circulation and rotational augmentation

The effects of unmatched inboard circulation and rotational augmentation are quantified by computing the differences in $\bar{u}/u_0$, $\overline{u'u'}/u_0^2$ or $\overline{u'v'}/u_0^2$ at different downstream locations. Results are shown in Fig. 9, where differences are computed subtracting the G178 solution from the G178-MC or G178-nRA ones. As indicated by the figure, these effects are extremely small, and possibly discernible from numerical noise only in the immediate proximity of the rotor.

https://doi.org/10.5194/wes-2020-115
Preprint. Discussion started: 10 November 2020

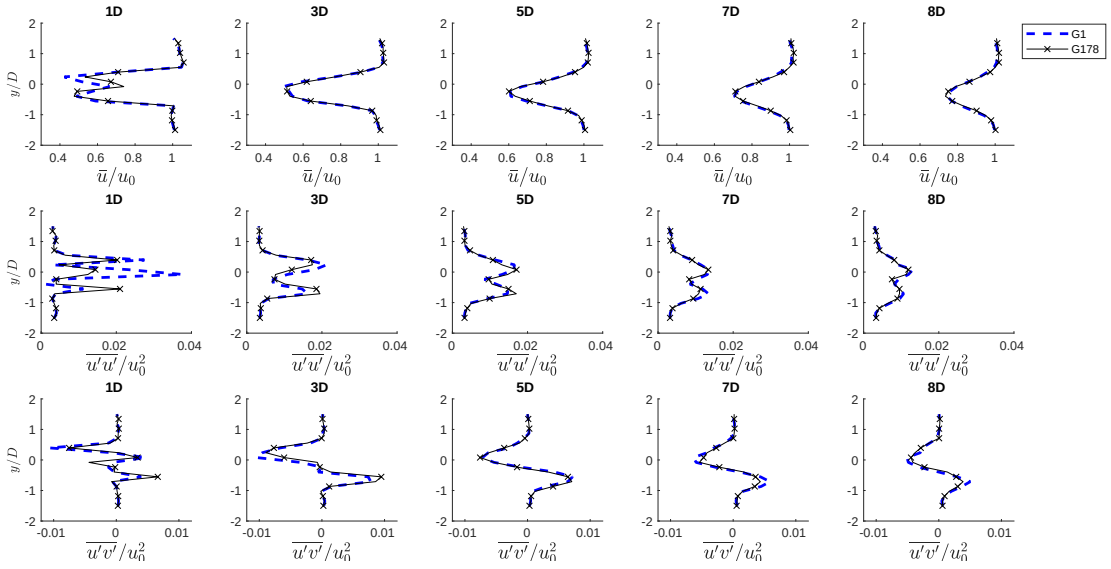

Figure 7. Hub-height profiles of normalized time-average streamwise velocity (top) and shear stresses (center and bottom), in the misaligned and medium TI condition.

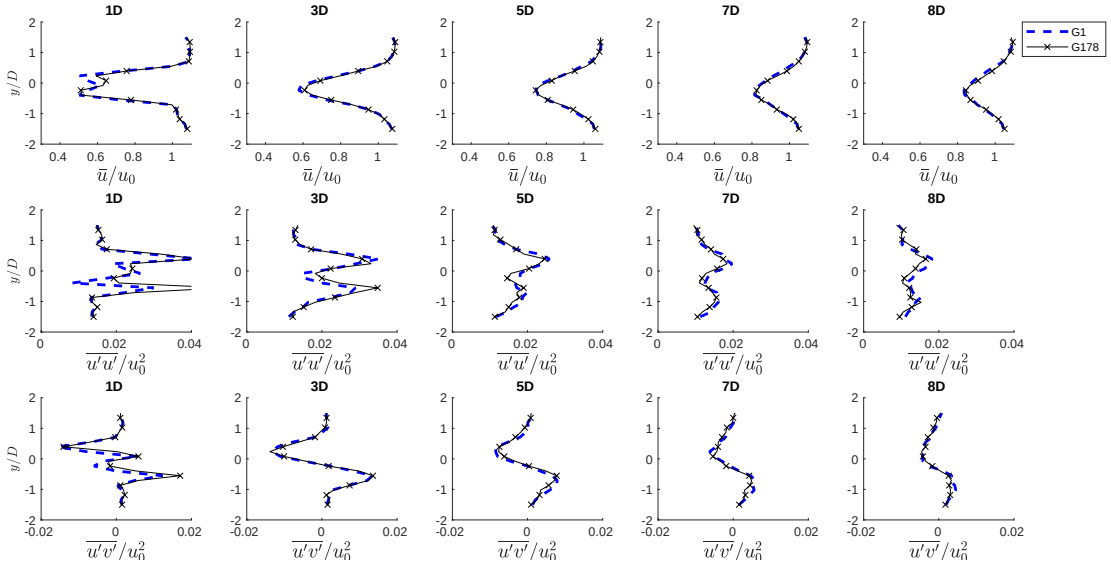

Figure 8. Hub-height profiles of normalized time-average streamwise velocity (top) and shear stresses (center and bottom), in the misaligned and high TI condition.

https://doi.org/10.5194/wes-2020-115
Preprint. Discussion started: 10 November 2020

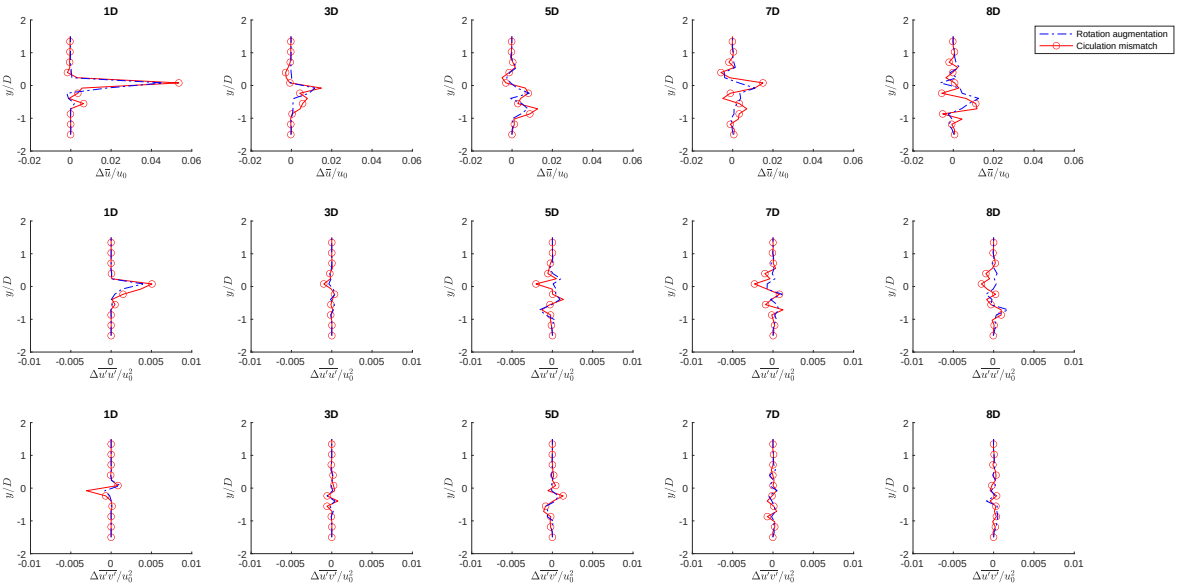

Figure 9. Difference in the profiles of the normalized time-average streamwise velocity (top) and shear stresses (center and bottom) along hub-height horizontal lines, caused by rotation augmentation (dash-dotted blue line) and by a mismatched circulation close to the root (red solid line and ○ symbols). Results are for the yaw misaligned and medium TI condition.

5.4 Effect of nacelle size and unmatched C_P on swirl

For the wind-aligned operating condition, Fig. 10 shows the delta wake velocity field obtained by subtracting the G178-MC from the G1 solution, looking upstream. The panel on the left represents the near wake 1 D immediately behind the rotor disk plane, while the panel on the right reports the far wake at 8 D. The color field represents the difference in the non-dimensional streamwise velocity component $\Delta(\bar{u}/u_0)$, whereas the arrows represent differences in the in-plane velocity vectors.

In this case, since the circulation is matched, there are only two factors that could result in non-zero difference fields: the larger frontal area of the nacelle (and, similarly, of the tower) of the G1, and its smaller power coefficient caused by the Reynolds mismatch. The impacts of these two factors are clearly visible in the near wake, respectively looking at the streamwise and in-plane velocities.

In fact, the negative streamwise velocity bubble at the center of the rotor is a result of the larger blockage of the G1 nacelle. The effect of the tower differs from that of the nacelle. While the nacelle is almost a pure blockage in the center of the rotor where wake recovery is the weakest, the presence of the tower wake can increase the local turbine wake recovery by increasing turbulence intensity. As the wake rotates counter-clockwise when looking upstream as in Fig. 10, the flow influenced by tower is also convected towards the negative y direction.

https://doi.org/10.5194/wes-2020-115
Preprint. Discussion started: 10 November 2020

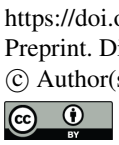

eawe european academy of wind energy
Open Access WIND ENERGY SCIENCE DISCUSSIONS

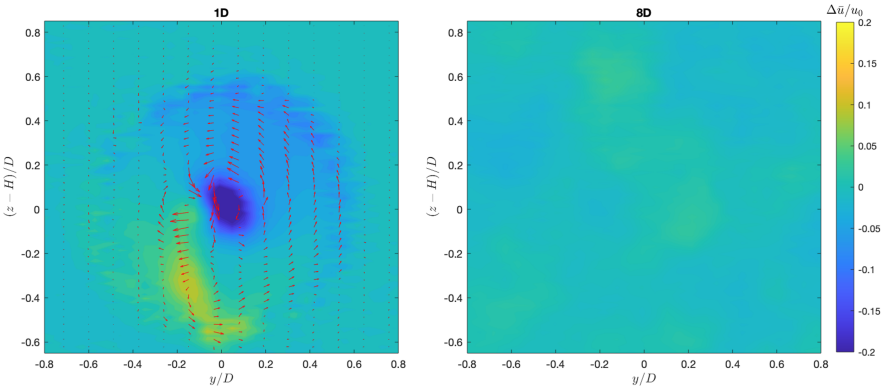

Figure 10. Difference in the wake velocity fields between the G1 and the G178-MC turbines, looking upstream. Color field: non-dimensional streamwise velocity difference $\Delta(\bar{u}/u_0)$; arrows: difference in the in-plane velocity vectors. Left: near wake 1 D immediately behind the rotor disk plane; right: far wake at 8 D.

When looking upstream, the rotor spins counterclockwise, whereas the wake rotates clockwise by the principle of action and reaction. Compared to the wake of the G178-MC turbine, the wake of the G1 rotates at a slower pace, as indicated by the counterclockwise rotation of the difference field shown in the picture. The slower rotation of the G1 wake is a direct consequence of its smaller power coefficient that, for the same TSR, implies also a reduced torque coefficient. As expected, the mismatch in the swirl rotation is only concentrated close to the hub, and decays quickly with radial position.

As the flow propagates downstream and the wake progressively recovers, differences between the velocity fields decay and the effects of the mismatches can hardly be seen at 8 D. The only difference that can still be identified is the effect of the larger tower. This results in some blockage close to the ground that has not yet fully recovered at this distance, resulting in about a 6% difference in the longitudinal velocity component immediately above the floor and, hence, in a slightly enhanced shear below hub height. Elsewhere, differences between the two fields never exceed 3%.

5.5 Effect of wind tunnel blockage

Considering the G1 turbine, the wind tunnel test chamber has a height $h_{wt} = 3.49$ D and a width $w_{wt} = 12.49$ D, resulting in a cross sectional area $A_{wt} = 43.59$ D. Although the resulting area ratio $A_{wt}/A = 55.5$ is relatively large, the small vertical ratio h_{wt}/D can cause some anisotropic blockage. To quantify this effect, numerical simulations were conducted in domains of increasing height from 1.75 D to 10.47 D, as shown in the left panel of Fig. 11. The actual wind tunnel height is indicated by a red square mark in the figure.

The right panel of Fig. 11 shows the non-dimensional power increase $\Delta P/P_\infty$ vs. the area ratio A_{wt}/A, where P_∞ is the power for the largest domain —assumed to be blockage-free. Results indicate a power increase caused by blockage of about 1.5%.

https://doi.org/10.5194/wes-2020-115
Preprint. Discussion started: 10 November 2020

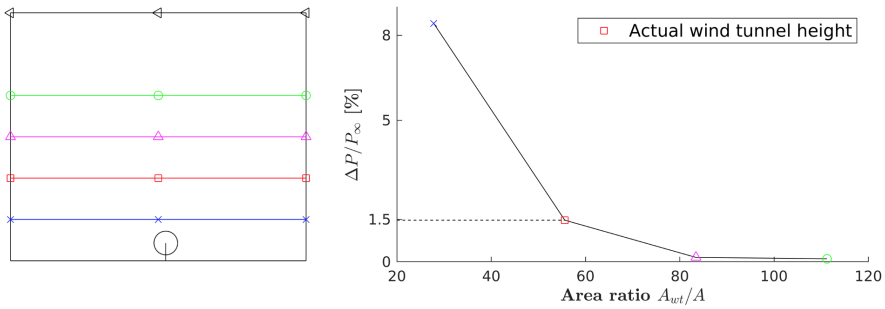

Figure 11. Wind tunnel blockage effect. Left: cross sectional areas; right: percent power increase with respect to the unrestricted flow.

5.6 Wind farm control metrics

The previous analysis has shown that the wake of the G1 turbine has a very close resemblance to the one of the full-scale G178, although some differences are present in the near wake region. However, it is difficult to appreciate the actual relevance of these differences, and a more practical quantification of the accuracy of the match would be desirable. The G1 turbine is mostly used for studying wake interactions within clusters of turbines, and for testing mitigating control strategies. This suggests the use of wind-farm-control-inspired metrics for judging the differences between the scaled and full-scale machines.

The first metric considered here is the available power ratio $P_a(x/D)/P_0 = \bar{V}^3(x/D)/V_\infty^3$ downstream of the turbine, where P_0 is the power output of the turbine, V_∞ is the ambient wind speed at hub height, and $\bar{V}(x/D)$ is the rotor-effective wind speed at the downstream location x/D. The available power ratio depends on the shape of the wake, its recovery and trajectory, and it was computed from the longitudinal flow velocity component in the wake on the area of the rotor disk at various downstream positions directly behind the wind turbine, as shown in Fig. 12.

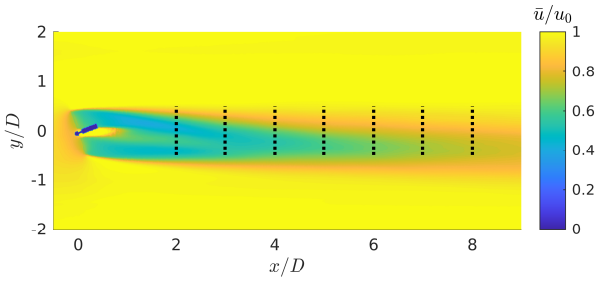

Figure 12. Wake of the G1 turbine for the yaw misaligned case. The black dashed lines indicate the locations of virtual downstream turbines.

For the 20 deg misaligned case, the available power ratio results are shown in the left panel of Fig. 13. As shown in the figure, the available power changes moving downstream because the wake expands, recovers and —since the turbine is misaligned

https://doi.org/10.5194/wes-2020-115
Preprint. Discussion started: 10 November 2020

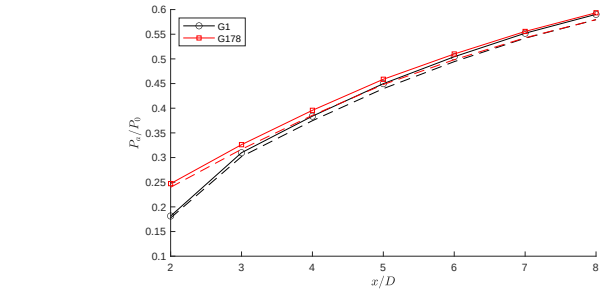

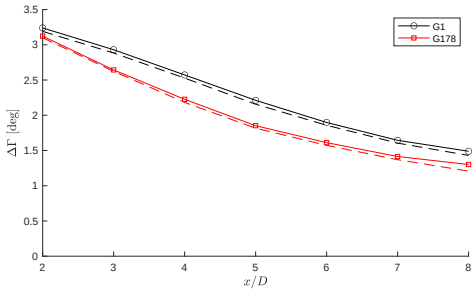

Figure 13. Left: available power ratio in the wake P_a/P_0 as a function of downstream position x/D. Right: change of wind direction $\Delta\Gamma$ caused by the curled wake as a function of downstream position x/D. Both results are for the 20 deg misaligned and medium TI case. Black ○ symbols: G1; red □ symbols: G178. Solid lines: actual wind tunnel size; dashed lines: unrestricted case (no blockage).

The second metric considered here is the ambient flow rotation in the immediate proximity of a deflected wake. By misaligning a wind turbine rotor with respect to the incoming flow direction, the rotor thrust force is tilted, thereby generating a cross-flow force that laterally deflects the wake. As shown with the help of numerical simulations by Fleming et al. (2018), this cross-flow force induces two counter rotating vortices that, combining with the wake swirl induced by the rotor torque, lead to a curled wake shape. As observed experimentally by Wang et al. (2018), the effects of these vortices result in additional lateral flow speed components, which are not limited to the wake itself but extend also outside of it. By this phenomenon, the flow direction within and around a deflected wake is tilted with respect to the upstream undisturbed direction. Therefore, when a turbine is operating within or close to a deflected wake, its own wake undergoes a change of trajectory —termed secondary steering— induced by the locally modified wind direction.

The change in ambient wind direction $\Delta\Gamma$ caused by the curled wake is reported in the right panel of Fig. 13 as a function of the downstream distance x/D; even in this case, the effects of blockage can be appreciated by comparing the solid and dashed lines. The angle $\Delta\Gamma$ was computed from the wake velocity components, averaging over the rotor disk areas already used for the analysis of the available power. Here again the difference in the change of ambient wind direction behind the G1 and G178 turbines is quite small. A non-perfect match is probably due to the slightly different strength of the central vortex generated in response to the rotor torque. On the other hand, the two counter-rotating vortices caused by the tilted thrust are well matched —given the good correspondence of this force component between the two models.

https://doi.org/10.5194/wes-2020-115
Preprint. Discussion started: 10 November 2020

eawe european academy of wind energy
Open Access WIND ENERGY SCIENCE DISCUSSIONS

5.7 Effect of integral length scale

The ILS of the wind tunnel flow was obtained by first computing the time-autocorrelation of the wind speed at one position in front of the turbine, and then multiplying the result by the mean wind speed. The length scales obtained from measurements in the wind tunnel and the simulated flow resulted in nearly identical values, as already shown by Wang et al. (2019). A second estimate of the ILS was based on the space-autocorrelation between simultaneous values of the simulated wind speed at two points in front of the turbine. For the size of the G1 turbine, this second estimate of the ILS resulted in a full-scale value of approximatively 142 m. On the other hand, the IEC 61400-1 international standards prescribe space-autocorrelation-based lengths of 170 m in Ed. 2 (IEC 61400-1, 1999) and of 340 m in Ed. 3 (IEC 61400-1, 2005). Although the ILS presents a significant natural variability at each location and across different sites (Kelly, 2018), the value achieved in the wind tunnel with the G1 is undoubtedly in the low range of naturally occurring scales.

To understand the effects of the partially mismatched ILS on wake behavior, two turbulent inflows were generated, differing only in this parameter. Unfortunately, however, the natural development of two inflows with different ILS values but exactly the same TI and vertical shear is clearly an extremely difficult task. To avoid this complication, the code TurbSim was used, selecting the Kaimal model and prescribing directly the turbulence scale parameter (see Eq. (23) in Jonkman (2009)). The resulting turbulent wind time histories were specified as Dirichlet inflow conditions for the subsequent LES-ALM simulations.

The two resulting developed CFD flows are characterized by an ILS of 176 m and 335 m, and have a vertical shear exponent 0.18 and hub-height speeds and TI of 11.3 ms^{-1} and 6.0%, respectively. These two different flows were used for conducting dynamic simulations with the G178 turbine in a 20 deg yaw misaligned condition.

The ILS indicates the dimension of the largest coherent eddies in the flow. Hence, the main effect of a larger ILS is that of inducing a more pronounced meandering of the wake. To quantify this effect, the instantaneous wake center was computed according to the deficit-weighted center of mass method (España et al., 2011). The standard deviation of the horizontal wake position 5 D downstream of the rotor was found to be equal to 0.089 D for the low ILS (176 m) case, and equal to 0.12 D for the high ILS (335 m) one, according to expectations.

The effects of a different ILS are much smaller, although still appreciable, when considering mean quantities. Figure 14 reports the profiles of speed and shear stresses at different downstream distances. The mean velocity profile is only very slightly affected, with a maximum change of about only 2%. A clearer effect is noticeable in the shear stresses at the periphery of the wake.

6 Conclusions

This paper has analyzed the realism of wind-tunnel-generated wakes with respect to the full-scale case. In the absence of comparable scaled and full-scale experimental measurements, a hybrid experimental-simulation approach was used here for this purpose. A LES-ALM code was first verified with respect to detailed measurements performed in a large boundary layer wind tunnel with the TUM G1 scaled wind turbine. Next, the same code —with the same exact algorithmic settings— was

https://doi.org/10.5194/wes-2020-115
Preprint. Discussion started: 10 November 2020

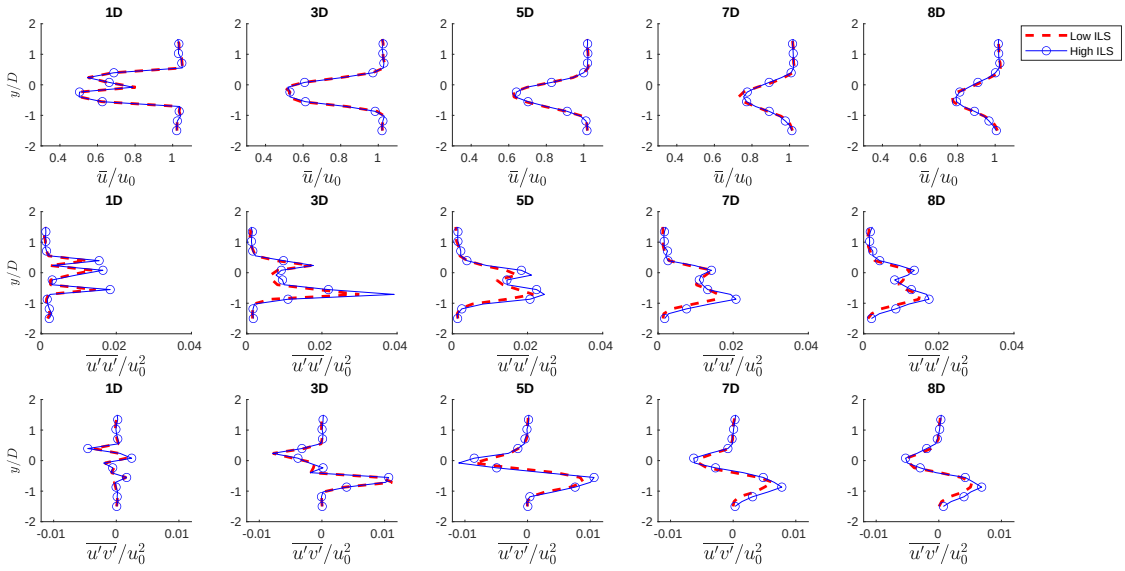

Figure 14. Hub-height profiles of normalized time-average streamwise velocity (top) and shear stresses (center and bottom), for the low and high ILS cases in yaw misaligned conditions.

used to simulate different full-scale versions of the scaled turbine. These different full-scale models were designed to highlight the effects of mismatched quantities between the two scales.

Clearly, this approach has some limits and therefore falls short of providing a comprehensive answer to the realism question. In fact, the comparison is clearly blind to any physical process that is not modelled or that is not accurately resolved by the numerical simulations. Additionally, it is assumed that a numerical model that provides good quality results with respect to reality at the small scale is also capable of delivering accurate answers at the full scale.

Keeping in mind these limits, the following conclusions can be drawn from the present study:

- Overall, the far (above approximatively 4 D) wake of the G1 scaled wind turbine is extremely similar to the wake of a corresponding full-scale machine considering all classical mean metrics, i.e. wake deficit, turbulence intensity, shear stresses, wake shape and path, both in aligned and misaligned conditions.

- Small differences of fractions of a degree are present in the local wind direction changes caused by the curled wake, because of a different swirl generated by the lower aerodynamic torque of the scaled model. The trends in terms of downstream distance and yaw misalignments (not shown here) are however extremely similar.

- The effects of blockage are very limited in the large wind tunnel of the Politecnico di Milano, with differences in power of about 1.5% and negligible effects on other metrics.

https://doi.org/10.5194/wes-2020-115
Preprint. Discussion started: 10 November 2020

eawe european academy of wind energy
Open Access WIND ENERGY SCIENCE DISCUSSIONS

– The effects of rotational augmentation, unmatched inboard circulation and nacelle size are clearly visible in the inner near wake region. However, they decay quickly with downstream distance, and are typically small enough not to alter the qualitative shape of the speed deficit, turbulence intensity and shear stresses distributions in this region of the wake.

– The lower ILS of the flow generated in the wind tunnel at the scale of the G1 has very modest effects on mean wake metrics, although it causes a reduced meandering.

In summary, it appears that the G1 scaled turbine faithfully represents not only the far wake behavior, but also produces a very realistic near wake. This is obtained by a design of the experimental setup that matches the turbulent inflow, the rotor vortex shedding, the geometry and strength of the helical tip vortices and the strength and shape of the speed deficit, which are all the main physical effects dictating the near-wake evolution. The mismatches that are present in the near-wake inner core (due to a different swirl, inboard circulation, rotational augmentation and a different geometry of the nacelle) do leave a visible mark, but overall do not seem to significantly alter the behavior of the wake, as expected. The larger size of the tower leaves a more visible trace further downstream, because it affects the wake recovery by generating a local extra turbulence intensity, in turn altering shear below hub height.

Overall, the realism of both the near and far wake justify the use of the TUM G1 (and similarly designed) scaled turbine for the study of wake physics and applications in wind farm control and wake mixing.

The present experimental setup can be further improved, for an even increased realism and expanded capabilities. Regarding the inflow, several facilities have been recently designed or upgraded to generate unstable boundary layers (Chamorro and Porté-Agel, 2010), tornadoes and downbursts (WindEEE, 2020), or for the active generation of turbulent flows (Kröger et al., 2018). Regarding the models, a more realistic geometry and size of the nacelle and tower can be achieved at the price of a further miniaturization. Aeroelastic effects can be included by using ad hoc scaling laws (Canet et al., 2020) to design flexible model rotor blades (Bottasso et al., 2014a; Campagnolo et al., 2014). Advances in 3D printing and component miniaturization will certainly lead to advancements in the design of ever more sophisticated and instrumented models. Regarding measurement technology, a more detailed characterization of salient features of the flow can be obtained by PIV or lidars, for example in support of the study of dynamic stall, vortex and stall-induced vibrations.

Although advancements in the testing of scaled wind turbines come with significant design, manufacturing, measurement and operational challenges, wind tunnel testing remains an extremely useful source of information for scientific discovery, the validation of numerical models and the testing of new ideas. A quantification of the realism of such scaled models is therefore a necessary step in the acceptance of the results that they generate.

Code and data availability. The LES-ALM program is based on the open-source codes foam-extend-4.0 and FAST 8. The data used for the present analysis can be obtained by contacting the authors.

https://doi.org/10.5194/wes-2020-115
Preprint. Discussion started: 10 November 2020

eawe european academy of wind energy
Open Access WIND ENERGY SCIENCE DISCUSSIONS

Author contributions. CW performed the simulations and analyzed the results; CLB devised the original idea of this research, performed the scaling analysis and supervised the work; FC was responsible for the wind tunnel experiments and the analysis of the measurements, and co-supervised the work; HC designed the full-scale turbine models; DB validated the full-scale turbine models with BEM and CFD codes. CW and CLB wrote the manuscript. All authors provided important input to this research work through discussions, feedback and by improving the manuscript.

Competing interests. The authors declare that they have no conflict of interest.

Acknowledgements. The authors express their appreciation to the Leibniz Supercomputing Centre (LRZ) for providing access and computing time on the SuperMUC-NG System.

Financial support. This work has been supported by the CL-WINDCON project, which received funding from the European Union Horizon 2020 research and innovation program under grant agreement No. 727477.

https://doi.org/10.5194/wes-2020-115
Preprint. Discussion started: 10 November 2020

eawe european academy of wind energy
Open Access WIND ENERGY SCIENCE DISCUSSIONS

References

Abkara, M., and Porté-Agel, F.: Influence of atmospheric stability on wind-turbine wakes: A large-eddy simulation study, Physics of Fluids, 27, 035104 https://doi.org/10.1063/1.4913695, 2015.

Bak, C., Zahle, F., Bitsche, R., Kim, T., Yde, A., Henriksen, L. C., Natarajan, A. and Hansen, M.: Description of the DTU 10 MW reference wind turbine, DTU Wind Energy Report-I-0092 5, 2013.

Bartl, J., and Sætran, L. R: Experimental testing of axial induction based control strategies for wake control and wind farm optimization, J. Phys. Conf. Ser., 753.3, https://doi.org/10.1088/1742-6596/753/3/032035, 2016.

Bastankhah, M. and Porté-Agel, F.: Experimental and theoretical study of wind turbine wakes in yawed conditions, J. Fluid Mech., 806, 506–541, https://doi.org/10.1017/jfm.2016.595, 2016.

Bisplinghoff, R. L. and Ashley, H.: Principles of Aeroelasticity, Dover Publications, Mineola, New York, USA, 2002.

Bottasso, C. L. and Campagnolo, F.: Handbook of Wind Energy Aerodynamics, chap. Wind Tunnel Testing of Wind Turbines and Farms, Springer, 2020.

Bottasso, C. L., Campagnolo, F. and Petrović, V.: Wind tunnel testing of scaled wind turbine models: Beyond aerodynamics, J. of Wind Eng. Indust. Aerodyn., 127, 11–28, https://doi.org/10.1016/j.jweia.2014.01.009, 2014.

Bottasso, C. L., Cacciola, S. and Iriarte, X.: Calibration of wind turbine lifting line models from rotor loads, Wind Eng. Ind. Aerod., 124, 29–45, https://doi.org/10.1016/j.jweia.2013.11.003, 2014.

Burton, T., Jenkins, N., Sharpe, D. and Bossanyi, E.: Wind energy handbook, John Wiley & Sons, West Sussex, UK, 2011.

Campagnolo, F., Bottasso, C. L., and Bettini, P.: Design, manufacturing and characterization of aero- elastically scaled wind turbine blades for testing active and passive load alleviation techniques within an ABL wind tunnel, J. Phys. Conf. Ser., 524 012061, https://doi.org/10.1088/1742- 6596/524/1/012061, 2014.

Campagnolo, F., Petrović, V., Schreiber, J., Nanos, E. M., Croce, A. and Bottasso, C. L.: Wind tunnel testing of a closed-loop wake deflection controller for wind farm power maximization, J. Phys. Conf. Ser., 753.3, https://doi.org/10.1088/1742-6596/753/3/032006, 2016.

Campagnolo, F., Weber, R., Schreiber, J. and Bottasso, C. L.: Wind tunnel testing of wake steering with dynamic wind direction changes, Wind Energy Sci. Discuss., https://doi.org/10.5194/wes-2020-70, 2020 .

Canet, H., Bortolotti, P., and Bottasso, C. L.: On the scaling of wind turbine rotors, Wind Energy Sci. Discuss., pp. 1–35, 2020.

Chamorro, L. P. and Porté-Agel, F.: A wind-tunnel investigation of wind-turbine wakes: boundary-layer turbulence effects, Bound.-Layer Meteorol., 132.1, 129–149, https://doi.org/10.1007/s10546-009-9380-8, 2009.

Chamorro, L. P. and Porté-Agel, F.: Effects of thermal stability and incoming boundary-layer flow characteristics on wind-turbine wakes: a wind-tunnel study, Bound.-Layer Meteorol., 136.3, 515–533, https://doi.org/10.1007/s10546-010-9512-1, 2010.

Chamorro, L. P., Arndt, R. E. A. and Sotiropoulos, F.: Reynolds number dependence of turbulence statistics in the wake of wind turbines, Wind Energy, 15.5, 733–742, https://doi.org/10.1002/we.501, 2012.

Chen, T. Y. and Liou, L. R.: Blockage corrections in wind tunnel tests of small horizontal-axis wind turbines, Exp. Therm. Fluid Sci., 35.3, 565–569, https://doi.org/10.1016/j.expthermflusci.2010.12.005, 2011.

Churchfield, M. J., Schreck, S., Martınez-Tossas, L. A., Meneveau, C., and Spalart, P. R.: An advanced actuator line method for wind energy applications and beyond, in: 35th Wind Energy Symposium, p. 1998, 2017.

Dowler J. L. and Schmitz, S.: A solution-based stall delay model for horizontal-axis wind turbines, Wind Energy, 18, 1793–1813, https://doi.org/10.1002/we.1791, 2015.

https://doi.org/10.5194/wes-2020-115
Preprint. Discussion started: 10 November 2020

España, G., Aubrun, S., Loyer, S., and Devinant, P.: Spatial study of the wake meandering using modelled wind turbines in a wind tunnel, Wind Energy, 14, 923–937, https://doi.org/10.1002/we.515, 2011.

Fleming, P. A., Pieter, M. O., Lee, S., Wingerden, J., Johnson, K., Churchfield, M., Michalakes, J., Spalart, P. and Moriarty, P.: Evaluating techniques for redirecting turbine wakes using SOWFA, Renew. Energy, 70, 211–218, https://doi.org/10.1016/j.renene.2014.02.015, 2014.

IEC 61400-1 Wind turbine generator systems – Part 1: Safety requirements. 2nd edition. Geneva, Switzerland: International Electrotechnical Commission, 1999.

IEC 61400-1 Wind turbines – Part 1: Design requirements. 3rd edition. Geneva, Switzerland: International Electrotechnical Commission, August 2005.

Jasak, H., Weller, H., and Gosman, A.: High resolution NVD differencing scheme for arbitrarily unstructured meshes, Int. J. Numer. Methods Fluids, 31, 431–449, https://doi.org/10.1002/(SICI)1097-0363(19990930)31:2<431::AID-FLD884>3.0.CO;2-T, 1999.

Jasak, H.: OpenFOAM: open source CFD in research and industry, Int. J. Nav. Arch. Ocean, 1.2, 89–94, https://doi.org/10.2478/IJNAOE-2013-0011, 2009.

Jasak, H. and Rigler, D.: Finite volume immersed boundary method for turbulent flow simulations, in: 9th OpenFOAM Workshop, 2014.

Jonkman, B.J.: TurbSim User's Guide: Version 1.50, Technical Report NREL/TP-500-46198, September 2009.

Jonkman, J. and Jonkman, B.J.: FAST 8, https://nwtc.nrel.gov/FAST8, 2018.

Kelly, M.: From standard wind measurements to spectral characterization: turbulence length scale and distribution, Wind Energ. Sci., 3, 533–543, https://doi.org/10.5194/wes-3-533-2018, 2018.

Kröger, L., Frederik, J., van Wingerden, J.-W., Peinke, J., and Hölling, M.: Generation of user defined turbulent inflow conditions by an active grid for validation experiments, J. Phys. Conf. Ser., 1037(5), 2018.

Fleming, P., Annoni, J., Churchfield, M., Martınez-Tossas, L. A., Gruchalla, K., Lawson, M., and Moriarty, P.: A simulation study demonstrating the importance of large-scale trailing vortices in wake steering, Wind Energy Science, 3, 243–255, https://doi.org/10.5194/wes-3-243-2018, 2018.

Lissaman, P. B. S.: Low-Reynolds-number airfoils, Annual Review of Fluid Mechanics, 15(1), https://doi.org/10.1146/annurev.fl.15.010183.001255, 1983.

Lyon, C. and Selig, M. S.: Summary of low speed airfoil data, Soartech Publications, Virginia, USA, 1997.

Martínez-Tossas, L. A., Churchfield, M. J. and Leonardi, S.: Large eddy simulations of the flow past wind turbines: actuator line and disk modeling, Wind Energy, 18.6, 1047–1060, https://doi.org/10.1002/we.1747, 2015.

Meinhart, C. D., Wereley, S. T., and Santiago, J. G.: PIV measurements of a microchannel flow, Exp. Fluids., 27.5, 414–419, https://doi.org/10.1007/s003480050366, 1999.

Mittal, R. and Iaccarino, G.: Immersed boundary methods, Annu. Rev. Fluid Mech, 37, 239–261, https://doi.org/10.1146/annurev.fluid.37.061903.175743, 2005.

Okulov, V. L. and Sørensen, J. N.: Stability of helical tip vortices in a rotor far wake, J. Fluid Mech. 576, 1–25, https://doi.org/10.1017/S0022112006004228, 2007.

Pitt, D. M., and Peters, D. A.: Theoretical prediction of dynamic-inflow derivatives, Vertica, 5.1, 21–34, https://doi.org/20.500.11881/1796, 1981.

Shipley, D. E., Miller, M. S., and Robinson, M. C.: Dynamic stall occurrence on a horizontal axis wind turbine blade, in: CONF-950116-8, National Renewable Energy Lab., Golden, CO, US, 1995.

https://doi.org/10.5194/wes-2020-115
Preprint. Discussion started: 10 November 2020

Smagorinsky, J.: General circulation experiments with the primitive equations: I. The basic experiment, Monthly weather rev., 91.3, 99–164, https://doi.org/10.1175/1520-0493(1963)091<0099:GCEWTP>2.3.CO;2, 1963.

Snel, H., Houwink, R. and Bosschers, J.: Sectional prediction of lift coefficients on rotating wind turbine blades in stall. Netherlands Energy Research Foundation, Petten, Netherlands, 1994.

Sørensen, J. N.: Instability of helical tip vortices in rotor wakes, J. Fluid Mech., 682, 1–4, https://doi.org/10.1017/jfm.2011.277, 2011.

Tian, W., Ozbay, A. and Hu, H.: An experimental investigation on the wake interferences among wind turbines sited in aligned and staggered wind farms, Wind Energy, 21.2, 100–114, https://doi.org/10.1002/we.2147, 2018.

Troldborg, N., Sørensen, J. N. and Mikkelsen, R.: Actuator line simulation of wake of wind turbine operating in turbulent inflow, J. Phys. Conf. Ser., 75.1, https://doi.org/10.1088/1742-6596/75/1/012063, 2007.

van der Laan, M. P., and Sørensen, N. N.: Why the Coriolis force turns a wind farm wake to the right in the Northern Hemisphere, J. Phys.: Conf. Ser. 753 032031, https://doi.org/10.1088/1742-6596/753/3/032031, 2016.

van Dooren, M. F., Campagnolo, F., Sjöholm, M., Angelou, N. and Mikkelsen, T.: Demonstration and uncertainty analysis of synchronised scanning lidar measurements of 2-D velocity fields in a boundary-layer wind tunnel, Wind Energy Science, 2, 329–341, https://doi.org/10.5194/wes-2-329-2017, 2017.

Wang, C., Wang, J., Campagnolo, F., Carraón, D. B. and Bottasso, C. L.: Validation of large-eddy simulation of scaled waked wind turbines in different yaw misalignment conditions, J. Phys. Conf. Ser., 1037 062007, https://doi.org/10.1088/1742-6596/1037/6/062007, 2018.

Wang, J., Wang, C., Campagnolo, F. and Bottasso, C. L.: Wake behavior and control: comparison of LES simulations and wind tunnel measurements, Wind Energy Sci., 4.1, 71–88, https://doi.org/10.5194/wes-4-71-2019, 2019.

Wang, C., Campagnolo, F. and Bottasso, C. L.: Identification of airfoil polars from uncertain experimental measurements, Wind Energy Sci., accepted, to appear, 2020.

Wang, C., Muñoz-Simón, A. Deskos, G., Laizet, S., Palacios, R., Campagnolo, F. and Bottasso, C. L.: Code-to-code-to-experiment validation of LES-ALM wind farm simulators, J. Phys. Conf. Ser. 1618 062041, https://doi.org/10.1088/1742-6596/1618/6/062041, 2020.

Wang, C., Campagnolo, F., Sharma, A. and Bottasso, C. L.: Effects of dynamic induction control on power and loads, by LES-ALM simulations and wind tunnel experiments, J. of Phys.: Conf. Ser. 1618 022036, https://doi.org/10.1088/1742-6596/1618/2/022036, 2020.

Whale, J., Papadopoulos, K. H., Anderson, C. G., Helmis, C. G., and Skyner, D. J.: A study of the near wake structure of a wind turbine comparing measurements from laboratory and full-scale experiments, Solar Energy, 56.6, https://doi.org/10.1016/0038-092X(96)00019-9, 1996.

WindEEE https://www.eng.uwo.ca/windeee/, last accessed: 13 October 2020.

Wu, Y. and Porté-Agel, F.: Large-eddy simulation of wind-turbine wakes: evaluation of turbine parametrisations, Boundary-layer Meteorol., 138.3, 345–366, https://doi.org/10.1007/s10546-010-9569-x, 2011.

Zhan, L., Letizia, S., and Iungo, G. V.: LiDAR measurements for an onshore wind farm: Wake variability for different incoming wind speeds and atmospheric stability regimes, Wind Energy, 23.3, 501–527, https://doi.org/doi.org/10.1002/we.2430, 2020.

[1] B. Looney, "Full report–bp statistical review of world energy 2020," BP plc, London,, Tech. Rep., 2020.

[2] S. Mann, I. Harris, and J. Harris, "Renewable and sustainable energy reviews," Citeseer, Tech. Rep., 2004.

[3] T. J. Stehly and P. C. Beiter, "2018 cost of wind energy review," National Renewable Energy Lab.(NREL), Golden, CO (United States), Tech. Rep., 2020.

[4] T. Knudsen, T. Bak, and M. Svenstrup, "Survey of wind farm control—power and fatigue optimization," *Wind Energy*, vol. 18, no. 8, pp. 1333–1351, 2015. doi: https://doi.org/10.1002/we.1760

[5] K. E. Johnson and N. Thomas, "Wind farm control: Addressing the aerodynamic interaction among wind turbines," in *2009 American Control Conference*. IEEE, 2009, pp. 2104–2109. doi: 10.1109/ACC.2009.5160152

[6] L. Ya-zhou and G. Lightbody, "An introduction on wind power grid code and dynamic simulation," *Power System Technology*, vol. 12, pp. 27–32, 2005.

[7] J.-W. van Wingerden, L. Pao, J. Aho, and P. Fleming, "Active power control of waked wind farms," *IFAC-PapersOnLine*, vol. 50, no. 1, pp. 4484–4491, 2017. doi: https://doi.org/10.1016/j.ifacol.2017.08.378

[8] F. Ebrahimi, A. Khayatiyan, and E. Farjah, "A novel optimizing power control strategy for centralized wind farm control system," *Renewable energy*, vol. 86, pp. 399–408, 2016. doi: https://doi.org/10.1016/j.renene.2015.07.101

[9] D. Simms, S. Schreck, M. Hand, and L. J. Fingersh, "Nrel unsteady aerodynamics experiment in the nasa-ames wind tunnel: a comparison of predictions to measurements," National Renewable Energy Lab., Golden, CO (US), Tech. Rep., 2001.

[10] Y.-T. Wu and F. Porté-Agel, "Large-eddy simulation of wind-turbine wakes: evaluation of turbine parametrisations," *Boundary-layer meteorology*, vol. 138, no. 3, pp. 345–366, 2011. doi: https://doi.org/10.1007/s10546-010-9569-x

[11] P. Gebraad, J. J. Thomas, A. Ning, P. Fleming, and K. Dykes, "Maximization of the annual energy production of wind power plants by optimization of layout and yaw-based wake control," *Wind Energy*, vol. 20, no. 1, pp. 97–107, 2017. doi: https://doi.org/10.1002/we.1993

[12] M. Adaramola and P.-Å. Krogstad, "Experimental investigation of wake effects on wind turbine performance," *Renewable Energy*, vol. 36, no. 8, pp. 2078–2086, 2011. doi: https://doi.org/10.1016/j.renene.2011.01.024

[13] H. Meng, F.-S. Lien, and L. Li, "Elastic actuator line modelling for wake-induced fatigue analysis of horizontal axis wind turbine blade," *Renewable Energy*, vol. 116, pp. 423–437, 2018. doi: https://doi.org/10.1016/j.renene.2017.08.074

[14] A. Kusiak and Z. Song, "Design of wind farm layout for maximum wind energy capture," *Renewable energy*, vol. 35, no. 3, pp. 685–694, 2010. doi: https://doi.org/10.1016/j.renene.2009.08.019

[15] A. N. Kolmogorov, "The local structure of turbulence in incompressible viscous fluid for very large reynolds numbers," *Proceedings of the Royal Society of London. Series A: Mathematical and Physical Sciences*, vol. 434, no. 1890, pp. 9–13, 1991. doi: https://doi.org/10.1098/rspa.1991.0075

[16] Y. Wu, S. Zhang, R. Wang, Y. Wang, and X. Feng, "A design methodology for wind farm layout considering cable routing and economic benefit based on genetic algorithm and geosteiner," *Renewable Energy*, vol. 146, pp. 687–698, 2020. doi: https://doi.org/10.1016/j.renene.2019.07.002

[17] C. L. Bottasso, F. Campagnolo, and V. Petrović, "Wind tunnel testing of scaled wind turbine models: Beyond aerodynamics," *Journal of wind engineering and industrial aerodynamics*, vol. 127, pp. 11–28, 2014. doi: https://doi.org/10.1016/j.jweia.2014.01.009

[18] E. Buckingham, "On physically similar systems; illustrations of the use of dimensional equations," *Physical review*, vol. 4, no. 4, p. 345, 1914. doi: https://doi.org/10.1103/PhysRev.4.345

[19] I. Ammara, C. Leclerc, and C. Masson, "A viscous three-dimensional differential/actuator-disk method for the aerodynamic analysis of wind farms," *J. Sol. Energy Eng.*, vol. 124, no. 4, pp. 345–356, 2002. doi: https://doi.org/10.1115/1.1510870

[20] S. Aubrun, S. Loyer, P. Hancock, and P. Hayden, "Wind turbine wake properties: Comparison between a non-rotating simplified wind turbine model and a rotating model," *Journal of Wind Engineering and Industrial Aerodynamics*, vol. 120, pp. 1–8, 2013. doi: https://doi.org/10.1016/j.jweia.2013.06.007

[21] L. Vermeer, J. N. Sørensen, and A. Crespo, "Wind turbine wake aerodynamics," *Progress in aerospace sciences*, vol. 39, no. 6-7, pp. 467–510, 2003. doi: https://doi.org/10.1016/S0376-0421(03)00078-2

[22] H. Snel, G. Schepers, and N. Siccama, "Mexico project: the database and results of data processing and interpretation," in *47th AIAA Aerospace Sciences Meeting Including the New Horizons Forum and Aerospace Exposition*, 2009, p. 1217.

[23] G. Diana, S. De Ponte, M. Falco, and A. Zasso, "A new large wind tunnel for civil-environmental and aeronautical applications," *Journal of Wind Engineering and Industrial Aerodynamics*, vol. 74, pp. 553–565, 1998. doi: https://doi.org/10.1016/S0167-6105(98)00050-6

[24] F. Berger, L. Kröger, D. Onnen, V. Petrović, and M. Kühn, "Scaled wind turbine setup in a turbulent wind tunnel," *Proceedings of the EERA DeepWind'2018*, 2018. doi: 10.1088/1742-6596/1104/1/012026

[25] F. Campagnolo, V. Petrović, J. Schreiber, E. M. Nanos, A. Croce, and C. L. Bottasso, "Wind tunnel testing of a closed-loop wake deflection controller for wind farm power maximization," in *Journal of Physics: Conference Series*, vol. 753. IOP Publishing, 2016, p. 032006. doi: 10.1088/1742-6596/753/3/032006

[26] C. L. Archer and A. Vasel-Be-Hagh, "Wake steering via yaw control in multi-turbine wind farms: Recommendations based on large-eddy simulation," *Sustainable Energy Technologies and Assessments*, vol. 33, pp. 34–43, 2019. doi: https://doi.org/10.1016/j.seta.2019.03.002

[27] P. M. Gebraad, F. Teeuwisse, J. Van Wingerden, P. A. Fleming, S. Ruben, J. Marden, and L. Pao, "Wind plant power optimization through yaw control using a parametric model for

wake effects—a cfd simulation study," *Wind Energy*, vol. 19, no. 1, pp. 95–114, 2016. doi: https://doi.org/10.1002/we.1822

[28] K. A. Kragh and M. H. Hansen, "Load alleviation of wind turbines by yaw misalignment," *Wind Energy*, vol. 17, no. 7, pp. 971–982, 2014. doi: https://doi.org/10.1002/we.1612

[29] P. A. Fleming, A. Ning, P. M. Gebraad, and K. Dykes, "Wind plant system engineering through optimization of layout and yaw control," *Wind Energy*, vol. 19, no. 2, pp. 329–344, 2016. doi: https://doi.org/10.1002/we.1836

[30] M. F. van Dooren, F. Campagnolo, M. Sjöholm, N. Angelou, T. Mikkelsen, and M. Kühn, "Demonstration and uncertainty analysis of synchronised scanning lidar measurements of 2-d velocity fields in a boundary-layer wind tunnel," *Wind Energy Science*, vol. 2, no. 1, p. 329, 2017. doi: https://doi.org/10.5194/wes-2-329-2017

[31] W. Munters and J. Meyers, "An optimal control framework for dynamic induction control of wind farms and their interaction with the atmospheric boundary layer," *Philosophical Transactions of the Royal Society A: Mathematical, Physical and Engineering Sciences*, vol. 375, no. 2091, p. 20160100, 2017. doi: https://doi.org/10.1098/rsta.2016.0100

[32] ——, "Towards practical dynamic induction control of wind farms: analysis of optimally controlled wind-farm boundary layers and sinusoidal induction control of first-row turbines," *Wind Energy Science*, vol. 3, no. 1, pp. 409–425, 2018. doi: https://doi.org/10.5194/wes-3-409-2018

[33] J. A. Frederik, R. Weber, S. Cacciola, F. Campagnolo, A. Croce, C. Bottasso, J.-W. van Wingerden *et al.*, "Periodic dynamic induction control of wind farms: proving the potential in simulations and wind tunnel experiments," Politecnico di Milano, Tech. Rep., 2020.

[34] E. A. Bossanyi, "Individual blade pitch control for load reduction," *Wind Energy: An International Journal for Progress and Applications in Wind Power Conversion Technology*, vol. 6, no. 2, pp. 119–128, 2003. doi: https://doi.org/10.1002/we.76

[35] ——, "Further load reductions with individual pitch control," *Wind Energy: An International Journal for Progress and Applications in Wind Power Conversion Technology*, vol. 8, no. 4, pp. 481–485, 2005.

[36] J. F. Manwell, J. G. McGowan, and A. L. Rogers, *Wind energy explained: theory, design and application*. John Wiley & Sons, 2010.

[37] C. L. Bottasso, S. Cacciola, and X. Iriarte, "Calibration of wind turbine lifting line models from rotor loads," *Journal of Wind Engineering and Industrial Aerodynamics*, vol. 124, pp. 29–45, 2014. doi: https://doi.org/10.1016/j.jweia.2013.11.003

[38] V. Klein and E. Morelli, "Aircraft system identification: Theory and practice. american institute of aeronautics and astronautics," Inc Virginia, Tech. Rep., 2006.

[39] R. V. Jategaonkar, *Flight vehicle system identification: A time-domain methodology*. American Institute of Aeronautics and Astronautics, Inc., 2015.

[40] J. Wang, C. Wang, F. Campagnolo, and C. L. Bottasso, "Wake behavior and control: comparison of les simulations and wind tunnel measurements," *Wind Energy Science*, vol. 4, no. 1, pp. 71–88, 2019. doi: https://doi.org/10.5194/wes-4-71-2019

[41] F. Campagnolo, R. Weber, J. Schreiber, and C. L. Bottasso, "Wind tunnel testing of wake steering with dynamic wind direction changes," *Wind Energy Science Discussions*, pp. 1–33, 2020. doi: https://doi.org/10.5194/wes-2020-70

[42] C. E. Carcangiu, *CFD-RANS study of horizontal axis wind turbines*. Università degli Studi di Cagliari, 2008.

[43] T. Stovall, G. Pawlas, and P. Moriarty, "Wind farm wake simulations in openfoam," in *48th AIAA Aerospace Sciences Meeting*, 2010, p. 825. doi: https://doi.org/10.2514/6.2010-825

[44] P. A. Fleming, P. M. Gebraad, S. Lee, J.-W. van Wingerden, K. Johnson, M. Churchfield, J. Michalakes, P. Spalart, and P. Moriarty, "Evaluating techniques for redirecting turbine wakes using sowfa," *Renewable Energy*, vol. 70, pp. 211–218, 2014. doi: https://doi.org/10.1016/j.renene.2014.02.015

[45] H. Jasak, "Openfoam: open source cfd in research and industry," *International Journal of Naval Architecture and Ocean Engineering*, vol. 1, no. 2, pp. 89–94, 2009. doi: 10.3744/JNAOE.2009.1.2.089

[46] N. Troldborg, J. N. Sørensen, and R. Mikkelsen, "Actuator line simulation of wake of wind turbine operating in turbulent inflow," in *Journal of physics: conference series*, vol. 75, no. 1. IOP Publishing, 2007, p. 012063. doi: 10.1088/1742-6596/75/1/012063

[47] S. Guntur, J. M. Jonkman, B. Jonkman, Q. Wang, M. A. Sprague, M. Hind, R. Sievers, and S. J. Schreck, "Fast v8 verification and validation for a mw-scale wind turbine with aeroelastically tailored blades," in *34th Wind Energy Symposium*, 2016, p. 1008. doi: https://doi.org/10.2514/6.2016-1008

[48] P. K. Jha and S. Schmitz, "Actuator curve embedding–an advanced actuator line model," *Journal of Fluid Mechanics*, vol. 834, 2018. doi: https://doi.org/10.1017/jfm.2017.793

[49] L. A. Martínez-Tossas, M. J. Churchfield, and S. Leonardi, "Large eddy simulations of the flow past wind turbines: actuator line and disk modeling," *Wind Energy*, vol. 18, no. 6, pp. 1047–1060, 2015. doi: https://doi.org/10.1002/we.1747

[50] P. K. Jha, M. J. Churchfield, P. J. Moriarty, and S. Schmitz, "Guidelines for volume force distributions within actuator line modeling of wind turbines on large-eddy simulation-type grids," *Journal of Solar Energy Engineering*, vol. 136, no. 3, 2014. doi: https://doi.org/10.1115/1.4026252

[51] L. A. Martínez-Tossas, M. J. Churchfield, and C. Meneveau, "Optimal smoothing length scale for actuator line models of wind turbine blades based on gaussian body force distribution," *Wind Energy*, vol. 20, no. 6, pp. 1083–1096, 2017. doi: https://doi.org/10.1002/we.2081

[52] L. A. Martinez, C. Meneveau, and R. Stevens, "Wind farm large-eddy simulations on very coarse grid resolutions using an actuator line model," in *34th Wind Energy Symposium*, 2016, p. 1261. doi: https://doi.org/10.2514/6.2016-1261

[53] M. J. Churchfield, S. Lee, S. Schmitz, and Z. Wang, "Modeling wind turbine tower and nacelle effects within an actuator line model," in *33rd Wind Energy Symposium*, 2015, p. 0214. doi: https://doi.org/10.2514/6.2015-0214

[54] H. Jasak, D. Rigler, and Ž. Tuković, "Finite volume immersed boundary method for turbulent flow simulations," in *9th OpenFOAM Workshop*, 2014.

[55] C. Wang, J. Wang, F. Campagnolo, D. Carraón, and C. Bottasso, "Validation of large-eddy simulation of scaled waked wind turbines in different yaw misalignment conditions," in *Journal of Physics: Conference Series*, vol. 1037, no. 6. IOP Publishing, 2018, p. 062007. doi: 10.1088/1742-6596/1037/6/062007

[56] M. J. Churchfield, L. Sang, and P. J. Moriarty, "Adding complex terrain and stable atmospheric condition capability to the openfoam-based flow solver of the simulator for on/offshore wind farm applications (sowfa)," National Renewable Energy Lab.(NREL), Golden, CO (United States), Tech. Rep., 2013.

[57] J. Nathan, "Application of actuator surface concept in les simulations of the near wake of wind turbines," Ph.D. dissertation, École de technologie supérieure, 2018.

[58] C. L. Bottasso and F. Campagnolo, *Handbook of Wind Energy Aerodynamics*. Springer, 2020.

[59] J. Whale, K. Papadopoulos, C. Anderson, C. Helmis, and D. Skyner, "A study of the near wake structure of a wind turbine comparing measurements from laboratory and full-scale experiments," *Solar energy*, vol. 56, no. 6, pp. 621–633, 1996. doi: https://doi.org/10.1016/0038-092X(96)00019-9

[60] L. P. Chamorro and F. Porté-Agel, "A wind-tunnel investigation of wind-turbine wakes: boundary-layer turbulence effects," *Boundary-layer meteorology*, vol. 132, no. 1, pp. 129–149, 2009. doi: https://doi.org/10.1007/s10546-009-9380-8

[61] ——, "Effects of thermal stability and incoming boundary-layer flow characteristics on wind-turbine wakes: a wind-tunnel study," *Boundary-layer meteorology*, vol. 136, no. 3, pp. 515–533, 2010. doi: https://doi.org/10.1007/s10546-010-9512-1

[62] L. P. Chamorro, R. Arndt, and F. Sotiropoulos, "Reynolds number dependence of turbulence statistics in the wake of wind turbines," *Wind Energy*, vol. 15, no. 5, pp. 733–742, 2012. doi: https://doi.org/10.1002/we.501

[63] H. Canet, P. Bortolotti, and C. L. Bottasso, "On the scaling of wind turbine rotors," *Wind Energy Science Discussions*, pp. 1–35, 2020. doi: https://doi.org/10.5194/wes-2020-66

[64] C. Wang, F. Campagnolo, and C. L. Bottasso, "Identification of airfoil polars from uncertain experimental measurements," *Wind Energy Science*, vol. 5, pp. 1537–1550, 2020. doi: https://doi.org/10.5194/wes-5-1537-2020

[65] C. Wang, A. Muñóz-Simon, G. Deskos, S. Laizet, R. Palacios, F. Campagnolo, and C. Bottasso, "Code-to-code-to-experiment validation of les-alm wind farm simulators," in *Journal of Physics: Conference Series*, vol. 1618, no. 6. IOP Publishing, 2020, p. 062041. doi: 10.1088/1742-6596/1618/6/062041

[66] C. Wang, F. Campagnolo, A. Sharma, and C. Bottasso, "Effects of dynamic induction control on power and loads, by les-alm simulations and wind tunnel experiments," in *Journal of Physics: Conference Series*, vol. 1618, no. 2. IOP Publishing, 2020, p. 022036. doi: 10.1088/1742-6596/1618/2/022036

[67] C. Wang, F. Campagnolo, and C. Bottasso, "Does the use of load-reducing IPC on a wake-steering turbine affect wake behavior?" in *Journal of Physics: Conference Series*, vol. 1618, no. 2. IOP Publishing, 2020, p. 022035. doi: 10.1088/1742-6596/1618/2/022035

[68] C. Wang, F. Campagnolo, H. Canet, D. J. Barreiro, and C. L. Bottasso, "How realistic are turbine wakes in wind tunnel tests?" *Wind Energy Science, in review*, 2020. doi: https://doi.org/10.5194/wes-2020-115

[69] A. Fortes-Plaza, F. Campagnolo, J. Wang, C. Wang, C. Bottasso *et al.*, "A POD reduced-order model for wake steering control," in *Journal of Physics: Conference Series*, vol. 1037, no. 3, 2018. doi: 10.1088/1742-6596/1037/3/032014

[70] L. Mydlarski and Z. Warhaft, "On the onset of high-reynolds-number grid-generated wind tunnel turbulence," *Journal of Fluid Mechanics*, vol. 320, pp. 331–368, 1996. doi: https://doi.org/10.1017/S0022112096007562

[71] P. Knebel, A. Kittel, and J. Peinke, "Atmospheric wind field conditions generated by active grids," *Experiments in fluids*, vol. 51, no. 2, pp. 471–481, 2011. doi: https://doi.org/10.1007/s00348-011-1056-8

[72] T. Aufderheide, C. Bode, J. Friedrichs, and D. Kozulovic, "The generation of higher levels of turbulence in a low-speed cascade wind tunnel by pressurized tubes," in *VI European Conference on Computational Fluid Dynamics (ECFD)*, 2014, pp. 20–25.

[73] A. J. Morales, M. K. Geikie, C. Engelmann, and K. Ahmed, "Development and characterization of a turbulence generator for low-speed wind tunnel applications," in *53rd AIAA/SAE/ASEE Joint Propulsion Conference*, 2017, p. 4966. doi: https://doi.org/10.2514/6.2017-4966

[74] S. G. Giappino, S. Muggiasca, L. P. Rosa, and A. Zasso, "Optimization of the boundary layer characteristics simulated at politecnico di milano boundary layer wind tunnel in a wide scale ratio range," in *6. Asia-Pacific Conference on Wind Engineering (APCWE VI)*, 2005, pp. 708–723. doi: http://hdl.handle.net/11311/250412

[75] C. Farell and A. K. Iyengar, "Experiments on the wind tunnel simulation of atmospheric boundary layers," *Journal of wind engineering and industrial aerodynamics*, vol. 79, no. 1-2, pp. 11–35, 1999. doi: https://doi.org/10.1016/S0167-6105(98)00117-2

[76] H. Glauert, "Airplane propellers," in *Aerodynamic theory*. Springer, 1935, pp. 169–360.

[77] J. F. Manwell, J. G. McGowan, and A. L. Rogers, *Wind energy explained: theory, design and application*. John Wiley & Sons, 2010.

[78] T. Burton, N. Jenkins, D. Sharpe, and E. Bossanyi, *Wind energy handbook*. John Wiley & Sons, 2011.

[79] Anonymous, *OpenFast documentation Release v2.3.0*. National Renewable Energy Laboratory, 2020.

[80] L. A. Martínez-Tossas, M. J. Churchfield, and C. Meneveau, "A highly resolved large-eddy simulation of a wind turbine using an actuator line model with optimal body force projection," in *Journal of Physics: Conference Series*, vol. 753, no. 8. IOP Publishing, 2016, p. 082014. doi: 10.1088/1742-6596/753/8/082014

[81] L. A. Martínez-Tossas and C. Meneveau, "Filtered lifting line theory and application to the actuator line model," *Journal of Fluid Mechanics*, vol. 863, pp. 269–292, 2019. doi: 10.1017/jfm.2018.994

[82] C. L. Bottasso, S. Cacciola, and X. Iriarte, "Calibration of wind turbine lifting line models from rotor loads," *Journal of Wind Engineering and Industrial Aerodynamics*, vol. 124, pp. 29–45, 2014. doi: https://doi.org/10.1016/j.jweia.2013.11.003

[83] V. Klein and E. A. Morelli, *Aircraft system identification: theory and practice*. American Institute of Aeronautics and Astronautics Reston, VA, 2006.

[84] R. V. Jategaonkar, *Flight vehicle system identification: A time-domain methodology*. American Institute of Aeronautics and Astronautics, Inc., 2015.

[85] M. S. Selig, *Summary of low speed airfoil data*. SOARTECH publications, 1995.

[86] M. Selig and B. McGranahan, "Wind tunnel aerodynamic tests of six airfoils for use on small wind turbines," in *42nd AIAA Aerospace Sciences Meeting and Exhibit*, 2004, p. 1188. doi: https://doi.org/10.1115/1.1793208

[87] C. Bak, F. Zahle, R. Bitsche, T. Kim, A. Yde, L. C. Henriksen, M. H. Hansen, J. P. A. A. Blasques, M. Gaunaa, and A. Natarajan, "The dtu 10-mw reference wind turbine," in *Danish Wind Power Research 2013*, 2013.

[88] R. Mittal and G. Iaccarino, "Immersed boundary methods," *Annu. Rev. Fluid Mech.*, vol. 37, pp. 239–261, 2005. doi: https://doi.org/10.1146/annurev.fluid.37.061903.175743

[89] U. Senturk, D. Brunner, H. Jasak, N. Herzog, C. W. Rowley, and A. J. Smits, "Benchmark simulations of flow past rigid bodies using an open-source, sharp interface immersed boundary method," *Progress in Computational Fluid Dynamics, an International Journal*, vol. 19, no. 4, pp. 205–219, 2019. doi: https://doi.org/10.1504/PCFD.2019.100870

[90] H. Jasak, D. Rigler, and Ž. Tuković, "Design and implementation of immersed boundary method with discrete forcing approach for boundary conditions," in *11th World Congress on Computational Mechanics, WCCM 2014*, 2014, pp. 5319–5332. doi: http://repozitorij.fsb.hr/id/eprint/4241

[91] P. Fleming, P. Gebraad, J.-W. van Wingerden, S. Lee, M. Churchfield, A. Scholbrock, J. Michalakes, K. Johnson, and P. Moriarty, "Sowfa super-controller: A high-fidelity tool for evaluating wind plant control approaches," National Renewable Energy Laboratory, Golden, CO (United States), Tech. Rep., 2013.

[92] W. Gropp, W. D. Gropp, E. Lusk, A. Skjellum, and A. D. F. E. E. Lusk, *Using MPI: portable parallel programming with the message-passing interface*. MIT press, 1999, vol. 1.

[93] J. Smagorinsky, "General circulation experiments with the primitive equations: I. the basic experiment," *Monthly weather review*, vol. 91, no. 3, pp. 99–164, 1963. doi: https://doi.org/10.1175/1520-0493(1963)091<0099:GCEWTP>2.3.CO;2

[94] J. Boussinesq, *Théorie de l'écoulement tourbillonnant et tumultueux des liquides dans les lits rectilignes a grande section*. Gauthier-Villars, 1897, vol. 1.

[95] R. I. Issa, "Solution of the implicitly discretised fluid flow equations by operator-splitting," *Journal of computational physics*, vol. 62, no. 1, pp. 40–65, 1986. doi: https://doi.org/10.1016/0021-9991(86)90099-9

[96] P. J. Mason, "Large-eddy simulation of the convective atmospheric boundary layer," *Journal of the atmospheric sciences*, vol. 46, no. 11, pp. 1492–1516, 1989. doi: https://doi.org/10.1175/1520-0469(1989)046<1492:LESOTC>2.0.CO;2

[97] F. Porté-Agel, C. Meneveau, and M. B. Parlange, "A scale-dependent dynamic model for large-eddy simulation: application to a neutral atmospheric boundary layer," *Journal of Fluid Mechanics*, vol. 415, pp. 261–284, 2000. doi: https://doi.org/10.1017/S0022112000008776

[98] C. Bak, F. Zahle, R. Bitsche, T. Kim, A. Yde, L. C. Henriksen, A. Natarajan, and M. Hansen, "Description of the dtu 10 mw reference wind turbine, dtu wind energy report-i-0092 5," Technical University of Denmark, Tech. Rep., 2013.

[99] H. Snel, R. Houwink, J. Bosschers *et al.*, *Sectional prediction of lift coefficients on rotating wind turbine blades in stall.* Netherlands Energy Research Foundation Petten, The Netherlands, 1994.

[100] F. Campagnolo, *Wind tunnel testing of scaled wind turbine models: aerodynamics and beyond.* Politecnico di Milano, 2013.

[101] J. A. Frederik, B. M. Doekemeijer, S. P. Mulders, and J.-W. van Wingerden, "The helix approach: Using dynamic individual pitch control to enhance wake mixing in wind farms," *Wind Energy*, 2020. doi: https://doi.org/10.1002/we.2513